Ultrafast mid-infrared studies on BH_4^- ions, $H_2PO_4^-$ ions, and a bulk plasmon in Ga-doped ZnO

DISSERTATION

zur Erlangung des akademischen Grades
d o c t o r r e r u m n a t u r a l i u m
(Dr. rer. nat.)
im Fach Physik

eingereicht an der
Mathematisch-Naturwissenschaftlichen Fakultät I
Institut für Physik
Humboldt-Universität zu Berlin

Präsident der Humboldt-Universität zu Berlin
Prof. Dr. Jan-Hendrik Olbertz

Dekan der Mathematisch-Naturwissenschaftlichen Fakultät
Prof. Dr. Elmar Kulke

von
Herr M.Sc. Tobias Tyborski

Gutachter:

1. Prof. Dr. Thomas Elsässer
2. Prof. Dr. Oliver Benson
3. Prof. Dr. Peter Hamm

Eingereicht am: 05.04.2016
Tag der mündlichen Prüfung: 05.07.2016

Abstract

Two-dimensional IR spectroscopy and IR pump/probe spectroscopy with a femtosecond time resolution were applied to investigate ultrafast vibrational dynamics of $H_2PO_4^-$ ions in an aqueous solution, of BH_4^- ions in liquid and crystalline environments, and the nonlinear response of a bulk plasmon in a layer system of highly Ga-doped ZnO layers.

Phosphates are important building blocks of biomolecules such as DNA or phospholipids and constitute their major hydration sites. Hence, a strong interaction occurs among phosphates and their surrounding water shells, which allows for a mapping of hydrogen bond dynamics and structural fluctuations within the network of water molecules. At interfacial sites such as a DNA-water interface, phosphate vibrations were successfully utilised as local probes for decelerated water dynamics, caused by spatial characteristics and restrictions. Here, phosphate vibrations of the ion $H_2PO_4^-$ dissolved in water are introduced as local probes for the full fluctuation dynamics of bulk water. Homogeneously broadened line shapes are observed in 2D-IR experiments for the asymmetric and symmetric phosphate vibrations $\nu_{AS}(PO_2^-)$ and $\nu_S(PO_2^-)$ with an underlying correlation time of 50 fs; a timescale typical for water librations. A second infinitely large correlation time is measured that describes a weak inhomogeneous contribution resulting from quasi-static spatial configurations of the phosphate-water system. Vibrational lifetimes of ≈ 300 fs are measured for $\nu_{AS}(PO_2^-)$, $\nu_S(PO_2^-)$, the asymmetric and symmetric P-$(OH)_2$ bending vibrations, and the asymmetric P-$(OH)_2$ stretching vibration, respectively. Cluster calculations reveal a strong sensitivity of phosphate vibrations on the hydration level and show that phosphate-water hydrogen bonds are stronger than water-water hydrogen bonds.

$NaBH_4$ is a complex hydride and, thus, a hydrogen carrier and potential energy carrier for mobile applications. It combines two crucial properties: i) a large volumetric hydrogen content, and ii) a low overall mass, especially in comparison to intermetallic compounds. Unfortunately, hydrogen uptake and release of hydrogen covalently bound in BH_4^- tetrahedrons are both energetically expensive. To get a detailed microscopic understanding of B-H vibrations and, therewith, of hydrogen dynamics, pump/probe experiments were performed on BH_4^- ions dissolved in a liquid solution and embedded in the crystalline environment $NaBH_4$. A strong Fermi resonance coupling of the asymmetric BH_4^- stretching vibration ν_3 with the first overtone of the BH_4^- bending vibration ν_4 enables the dissipation of excess energy from ν_3 over ν_4 into either the vibrational manifold of the solvent or the low-frequency phonon modes of $NaBH_4$, revealed by two-colour pump/probe measurements. In one-colour pump/probe measurements, excited state lifetimes of 3.0 ps for ν_3 and of 3.6 ps for ν_4 are observed. Due to the high packing density of BH_4^- tetrahedrons in the $NaBH_4$ crystal, a radiative coupling occurs among them, which leads to a quick reemission of absorbed excess energy on a sub-500 fs timescale. Furthermore, a strong anharmonic coupling of excited low-frequency modes in $NaBH_4$ to ν_3 and ν_4 leads to significantly more intense thermal pump/probe signatures in the $NaBH_4$ crystal compared to the liquid solution.

Bulk plasmons represent collective longitudinal excitations of free electron gases in ionic or polar crystal lattices. In contrast to widely explored surface plasmon polaritons, the nonlinear response of a bulk plasmon has not been investigated so far with optical methods and a femtosecond time resolution, but it is very meaningful for ultrafast applications. A

bulk plasmon resonance of a highly Ga-doped ZnO layer in a particularly designed layer system is investigated with pump/probe spectroscopy. Intraband excitation of conduction band electrons in ZnO leads to a heating of the electron gas. Due to hyperbolic non-parabolicities in the conduction band structure of ZnO, the heating results in an increase of the ensemble averaged electron mass and, consequently, in a reduction or redshift of the bulk plasmon frequency. Due to a strong polar-optical coupling of the electron gas with longitudinal optical phonons in ZnO, the relaxation of excess energy proceeds via the emission of longitudinal optical phonons on a 300 fs timescale. The time-dependent redshift is accompanied by a broadening of the plasma resonance.

List of publications

Publications related to this work

1. T. Tyborski, R. Costard, M. Woerner, and T. Elsaesser, "Ultrafast vibrational dynamics of BH_4^- ions in liquid and crystalline environments", *J. Chem. Phys.*, vol. 141, no. 3, p. 034506, 2014

2. T. Tyborski, S. Kalusniak, S. Sadofev, F. Henneberger, M. Woerner, and T. Elsaesser, "Ultrafast nonlinear response of bulk plasmons in highly doped ZnO layers", *Phys. Rev. Lett.*, vol. 115, no. 14, p. 147401, 2015

3. R. Costard, T. Tyborski, B. P. Fingerhut, T. Elsaesser, "Ultrafast phosphate hydration dynamics in bulk H_2O", *J. Chem. Phys.*, vol. 142, no. 21, p. 212406, 2015

4. R. Costard, T. Tyborski, and B. P. Fingerhut, "Anharmonicities and coherent vibrational dynamics of phosphate ions in bulk H_2O", *Phys. Chem. Chem. Phys.*, vol. 17, no. 44, pp. 29906-29917, 2015

Further publications

5. T. Tyborski, C. Merschjann, S. Orthmann, F. Yang, M. Lux-Steiner, and T. Schedel-Niedrig, "Tunable optical transition in polymeric carbon nitrides synthesized via bulk thermal condensation", *J. Phys.: Condens. Matter*, vol. 24, no. 16, p. 162201, 2012

6. T. Tyborski, C. Merschjann, S. Orthmann, F. Yang, M. Lux-Steiner, and T. Schedel-Niedrig, "Crystal structure of polymeric carbon nitride and the determination of its process-temperature-induced modifications", *J. Phys.: Condens. Matter*, vol. 25, no. 39, p. 395402, 2013

7. C. Merschjann, T. Tyborski, S. Orthmann, F. Yang, K. Schwarzburg, M. Lublow, M. Lux-Steiner, and T. Schedel-Niedrig, "Photophysics of polymeric carbon nitride: An optical quasimonomer", *Phys. Rev. B*, vol. 87, no. 20, p. 205204, 2013

8. M. Guk, C. Merschjann, I. Bodnar, T. Tyborski, T. Schedel-Niedrig, M. Lux-Steiner, and E. Arushanov, "Photoluminescence spectra of $MnIn_2S_4$", *Opt. Mater.*, vol. 34, no. 5, pp. 915-919, 2012

9. F. Yang, M. Lublow, S. Orthmann, C. Merschjann, T. Tyborski, M. Rusu, S. Kubala, A. Thomas, R. Arrigo, M. Hävecker, and T. Schedel-Niedrig, "Metal-Free Photocatalytic Graphitic Carbon Nitride on p-Type Chalcopyrite as a Composite Photocathode for Light-Induced Hydrogen Evolution", *ChemSusChem*, vol. 5, no. 7, pp. 1227-1232, 2012

10. C. Merschjann, S. Tschierlei, T. Tyborski, K. Kailasam, S. Orthmann, D. Hollmann, T. Schedel-Niedrig, A. Thomas, and S. Lochbrunner, "Complementing graphenes: One-dimensional interplanar charge transport in polymeric graphitic carbon nitrides", *Adv. Mater.*, vol. 27, no. 48, pp. 7993-7999, 2015

Contents

1 Introduction

Infrared (IR) spectroscopy is a powerful tool and one of the most widely used techniques in physics, chemistry, and natural sciences [1]. It comprises a manifold of different methods, e.g. Fourier transform spectroscopy (FTIR) or two-dimensional spectroscopy (2D-IR), which allow for the investigation of various sample systems and give detailed insights into structural properties or molecular interactions, to name only a few possibilities [2].
The research on molecular vibrations and low-energy excitations in solids, such as phonons or electronic inter- and intraband transitions, constitutes two major fields for the application of IR spectroscopy [1–5]. Especially in combination with a femtosecond (fs) time resolution, vibrational excitations of e.g. molecules dissolved in water or electronic transitions in semiconductors can be addressed on their intrinsic timescales [6–14]. This opens the door to a precise understanding of intermolecular couplings and structural fluctuations in molecular systems, interactions among electrons in semiconductors, or many further aspects.

Within this work, comprehensive experimental studies on molecular vibrations of $H_2PO_4^-$ ions, BH_4^- ions, phonons in $NaBH_4$, as well as on a bulk plasmon in Ga-doped ZnO are performed. FTIR, fs 2D-IR, and fs IR pump/probe spectroscopies are applied in transmission and reflection geometry in order to consider the particular nature of the studied samples. Phosphate solutions are measured in a free-standing liquid jet, borohydride solutions and polycrystalline $NaBH_4$ in particularly designed sample holders, and a highly reflecting layer system of Ga-doped ZnO layers, spanning a plurality of different sample consistencies. Spectrally tunable fs IR light pulses are used to address the absorption resonances of the investigated samples and to analyse their optical responses in nonequilibrium states with a fs time resolution. Thus, IR spectroscopy is applied in this work to achieve in-depth insights of dynamical processes in differently constituted sample systems that are each of particular interest.

The present thesis is structured in seven chapters. After this introduction (chapter 1), fundamental theoretical aspects about light-matter interactions and molecular vibrations are discussed in chapter 2. It is followed by chapter 3 that introduces the experimental techniques applied for e.g. fs IR pulse generation or fs 2D-IR spectroscopy. In chapter 4, phosphate vibrations of $H_2PO_4^-$ ions dissolved in water are discussed. Chapter 5 comprises vibrational studies on the anion BH_4^- of the complex metal hydride $NaBH_4$ in a liquid and a crystalline environment, and chapter 6 covers the optical nonlinear response of a bulk plasmon in a layer system of highly Ga-doped ZnO layers. All experimental findings are briefly listed in the summary (chapter 7).

2 Basic concepts

In this thesis, the nonlinear optical responses of molecules in the condensed phase and of a bulk plasmon in ZnO:Ga are measured in the mid-IR with spectroscopic methods possessing a femtosecond time resolution. The present chapter contains the theoretical framework to describe vibrational excitations of molecules, couplings among them, and how ultrafast interactions between a solvent and the solvated molecule contribute to the line shape of vibrational absorption resonances. Furthermore, the applied spectroscopic methods are discussed with emphasis on nonlinear response functions, that are particularly sensitive on e.g. population lifetimes or structural fluctuations and, thus, go beyond linear spectroscopy. A detailed description of the experimental realisation is given subsequently. Fundamental aspects about bulk plasmons are discussed in chapter 6.
Four different text books edited by Shaul Mukamel [15], Martin Zanni and Peter Hamm [2], Gerhard Herzberg [16], and Robert W. Boyd [17] have mainly been used to create this chapter.

2.1 Vibrational excitations in molecules

Vibrational modes in molecules represent a certain form of excitation. They allow for the deduction of a manifold of information about molecules such as e.g. structural characteristics or the nature of interaction with surrounding media [1]. In general, a molecule consisting of N atoms exhibits $3N-6$ degrees of freedom along the normal coordinates $q_{1,...,3N-6}$ that represent the vibrational modes [16]. IR spectra result from transitions between quantised vibrational energy states that are denoted by vibrational quantum numbers $\mathrm{v} = 0, 1, 2, ...$. The transition frequencies of vibrational modes depend on the vibrational potential $V(\mathbf{q})$. For purely harmonic potentials (cf. Fig. 2.1), the vibrational modes of a molecule possess the energy of quantum mechanical harmonic oscillators, so that their vibrational energy can be expressed with [16]

$$E(\mathrm{v}_1, ..., \mathrm{v}_{3N-6}) = \sum_{i}^{3N-6} \hbar\omega_i \left(\mathrm{v}_i + \frac{1}{2}\right). \tag{2.1}$$

In eqn. (2.1), v_i describes the vibrational quantum number of the ith vibrational mode, ω_i its transition frequency, and $\hbar$ the Planck's constant.
In real molecules, the displacements of atoms along the normal coordinates deviate from harmonic behaviours. A more general potential for non-degenerate vibrations and small atomic elongations is therefore given as a Taylor series expansion for distortions of the nuclear framework [1, 16]

$$V(\mathbf{q}) = V_0 + \sum_{i}^{3N-6} \frac{\partial V}{\partial q_i} q_i + \frac{1}{2!} \sum_{i,j}^{3N-6} \frac{\partial^2 V}{\partial q_i \partial q_j} q_i q_j + \frac{1}{3!} \sum_{i,j,k}^{3N-6} \frac{\partial^3 V}{\partial q_1 \partial q_j \partial q_k} q_i q_j g_k + ... \tag{2.2}$$

In this description, forces, higher-order forces, and elongations along different vibrational coordinates become relevant, which leads to couplings among vibrational modes and correction terms for the corresponding transition frequencies. These can be expressed as

$$E(\mathrm{v}_1, ..., \mathrm{v}_{3N-6}) = \sum_{i}^{3N-6} \hbar\omega_i \left(\mathrm{v}_i + \frac{1}{2}\right) + \sum_{i}^{3N-6} \sum_{j\geq i}^{3N-6} \Delta_{ij} \left(\mathrm{v}_i + \frac{1}{2}\right)\left(\mathrm{v}_j + \frac{1}{2}\right) + ... \qquad (2.3)$$

for non-degenerate vibrations with anharmonic corrections Δ_{ij} termed anharmonicites [16]. Diagonal anharmonicities $\Delta_{i=j}$ typically have negative signs which results in redshifts of the transition frequencies of excited vibrational modes. Fig. 2.1 represents the vibrational potentials for a harmonic and an anharmonic vibrational oscillator with the quantum mechanical states v=0,1,2, as well as the corresponding transition frequencies, and $\Delta_{i=j}$.

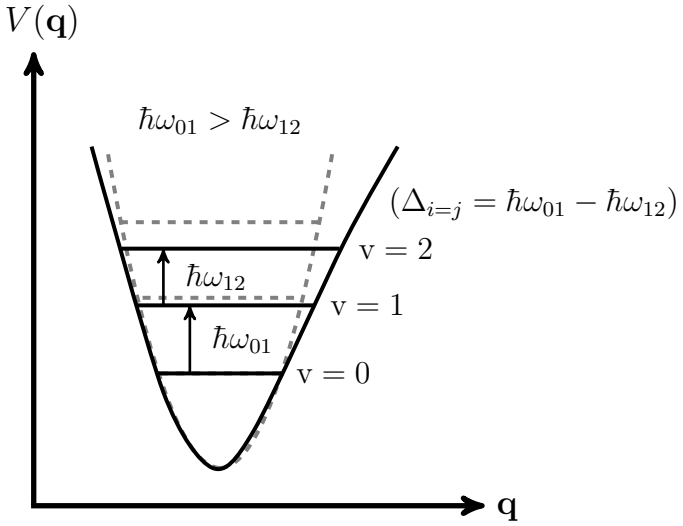

Figure 2.1: Harmonic (gray dashed line) and anharmonic (black solid line) vibrational potential $V(\mathbf{q})$ as a function of the vibrational coordinate $\mathbf{q}$. The diagonal anharmonicity $\Delta_{i=j}$ causes shifted energy levels for the vibrational quantum numbers $\mathrm{v} = 0, 1, 2, ...$ and decreasing transition frequencies between higher order vibrational states ($\hbar\omega_{01} > \hbar\omega_{12}$).

2.2 Vibrational couplings

As discussed in the previous section, deviations from a harmonic vibrational potential lead to anharmonic corrections for the transition frequencies of vibrational modes and mode couplings. In the representation of vibrational excitons that is based on coupled local modes, one can introduce a microscopic description of coupling with the help of transition dipole moments $\boldsymbol{\mu}_n$, the so-called transition dipole coupling [2]. For a pair of two coupled local modes i and j, the orientation of their transition dipoles $\boldsymbol{\mu_i}$ and $\boldsymbol{\mu_j}$ define in combination with their spatial distance $\boldsymbol{r_{ij}}$ the coupling strength β_{ij}, given by

$$\beta_{ij} = \frac{1}{4\pi\epsilon_0\epsilon_\mathrm{r}} \left(\frac{\boldsymbol{\mu_i} \cdot \boldsymbol{\mu_j}}{r_{ij}^3} - 3\frac{(\boldsymbol{r_{ij}} \cdot \boldsymbol{\mu_i})(\boldsymbol{r_{ij}} \cdot \boldsymbol{\mu_j})}{r_{ij}^5} \right). \qquad (2.4)$$

In eqn. (2.4), ϵ_0 and ϵ_r denote the permittivity of the free space and the relative permittivity, respectively. In the domain of linear absorption, a one-exciton Hamiltonian including the coupling strength β_{ij} reveals the excitonic eigenvalues [2]

$$E_{1,2}^{\mathrm{ex}} = \frac{\hbar\omega_1 + \hbar\omega_2 \mp \sqrt{4\beta_{12}^2 + (\hbar\omega_2 - \hbar\omega_1)^2}}{2}. \tag{2.5}$$

These eigenvalues are essentially determined by the transition frequencies $\hbar\omega_{1,2}$ and corrected by the difference of $\hbar\omega_1$ and $\hbar\omega_2$ and the coupling strength squared β_{12}^2. Once $|\beta_{12}| << |\hbar\omega_2 - \hbar\omega_1|$ is fulfilled, eqn. (2.5) simplifies to

$$E_{1,2}^{\mathrm{ex}} \approx \hbar\omega_{1,2} \mp \frac{2\beta_{12}^2}{\hbar\omega_2 - \hbar\omega_1} \tag{2.6}$$

and defines the so-called weak coupling regime with localised exciton states and minorly shifted transition frequencies [2]. In the strong coupling regime for $|\beta_{12}| >> |\hbar\omega_2 - \hbar\omega_1|$, the excitonic energies are approximated with

$$E_{1,2}^{\mathrm{ex}} \approx \frac{\hbar\omega_1 + \hbar\omega_2}{2} \mp \beta_{12}. \tag{2.7}$$

Accordingly, the excitonic states are delocalised and strongly shifted transition frequencies or large energy splittings occur. An exemplary energy splitting of two coupled local modes is shown schematically in Fig. 2.2.

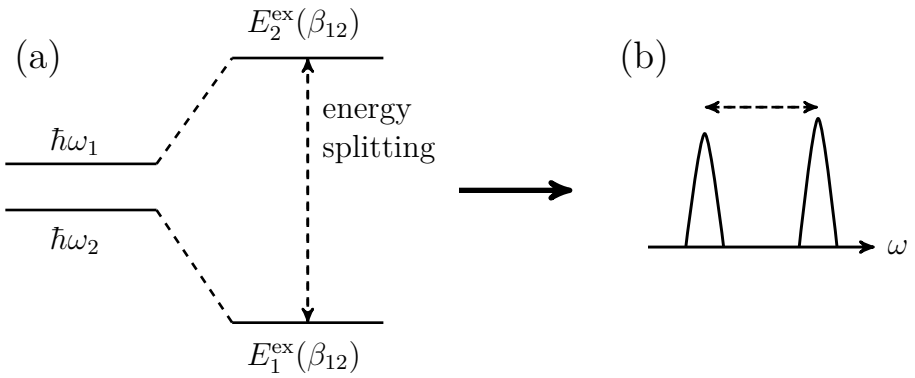

Figure 2.2: (a) Energy splitting due to the coupling of two local modes with the coupling constant β_{12}. In the strong coupling regime the energy splitting is large compared to the energy difference $|\hbar\omega_2 - \hbar\omega_1|$, whereas in the weak coupling regime the energy splitting deviates only slightly from $|\hbar\omega_2 - \hbar\omega_1|$ [2]. (b) Linear absorption spectrum of the two coupled oscillators.

Vibrational couplings can be measured with linear spectroscopy, but only nonlinear 2D-IR spectroscopy allows for the determination of numerical values for coupling strengths. In the weak coupling regime, β_{12} is related to the diagonal ($\Delta_{ii} = \Delta$) and off-diagonal anharmonicites (Δ_{ij}) via

$$\Delta_{12} = 4\Delta \frac{\beta_{12}^2}{(\hbar\omega_2 - \hbar\omega_1)^2}. \tag{2.8}$$

Since Δ_{12} and Δ are experimentally accessible, β_{12} can in principle be deduced from 2D spectra.

2.2.1 Fermi resonance

A Fermi resonance is a special kind of intermode coupling. It occurs once a vibrational transition, e.g. $\nu_{\mathrm{a}}(\mathrm{v} = 0 \rightarrow 1)$, is very close in energy to another vibrational transition, e.g. $\nu_{\mathrm{b}}(\mathrm{v} = 0 \rightarrow 2)$, of the same species, meaning both vibrational modes have to transform corresponding to the same irreducible representation of the molecular point group [16]. Consequently, the eigenfunctions of the vibrational modes start to mix and an energy splitting of the transition frequencies occurs, as shown schematically in Fig. 2.3 [16]. This coupling can lead to the particular case in which an actually dipole forbidden transition, such as $\nu_{\mathrm{b}}(\mathrm{v} = 0 \rightarrow 2)$, gains oscillator strength from a dipole allowed transition and, thus, becomes accessible in IR-spectroscopy.

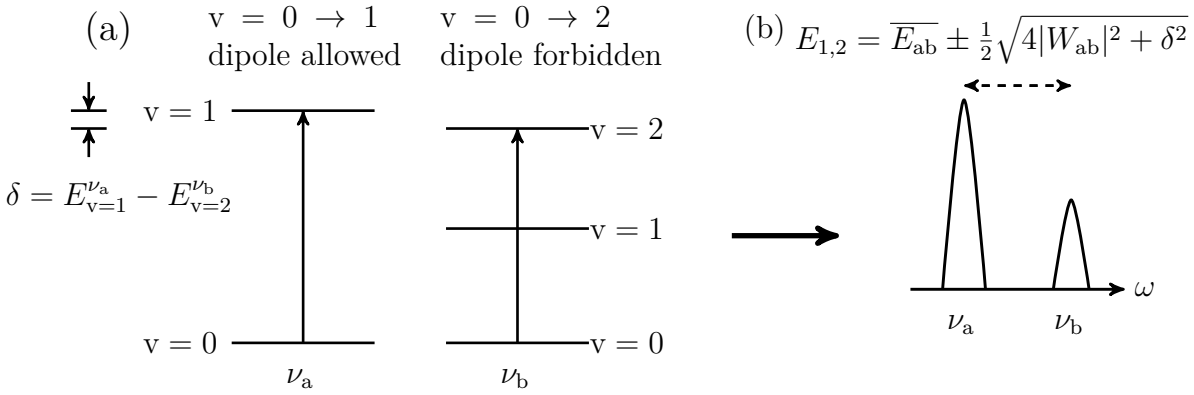

Figure 2.3: (a) Fermi-resonance coupling between the vibrational modes ν_{a} and ν_{b} which belong to the same species. The upward arrows illustrate excitations of $\nu_3(\mathrm{v} = 1)$ $\nu_4(\mathrm{v} = 2)$ that are close in energy with a splitting of δ. (b) Linear absorption spectrum coupled modes ν_3 and ν_4. The coupling leads to the shifted energy levels $E_{1,2}$ for ν_{a} and ν_{b} and to an increased transition dipole moment for $\nu_{\mathrm{b}}(\mathrm{v} = 0 \rightarrow 2)$.

While $\overline{E_{\mathrm{ab}}}$ is given by $\overline{E_{\mathrm{ab}}} = (E^{\nu_{\mathrm{a}}}_{\mathrm{v}=1} + E^{\nu_{\mathrm{b}}}_{\mathrm{v}=2})/2$, W_{ab} is the matrix element of the perturbation function W,

$$W_{\mathrm{ab}} = \int \Psi^0_{\mathrm{a}} W \Psi^{0*}_{\mathrm{b}} d\tau, \tag{2.9}$$

that is determined by anharmonic terms in the vibrational potential and defines the strength of the coupling [16]. Ψ^0_{a} and Ψ^{0*}_{b} denote the zero approximation eigenfunctions of the two coupled vibrational modes ν_{a} and ν_{b}.

2.2.2 Radiative coupling and damping

Radiative coupling and damping are coherent and collective effects of a dense array of optical excitations, such as quantum-well excitons or excited vibrational oscillators, driven by an external electromagnetic field [18–23]. Once the coupling among the excitations is strong, the optical properties of the entire array can be dominated by the collective coherent effects rather than by the response of singular excitations. The effect of radiative coupling is a modification of the interacting electromagnetic field that is very sensitive on the detailed geometry and structure of the excited system. For example, the radiative coupling can lead to a stimulated decay of electronic or vibrational excitation and, hence, to the re-emission of an electromagnetic field (damping). The coherently emitted light field strongly differs from spontaneous emission. Three conditions need to be fulfilled for radiative coupling and damping to occur: i,ii) the spatial separation distance of excitations as well as the thickness of the array of excitations have to be small compared to the

wavelength of the exciting field, and iii) a high optical density of the array is required. R. Friedberg and S. R. Hartmann have formulated these geometric considerations in form of $\alpha L \geq 1$, and defined the superradiant damping time τ_{rad} as [24, 25]

$$\tau_{\mathrm{rad}} = 2T_2^*/\alpha L. \tag{2.10}$$

This equation contains the pure dephasing time T_2^*, the absorption coefficient α, and the sample thickness L. As is evident for large αL, τ_{rad} can take values shorter than the inverse line width given by the transition of an excited oscillator in the array.

2.3 Vibrational line shapes and dephasing

Molecules in solutions stand in a permanent interaction with the solute that forms distinct solvation shells [26, 27]. Changes within the spatial geometry of the solvation shells cause non-static interactions of the solvated molecule with the solute, such as the formation and breaking of hydrogen bonds or dipole-dipole interactions [28]. These time-dependent interactions deform the potential energy surface of the solvated molecule and, thereby, its vibrational transition frequencies [2]. Consequently, the transition frequencies are also time-dependent, which leads to inhomogeneous broadening. In an ensemble of coherently excited vibrational oscillators, the individual variations of transition frequencies lead to a dephasing and, therewith, a loss of the ensemble-averaged coherence. To approximate the individual behaviour, one can describe the time-dependent transition frequency $\omega_{01}(t)$ of a vibrational transition with [2]

$$\omega_{01}(t) = \omega_{01} + \delta\omega_{01}(t). \tag{2.11}$$

Eqn. (2.11) includes a time-independent term ω_{01}, the mean frequency, and the fluctuating term $\delta\omega_{01}(t)$ whose time average vanishes. Furthermore, the interaction with the solution is considered to be weak so that the quantum state of the molecule under study stays unchanged. In the linear limit one can utilise eqn. (2.11) to reformulate the response function (2.38) with

$$R_1(t_1) = i\mu_{01}^2 e^{-i\omega_{01}t_1} \left\langle \exp\left(-i\int_0^{t_1} d\tau \delta\omega_{01}(\tau)\right)\right\rangle \tag{2.12}$$

in order to get a linear response function that includes a model for dephasing. The applied Condon approximation considers the dipole moment μ_{01} to be time-independent, whereas the only time-dependent contributions are the fluctuations of the transition frequencies of individual oscillators $\delta\omega_{01}$ averaged over the ensemble, denoted with $\langle\rangle$ [2]. Only pure dephasing is considered here whereas dephasing contributions from population transfers are neglected. Based on the so-called cumulant expansion the highly oscillating ensemble-averaged exponential function can be approximated with the equation [2]

$$\left\langle \exp\left(-i\int_0^{t_1} d\tau \delta\omega_{01}(\tau)\right)\right\rangle = e^{-g(t)} \tag{2.13}$$

which contains the line shape function $g(t)$ defined by

$$g(t) = \int_0^t \int_0^t d\tau' d\tau'' \overbrace{\langle \delta\omega_{01}(\tau')\delta\omega_{01}(\tau'')\rangle}^{C(\tau',\tau'')}. \tag{2.14}$$

The line shape function is dependent on the important frequency fluctuation correlation function (FFCF) $C(\tau', \tau'')$ that represents a correlation of frequency fluctuations at two different instants of time (τ', τ''). Thus, it is a microscopic description of dephasing. It further defines the stationary line shape of a vibrational transition measured in a linear absorption experiment in which the absorption $\mathrm{A}(\omega)$ can be expressed as

$$\mathrm{A}(\omega) \propto \mathrm{Re} \int_0^\infty e^{i(\omega-\omega_{01})t} e^{-g(t)} dt, \tag{2.15}$$

where Re denotes the real part.
The concept of implementing $g(t)$ into response functions is also applicable for the description of higher order experiments, such as 2D-IR experiments (cf. Secs. 2.7.2, 2.9). The strength of time-resolved 2D-IR spectroscopy is that the temporal evolution of line shapes and correlation functions can be mapped directly.
An analytical approach for the FFCF was introduced by Kubo [2,29]. Under consideration of Gaussian fluctuations, the Kubo function is defined by

$$C(t) = \langle \delta\omega(t)\delta\omega(0) \rangle = (\Delta\omega)^2 e^{-\frac{|t|}{\tau_\mathrm{C}}} \tag{2.16}$$

and includes a parameter for the fluctuation amplitude $\Delta\omega$ as well as a parameter for the correlation time τ_C. Here, τ_C is a measure for the duration of the vibrational coherence of an ensemble of oscillators [29]. An example for $C(t)$ in combination with frequency fluctuations $\delta\omega_{01}$ is given in Fig. 2.4.

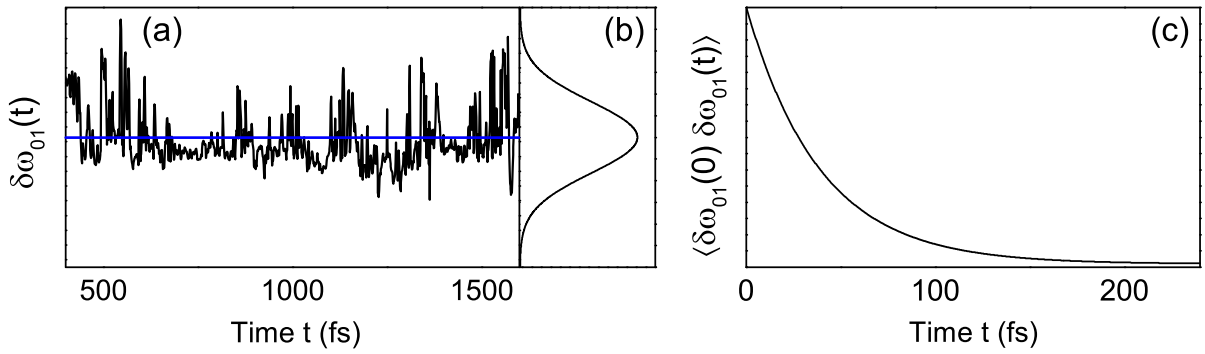

Figure 2.4: (a) Temporal evolution of frequency fluctuations $\delta\omega_{01}$ (or instantaneous frequencies) for a ω_{01} transition with its Gaussian distribution (b) [2]. (c) Resulting FFCF ($C(t)$) based on the Kubo approach showing a quick loss of correlation.

An insertion of the analytical approach eqn. (2.16) into the line shape function (2.14) reveals the Kubo line shape function

$$g(t) = (\Delta\omega)^2 \tau_\mathrm{C}^2 \left(e^{-\frac{t}{\tau_\mathrm{C}}} + \frac{t}{\tau_\mathrm{C}} - 1 \right) \tag{2.17}$$

with which two limiting cases can be defined [2]. Small or rapid frequency fluctuations approximated by $\Delta\omega \cdot \tau_\mathrm{C} \ll 1$ determine the fast modulating or homogeneous limit. The appropriate Kubo line shape function then simplifies to

$$g(t) = (\Delta\omega)^2 \tau_\mathrm{C} t = \frac{t}{T_2^*}, \tag{2.18}$$

including the pure dephasing time T_2^* that is only determined by the correlation time and the fluctuation amplitude

$$T_2^* = \frac{1}{(\Delta\omega)^2 t_\mathrm{C}}. \tag{2.19}$$

In the homogeneous limit, the line shape function (2.18) creates a Lorentzian line with a width equal to T_2^{*-1}. Therefore, the line width decreases with decreasing correlation time and the line width is mainly determined by an average transition frequency; a phenomenon called motional narrowing [2]. The second limit, the slow modulation or inhomogeneous limit, is approximated by $\Delta\omega \cdot \tau_C \gg 1$. In this case, the Kubo line shape function has the form

$$g(t) = \frac{(\Delta\omega)^2}{2} t^2 \tag{2.20}$$

that yields a Gaussian line with a width of $\Delta\omega$. It, therefore, represents the static distribution of transition frequencies present in the ensemble [2].

2.4 Nonlinear polarisation

Nonlinear polarisation is a consequence of the interaction of a strong light field with a material system [17]. To cover this kind of interaction it is insufficient to treat the polarisation $P(t)$ of a material system, that is the dipole moment per unit volume, in a linear way with respect to the interacting light field $E(t)$. The linear case is given by

$$P(t) = \epsilon_0 \chi^{(1)} E(t), \tag{2.21}$$

whereas in the nonlinear case, the polarisation is described as a power series in $E(t)$ [17]

$$\begin{aligned} P(t) &= \epsilon_0 \left[\chi^{(1)} E(t) + \chi^{(2)} E^2(t) + \chi^{(3)} E^3(t) + ... \right] && (2.22)\\ &= P^{(1)}(t) + P^{(2)}(t) + P^{(3)}(t) + ... && (2.23)\\ &= P^{(1)}(t) + P^{\mathrm{nl}}(t). && (2.24) \end{aligned}$$

Higher-order contributions $P^{(n)}(t)$ $(n > 1)$ to the nonlinear polarisation (summarised as $P^{\mathrm{nl}}(t)$) are formulated in terms of the nth-order optical susceptibility $\chi^{(n)}$. The susceptibilities $\chi^{(n)}$ are properties of the interacting material system. Eqn. (2.22) assumes an instantaneous polarisation, as well as a lossless and dispersionless interaction. In general, $P(t)$ and $E(t)$ are vectorial quantities and $P(t)$ also depends on the frequency of the interacting light field. As a consequence, $\chi^{(n)}$ become tensors.
Nonlinear polarisations occur for electric field amplitudes of the order $E \approx e/(4\pi\epsilon_0 a_0^2) \approx 5 \cdot 10^{11}\,\mathrm{V/m}$, where a_0 denotes the Bohr radius of a hydrogen atom and e the charge of an electron [17]. They are important to understand effects like parametric amplification, self-phase modulation, n-wave mixing or spectroscopic methods, such as pump/probe spectroscopy or the generation of photon echoes [15].

2.5 Coupled-wave equation

A nonlinear process with a high significance for the generation of mid-infrared laser pulses and photon echo experiments is n-wave mixing [15]. This process involves n incoming electric fields, described as plane waves $\mathbf{E}(\mathbf{r},t) = \sum_i^n (\mathbf{E}_i(\mathbf{r},t) + c.c._i)$ with frequencies ω_i, that interact with a material system to generate a new field. Applying the Maxwell equations and assuming a vanishing imaginary part of the linear susceptibility $\chi^{(1)}$, a lossless interacting medium, as well as a spatially local response over all frequencies, one can deduce the coupled wave equation [15]

$$\nabla \times \nabla \times \mathbf{E}(\mathbf{r},t) + \frac{n^2}{c^2} \frac{\partial^2 \mathbf{E}(\mathbf{r},t)}{\partial t^2} = -\frac{4\pi}{c^2} \frac{\partial^2 \mathbf{P}^{(\mathrm{nl})}(\mathbf{r},t)}{\partial t^2}. \tag{2.25}$$

Eqn. (2.25) contains the velocity of light c and the refractive index n. The incoming light fields interact with the medium and generate a nonlinear polarisation, which can be expressed as [15]

$$\mathbf{P}^{(\mathrm{nl})}(\mathbf{r},t) = \sum_{2,3,...} \sum_s P_{\mathrm{s}}^{(n)}(t) \exp\left(i\mathbf{k}_{\mathrm{s}} \cdot \mathbf{r} - i\omega_{\mathrm{s}} t\right). \tag{2.26}$$

Eqn. (2.26) depends on all nonlinear orders of $P^{(n)}(t)$ and especially on any combination of the incoming wave vectors $\mathbf{k}_{\mathrm{s}}$ and frequencies ω_{s},

$$\mathbf{k}_{\mathrm{s}} = \pm\mathbf{k}_1 \pm \mathbf{k}_2 \pm \mathbf{k}_3 ... \pm \mathbf{k}_{\mathrm{n}}, \quad \omega_{\mathrm{s}} = \pm\omega_1 \pm \omega_2 \pm \omega_3 ... \pm \omega_{\mathrm{n}}. \tag{2.27}$$

$\mathbf{P}^{(\mathrm{nl})}(\mathbf{r},t)$ is the source of a new emitted light field that is a solution of eqn. (2.25) and very sensitive on the wave vector mismatch between the n incoming and the emitted light fields [15]. The hereby generated light field can either be used to drive further nonlinear processes or to study the medium the light field was generated in.

2.6 Microscopic description of nonlinear polarisation

A microscopic treatment of the interaction between electromagnetic waves and polarisable matter can be carried out in a semiclassical way with the help of Maxwell-Liouville equations [15]. Here, the focus is on the interaction between a classically described electromagnetic wave $E(t)$ with a vibrational oscillator embedded in a solvent, whose vibrational states are described quantum-mechanically. The electromagnetic wave is considered to be sufficiently small so that perturbation theory can be applied. The Hamiltonian for this kind of system is given by [2, 30]

$$H = H_0 + H_{\mathrm{bath}} + H_{\mathrm{int}}(t). \tag{2.28}$$

It includes three different contributions, the Hamiltonian of the isolated oscillator H_0, perturbations of the oscillator by the surrounding bath H_{bath}, and the time-dependent radiation-matter interaction H_{int}. Due to solvent or bath fluctuations, H_{bath} is, in principle, also time-dependent which is, however, not further considered here. H_{int} describes the microscopic interaction leading to the light-induced polarisation. For small oscillator dimensions with respect to the wavelength of the interacting electromagnetic wave, a situation easily achieved in the mid-infrared, the dipole approximation can be applied. It treats the oscillator as a point dipole so that the interaction can be defined as [2, 30]

$$H_{\mathrm{int}}(t) = -E(t) \cdot \mu. \tag{2.29}$$

where μ denotes the oscillator's dipole moment. Normally, H_{int} also depends on spatial coordinates so that a more general description is given by $H_{\mathrm{int}}(\mathbf{r},t) = -\mathbf{E}(\mathbf{r},t) \cdot \mu(\mathbf{r},t) \cdot N(\mathbf{r})$. Here, $N(\mathbf{r})$ denotes the density of oscillators in a statistical ensemble.
Not considering the spatial dependencies, such an ensemble of oscillators in different vibrational states is described by the density operator $\rho(t) = \sum_k p_{\mathrm{k}} \left|\Psi_{\mathrm{k}}(t)\right\rangle \left\langle\Psi_{\mathrm{k}}(t)\right|$. $\left|\Psi_{\mathrm{k}}(t)\right\rangle$ denote the eigenstates of the ensemble and p_{k} stands for the probability of the oscillators to be in the state $\left|\Psi_{\mathrm{k}}(t)\right\rangle$. Populations are described by diagonal elements of the density matrix (ρ_{ii}) and coherences by off-diagonal elements (ρ_{ij} for $i \neq j$). The dynamics of this ensemble interacting with the light field is described by the Liouville-von Neumann equation that includes the full Hamiltonian [2]

$$\frac{d\rho}{dt} = -\frac{i}{\hbar}[H_0, \rho] - \frac{i}{\hbar}[H_{\mathrm{bath}}, \rho] - \frac{i}{\hbar}[H_{\mathrm{int}}(t), \rho]. \tag{2.30}$$

In a two-level system, as shown in Fig. 2.5 (c), populations of the first excited state (ρ_{11}) relax with the lifetime or population time T into the ground state. Coherences (ρ_{ij} for $i \neq j$) decay with the phenomenological dephasing time T_2 and oscillate with the transition frequency ω_{01} [2, 3, 31]. T_2 is a deduced time constant dependent on the lifetime T and the pure dephasing time T_2^* given by

$$\frac{1}{T_2} = \frac{1}{T_2^*} + \frac{1}{2T}. \tag{2.31}$$

T_2^* describes pure phase decay that, in combination with T, leads to a loss of phase coherence between the states ρ_{ij} for $i \neq j$. Pure dephasing is a consequence of the interaction between an oscillator with its environment such as the vibrational manifold or fluctuations of a solvent.

Based on the density matrix, the nonlinear polarisation $P(t)$ of the vibrational oscillators can be compactly described in the interaction picture in which both, the density matrix $\rho(t)$ and the dipole operator $\mu(t)$ become time-dependent. The advantage is that the interaction with the light field and the time evolution of the density matrix can be described separately. In this formalism, the nonlinear polarisation can be expressed in the form of [2]

$$P(t) = \mathrm{Tr}[\mu(t)\rho(t)] = \langle \mu(t)\rho(t) \rangle. \tag{2.32}$$

This central equation (2.32) directly links the expectation value of the dipole operator with the nonlinear polarisation. Tr represents the trace of the matrix in the brackets. Eqn. (2.32) is also valid for higher-order nonlinear polarisations as given by [2]

$$P^{(n)}(t) = \langle \mu(t)\rho^{(n)}(t) \rangle. \tag{2.33}$$

Here, the nth-order nonlinear polarisation is related to the perturbatively expanded nth-order of the time-dependent density matrix $\rho^{(n)}$ that includes n electric field interactions. From eqn. (2.33), the time evolution of the nonlinear polarisation $P^{(n)}(t)$ can be written in dependence of the so-called nth-order response function $R^{(n)}$ [2, 15]

$$\begin{aligned} P^{(n)}(t) &= \int_0^\infty dt_n \int_0^\infty dt_{n-1} ... \int_0^\infty dt_1 \cdot \\ &\quad E(t-t_n)E(t-t_n-t_{n-1})...E(t-t_n-...-t_1)R^{(n)}(t_n,...,t_1). \end{aligned} \tag{2.34}$$

The nonlinear response function is a central quantity since it contains the complete microscopic information necessary to describe the optical interactions and, thereby, the light-induced polarisation of the studied matter. The nth-order response function is defined by [2]

$$R^{(n)}(t_n,...,t_1) = -\left(-\frac{i}{\hbar}\right)^n \langle \mu(t_n+...+t_1)[\mu(t_{n-1}+...+t_1),...[\mu_0,\rho(-\infty)]...] \rangle \tag{2.35}$$

and contains field-matter interactions of the dipole operator acting on the density matrix at different times $t_1, ..., t_n$. Every single commutator constitutes one interaction with the light field and, therefore, the amount of interactions is represented by the order of the response function and the polarisation, respectively. $\rho(-\infty)$ is the equilibrium density matrix that is transferred into non-equilibrium states after the interactions with the dipole operators.

2.7 Response functions

2.7.1 Feynman diagrams for linear absorption

A graphical method to describe the response functions of polarisable systems upon interacting with light is given by so-called Feynman diagrams [2, 15]. Each Feynman diagram

is a representation of a Liouville pathway. In the most simple case of a linear interaction, the first order polarisation (eqn. (2.34)) simplifies to

$$P^{(1)}(t) = \int_0^\infty dt_1 \left(E(t-t_1)\right) R^{(1)}(t_1). \tag{2.36}$$

The interaction with the light field $E(t)$ occurs at time t whereas the response of the system arises at time t_1. $P^{(1)}(t)$ depends on the first-order response function $R^{(1)}(t_1)$ given by

$$R^{(1)}(t_1) = \frac{i}{\hbar}\langle \mu(t_1)\mu(0)\rho(-\infty) - \rho(-\infty)\mu(t_1)\mu(0)\rangle \tag{2.37}$$

that is defined according to eqn. (2.35). So the dipole operator operates twice on the *ket* side of $\rho(-\infty)$ and twice on the *bra* side whereupon one interaction creates a coherence and the second a population, respectively [2]. For a two-level system, an interacting light field resonant to the ω_{01}-transition (cf. Fig. 2.38 (c)) and under utilisation of the rotating wave approximation (RWA), $R^{(1)}(t)$ obeys the explicit form [2]

$$R^{(1)}(t_1) \propto i\mu_{01}^2 \left(e^{(-i\omega_{01}t)} - e^{(+i\omega_{01}t)}\right) e^{\left(\frac{-t}{T_2}\right)}. \tag{2.38}$$

So the linear response is proportional to the dipole moment squared μ_{01}^2, oscillates with the transition frequency ω_{01}, and decays with the dephasing time constant T_2. The leading Feynman diagrams for this kind of interaction are given in Fig. 2.5 and show how light fields act on the density matrix.

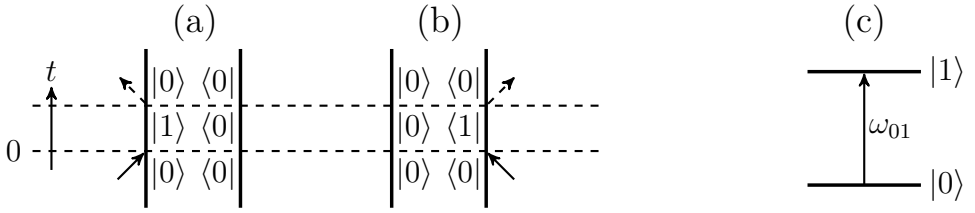

Figure 2.5: Double sided Feynman diagrams to describe the linear response of a two-level system [2]. The interaction of the two-level system with a light field resonant to ω_{01} leads to its excitation and to a subsequent emission of a signal light field equivalent to a deexcitation. ρ is in the ground state before and after all interactions. (a) Represents the interaction of $E(t)$ with the *ket* and (b) of E^* with the *bra* of the density matrix, respectively. General notes on Feynman diagrams [15]: (I) Time runs from the bottom to the top. (II) Interactions with the dipole operator at a certain time are depicted with arrows. (III) Arrows pointing to the right contribute $E_\mathrm{j} \exp\left(-i\omega_\mathrm{j} t + i\mathbf{k_j r}\right)$ to the polarisation and arrows pointing to the left $E_\mathrm{j}^* \exp\left(+i\omega_\mathrm{j} t - i\mathbf{k_j r}\right)$. (IV) The time-dependent density matrix is represented in the *bra-ket* notation between two thick vertical lines. (V) The overall sign of a diagram is given by $(-1)^n$, where n denotes the amount of interactions from the right. (c) Two-level system with the states $|0\rangle$ and $|1\rangle$ and the corresponding transition frequency ω_{01}.

In Fig. 2.5, the incoming light field is illustrated as a black arrow creating a coherence. The emission of a signal light field leads to a relaxation of the coherence and is depicted as a dashed arrow. Under utilisation of $R^{(1)}(t)$ one can deduce the linear polarisation $P^{(1)}(t)$ that is the source of the emitted light field $E_\mathrm{sig}(t)$. $E_\mathrm{sig}(t)$ is proportional to the macroscopic polarisation and is defined as [2]

$$E_\mathrm{sig}(t) \propto iP^{(1)}(t) \propto -E(t). \tag{2.39}$$

So, the emitted light field interferes destructively with the incident light field and, thus, reduces its amplitude which represents linear absorption.

2.7.2 Feynman diagrams for four-wave mixing (2D-IR)

Four-wave mixing is an interaction of a sample with four different light fields and is used for 2D-IR or photon-echo experiments. It relies on the third-order response of the investigated sample system. In isotropic media with inversion symmetry, such as liquids, the third-order response is the lowest order nonlinearity because the second order polarisation $\mathbf{P}^{(2)}(\mathbf{r},t)$ vanishes. In the following it will be discussed how the third-order response of a three-level system can be treated microscopically in order to describe the light-matter interaction in a four-wave mixing process.
According to eqn. (2.34), a convolution of the third-order nonlinear response function $R^{(3)}(t)$ with three incoming light fields describes the third-order nonlinear polarisation given by

$$\begin{aligned} P^{(3)}(t) \quad \propto \quad & \int_0^\infty dt_3 \int_0^\infty dt_2 \int_0^\infty dt_1 R^{(3)}(t_3,t_2,t_1) \\ & E(t-t_1)E(t-t_1-t_2)E(t-t_1-t_2-t_3). \end{aligned} \tag{2.40}$$

The time evolution of $P^{(3)}(t)$ is determined by the interaction with three real-valued light fields $E(t-t_1)$, $E(t-t_1-t_2)$, and $E(t-t_1-t_2-t_3)$ at three different instants of time. Eqn. (2.35) provides the general expression for the required third-order response function that can be written as

$$R^{(3)}(t_3,t_2,t_1) \propto -i\langle\mu(t_1+t_2+t_3)[\mu(t_2+t_1),[\mu(t_1),[\mu(0),\rho(-\infty)]]]\rangle. \tag{2.41}$$

In the strictly sequential limit for $0 < t_1 < t_2 < t_3$, the first light field creates a coherence in the investigated system, similar to the linear response discussed in Sec. 2.7.1. The generated off-diagonal density matrix elements decay with the dephasing time T_2. After a so-called coherence time τ, the second light field generates populations and, therewith, diagonal elements in the density matrix. These diagonal elements decay with their specific lifetimes until the third light field generates a further coherence after the so-called population time T. According to eqn. (2.25), the in this way generated polarisation of the investigated material system is the origin of an emitted fourth signal light field.
Momentum conservation needs to be fulfilled and phase-matching determines the direction of the emitted signal light field [2]. In the used experimental interaction geometry, the so-called "boxcar geometry" (cf. Sec. 3.5), all three exciting light fields denoted with $\mathbf{k}_1$, $\mathbf{k}_2$, and $\mathbf{k}_3$ are arranged noncollinearly so that the emitted signal field from the third-order nonlinear response is spatially separated from other contributions [2, 32–34]. This geometry leads to two phase-matching directions, $\mathbf{k}_\mathrm{r} = -\mathbf{k}_1 + \mathbf{k}_2 + \mathbf{k}_3$ (rephasing phase-matching condition) and $\mathbf{k}_\mathrm{nr} = +\mathbf{k}_1 - \mathbf{k}_2 + \mathbf{k}_3$ (non-rephasing phase-matching condition). Accordingly, energy conservation is fulfilled for $\omega_\mathrm{sig} = \mp\omega_{\mathbf{k}_1} \pm \omega_{\mathbf{k}_2} + \omega_{\mathbf{k}_3}$.
Once the commutators in eqn. (2.41) act on the ground state density matrix $\rho(-\infty)$ of a three-level system given by a singular oscillator (shown in Fig. 2.6 (a)), six leading Liouville pathways arise that are illustrated in Fig. 2.6. Six further pathways occur under consideration of the complex conjugate light fields that are neglected here, because they do not contain additional information.

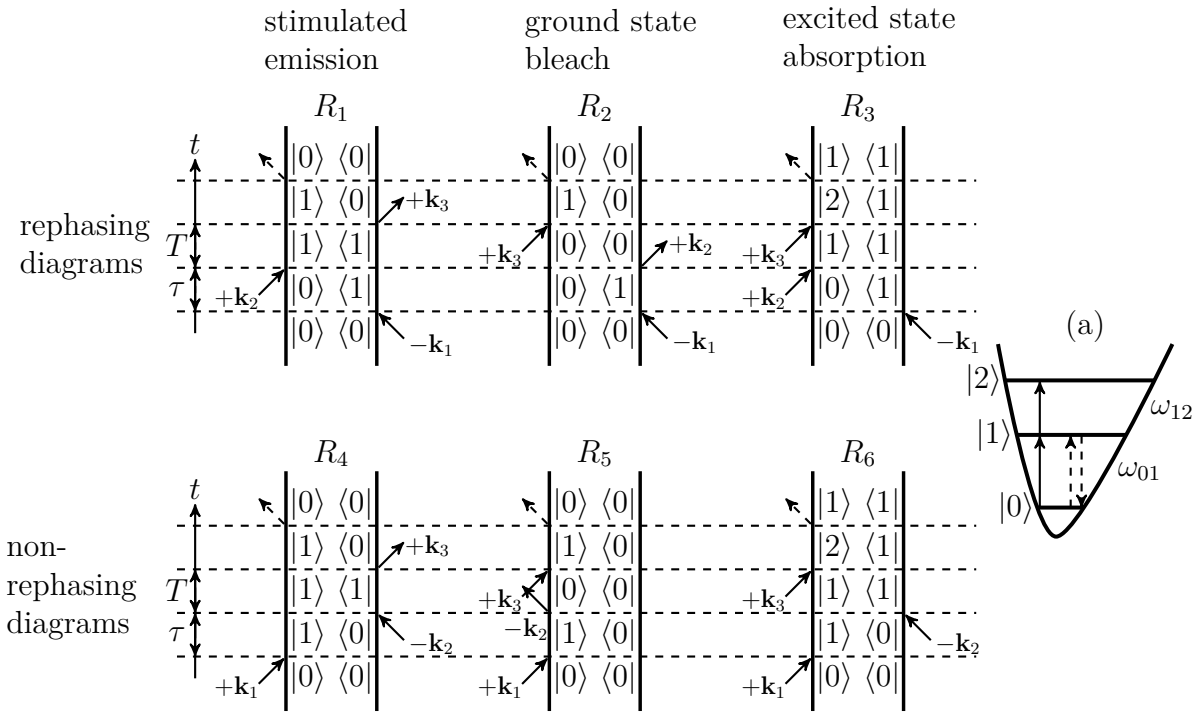

Figure 2.6: Leading Feynman diagrams to describe the third-order nonlinear response of a three-level system measured in the photon echo boxcar geometry [2]. The three-level system is initially prepared in the ground state. (a) Potential energy surface of an anharmonic oscillator for a three-level system with the states $|0\rangle$, $|1\rangle$, $|2\rangle$ and the corresponding transition frequencies ω_{01} and ω_{12} with $\omega_{01} > \omega_{12}$. The upward dashed arrow illustrates a ground state bleach signal and the downward arrow represents stimulated emission. Denotation as in Fig. 2.5

Three different Liouville pathways can be distinguished which are termed stimulated emission, ground state bleach, and excited state absorption. Stimulated emission proceeds via the excited state $|1\rangle\langle 1|$, and the (last) interaction with $\mathbf{k}_3$ leads to a dephasing coherence and a resulting emitted light field. Its frequency is ω_{01} and, thereby, resonant to the incoming pump light fields (cf. Fig. 2.6 (a)). Ground state bleach advances via the ground state $|0\rangle\langle 0|$. Excited state absorption proceeds via the population state $|1\rangle\langle 1|$. In this case, the third interaction creates a dephasing $|2\rangle|1\rangle$ coherence with a subsequent emission of a light field, whereby the initially excited state is probed.
The rephasing diagrams go along with a recurrence of an initial macroscopic polarisation after all interactions that is called the photon echo [35,36]. This process involves the creation of a coherence and, thereby, a macroscopic polarisation by the interaction with $\mathbf{k}_1$ that decays with the dephasing time. After a time delay τ, a second and third interaction with $\mathbf{k}_2$ and $\mathbf{k}_3$ reverse the time evolution and the macroscopic polarisation recurs after 2τ, leading to the emission of the signal light field $\mathbf{k}_\mathrm{r}$, in dependence on spin echoes in magnetic resonance spectroscopy. The non-rephasing diagrams constitute virtual photon echos and the signal field $\mathbf{k}_\mathrm{nr}$ is emitted.
According to eqn. (2.41), one can approximate the third-order response functions $R^{(3)}_{1-6}$ with explicit dipole moments and time constants [2]. Utilising $\mu_{12} = \sqrt{2}\mu_{01}$ which is valid for (nearly) harmonic oscillators and that the dephasing times of the $|0\rangle \rightarrow |1\rangle$ and $|1\rangle \rightarrow |2\rangle$ transitions are identical ($T_{2,|0\rangle\rightarrow|1\rangle} = T_{2,|1\rangle\rightarrow|2\rangle}$), one receives

$$\begin{aligned} R^{(3)}_{1,2,3}(\tau,T,t) &= 2i\mu_{01}^4 \left(e^{-i\omega_{01}(t-\tau)} - e^{-i((\omega_{01}-\Delta)t-\omega_{01}\tau)}\right) e^{-(\tau+t)/T_2} \\ R^{(3)}_{4,5,6}(\tau,T,t) &= 2i\mu_{01}^4 \left(e^{-i\omega_{01}(t-\tau)} - e^{-i((\omega_{01}-\Delta)t+\omega_{01}\tau)}\right) e^{-(\tau+t)/T_2}, \end{aligned} \tag{2.42}$$

where $R^{(3)}_{1,2,3}$ belong to the rephasing and $R^{(3)}_{4,5,6}$ to the non-rephasing diagrams. All these third-order response functions are proportional to the dipole moment to the power of 4 and decay with the dephasing time T_2. $\Delta = \omega_{01} - \omega_{12}$ denotes the frequency shift due to anharmonicity.
In a further step, one can include a theoretical model to describe dephasing microscopically that e.g. is important to model vibrational dephasing of molecules in an aqueous solution (cf. Ch. 4 and Sec. 2.3). Then, eqn. (2.42) can be reformulated with the help of the Kubo model and Kubo line shape functions $g(\tau, T, t)$ [2]

$$\begin{aligned} R^{(3)}_{1,2,3}(\tau,T,t) &= 2i\mu_{01}^4 \left(e^{-i\omega_{01}(t-\tau)} - e^{-i((\omega_{01}-\Delta)t-\omega_{01}\tau)}\right) \cdot \\ &\quad e^{-g(\tau)+g(T)-g(t)-g(\tau+T)-g(T+t)+g(\tau+T+t)} \\ R^{(3)}_{4,5,6}(\tau,T,t) &= 2i\mu_{01}^4 \left(e^{-i\omega_{01}(t+\tau)} - e^{-i((\omega_{01}-\Delta)t+\omega_{01}\tau)}\right) \cdot \\ &\quad e^{-g(\tau)-g(T)-g(t)+g(\tau+T)+g(T+t)-g(\tau+T+t)}. \end{aligned} \tag{2.43}$$

2.7.3 Feynman diagrams for pump/probe measurements

Pump/probe measurements are an experimental technique to measure transient variations in the absorption spectra of an investigated system. This technique is based on the interaction of the investigated system with short light pulses. The interaction is described in the picture of a third-order response exactly like a four-wave mixing process. From a theoretical point of view, it is a simplified variation of a four-wave mixing process with two major simplifications. The first comprises a reduction of participating light field directions, the wave vectors $\mathbf{k}_1$ and $\mathbf{k}_2$ (cf. Fig. 2.6) are identical in the pump/probe geometry and are denoted as $\mathbf{k}_1$ only (cf. Fig. 3.4). The second comprises a reduction of relative time delays, the coherence time τ is set to be zero, so that the two interactions with $\mathbf{k}_1$ occur at the same instant of time. Hence, the corresponding Feynman diagrams are identical to the ones depicted in Fig. 2.6 after substituting $\mathbf{k}_2$ with $\mathbf{k}_1$ and τ with $\tau = 0$. The population time T is preserved.
This kind of interaction is experimentally implemented using a strong pump pulse in the $\mathbf{k}_1$ direction and a weak probe pulse in the $\mathbf{k}_3$ direction. Pump/probe signals are collected in the probe-direction $\mathbf{k}_3$, so that phase matching is fulfilled for $\mathbf{k}_{\mathrm{sig}} = \pm\mathbf{k}_1 \mp \mathbf{k}_1 + \mathbf{k}_3$ and energy conservation for $\omega_{\mathrm{sig}} = \pm\omega_{\mathbf{k}_1} \mp \omega_{\mathbf{k}_1} + \omega_{\mathbf{k}_3}$.

2.8 Pump/probe spectroscopy

The third order nonlinear response of a sample system is experimentally accessible with pump/probe spectroscopy. This method is sensitive to pump pulse induced absorption changes that are mapped with weak probe pulses. In contrast to 2D-IR spectroscopy, the pump pulse $\mathbf{k}_{\mathrm{pump}}$ comprises two interactions with the sample at the same time in order to generate significant populations in excited states. One further interaction occurs with the probe pulse $\mathbf{k}_{\mathrm{probe}}$.
The signal field E_{sig} emitted by the sample propagates parallel to the probe pulse $\mathbf{k}_{\mathrm{probe}}$ (inset (a), Fig. 3.4). Intensity changes of two successively measured and spectrally resolved probe pulses, that interacted with an optically pumped and unpumped sample, respectively, represent the measuring signal in pump/probe experiments. It is typically described as a logarithmic absorption difference $\Delta\mathrm{A}(T, \nu)$, dependent on the delay time

T and the detection frequency ν, given by

$$\Delta\mathrm{A}(T,\nu) = -\log\left(\frac{I(T,\nu)}{I_0(T,\nu)}\cdot\frac{I_0^{\mathrm{ref}}(T,\nu)}{I^{\mathrm{ref}}(T,\nu)}\right). \tag{2.44}$$

In this equation, $I(T,\nu)$ denotes the spectral density of the probe pulse after the interaction with an optically pumped sample and $I_0(T,\nu)$ the spectral density of the probe pulse after the interaction with an unpumped sample. To enhance the sensitivity on absorption changes, the spectral densities of reference pulses $I^{\mathrm{ref}}(T,\nu)$ and $I_0^{\mathrm{ref}}(T,\nu)$ can be measured at the same time. This leads to a reduction of shot-to-shot noise in the measured nonlinear signal and experimentally accessible absorption changes smaller than 0.1 mOD.
A reduced absorption has got a negative sign following the above definition and an enhanced absorption a positive sign. Positive and negative contributions occur due to anharmonicity of the underlying (investigated) oscillators. Redshifted enhanced absorption can be measured as long as the v = 1 states are populated, giving rise to their lifetimes. Reduced absorption around the fundamental absorption band arises because of ground state bleaching on the one hand and stimulated emission v = 1 → 0 on the other hand. Further signal contributions might be measured due to e.g. anharmonic couplings between the investigated oscillators and surrounding oscillators from a solvent.
Typically, the investigated samples in mid-IR pump/probe experiments show absorption resonances that are spectrally smaller than the spectral widths of the interacting pump and probe pulses with pulse durations of 100 fs and bandwidths of $\approx 200\,\mathrm{cm}^{-1}$ (cf. Ch. 4). Multiple probe pulses with shifted centre frequencies are necessary to measure an absorption resonance that is broader than the spectral width of the probe pulses, e.g. an absorption resonance of a bulk plasmon in ZnO:Ga (cf. Ch. 6). An approach to combine individual pump/probe measurements with probe pulses at different centre frequencies is given by [37]

$$\Delta\mathrm{A}(T,\nu) = \frac{\sum_{n=1}^{16}\Delta\mathrm{A}_n(T,\nu_n)I_n^{\mathrm{probe}}(T,\nu_n)}{\sum_{n=1}^{16}I_n^{\mathrm{probe}}(T,\nu_n)} \tag{2.45}$$

where $I_n^{\mathrm{probe}}(T,\nu_n)$ denotes the spectral density of the nth probe pulse. In the special case of the bulk plasmon in ZnO:Ga, 16 pump/probe experiments were combined to cover its entire absorption resonance but eqn. (2.45) is also valid for arbitrary n as long as two conditions are fulfilled. These conditions are i) the difference of centre frequencies among two neighbouring pulses should not be larger than the their spectral widths, and ii) $T > 0$ so that the ordering of the interactions with the pump and probe pulses is in the strictly sequential limit [37, 38].

2.9 Two-dimensional infrared spectroscopy

2D-IR spectroscopy is a spectroscopic method to measure the third order nonlinear response of a sample with the maximal possible information content [2]. It can either be performed in the time domain or in the frequency domain. In this work, all experiments were executed in the time domain. This requires the interaction of the sample with three light fields, $\mathbf{k}_1$, $\mathbf{k}_2$, and $\mathbf{k}_3$, at certain, adjustable instants of time. For this reason, three time variables τ, T, and t are introduced. τ is the coherence time that defines the temporal delay between $\mathbf{k}_1$ and $\mathbf{k}_2$, T is the delay time that defines the temporal delay between $\mathbf{k}_2$ and $\mathbf{k}_3$ and t is the propagating time. The time variables τ and T are experimentally adjustable from negative to positive values. So with 2D-IR spectroscopy in the time

domain, the Liouville pathways or response functions introduced in Sec. 2.7.2 possessing the form $R^{(3)}_{1,\ldots,6}(\tau,T,t)$ are directly accessible. Formally, a 2D Fourier transformation can convert $R^{(3)}_{1,\ldots,6}(\tau,T,t)$ into $R^{(3)}_{1,\ldots,6}(\nu_1,T,\nu_3)$ with the excitation frequency ν_1 and the detection frequency ν_3. Hereby, ν_1 and ν_3 are correlated. Absorptive 2D spectra are a widely used possibility to illustrate response functions. To obtain them, rephasing and non-rephasing response functions need to be added according to [2, 31, 34, 39]

$$S(\nu_1,T,\nu_3) = \mathrm{Re}\left[i\left(\sum_{n=1}^{3} R_n^{(3)}(-\nu_1,T,\nu_3) + \sum_{n=4}^{6} R_n^{(3)}(\nu_1,T,\nu_3)\right)\right] \tag{2.46}$$

and plotted as a function of ν_1 and ν_3. Re denotes the real part of $S(\nu_1,T,\nu_3)$. The rephasing response functions $R^{(3)}_{1,2,3}$ are added as a function of $-\nu_1$ in order to map them into the first quadrant of the (ν_1,ν_3)-plane where the non-rephasing response functions $R^{(3)}_{4,5,6}$ are located.
In the 2D-IR experiment (cf. Sec. 3.4), the response functions are measured in the form of spectral interferograms that depend on (τ, T, $\nu_3 = \nu_{\mathrm{det}}$). A couple of computational steps are necessary in order to derive 2D spectra as in Fig. 2.7 from those data, discussed in detail in [31,36,40–42]. Firstly, the ν_3 axis of the measured interferograms (cf. Sec. 3.4) is Fourier transformed into the time domain. A supergaussian filter extracts positive time components because only they correspond to real signal contributions. The obtained signal is divided by the residual field amplitude of the local oscillator. Furthermore, phase contributions of $\mathbf{k}_1$, $\mathbf{k}_2$, $\mathbf{k}_3$, and $\mathbf{k}_{\mathrm{LO}}$ are approximated. In a final step, a 2D Fourier transformation is performed to receive response functions dependent on ν_1 and ν_3 that are added according to eqn. (2.46). Two examples of such absorptive 2D spectra are given in Fig. 2.7 (c) and (f) in combination with linear absorption and pump/probe spectra to schematically outline their information content. Absorption changes ΔA of excited vibrational oscillators ν_{a} and ν_{b} measured in a pump/probe experiment reveal a bleaching (negative signal amplitude) at the fundamental transitions and redshifted enhanced absorptions (positive signal amplitude) as discussed in Sec. 2.9. The bleaching is caused by the depopulation of the ground state via the $0 \rightarrow 1$ transition and stimulated emission from $1 \rightarrow 0$ (cf. Fig. 2.6 (a)). The redshifted enhanced absorption originates from the excited state absorption $1 \rightarrow 2$ that decreases with the lifetime of the v=1 state. The spectral distance between the maxima of the bleaching and excited state contributions is an indication for the anharmonicity of the underlying oscillator.
2D spectra possess a higher and more complex information content [2]. Diagonal peaks that are located along the diagonal $\nu_1 = \nu_3$ represent bleaching and (redshifted) excited state contributions. They are spectrally separated according to the diagonal anharmonicity Δ_{ii}. In contrast to pump/probe spectra, bleaching contributions in 2D spectra have a positive sign (orange-yellow contours), whereas excited state contributions have a negative sign (blue-cyan contours). While the one-dimensional line shapes measured with e.g. Raman- or infrared spectroscopy do not allow for an unambiguous assignment of underlying dynamics, such as dephasing or population relaxation that lead to line broadening, 2D line shapes explicitly allow for their distinct separation [43].
Couplings between measured vibrational modes lead to distinct signatures in a 2D spectrum [2]. So-called cross peaks occur at off-diagonal frequency positions with bleaching and excited state contributions that are separated by the off-diagonal anharmonicity $\Delta_{ij} (i \neq j)$. These cross peaks correlate the excitation and detection frequencies of a vibrational mode ν_{a} with the detection and excitation frequencies of another vibrational mode ν_{b}. They occur once the interacting light fields trigger processes that involve both

anharmonic oscillators such as coherences or population transfer among them, or the population of a combined state.

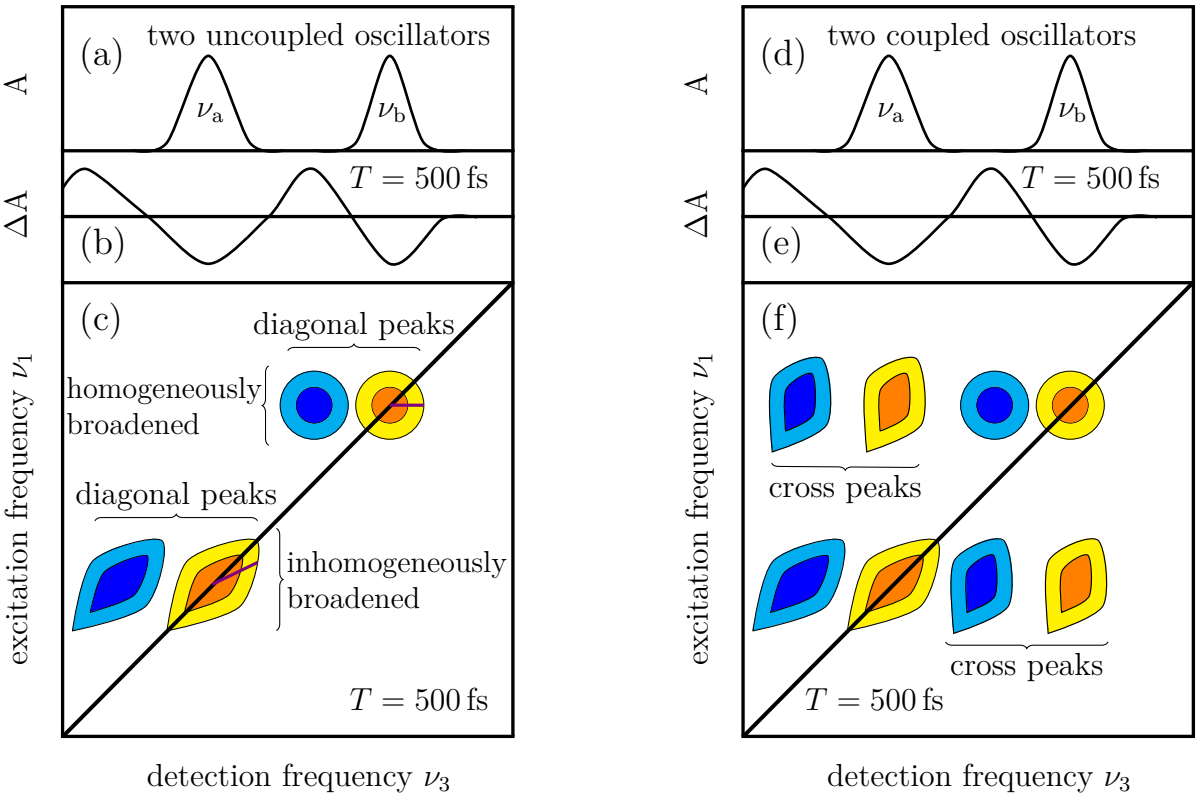

Figure 2.7: (a,d) Linear absorption spectra, (b,e) pump/probe spectra at a given delay time $T = 500\,\mathrm{fs}$, (c,f) absorptive 2D-IR spectra at $T = 500\,\mathrm{fs}$ for a pair of uncoupled oscillators (left) and a pair of coupled oscillators (right) ν_a and ν_b [44]. Pump/probe spectra enable the determination of excited state lifetimes via probing the redshifted $1 \rightarrow 2$ transitions. The strength of 2D-IR vibrational spectroscopy is the direct access to vibrational line shapes and mode couplings, corresponding features are highlighted in (c) and (f). Violet lines in (c): centre line slopes (CLS).

2D spectra represent functions of two independent frequencies and, thereby, map correlated frequency fluctuations that enable the deduction of frequency fluctuation correlation functions. A strong correlation among the excitation and the detection frequency is manifested in persisting inhomogeneously broadened line shapes that are elongated along the diagonal. These inhomogeneously broadened line shapes involve a memory of initial transition frequencies. In contrast, homogeneous and round line shapes involve a loss of a correlations and, therewith, a loss of memory of initial transition frequencies. So the ellipticity of the line shape defines the extent of inhomogeneous broadening. Elongation along the diagonal reproduces the width of the linear absorption spectrum, whereas the antidiagonal width represents the homogeneous line width [43].
A quantitative measure of the line shape in 2D spectra is the so-called centre line slope (CLS) [45]. It is graphically composed via connecting the points of maximal signal amplitude along the detection frequency ν_3. Horizontally aligned CLS (slope 0) represent homogeneously broadened and CLS aligned along the diagonal inhomogeneously broadened line shapes. The temporal evolution of the line shape from inhomogeneous to homogeneous is called spectral diffusion.

2.10 Pump/probe coupling and perturbed free induction decay

So far, only third-order responses in the so-called strictly sequential ordered regime were regarded in which the time ordering follows $\mathbf{k}_1$, $\mathbf{k}_2$, $\mathbf{k}_3$, and in which the interacting light pulses are temporally separated from each other.
Once the time delays are shifted such that the pulses temporally overlap, $\tau \approx T \approx 0$, further Feynman diagrams contribute to the nonlinear response that are commonly termed "coherent artifacts" or "coherent coupling artifacts" [2,15,30,46]. These interactions do not proceed via population states, but exclusively via coherences so they follow nonresonant processes.
Such a process is pump/probe coupling for which the time ordering is $\mathbf{k}_1$, $\mathbf{k}_3$, $\mathbf{k}_2$; i.e. a pump pulse interaction is followed by a probe pulse interaction and another pump pulse interaction. A microscopic interpretation of this process is the occurrence of a polarisation of the sample in the form of a phase grating induced by one pump and one probe pulse interaction. Some intensity of the second pump pulse is then scattered at the phase grating into the direction of the probe pulse $\mathbf{k}_3$ [46].
In the limit of so-called negative delay times, the first interaction with the sample occurs with the probe pulse $\mathbf{k}_3$ and the second and third with the pump pulses $\mathbf{k}_1$ and $\mathbf{k}_2$, the opposite time-ordering compared to the strictly sequential ordering. In this limit, an effect called perturbed free induction decay (PFID) is measurable up to $-1000\,\mathrm{fs}$ [47–49]. Typically, PFID occurs measuring vibrational modes in solution that exhibit bandwidths of less than $20\,\mathrm{cm}^{-1}$. These modes have phase relaxation times of up to 1000 fs and, thus, are long compared to 100 fs pulse durations. The underlying interaction includes a probe pulse induced coherent polarisation whose decay (with the intrinsic dephasing time T_2) is perturbed by a subsequent interaction with the pump pulse. The consequence is a light field emitted into the $\mathbf{k}_3$ direction that decays toward negative delay times. PFID possesses oscillating characteristics with respect to the time, as well as to the spectral axis, and is only measurable when the emitted light field is spectrally resolved. Beyond, it is dependent on the probe pulse centre frequency, its bandwidth and also on the investigated vibrational mode with its distinct spectral width and spectral separation to other vibrational modes [49].

3 Experimental techniques

The exploration of the nonlinear optical responses of $H_2PO_4^-$, BH_4^-, $NaBH_4$, and ZnO:Ga necessitates the generation of fs pulses in the mid-IR. Within this chapter, the experimental techniques of their generation are discussed as well as the experimental setups used for the pump/probe- and 2D-IR experiments. How the different sample systems are integrated in the experiments and, thus, how their optical responses are accessible is also presented in this chapter.

3.1 Utilised laser systems

Commercial titanium doped sapphire (Ti:Sa) based laser systems for the generation and the amplification of short laser pulses have been used on the one hand and non-commercial frequency converters for the mid-IR generation and measuring setups on the other hand. Fig. 3.1 shows a scheme of a utilised laser system in combination with a frequency converter to drive the optical experiments.

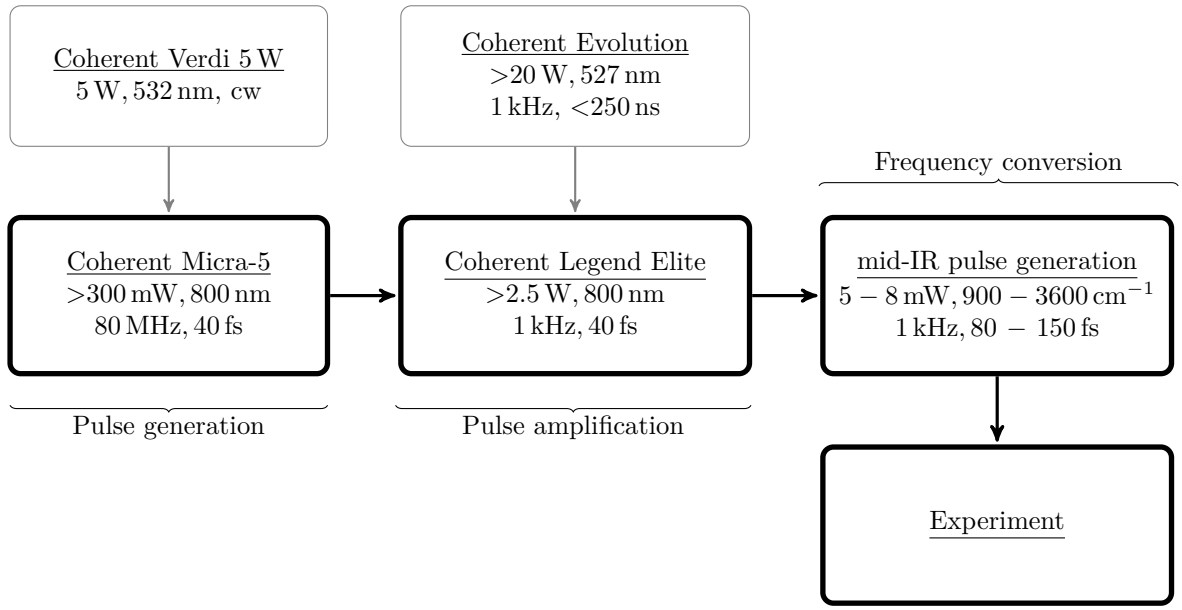

Figure 3.1: Schematic illustration of the laser system utilised to drive optical experiments with a fs time resolution in the mid-IR. It consists of two pump lasers (upper row), an oscillator (middle row left), an amplifier (middle row centre), and a frequency converter (middle row right). The output parameters of the particular system modules are indicated in the boxes.

As shown in Fig. 3.1, the pulse generation in the mid-IR proceeds in three consecutive steps. A Ti:Sa based oscillator continuously pumped with a frequency-doubled solid-state laser (Nd:YVO_4) generates fs pulses with a centre wavelength of 800 nm in the first step [50]. It relies on Kerr-lens mode locking within the Ti:Sa crystal [51]. Its limited

output pulse energies of about 4 nJ are significantly enhanced in the subsequent, likewise Ti:Sa based amplifier, representing the second step. The amplifier is periodically pumped by a second solid-state (Nd:YLF) pump laser. With chirped pulse amplification (CPA), the pulse energy is increased by a factor of 10^6 at the costs of a 10^5 times reduced repetition rate. Consequently, pulse energies of more than 2.5 mJ are reached at a repetition rate of 1 kHz while the centre wavelength of 800 nm is preserved and the pulse duration accounts for 40 fs. In the third and last step, a frequency converter is used to tune the centre wavelengths of the amplified pulses into the mid-IR. A number of further nonlinear processes are required for the last step that are described in detail in the following section 3.2. Finally, the generated fs mid-IR pulses are used in the pump/probe and 2D-IR experiments, introduced in sections 3.3 and 3.4.
Two different laser systems were used for the pump/probe- and 2D-IR experiments. The one illustrated in Fig. 3.1 for 2D-IR measurements on $H_2PO_4^-$ and a very similar laser system (Coherent Libra HE) for the measurements on BH_4^-, $NaBH_4$ and ZnO:Ga.

3.2 Pulse generation in the mid-IR

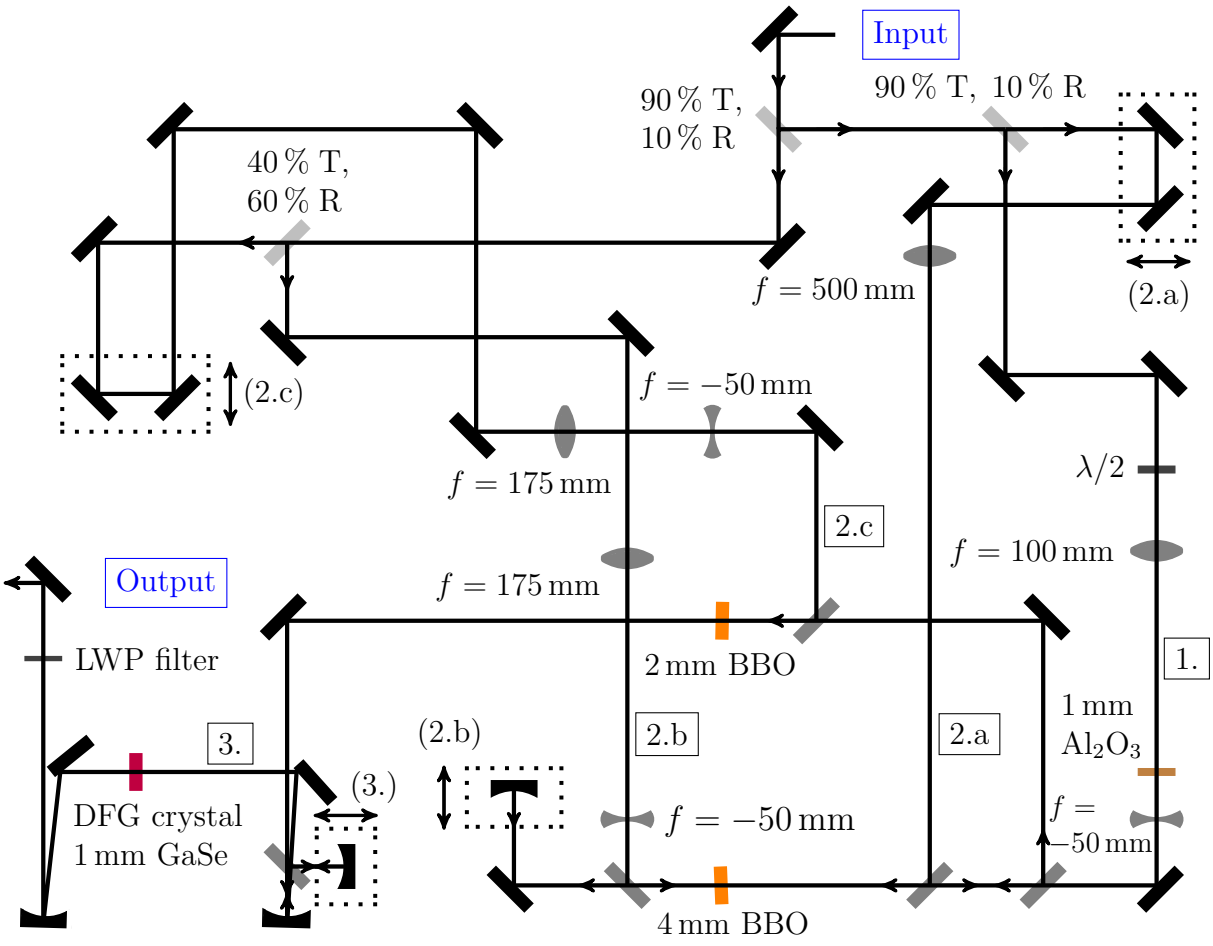

(a)

Input parameters	Output parameters
900 mW	5 − 8 mW
800 nm	900 − 3600 cm^{-1}
1 kHz	1 kHz
80 fs	80 − 150 fs

Figure 3.2: Schematic illustration of an OPA used for the generation of fs pulses in the mid-IR. Black rectangles: high-reflection dielectric 800 nm mirrors, black rectangles with curvature: focussing, high-reflection dielectric 800 nm mirrors, light grey rectangles: beamsplitter, grey rectangles: dichroic mirrors, grey rectangles with curvatures: convex and concave lenses, dark grey rectangle: $\lambda/2$-waveplate, LWP filter, small arrows: propagation direction of the light pulses, big arrows: shifting axis of the delay stages (1.)-(3.). All optics are spatially adjustable. (a) Table for the input and output pulse parameters.

Fig. 3.2 illustrates a frequency converter used that is based on nonlinear parametric frequency conversion and named optical parametric amplifier (OPA) [3, 31, 41, 52–54]. It provides fs pulses in the mid-IR and is driven by the amplified (fundamental) 800 nm pulses. Their pulse energy is reduced to 0.9 mJ and their pulse duration increased to 80 fs, in order to avoid undesirable nonlinear effects in the used nonlinear crystals, such as two-photon absorption, and to optimise the OPA output parameters. BBO (β-BaB_2O_4) and GaSe crystals serve as nonlinear crystals due to their birefringence and large nonlinear coefficients [3].

The frequency conversion takes place in different consecutive steps, denoted with 1.-3.. The first step 1. involves the generation of a white light continuum in a 1 mm thick sapphire crystal with ≈ 1 % of the OPA input pulse energy.
A small spectral portion of the white light continuum is amplified in an initial amplification stage 2.a. This amplification stage comprises a 4 mm thick BBO crystal ($\Theta = 25°$, $\phi = 0°$), in which the white light pulses are temporally (using delay stage (2.a)) and spatially overlapped with focused and delayed fundamental 800 nm pulses of ≈ 10 % OPA input pulse energy. Here, both beams pass the BBO crystal from the right, resulting in a parametric amplification with signal and idler pulse energies of <1 µJ and wavelengths between 1.2 µm and 2.4 µm, respectively. The once amplified signal pulses gain further energy of up to ≈ 20 µJ in a second amplification stage 2.b, passing the BBO crystal from the left. This time, the pump pulses and the signal pulses pass the BBO crystal at a slightly different height, so that the two amplifications do not disturb each other. Aligning the delay stage (2.b) affords the necessary temporal overlap in the BBO crystal for the second amplification. A third amplification stage 2.c is used in order to increase the signal and idler pulse energies to final values of about 100 µJ, respectively, within another, second BBO crystal ($\Theta = 25°$, $\phi = 0°$) of 2 mm thickness. Comparable to 2.b, the diameter of the pump pulses are size adapted and collimated with a telescope, and the temporal overlap is tuned with the delay stage (2.c).
The final third step 3. is the difference frequency generation (DFG) between the amplified and collinear propagating signal and idler pulses within the DFG-crystal GaSe (z-cut, $\Theta = 14°$). With the help of a longwave pass filter (LWP), e.g. Ge, residual transmitted signal, idler, and fundamental pulses can be absorbed resulting in isolated light pulses in the mid-IR with energies between $5 - 8$ µJ, pulse durations of ≈ 120 fs and centre frequencies between $900 - 3600\,\mathrm{cm}^{-1}$. Tuning of the OPA output frequency is achieved by adjusting the phase-matching angles and overlaps in the two BBO crystals, as well as in the DFG crystal.
The parametric amplification fulfills the type II phase-matching conditions $\omega_{\mathrm{pump}} = \omega_{\mathrm{signal}} + \omega_{\mathrm{idler}}$ and $\omega_{\mathrm{pump}} n_{\mathrm{eo}}(\omega_{\mathrm{pump}}, \alpha) = \omega_{\mathrm{signal}} n_{\mathrm{o}}(\omega_{\mathrm{signal}}) + \omega_{\mathrm{idler}} n_{\mathrm{eo}}(\omega_{\mathrm{idler}}, \alpha)$ with the angular pump pulse frequency ω_{pump}, the angular signal pulse frequency ω_{signal}, and the angular idler frequency ω_{idler} [3]. n_{eo} and n_{o} denote refractive indexes with respect to the extraordinary (eo) and ordinary (o) optical axis of the BBO crystal and α the freely adjustable phase-matching angle. The DFG process in GaSe also relies on type II phase-matching.
The overall conversion efficiency amounts to about 1 % and is dependent on the adjusted centre frequency of the generated pulses [3, 52–54].
The described OPA was ultilised for 2D-IR measurements on $H_2PO_4^-$, whereas measurements on BH_4^-, $NaBH_4$, and ZnO:Ga were performed with similar working OPAs exhibiting only two amplifying stages and essentially similar output parameters.

3.2.1 Pulse characterisation in the mid-IR

The generated mid-IR pulses are characterised in the 2D-IR setup (cf. Fig. 3.5) with frequency-resolved-optical-gating (FROG) [55, 56]. It uses a $\chi^{(3)}$-nonlinearity in a thin (1 mm) ZnSe crystal in order to generate a self-diffraction signal $E_{\mathrm{sig}}^{\mathrm{SD}}$ originating from the interaction with the three pulses $\mathbf{k}_1$, $\mathbf{k}_2$, and $\mathbf{k}_3$. It can be described by the equation [55]

$$E_{\mathrm{sig}}^{\mathrm{SD}}(t, \tau) = E^2(t) E^*(t - \tau). \tag{3.1}$$

The pulses $\mathbf{k}_1$ and $\mathbf{k}_2$ with similar electric fields $E(t)$ interact at the same instant of time with the nonlinear crystal ZnSe and have a relative time delay τ to $\mathbf{k}_3$ with the electric

field $E^*(t)$. Tuning τ and integrating over the time t leads to the spectrally resolved intensity of the self-diffraction signal measured by the detector

$$I_{\mathrm{FROG}}(\omega,\tau) = \left| \int_{-\infty}^{+\infty} \mathrm{d}t E_{\mathrm{sig}}^{\mathrm{SD}}(t,\tau) \exp\left(i\omega t\right) \right|^2 . \tag{3.2}$$

The thus achieved FROG trace is formally equivalent to a spectrogram and contains information about the spectral and temporal properties of the involved pulses [55]. An example for a mid-IR light pulse used for the nonlinear experiments is given in Fig. 3.3.

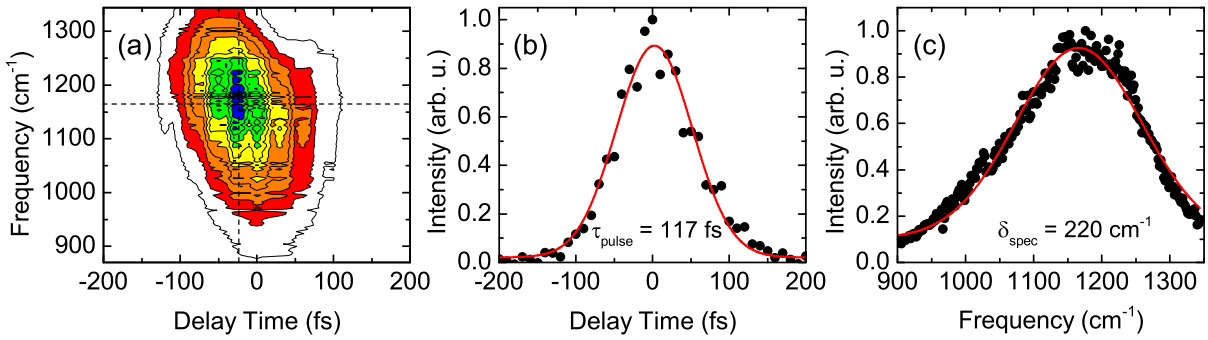

Figure 3.3: Characterisation of a fs mid-IR light pulse generated with the described OPA (cf. Fig. 3.2) and utilised for measurements on $H_2PO_4^-$. Panel (a) illustrates the FROG trace, (b) a horizontal cut through the FROG trace at 1149 cm^{-1}, and (c) a vertical cut at -23 fs with Gaussian fits (red lines), respectively. The cuts are a measure of the pulse duration $\tau_{\mathrm{pulse}} = 117$ fs and its spectral width $\delta_{\mathrm{spec}} = 220\,\mathrm{cm}^{-1}$. The centre frequency is 1166 cm^{-1}.

3.3 IR two-colour pump/probe setup

In pump/probe experiments, the third order nonlinear response of a given sample is measured. The two-colour pump/probe setup used here is driven by two independently operating OPAs. This enables time-resolved measurements with different pump and probe frequencies, respectively. Once the desired pump and probe pulses are generated, their interaction with the sample is organised as illustrated in Fig. 3.4 [31, 36, 41].
The pump and probe pulses are guided into the setup from the right, where they traverse different paths. The pump path (thick solid lines) is equipped with a chopper and a mechanical delay stage. The probe path (thin solid lines) contains a BaF_2 wedge that is used to reduce the probe pulse energies and to create additional reference pulses (second thin line) via reflections at its front and back facets. Both paths are combined within the sample in a noncollinear transmission geometry, explicitly given in panel (a). In the sample, the pump and probe pulses are spatially overlapped using one 30° off-axis parabolic mirror and focussed into spots with diameters of $\approx 150\,\mu$m for the pump and of $\approx 100\,\mu$m for the probe pulses. The reference pulses pass the sample spatially shifted. A second identical 30° off-axis parabolic mirror re-collimates the pulses after their interactions with the sample. Subsequently, the pump pulses are blocked in contrast to the probe and reference pulses which are dispersed and mapped onto two independent nitrogen-cooled 64 pixel MCT (HgCdTe) detector arrays, illustrated on the left of Fig. 3.4.

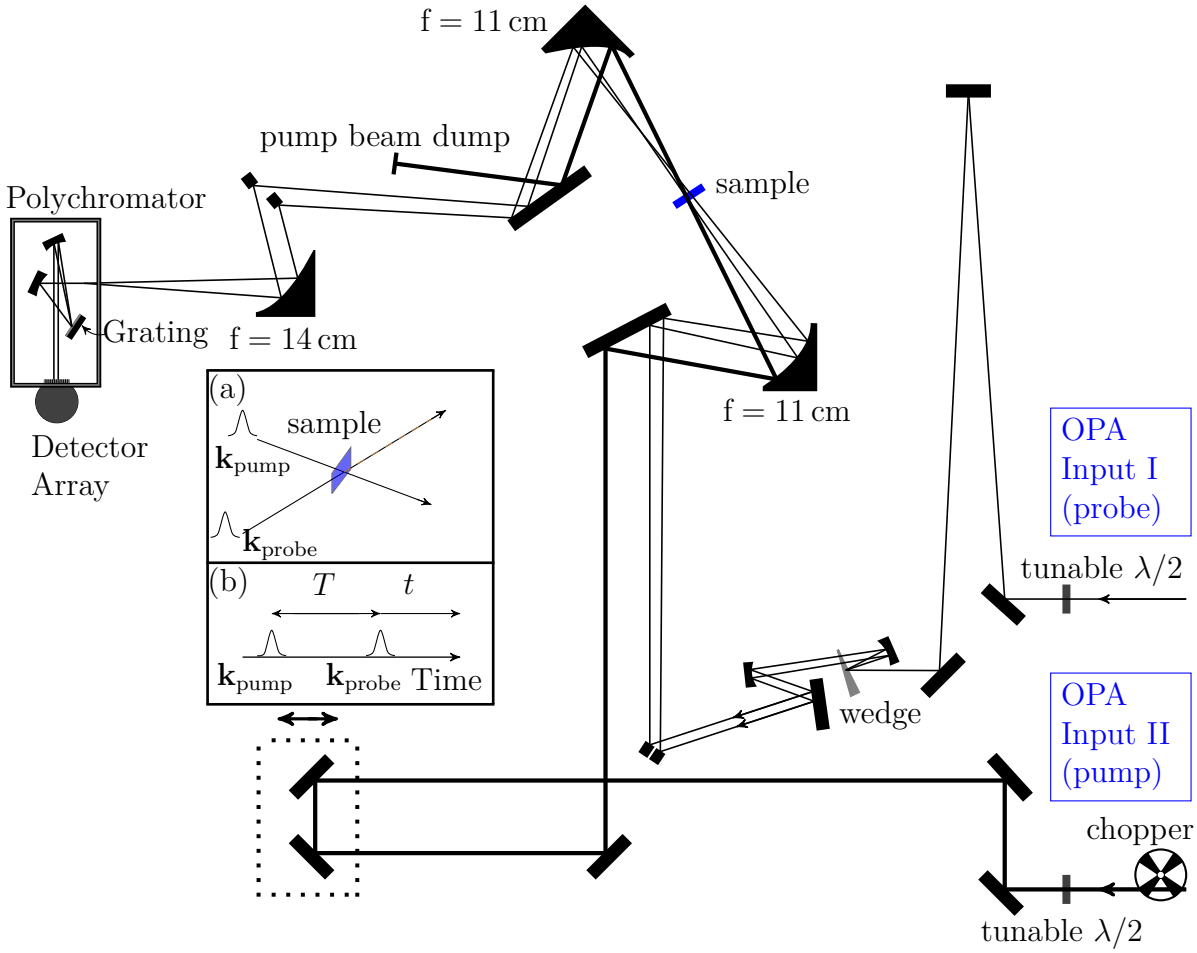

Figure 3.4: Schematic illustration of the setup used for pump/probe measurements in the mid-IR. Black rectangles: gold mirrors, items with curvatures: parabolic and spherical gold mirrors, dark grey rectangles: tunable $\lambda/2$-waveplates, big arrows: shifting axis of the delay stage, small arrows: propagating directions of the pump and probe pulses. Inset (a): Noncollinear pump/probe geometry with highlighted signal field direction. Inset (b): Pulse sequence of the pump/probe measurement.

A simultaneous measuring of the probe pulses and the reference pulses on the two detector arrays reduces the shot-to-shot noise in the nonlinear signals. Three different, exchangeable gratings within the polychromator enable sufficient diffraction efficiency and spectral resolution ($\approx 5\,\text{cm}^{-1}$) over the wide range of $900\,\text{cm}^{-1} - 3600\,\text{cm}^{-1}$.
Synchronisation between the pump and probe pulses is inherently given due to the commonly used light source. The delay stage in the pump path is electronically driven in order to introduce the delay time T between the pump and probe pulses, as illustrated in panel (b). Dispersed probe pulses are measured with a frequency of 1000 Hz. The chopper mechanically blocks every second pump pulse ($f_{\text{pump}} = 500\,\text{Hz}$) so that every second probe pulse interacts with an optically unexcited sample, whereas every second +1 probe pulse interacts with an optically excited sample. Spectrally resolved intensity changes of two subsequently measured probe pulses constitute the measuring signal in the pump/probe experiment (cf. Sec. 2.8). Pump pulse energies amount to $\approx 2\,\mu\text{J}$ and probe pulse energies to $\approx 50\,\text{nJ}$. The time resolution of the two-colour pump/probe experiment is on the order of $100 - 150\,\text{fs}$. A nitrogen atmosphere within the experimental setup can be generated in order to suppress light absorption by H_2O and CO_2. Under utilisation of suitable reflecting optics introduced in Sec. 3.6, the setup can also be used in a reflection geometry.

3.4 Heterodyne-detected three pulse photon echo setup

The detection of heterodyned three pulse photon echoes is a coherent, multidimensional spectroscopic method that gives in-depth insights into the third order nonlinear response of the analysed sample, especially in comparison with pump/probe spectroscopy [2]. Two independently adjustable delay stages and a selective interaction ordering of the involved pulses make it possible to deduce multidimensional or 2D-IR spectra (cf. Sec. 2.9). The corresponding setup used in this work is illustrated in Fig. 3.5 [31, 36, 41, 57].

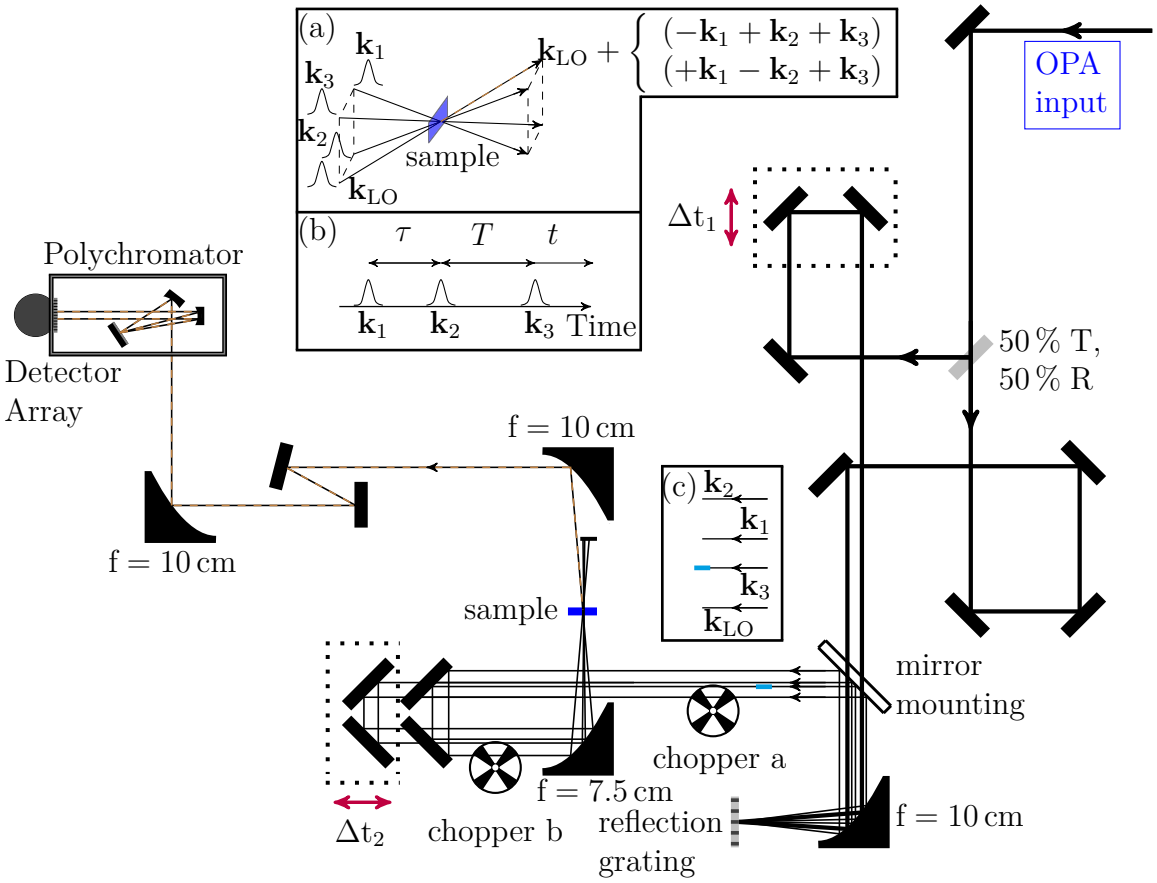

Figure 3.5: Schematic illustration of the setup used for the phase-senstitive measurement of the third-order nonlinear response in a 2D-IR experiment. Mid-IR pulses are guided into the setup from the right. Black rectangles: gold mirrors, items with curvatures: parabolic and spherical gold mirrors, cyan rectangle: 0.5 mm ZnSe crystal in the $\mathbf{k}_3$ path, purple arrows: shifting axis of the delay stages, black arrows: propagation directions of the light pulses, light grey rectangle: beamsplitter, brown dashed line: emitted signal field superimposed with a weak reference field (local oscillator) for the heterodyne signal field detection. The inset (a) exemplifies the noncollinear (boxcar) interaction geometry of the light fields $\mathbf{k}_1$, $\mathbf{k}_2$, and $\mathbf{k}_3$ with the sample and the spatial superposition of $\mathbf{k}_{LO}$ with the emitted light fields $\mathbf{k}_r$ and $\mathbf{k}_{nr}$. Inset (b) shows the pulse sequence for the generation of the third-order nonlinear response with the coherence time τ introduced by the delay stage Δt_2 and the delay time T introduced by the delay stage Δt_1. A denotation of the interacting pulses with the wave vectors $\mathbf{k}_i$ and $\mathbf{k}_{LO}$ is given in inset (c).

Mid-IR pulses generated in an OPA are guided into the 2D-IR setup from the right and are split into a pair of light pulses with identical pulse energies at a 50/50 beamsplitter. The beamsplitter spatially separates the incoming light pulses into two optical paths. The upper path can be extended or contracted with the mechanical delay stage Δt_1, thus introducing the delay time T between the once split pulses. This delay time moves the

pair $\mathbf{k}_1$, $\mathbf{k}_2$ relative in time to $\mathbf{k}_3$, $\mathbf{k}_{\mathrm{LO}}$.
With the help of reflecting optics, the light pulses of both paths are deflected to propagate parallel to each other through a mirror mounting onto a parabolic mirror from where they are focussed onto a reflecting grating. The grating is optimised to diffract incoming light pulses with a frequency around $1250\,\mathrm{cm}^{-1}$ into the first diffraction order, thereby generating two pairs of phase-locked light pulses. The horizontally ordered lines of the grating cause a height offset for the reflected pulses that are collimated again with the parabolic mirror.
Subsequently, a pair of mirrors deflects the light pulses to pass the chopper a and the second delay stage Δt_2 parallelly. Δt_2 introduces the coherence time τ. At this delay stage, the pair $\mathbf{k}_2$, $\mathbf{k}_{\mathrm{LO}}$ is moved relative in time to $\mathbf{k}_1$, $\mathbf{k}_3$.
Another parabolic mirror focuses the four light pulses after passing chopper b into the sample with spot sizes exhibiting diameters of $\approx 150\,\mu\mathrm{m}$, whereupon the pulses $\mathbf{k}_{1,2,3}$ with pulse energies of $\approx 1.5\,\mu\mathrm{J}$, respectively, are blocked. The thus achieved noncollinear phase-matching geometry is called boxcar geometry and is illustrated explicitly in the inset (a). Its idea is to spatially select the emitted light fields $\mathbf{k}_{\mathrm{r}}$ and $\mathbf{k}_{\mathrm{nr}}$ of the third-order response after the interaction with the three light pulses $\mathbf{k}_1$, $\mathbf{k}_2$, and $\mathbf{k}_3$ from other signal contributions [2]. Consequently, $\mathbf{k}_{\mathrm{r}}$ and $\mathbf{k}_{\mathrm{nr}}$ are background free signals. The relative time delays between the light pulses, and, thereby, the time ordering of the interaction with the sample, define the two directions $\mathbf{k}_{\mathrm{r}} = -\mathbf{k}_1 + \mathbf{k}_2 + \mathbf{k}_3$ and $\mathbf{k}_{\mathrm{nr}} = +\mathbf{k}_1 - \mathbf{k}_2 + \mathbf{k}_3$, denoted as rephasing ($\mathbf{k}_{\mathrm{r}}$) and non-rephasing ($\mathbf{k}_{\mathrm{nr}}$) signal contributions. For positive coherence times $\tau > 0$, $\mathbf{k}_1$ interacts with the sample before $\mathbf{k}_2$ (inset (b)), which corresponds to rephasing signal contributions. For negative coherence times $\tau < 0$, $\mathbf{k}_1$ interacts with the sample after $\mathbf{k}_2$, which, that way, corresponds to non-rephasing signal contributions [31, 41]. Overall, a temporal resolution of 100 - 150 fs can be achieved.
The emitted light fields $\mathbf{k}_{\mathrm{r}}$ and $\mathbf{k}_{\mathrm{nr}}$ propagate collinear with a strongly attenuated reference light field $\mathbf{k}_{\mathrm{LO}}$, the local oscillator. It is relatively advanced in time via an implemented ZnSe crystal in the $\mathbf{k}_3$ beam path, which delays $\mathbf{k}_3$, in order to prohibit $\mathbf{k}_{\mathrm{LO}}$-related signal contributions from the sample. The collinear light fields form a spectral interference on the HgCdTe-detector array with 64 pixels. Therewith, the emitted signal light fields E_{sig}, that contain rephasing and non-rephasing contributions, are heterodyne-detected. The overall intensity of this superposition with the electric field of the local oscillator E_{LO} is measured as a function of the detection frequency ν_{det} and can be quantified with [31]

$$I_{\text{2D-IR}}(\nu_{\mathrm{det}}) = |E_{\mathrm{LO}}(\nu_{\mathrm{det}}) + E_{\mathrm{sig}}(\nu_{\mathrm{det}})|^2. \tag{3.3}$$

Taking benefit of the much smaller field amplitudes of E_{sig} compared to E_{LO}, eqn. (3.3) simplifies to

$$I_{\text{2D-IR}}(\nu_{\mathrm{det}}) = |E_{\mathrm{LO}}(\nu_{\mathrm{det}})|^2 + 2|E_{\mathrm{LO}}(\nu_{\mathrm{det}})||E_{\mathrm{sig}}(\nu_{\mathrm{det}})| \cdot \cos\left(\Phi_{\mathrm{sig}} - \Phi_{\mathrm{LO}}\right). \tag{3.4}$$

Hence, the measured spectral interference is not only a function of the electric field amplitudes E_{LO} and E_{sig}, but also of their phases Φ_{sig} and Φ_{LO}, whereas Φ_{LO} is locked. Furthermore, Φ_{sig} depends on the phases of the interacting light fields $\Phi_{\mathrm{sig}} = \Phi_{\mathrm{sig}}(\Phi_{\mathbf{k}_1}, \Phi_{\mathbf{k}_2}, \Phi_{\mathbf{k}_3})$. Relative phase fluctuations of the particular fields need to be small for a heterodyne detection. This is experimentally achieved by using only one primary mid-IR pulse to generate $\mathbf{k}_1$, $\mathbf{k}_2$, $\mathbf{k}_3$, and $\mathbf{k}_{\mathrm{LO}}$ with the diffraction optic and similar beam paths for all pulses [57]. The strong contribution $|E_{\mathrm{LO}}(\omega_{\mathrm{det}})|^2$ is subtracted with the help of chopper a. It blocks every second pump pulse $\mathbf{k}_2$ ($f_{\mathbf{k}_2} = 500\,\mathrm{Hz}$), so that the difference of two subsequent measured spectral interferences only contains contributions from $2|E_{\mathrm{LO}}||E_{\mathrm{sig}}| \cdot \cos\left(\Phi_{\mathrm{sig}} - \Phi_{\mathrm{LO}}\right)$.

The second chopper b runs at a frequency of $f_{\mathbf{k}_3} = 250\,\mathrm{Hz}$ and blocks every fourth $\mathbf{k}_3$-pulse in order to allow for a subtraction of scattered pump pulse intensity from $\mathbf{k}_1$ or $\mathbf{k}_2$. For a complete measurement series, the coherence time τ and the delay time T need to be tuned. One spectral interferogram is measured for one pair (τ, T). One absorptive 2D-IR spectrum consists of many interferograms and is measured over many different coherence times while T stays unchanged. A set of 2D-IR spectra is created with coherence time τ scans at different fixed delay times T.

3.5 Free-standing liquid jet

A free-standing liquid jet was designed in the present work in order to perform nonlinear measurements on a water solution containing $H_2PO_4^-$ ions. The liquid jet illustrated in Fig. 3.6 was characterised first and then implemented in the optical setup for 2D-IR measurements illustrated in Fig. 3.5.

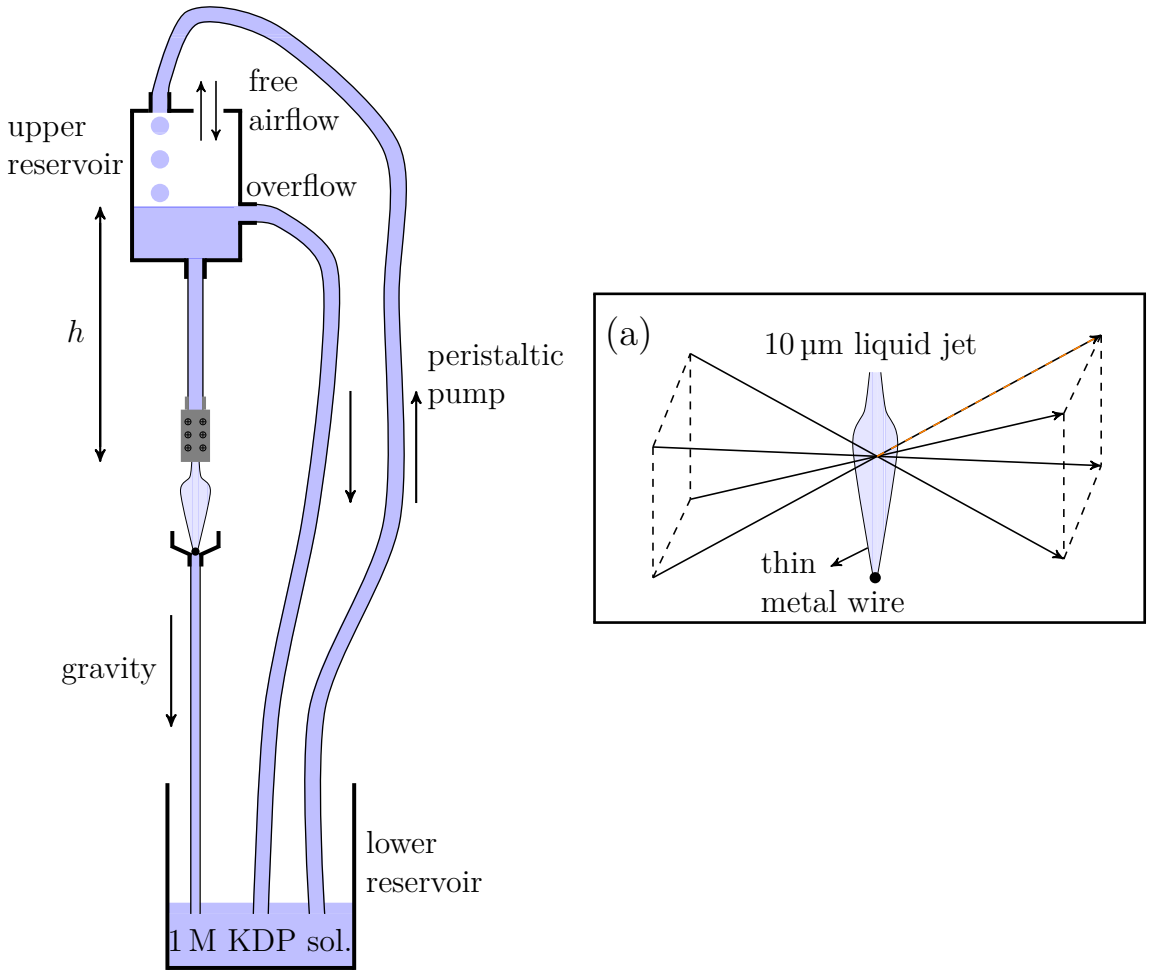

Figure 3.6: Schematic illustration of the self-made, free-standing liquid jet, according to a concept discussed in [58]. A slightly tilted and enlarged liquid jet is shown in inset (a). Here, it is embedded in the 2D-IR experiment interacting with four different light pulses, previously described in Fig. 3.5. Minimal film thicknesses of 10 µm can be achieved with this setup.

The main components of the used liquid jet are a lower reservoir, an upper reservoir, a peristaltic pump, and a shaped thin metal wire. The peristaltic pump promotes the aqueous solution from the lower reservoir ($V = 80\,\mathrm{ml}$) to the upper reservoir ($V = 60\,\mathrm{ml}$), from

where it passes the shaped metal wire gravity-driven and is guided back into the lower reservoir. Thus, the setup is a closed cycle. Silicon tubes connect the components to each other. The upper reservoir is equipped with four openings, one for the incoming aqueous solution, one for a pressure exchange, and two drains. The overflow ensures a static solution content in the upper reservoir and prevents its dependence on the non-constant delivery rate of the peristaltic pump. Two metal blocks, that are screwed together tightly and sealed with teflon stripes, mount the metal wire. It is shaped by hand and possesses a diameter of 0.2 mm. The area spanned with the metal wire has an overall length of 50 mm and a maximal width of 9 mm. A thinner wire and larger spanned areas result in reduced film thicknesses, but on the cost of a decreased film stability concerning film ruptures. Its specific shape strongly influences the achievable film thickness and stability, sharp edges and angles need to be avoided. The height differences h between the upper reservoir and the liquid jet significantly determines the film thickness, larger heights lead to larger film thicknesses [58]. A value of $h = 2\,\mathrm{cm}$ was chosen for the measurements, since a thin film was required. A round metallic termination mechanically connects the wire with a tailrace pool.
The practical application of the liquid jet requires a surfactant to reduce the surface tension of the solution. A non-ionic surfactant called *IGEPAL*® 890 was selected and added with a concentration of 6 mM. No surfactant-related influences on the linear spectrum of an aqueous KDP solution (1 M) could be measured (cf. Sec. 4.2).
Falling droplets should be avoided in the upper reservoir. Instead, a smooth flow at the inner reservoir walls is gainful for low thickness fluctuations of the liquid jet. Air currents in the direct environment should be suppressed. Tweezers were used to establish the thin film between the metal wires since it does not emerge spontaneously. The flow rate of the solution in the liquid jet added up to 10 ml in 335 s which corresponds to 30 nl/ms. Regarding the overall volume $V_{\mathrm{jet}} = 3.2\,\mu\mathrm{l}$ of the liquid jet and the experimental parameters for the interacting light pulses ($\approx 150\,\mu\mathrm{m}$ diameter in the focus, 1 kHz repetition rate), the illuminated area is exchanged nearly three times between two subsequent pump pulses. Thus, a fresh part of the solution is used for every interaction sequence.

3.6 Reflection measurements

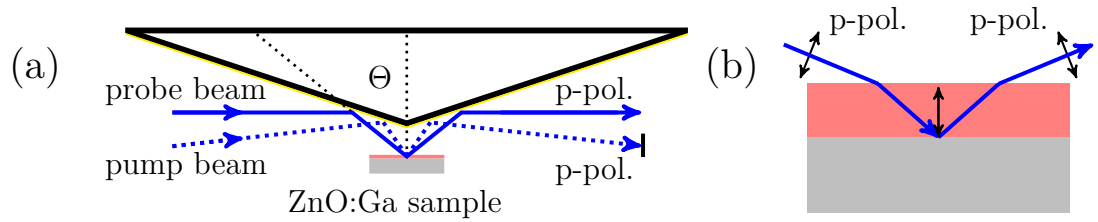

Figure 3.7: Schematic illustration of the reflection geometry used for the pump/probe measurements on ZnO:Ga. (a) Prism-mounting with an Au-coating (yellow) reflecting twice the p-polarised pump and probe pulses. The angle of incidence is $\Theta = 45°$ for the probe pulses and slightly different for the pump pulses. (b) The incoming pulses are reflected at the highly doped, mirror-like bottom layer of the sample, such that the vectorial sum of the **E**-field components of the incoming and outgoing pulses result in an electric field oscillating parallel to the surface normal. Thus, a coupling between the interacting light fields and the bulk plasmon in the upper layer is possible (cf. Fig. 6.1).

Since the pump/probe setup described in Sec. 3.3 has originally been designed for transmission geometries, some modifications need to be implemented in order to perform a pump/probe experiment in reflection geometry. The reflection geometry is necessary to investigate the nonlinear response of a bulk plasmon in a ZnO:Ga multilayer structure that is schematically shown in Fig. 3.7 (b). Details of this experiment are presented in Ch. 6.
Two conditions need to be fulfilled for measurements in reflection geometry using the setup discussed in Sec. 3.3. These conditions are i) an unaltered probe beam direction after all interactions, and ii) a minimal prolongation of the probe beam path. Otherwise, a distortion-free mapping of the dispersed probe pulses on the detector would not be possible. A geometry that satisfies the necessary conditions is illustrated in Fig. 3.7 (a). In this reflection geometry, the incoming p-polarised pump and probe pulses are reflected twice from a prism and once from the sample. The angle of incidence is $\Theta = 45°$ for the probe pulses and only slightly different for the pump pulses. A 100 nm thick Au-coating on top of two prism facets provides for a high reflectivity in the IR spectral range. After the first reflection at the front of the prism, the pump and probe pulses propagate through the lower doped first layer (red, $N_e = 1 \cdot 10^{20}\,cm^{-3}$) of the sample and are reflected at the second mirror-like higher doped layer (grey, $N_e = 6 \cdot 10^{20}\,cm^{-3}$), illustrated in Fig. 3.7 (b). Then, the pulses propagate again through the first layer of the sample and are reflected at the back of the prism such that the outgoing probe pulses proceed collinearly to the incoming probe pulses, whereas the outgoing pump pulses are blocked. This geometry allows for spatially overlapped pump and probe pulses in the top layer of the ZnO:Ga sample with electric field components parallel to the surface normal and, thus, parallel to the **k**-vector of the bulk plasmon oscillation (cf. Fig. 6.1).
Three translational and three rotational axis were used to position the prism mounting for an optimal alignment. The distance between the sample and the top of the prism was less than 2 mm. Cross correlations of the pump and probe pulses were measured to be shorter than 150 fs and the irradiated area on the sample exhibited a diameter of $\approx 150\,\mu m$.
A pump frequency of 360 meV was chosen in combination with pump pulse energies of 1.8 µJ, 0.7 µJ, and 0.3 µJ, attenuated by different copper meshs, respectively. Different probe pulse frequencies were used with probe pulse energies of ≈ 50 nJ.
The p-polarisations of the pump and probe pulses were achieved by two different $\lambda/2$-waveplates (ALPHALAS PO-TWP-L2-25-FIR), one for the pump pulses and one for the probe pulses. These waveplates are fs-suitable and spectrally tuneable from $1 - 19\,\mu m$.

3.7 ZnO:Ga sample fabrication

The ZnO:Ga sample has been manufactured with molecular beam epitaxy (MBE) in a two-dimensional growth mode [59]. A thin ZnO layer is deposited on top of a 0.5 mm thick sapphire substrate with a defined a-plane $(11\bar{2}0)$ surface orientation. This thin layer spatially separates the Ga-atoms in the upper layers from the sapphire substrate in order to avoid chemical reactions among them. A highly Ga-doped ZnO layer ($N_e = 6 \cdot 10^{20}\,cm^{-3}$) with a thickness of 400 nm is deposited on top of the pure ZnO layer. A slightly less Ga:doped ZnO layer ($N_e = 1 \cdot 10^{20}\,cm^{-3}$) with a thickness of 100 nm forms the top of the sandwich structure. All ZnO and ZnO:Ga layers have an $(00\bar{1})$ orientation and, thus, O-termination with oxygen atoms pointing out of the crystal. The total Ga-content adds up to $\approx 1\,\%$. Zn-atoms within the wurtzite crystal structure

of ZnO are substituted with the Ga-atoms which act as electron donors. Hence, the investigated ZnO:Ga sample is heavily n-doped exhibiting a "free electron gas". Carrier mobilities of around $50\,cm^2V^{-1}s^{-1}$ are documented for the Ga-doped ZnO layers [59]. Ga-concentrations in ZnO of up to a mole fraction of 6.5 % can be reached with only minor deviations from the original crystal structure [59].
This specific sample fabrication allows for planar and atomically sharp ZnO and Ga-doped ZnO layers with defined metal-air and metal-metal interfaces in a subwavelength regime [60–63]. The interfaces of the described sandwich structure features polariton dispersion curves with plasma frequencies in the mid-IR, discussed in detail in section 6.2.2 [64].

3.8 $NaBH_4$ sample preparation

Solid $NaBH_4$ films were prepared with $NaBH_4$ (> 98 % purity) in powder form by Sigmar Aldrich. The powder and a 0.5 M stock solution of $NaBH_4$ dissolved in isopropylamine were stored in a glove box with inert Ar atmosphere, since $NaBH_4$ quickly decomposes under the presence of H_2O or O_2 [65]. In the glove box, a small amount of the solution was deposited on a 100 µm thin MgF_2 window from where the solvent isopropylamine evaporated within seconds, supported by its low boiling temperature of 32 °C [66]. The MgF_2 window has a diameter of 3 mm and is embedded in the lower part of a gas-tight metallic cell. After complete evaporation of the solvent, a $\approx$ 1 µm thick polycrystalline $NaBH_4$ film remained on the MgF_2 window. The $NaBH_4$ containing part of the cell was then screwed together with the upper part, equipped with another thin MgF_2 window, and sealed with a circular rubber band. The cells manufactured in that way kept the generated $NaBH_4$ films stable for more than a week, tested in IR absorption measurements. For the liquid samples, $NaBH_4$ was dissolved in isopropylamine with concentrations of either 0.8 M or 0.5 M. Small amounts of these solutions were deposited in Harrick demountable liquid cells with two 1 mm thick BaF_2 windows. 1 or 25 µm spacers between the windows adjusted the thickness of the liquid films that were stable one day long.

4 Ultrafast phosphate hydration dynamics in bulk H_2O

4.1 Phosphates as biomolecular hydration sites

About 80 % of the mass of most living cells is comprised of intercellular water [67, 68]. Thus, water plays a significant role in biochemical processes as for instance the ATP metabolism or ion transport across cell membranes [69–71]. Next to ATP, DNA, and phospholipids represent essential biomolecules that feature a manifold of functional groups, respectively, which are involved in the biochemical processes [72–74]. One very important functional group are charged phosphate groups that strongly interact with polar (intercellular) water. Phosphate groups in biomolecules constitute structuring building blocks on the one hand and major hydration sites on the other hand [75–78]. Fig. 4.1 represents a compilation of prominent phosphate containing biomolecules with highlighted phosphate groups.

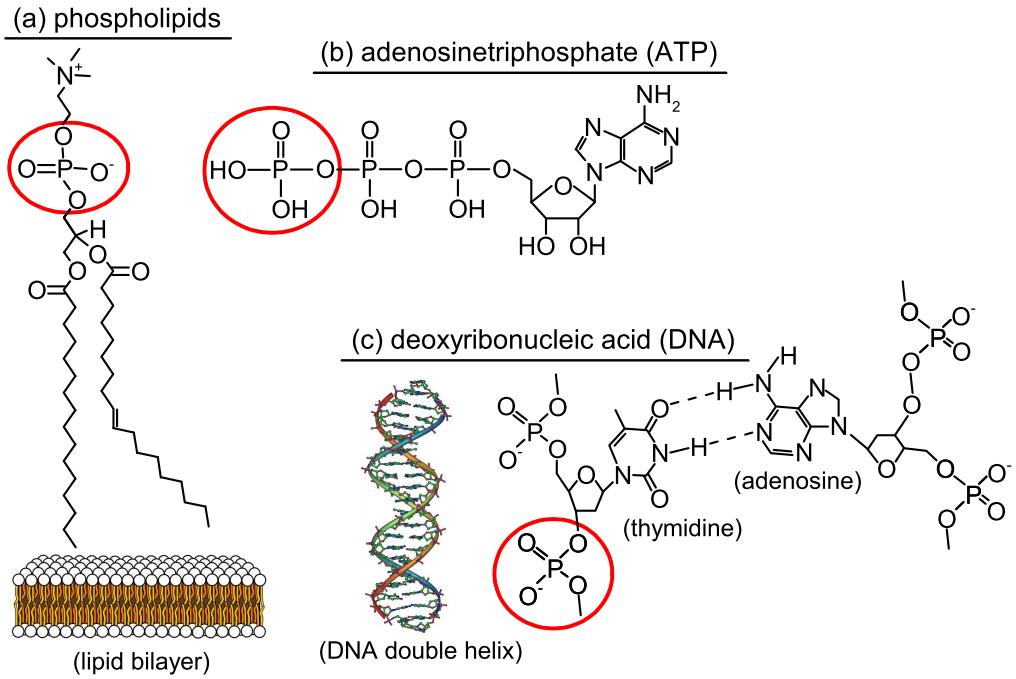

Figure 4.1: Compilation of prominent phosphate group (red highlighted) containing biomolecules. (a) Phospholipids, here a phosphatidylcholine, form lipid bilayers that are the major structure in biological cell membranes [79–81]. (b) ATP is a crucial energy carrier for intracellular energy transfer that releases energy via dephosphorylation, the removal of a phosphate group [82, 83]. (c) Phosphate groups are the linking unit for nucleobases in the backbone of DNA and, therewith, codetermine its secondary structure [84]. A DNA double helix in the *B*-form is shown on the left [85–87].

Due to the ionic character of phosphate groups and the high water content of biological cells, phosphates are surrounded by a plurality of water molecules and, accordingly, serve as hydration sites. The particular hydration level and geometrical structure of the hydrating water molecules can have a strong impact on the properties of the hydrated biomolecules. For example, the hydration level of DNA determines decisively its secondary structure [87, 88]. The equilibrium or time-averaged structures of the biomolecular systems shown in Fig. 4.1 are well characterised. Nevertheless, the intrinsic interaction with water in biological cells requires the consideration of a manifold of timescales, in particular ultrafast timescales, to properly account for elementary processes such as phosphate-water interactions in living organisms [89, 90].
For example, DNA interacts with water on a fs-timescale, a ps-timescale, and a ns-timescale, correlated with structural reorientations of water molecules around phosphate groups on the fs-timescale, breaking and formation of phosphate-water hydrogen bonds (HBs) on the ps-timescale and exchanges of water molecules among hydration shells on the ns-timescale [9, 71, 91–95].
Molecular dynamics (MD) simulations allow for theoretical insights into the ultrafast phos-phate-water interactions, whereas nonlinear spectroscopy is appropriate to gain experimental access into underlying interactions that lead to vibrational absorption spectra with distinctive line shapes and vibrational frequencies [2, 7, 96]. Especially two-dimensional infrared (2D-IR) spectroscopy with a fs time resolution permits direct insight into e.g. the transient behaviour of phosphate vibrations or vibrational dephasing due to water fluctuations and, thus, structural fluctuations within the phosphate-water system.
The comprehension of the ultrafast vibrational dynamics of bulk water is one key to understand the molecular interactions at phosphate hydration sites. These dynamics of bulk water have been studied intensively over the last years [8, 97–108]. HB lifetimes between neighboring water molecules of 1-2 ps are documented as well as librational motions of water molecules on a sub-50 fs timescale that mediate fluctuating electric fields and result in ultrafast vibrational frequency fluctuations [7, 9]. These high-frequency librations also cause vibrational dephasing of the OH-stretching mode to occur within ≈ 50 fs, revealed by spectral diffusion, i.e., initially inhomogeneously broadened line shapes and homogeneously broadened line shapes after a delay time of 100 fs in 2D-IR experiments [8]. The water molecule itself is a convenient probe to study, since the OH-stretching oscillator exhibits a very large diagonal anharmonicity of $\approx 150\,\mathrm{cm}^{-1}$ once it is bonded to the HB network in liquid water which makes it very sensitive to structural fluctuations [7, 8, 109].
Compared to bulk water, water at interfacial sites such as water surfaces, DNA-water or phospholipid-water boundary layers exhibits modified vibrational dynamics [9, 27, 45, 92, 96, 110–114]. Experimentally, it is hard to distinguish contributions from bulk water and interfacial water. A concept to perform experiments with spatial sensitivity was introduced recently [34, 76, 115–118]. There, phosphate vibrations were used as specific probes for phosphate-water interactions located at DNA-water interfaces and within phospholipid reverse micelles at phospholipid-water interfaces.
It was observed that structural dynamics of water at those interfaces are significantly decelerated due to more rigid hydration shells with reduced water fluctuations. This was demonstrated in slower spectral diffusion kinetics of the OH-stretching vibration and persisting inhomogeneous broadening of 2D line shapes of phosphate vibrations up to 10 ps [34, 45, 119]. Furthermore, the vibrational lifetimes of excited phosphate vibrations have been reported to be sensitive to the hydration level [9, 31, 76, 115, 116, 120, 121].
Thus, phosphate groups are very sensitive probes to map decelerated water dynamics and phosphate-water interactions at interfacial sites such as the phospholipid-water - or the

DNA-water interface.

Within this work, phosphate vibrations of the ion $H_2PO_4^-$ were measured in bulk H_2O. It is a priori uncertain whether phosphate vibrations of phosphate ions are appropriate probes to map the ultrafast fluctuation dynamics of bulk water. They exhibit with $\approx 10\,\mathrm{cm}^{-1}$ a significantly smaller diagonal anharmonicity compared to the OH-stretching vibration of water molecules and, hence, should not be as sensitive as water to ultrafast structural modifications and the accompanied frequency fluctuations. Therefore, phosphate vibrations of "isolated" phosphate ions in bulk water are introduced here to evaluate their suitability as local probes for the ultrafast structural fluctuations of bulk water. Beyond, the obtained results serve as a benchmark for measurements on phosphate vibrations at interfacial sites.

A free-standing liquid jet for the measurement of a phosphate water solution was designed and applied. The liquid jet extends the temporal resolution of the experiments into the region between 0 fs and 100 fs at which librational motions of water and the relaxation of phosphate vibrations occur. The investigated absorption lines span a spectral range from $850\,\mathrm{cm}^{-1}$ to $1350\,\mathrm{cm}^{-1}$ that was addressed with tunable 100 fs light pulses.

The obtained results were embedded in a theoretical context in a joint experimental and theoretical work at the Max-Born-Institute. Benjamin P. Fingerhut performed the numerical calculations that can be found together with numerical details in ref. [76]. Chapter 4 refers to ref. [76] where the major experimental and theoretical results are published.

4.2 Vibrations of $H_2PO_4^-$

Potassium dihydrogen phosphate (KDP) is a salt of phosphoric acid. Dissolved in water, it forms a negatively charged anion $H_2PO_4^-$, the dihydrogen phosphate ion, and a positively charged cation K^+. For $H_2PO_4^-$-concentrations below the solubility limit of 1.6 M at ambient conditions, the individual phosphate ions are well separated from each other and exhibit distinct hydration shells. The infrared absorption spectrum of a 1 M aqueous KDP solution is illustrated in Fig. 4.2 together with a characterisation of the individual absorption lines. The spectra were measured with a 10 µm thin liquid jet (cf. Fig. 3.6).

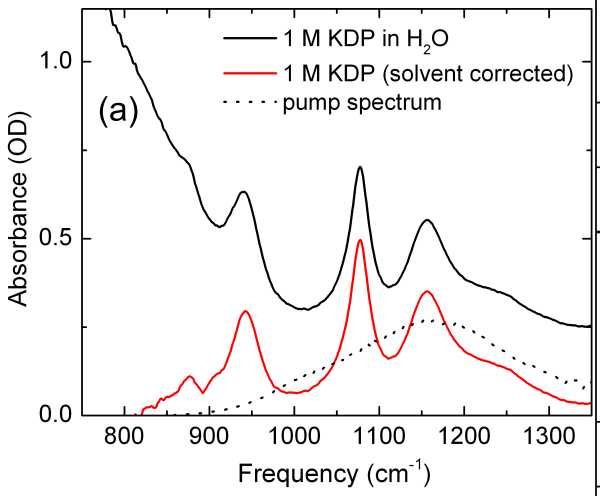

(b)	ν_S(P-(OH)$_2$)	ν_{AS}(P-(OH)$_2$)	ν_S(PO_2^-)
exp.	877 cm^{-1}	942 cm^{-1}	1077 cm^{-1}
theo.		921 cm^{-1}	1074 cm^{-1}
	ν_{AS}(PO_2^-)	δ_S(P-(OH)$_2$)	δ_{AS}(P-(OH)$_2$)
exp.	1157 cm^{-1}	1250 cm^{-1}*	1250 cm^{-1}*
theo.	1143 cm^{-1}	1170 cm^{-1}	1271 cm^{-1}

Figure 4.2: Vibrational absorption spectra and normal modes of $H_2PO_4^-$ molecules in aqueous solution. Panel (a) shows an absolute absorption spectrum (black line) and a solvent-corrected absorption spectrum (red line) of an aqueous 1 M KDP solution in combination with a pump pulse spectrum (dotted line) used for the pump/probe and 2D-IR measurements. A 10 µm thin liquid jet was used to measure the shown spectra. (b) Graphical charts of the normal modes shown together with the corresponding experimental (from (a)) and theoretical frequency positions, orange: phosphorous, red: oxygen, white: hydrogen. Band assignment according to [122–125]. The theoretical frequencies were obtained by MP2 normal mode analysis of a $H_2PO_4^-$/water cluster containing 7 water molecules. The molar absorption coefficients of $H_2PO_4^-$ in water are: $\epsilon(877\,\mathrm{cm^{-1}}) = 100\,\mathrm{M^{-1}cm^{-1}}$, $\epsilon(942\,\mathrm{cm^{-1}}) = 280\,\mathrm{M^{-1}cm^{-1}}$, $\epsilon(1077\,\mathrm{cm^{-1}}) = 470\,\mathrm{M^{-1}cm^{-1}}$, $\epsilon(1157\,\mathrm{cm^{-1}}) = 330\,\mathrm{M^{-1}cm^{-1}}$, $\epsilon(1250\,\mathrm{cm^{-1}}) = 120\,\mathrm{M^{-1}cm^{-1}}$.

$H_2PO_4^-$ ions in aqueous solution exhibit five absorption bands in the illustrated range from 750 cm^{-1} to 1350 cm^{-1}. The strongest absorption bands are assigned to the symmetric PO_2^- stretching vibration $\nu_S(PO_2^-)$ at 1077 cm^{-1} and to the asymmetric PO_2^- stretching vibration $\nu_{AS}(PO_2^-)$ at 1157 cm^{-1}. A spectrally broad shoulder is evident in the high-frequency range at 1250 cm^{-1} which is theoretically related (indicated by * in (b)) to the symmetric and asymmetric P-$(OH)_2$ bending vibrations $\delta_S(P-(OH)_2)$ and $\delta_{AS}(P-(OH)_2)$ that cannot be distinguished experimentally. There are two absorption bands in the low-frequency range, the asymmetric P-$(OH)_2$ stretching vibration $\nu_{AS}(P-(OH)_2)$ at 942 cm^{-1} and the symmetric P-$(OH)_2$ stretching vibration $\nu_S(P-(OH)_2)$ at 877 cm^{-1} which is the weakest one. High-frequency O-H stretching vibrations (≈ 3500 cm^{-1}), low-frequency PO_2^- bending vibrations (≈ 500 cm^{-1}) and Raman-active modes complete the vibrational spectrum of $H_2PO_4^-$ [122,123]. Furthermore, solvent-related absorption bands within the spectral range illustrated in Fig. 4.2 occur. The librational L2 band of water

centred around 670 cm^{-1} causes the strong additional absorption in the low-frequency range, whereas high-frequency librations determine the absorption structure of water in the high-frequency range [126, 127].
The absolute absorption spectrum in (a) and the complete assignment of the absorption bands suggest that the utilised surfactant necessary to run the liquid jet has no significant influence on the vibrational structure of $H_2PO_4^-$. Nevertheless, explicit reference measurements were performed in addition to ensure that also the nonlinear spectra are not influenced by surfactant contributions (cf. Sec. 4.4.1).

4.3 Hydration of $H_2PO_4^-$

To get detailed microscopic insights into the underlying hydration structure of $H_2PO_4^-$, model calculations were performed with phosphate-water clusters containing different numbers of water molecules. These calculations rely on i) DFT/MP2 normal mode analysis and ii) Molecular Dynamics (MD) simulations, with the phosphate ion embedded in a cubic box containing 1226 water molecules simulated by the TIP5P water model [76].
In a first step, normal mode frequencies of phosphate vibrations were determined for different phosphate-water clusters. In a second step, radial distribution functions (rdfs) and dynamical aspects, such as the occurrence of HB breaking, were derived. HBs in the following discussion were defined with oxygen-oxygen distances < 3.5 Å and bonding angles P=O$\cdots$O^W-H^W $< 30°$, according to [128, 129].

4.3.1 Sensitivity of $H_2PO_4^-$ vibrations to the hydration level

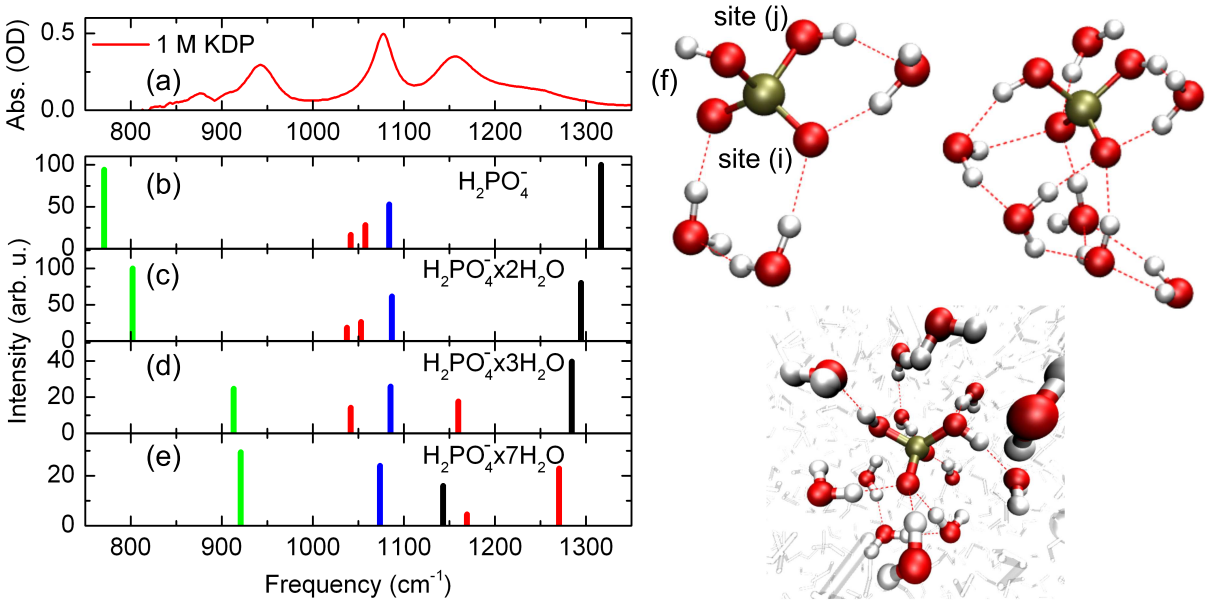

Figure 4.3: Normal mode frequencies for different phosphate-water clusters calculated with MP2 normal mode analysis. (a) Absorption spectrum from Fig. 4.2. (b-e) Frequencies of phosphate vibrations and absorption intensities for $H_2PO_4^- \times xH_2O$ clusters. Additional water molecules induce a blueshift of ν_{AS}(P-$(OH)_2$) (green), a blueshift of both δ(P-$(OH)_2$) bending modes (red), and a redshift of $\nu_{AS}(PO_2^-)$ (black) causing a coupling between $\nu_{AS}(PO_2^-)$ and the bending modes δ(P-$(OH)_2$). (f) Geometrical structure of $H_2PO_4^- \times xH_2O$ clusters with highlighted HBs (red dashed lines). Bottom: Phosphate ion with a full solvation shell within 3.5 Å. Site (i): PO_2^- coordination site, site (j): P-$(OH)_2$ coordination site.

The calculated absorption spectra in Fig. 4.3 show that an isolated $H_2PO_4^-$ ion in the gas phase exhibits absorption bands that deviate significantly from the absorption bands of a hydrated $H_2PO_4^-$ ion. In the high-frequency range at $1320\,cm^{-1}$ emerges the asymmetric stretching vibration $\nu_{AS}(PO_2^-)$ (black). The symmetric stretching vibration $\nu_S(PO_2^-)$ (blue) is located at $1087\,cm^{-1}$, whereas both bending modes $\delta_{AS}(P-(OH)_2)$ and $\delta_S(P-(OH)_2)$ (red) can be found at $1048\,cm^{-1}$ and $1031\,cm^{-1}$, respectively. At a low frequency of $786\,cm^{-1}$ emerges the asymmetric stretching vibration $\nu_{AS}(P-(OH)_2)$ (green).
Once the $H_2PO_4^-$ ion is solvated with two water molecules at the HB accepting PO_2^- site (site (i)), $\nu_{AS}(P-(OH)_2)$ is $\approx 20\,cm^{-1}$ blueshifted and $\nu_{AS}(PO_2^-) \approx 20\,cm^{-1}$ redshifted.
The addition of a third water molecule leads to the formation of two further HBs, one at the HB accepting PO_2^- position and one at the HB donating P-$(OH)_2$ position (site (j)) that strongly influences the P-$(OH)_2$ related normal modes. The HB to the hydroxyl group induces a strong $\approx 100\,cm^{-1}$ blueshift of $\delta_{AS}(P-(OH)_2)$. As a consequence, $\nu_{AS}(PO_2^-)$ and $\delta(P-(OH)_2)$ mix in mode character and delocalise. ν_{AS}(P-$(OH)_2$) also undergoes a blueshift of $\approx 100\,cm^{-1}$.
Solvation with 7 water molecules only weakly affects ν_{AS}(P-$(OH)_2$) and the $\nu_S(PO_2^-)$ mode [78,115]. In contrast, $\nu_{AS}(PO_2^-)$ is redshifted by more than $100\,cm^{-1}$, whereas both $\delta(P-(OH)_2)$ bending modes are strongly blueshifted. Hence, $\nu_{AS}(PO_2^-)$ interchanges with both P-$(OH)_2$ bending vibrations [124,125].
A total amount of 8 HBs to the phosphate ion are formed within the $H_2PO_4^- \times 7H_2O$ cluster, 6 HBs at the hydrogen bond accepting PO_2^- site (i) and 2 at the hydrogen bond donating P-$(OH)_2$ site (j) (cf. Fig. 4.3 (f)).
The comparison of the absorption bands of the $H_2PO_4^- \times 7H_2O$ cluster with the experimental curve reveals strong similarities. The frequencies of ν_{AS}(P-$(OH)_2$) and $\nu_S(PO_2^-)$, $\nu_{AS}(PO_2^-)$ are well reproduced as well as the mode splitting of both PO_2^- stretching vibrations of $80\,cm^{-1}$.
For both $\delta(P-(OH)_2)$ modes a qualitative agreement is observed. The slightly redshifted frequencies of $\nu_S(PO_2^-)$, $\nu_{AS}(PO_2^-)$, and $\nu_{AS}(P-(OH)_2)$ are a result of an overbinding of the first solvation shell with the $H_2PO_4^-$ ion since the second solvation shell is absent in the cluster calculations.
Thus, the cluster calculations have demonstrated that the vibrational absorption spectrum of $H_2PO_4^-$ is significantly determined by HBs and couplings to the surrounding first water shell. Consequently, phosphate vibrations of the $H_2PO_4^-$ ion are very sensitive probes to study the dynamics of phosphate-water and ion-water interactions.

4.3.2 Time-averaged hydration structure

The second step of hydration structure analysis comprises time-averaged radial distribution functions (rdfs) and dynamical aspects derived from MD simulations. Rdfs can be used to describe the spatial arrangement of particles with respect to a central point. They are normalised and dimensionless functions that peak for radial distances with a high density of particles and reach the value 1 for spatial distances at which an average density of disordered particles occurs. Rdfs of $H_2PO_4^-$ embedded in bulk water are shown in Fig. 4.4 in comparison with the reference system pure bulk water.

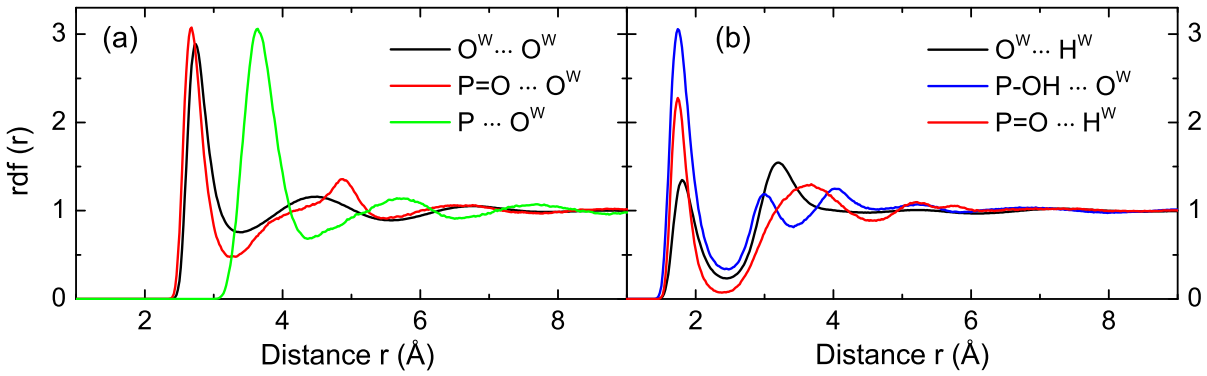

Figure 4.4: Radial distribution functions (rdfs) for $H_2PO_4^-$ dissolved in water in combination with reference rdfs from pure water [125, 130–132]. (a) Rdfs for oxygen-oxygen distances and phosphorous-oxygen distances and (b) for hydrogen-oxygen distances. Hydrogen and oxygen from water molecules are denoted as H^W and O^W, respectively.

Generally, all rdfs are flat beyond a distance of 8 Å so that water molecules located at these distances are stochastically distributed. Distinct structures can be found below 8 Å. The first maximum for $P{=}O\cdots O^W$ distances is evident at ≈ 2.7 Å (red line in (a)), with $\Delta r = 0.06$ Å slightly below the $O^W\cdots O^W$ distance in pure water (black line). Also the rdfs for $P\text{-}OH\cdots O^W$ and $P{=}O\cdots H^W$ apparent as blue and red lines in (b) exhibit first maxima at 1.74 Å, respectively, below the one of pure water at 1.8 Å (black line). Consequently, the phosphate molecule forms stronger HBs to the aqueous solvation shell than a water molecule, in line with former investigations [125, 130, 133]. The rdf for $P\cdots O^W$ (green line in (a)) has its first maximum at 3.6 Å. The observed second maxima are much weaker and appear for e.g. $P\cdots O^W$ around 5.75 Å pointing to a minor orientation of the water molecules in the second solvation shell. Weak third maxima can be found up to ≈ 7.5 Å.

On average, 12 water molecules form the first hydration shell of $H_2PO_4^-$. This configuration leads to a total amount of 9.7 HBs between the phosphate ion and its surrounding water molecules. The PO_2^- coordination site represents the major hydration site.

MD simulations also allow for an access to dynamical aspects of the spatial arrangement between $H_2PO_4^-$ and water molecules such as the lifetimes of HBs [134]. They have been found to persist for 10.9 ps averaged over both coordination sites, the HB donating $P\text{-}(OH)_2$ and the HB accepting PO_2^- site. HBs in bulk water exhibit lifetimes of about 1-2 ps and, hence, are substantially shorter underlining the considerably stronger bonds between $H_2PO_4^-$ and water [100, 131]. HB breaking events are induced by short time fluctuations. In the vicinity of the negatively charged ion $H_2PO_4^-$ with its strong Coulomb field, the spatial reorientation of water molecules after HB breaking is decelerated compared to pure bulk water.

4.4 Vibrational lifetimes of phosphate vibrations

Femtosecond pump/probe experiments with different pump frequencies in a spectral range between 850 cm^{-1} and 1350 cm^{-1} revealed the vibrational lifetimes of $\nu_{AS}(P\text{-}(OH)_2)$, $\nu_S(PO_2^-)$, $\nu_{AS}(PO_2^-)$, and both $\delta(P\text{-}(OH)_2)$ modes. The liquid jet introduced in Sec. 3.5 was used to measure the $H_2PO_4^-$ containing water solution with a phosphate concentration of 1 M and a film thickness of 10 µm while any nonlinear signal contributions by window materials could be avoided. Initially, nonlinear signals caused by resonantly excited water librations and the utilised surfactant were evaluated in reference measurements in the mentioned spectral region. Subsequently, the transient behaviour of resonantly excited phosphate vibrations is discussed in detail.

4.4.1 Reference measurements on water

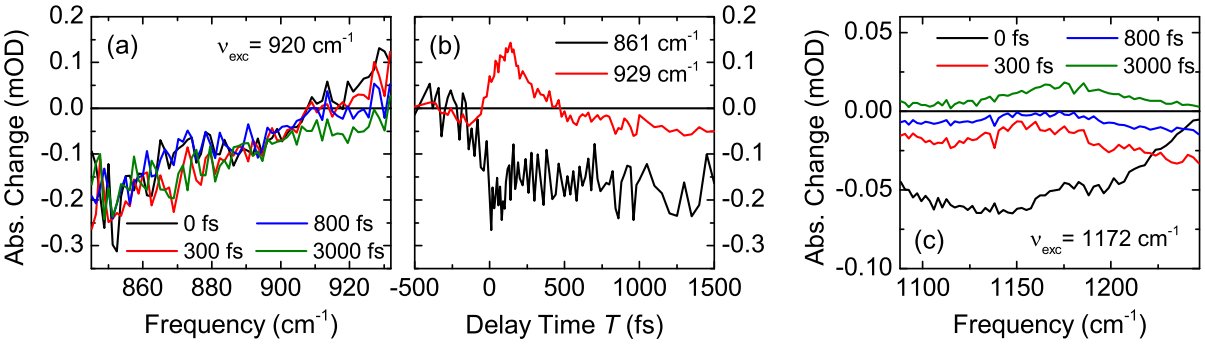

Figure 4.5: Reference pump/probe measurements on pure water with the surfactant *IGEPAL*® 890 (6 mM). (a,b) Transient spectra for delay times between 0 fs and 3 ps in the spectral region of the $\nu_{AS}(P-(OH)_2)$ absorption band illustrated together with transients at two different probe frequencies; $\Delta A = -\log(I/I_0)$. (c) Transient spectra for delay times between 0 fs and 3 ps in the spectral region of the $\nu_{AS}(PO_2^-)$ absorption band. The shown data exhibit small signal amplitudes and essentially flat nonlinear spectra in strong contrast to the nonlinear signals of the 1 M KDP solution (cf. Fig. 4.6). All measured results are in line with former investigations on pure water [127, 135–137].

Fig. 4.5 shows reference measurements on water containing only the dissolved surfactant *IGEPAL*® 890 at a concentration of 6 mM in the spectral range of the investigated phosphate absorption bands. The resonant excitation of water within the high-frequency tail of the L2-band (cf. Fig. 4.2, $\nu_{exc.} = 920\,cm^{-1}$) leads to persisting bleach signals in the transient spectra below 910 cm^{-1} (panel (a)). In the transients (panel (b)), an enhanced absorption with a maximum around 150 fs is observed at 929 cm^{-1} that decays on a sub 200 fs timescale and subsequently evolves into a persisting bleaching at late delay times $\geq$ 500 fs. A steplike behaviour and solely negative signals can be observed for transients below 910 cm^{-1}.

Under excitation of the high frequency librations of water at $\nu_{exc.} = 1172\,cm^{-1}$, spectrally flat nonlinear spectra with negative signs can be observed for delay times of 0 fs, 300 fs, and 800 fs. At 3 ps, a flat nonlinear spectrum with a positive sign is measured. All nonlinear spectra have small signal amplitudes with $\Delta A < 0.05$ mOD.

Former investigations on water document similar transient behaviours as measured here [36, 127, 136, 137]. A transient redshift of the L2-band explains the results shown in panels (a,b) whereas the small dipole moment of the high frequency librations between 1000 cm^{-1} and 1600 cm^{-1} causes the small linear absorption and, thus, the small transient absorption changes. This leads to the conclusion that the surfactant *IGEPAL*® 890 can

only have a negligible influence on the nonlinear responses of the measured water and the phosphate-water solution.

4.4.2 Lifetimes of phosphate vibrations

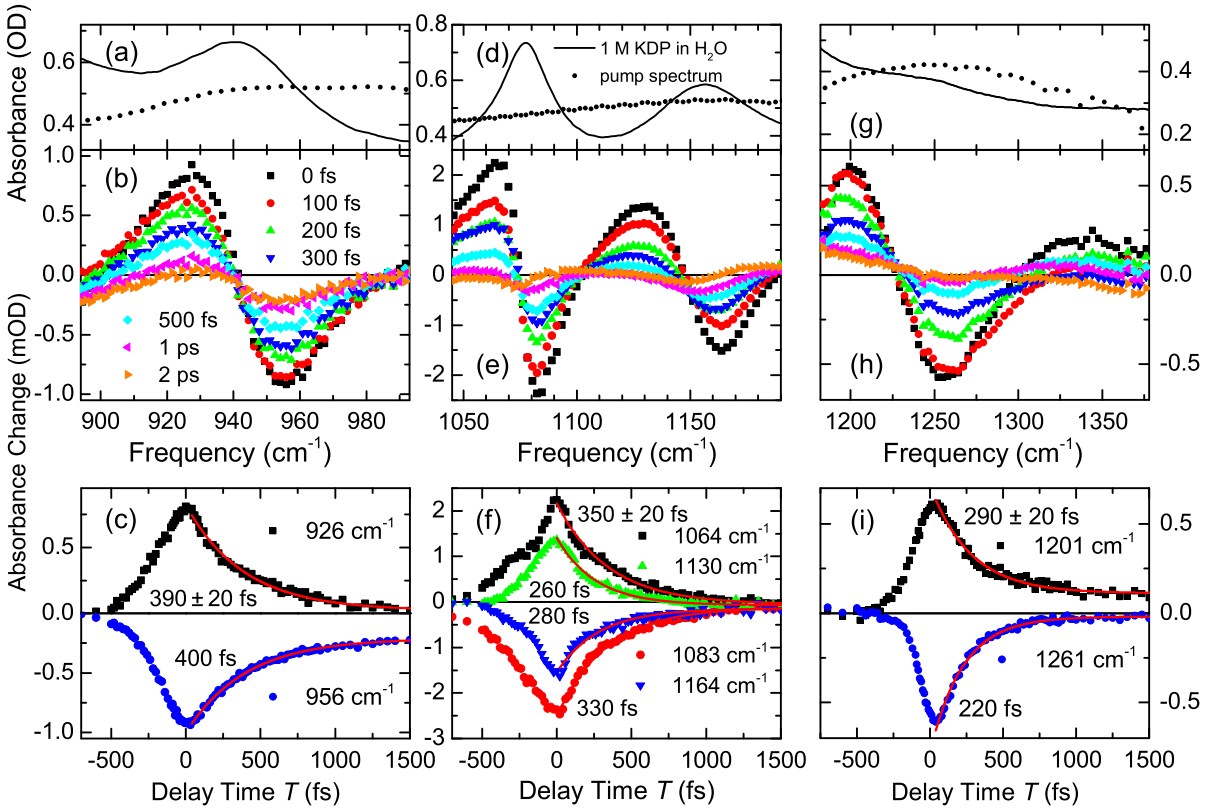

Figure 4.6: Nonlinear spectra and transients of pump/probe measurements on ν_{AS}(P-$(OH)_2$) (left), $\nu_S(PO_2^-)$ and $\nu_{AS}(PO_2^-)$ (middle), δ_S(P-$(OH)_2$) and δ_{AS}(P-$(OH)_2$) (right) of an aqueous 1 M $H_2PO_4^-$ solution, measured in a 10 µm liquid jet; $\Delta A = -\log(I/I_0)$. (a,d,g) Linear absorption spectra (solid lines) of the measured solution shown together with partial pump pulse spectra (dotted lines) utilised for the time-resolved experiments. A complete pump pulse spectrum is given in Fig. 4.2. (b,e,h) Time-resolved spectra for delay times between 0 fs and 2 ps. (c,f,i) Transients at particular probe frequencies (symbols) with monoexponential fits to deduce the corresponding time constants (red lines). All modes show a pronounced decrease of absorption at the fundamental transitions and redshifted excited state absorptions. At delay times of ≈ 2 ps, a heated phosphate-water solution causes the signature of thermal pump/probe signals. For $T < 0$ fs, PFID leads to the measured nonlinear signals [49]. Pump pulse energy: $E_{pump} \approx 1.5\,\mu J \mathrel{\widehat{=}} 6 \cdot 10^{10}\,W/cm^{-2}$.

Fig. 4.6 represents the nonlinear absorption changes of ν_{AS}(P-$(OH)_2$), $\nu_S(PO_2^-)$, $\nu_{AS}(PO_2^-)$, and the bending modes δ(P-$(OH)_2$). Nonlinear spectra at different delay times are given in the panels (b), (e), and (h) and transients at fixed probe frequencies in the panels (c), (f), and (i). Due to excitation by the pump pulses, a depopulation of the vibrational ground states and a population of the first excited states occur, v=0→1. As a consequence, the v=0 states are bleached and stimulated emission from the v=1 states arises which both together results in a decrease of probe pulse absorption on the fundamental transitions of ν_{AS}(P-$(OH)_2$), $\nu_S(PO_2^-)$, $\nu_{AS}(PO_2^-)$, and both bending modes δ(P-$(OH)_2$). The diagonal anharmonicities of the excited oscillators cause the excited state absorptions v=1→2 to be redshifted. They decay with time constants between 260 fs for $\nu_{AS}(PO_2^-)$ and 390 fs for ν_{AS}(P-$(OH)_2$). An estimation of the anharmonicities via line shape analysis

revealed numerical values of $\approx 10\,\mathrm{cm}^{-1}$ for all modes shown in Fig. 4.6 that are consistent with vibrational self-consistent field (vscf) calculations [76]. The measured bleaching signals decay on the same timescale as the corresponding excited state absorptions.
All pump/probe spectra exhibit small residual signals at delay times $\geq 1.5\,\mathrm{ps}$. For $\nu_{\mathrm{S}}(\mathrm{PO}_2^-)$ and $\nu_{\mathrm{AS}}(\mathrm{PO}_2^-)$, these signals are in line with a blueshift of the fundamental transitions that extend to frequencies $\geq 1200\,\mathrm{cm}^{-1}$, also causing the small offset at late delay times evident in panel (i). A heat jump of $\approx 1\,\mathrm{K}$ of the phosphate surrounding water due to resonant excitation of the phosphate vibrations, as well as of water librations, weakens the phosphate-water HBs and leads to the blueshifts (cf. Fig. 4.3). In contrast, $\nu_{\mathrm{AS}}(\mathrm{P\text{-}(OH)_2})$ shows a small redshift at late delay times in panels (b) and (c) that is superimposed by negative signal contributions from the excited high frequency tail of the L2 band of water (cf. Fig. 4.5) [127]. This behaviour can be understood from the afore mentioned $\mathrm{H_2PO_4^-} \times x\mathrm{H_2O}$ cluster calculations that demonstrated a redshift of $\nu_{\mathrm{AS}}(\mathrm{P\text{-}(OH)_2})$ upon desolvation (cf. Fig. 4.3).
A comparison with the nonlinear response of pure water (cf. Fig. 4.5) reveals substantial differences with respect to the amplitudes of the measured nonlinear signals and their spectral shapes. The essentially spectrally flat response of water and the one order of magnitude smaller signal amplitudes clearly show that resonantly excited water librations do not contribute directly to the nonlinear response of $\mathrm{H_2PO_4^-}$ shown in Fig. 4.6.
The general ultrafast sub-400 fs timescale of vibrational relaxation should be discussed. Current investigations on intramolecular couplings of $\mathrm{H_2PO_4^-}$ in an aqueous environment predict a Fermi resonance between the overtone of a low frequency tetrahedron skeleton mode $\delta(\mathrm{O{=}P\text{-}O})$ ($\nu_{\delta(\mathrm{O=P-O})} = 506\,\mathrm{cm}^{-1}$) with the redshifted excited state of $\nu_{\mathrm{S}}(\mathrm{PO}_2^-)$ around $1030\,\mathrm{cm}^{-1}$ [138]. Hence, a relaxation of the v=1 state of $\nu_{\mathrm{S}}(\mathrm{PO}_2^-)$ can occur via the v=2 state of $\delta(\mathrm{O{=}P\text{-}O)}$ with subsequent energy dissipation into the water environment. This process is very efficient since the transition frequencies of the $\delta(\mathrm{O{=}P\text{-}O)}$ oscillator are resonant to the broad L2 band of water [127]. Similar relaxation channels can be expected for $\nu_{\mathrm{AS}}(\mathrm{PO}_2^-)$, $\nu_{\mathrm{AS}}(\mathrm{P\text{-}(OH)_2})$ and the bending modes $\delta(\mathrm{P\text{-}(OH)_2})$.
Contrasting the vibrational lifetimes measured here with vibrational lifetimes of phosphate groups in phospholipids and DNA systems reveals strong similarities and differences [31, 115–118]. In those systems, $\nu_{\mathrm{S}}(\mathrm{PO}_2^-)$ exhibits v=1 lifetimes that sensitively depend on the water content in the direct environment. Lifetimes of 1.5 ps are documented for a low hydration level of one water molecule per phosphate group that decrease to 1 ps for a higher hydration level of 16 water molecules per phosphate group [34]. Both lifetimes are longer than the 350 fs measured here. As opposed to this, 300 fs v=1 lifetimes are documented for $\nu_{\mathrm{AS}}(\mathrm{PO}_2^-)$ that do not depend on the hydration level, similar to the 260 fs shown in Fig. 4.6. This behaviour points to a relaxation mechanism for $\nu_{\mathrm{AS}}(\mathrm{PO}_2^-)$ that also involves low-frequency phosphate vibrations on the one hand, and to a more complex relaxation behaviour for ν_{AS} in DNA and phospholipids on the other hand.

4.5 Structural dynamics from 2D-IR spectra

Structural dynamics and intermolecular couplings of vibrational modes are experimentally accessible with nonlinear spectroscopy and especially with 2D-IR spectroscopy (cf. Sec. 2.7) [44,96,115]. Here, 2D-IR spectroscopy was applied to investigate the interaction between phosphate ions and their fluctuating hydration shells, as well as couplings among phosphate vibrations. The investigated sample is a 1 M aqueous $H_2PO_4^-$ (KDP) solution measured as a 10 µm thin liquid jet, similar to the pump/probe experiments.

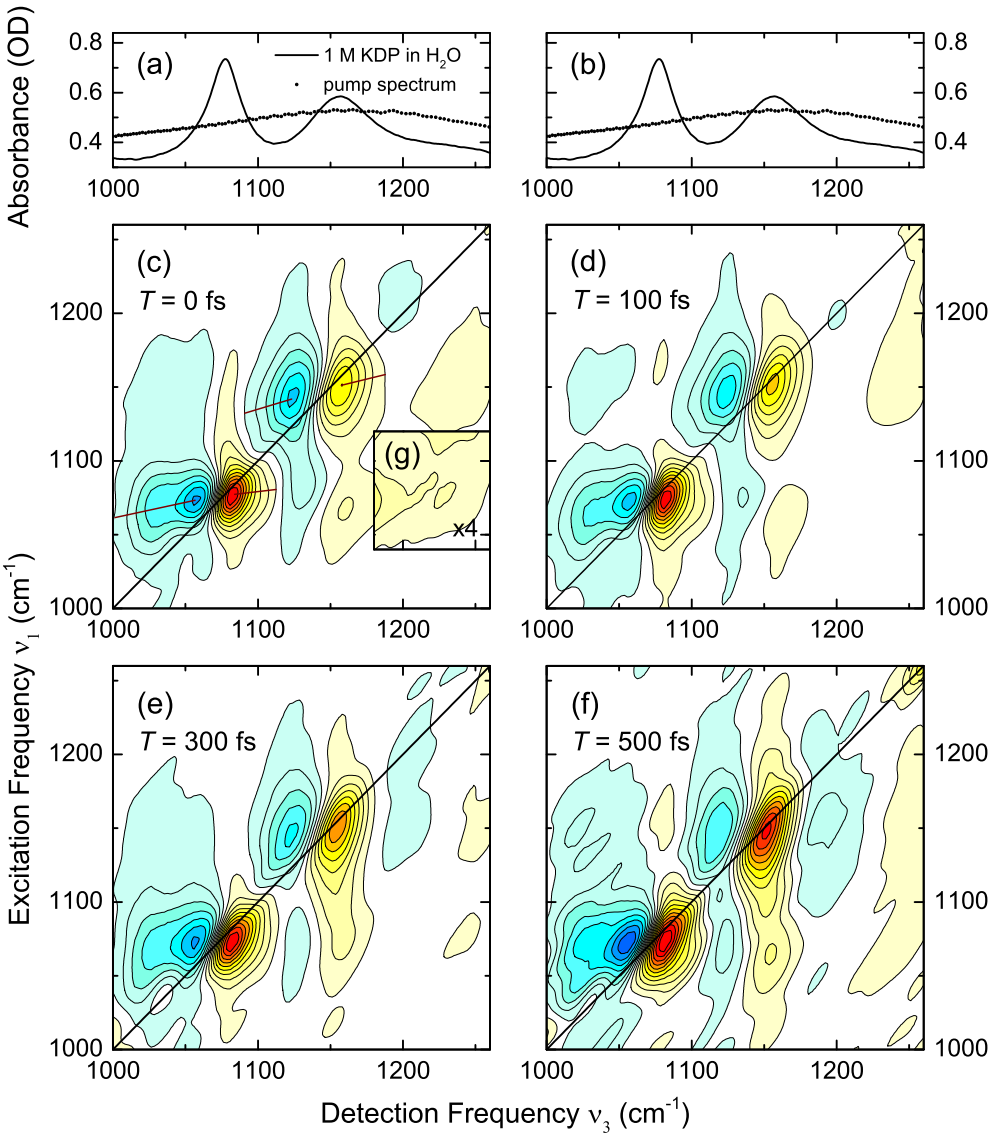

Figure 4.7: Broadband 2D-IR spectra for phosphate vibrations between 1000 cm^{-1} and 1260 cm^{-1} measured with an aqueous 1 M $H_2PO_4^-$ solution in a 10 µm liquid jet. The panels (a,b) display linear absorption spectra of the solution and a partial pump pulse spectrum. (c-f) Normalised contour plots exhibiting absorptive 2D signals with signal contributions from $\nu_S(PO_2^-)$, $\nu_{AS}(PO_2^-)$ and δ_S(P-$(OH)_2$), δ_{AS}(P-$(OH)_2$) for delay times T between 0 and 500 fs. Adjacent contour lines differ in 10 percentage points. Panel (g) shows an upscaled (factor 4) spectral range between ν_1 = 1040 cm^{-1} − 1120 cm^{-1} and ν_3 = 1180 cm^{-1} − 1260 cm^{-1}. Positive signals are shown as yellow-red contours and negative signals as blue contours. Diagonal peaks around the fundamental transition frequencies are the strongest features in the 2D plots. Anharmonic couplings among the phosphate vibrations lead to the measured off-diagonal cross peaks. The general upright shape of the diagonal peaks with centre lines (brown lines) almost parallel to the ν_3-axis reveals prevalent homogeneous broadening. Pump pulse energies: $E_{pump} \approx 1.5\,\mu J \mathrel{\widehat{=}} 6 \cdot 10^{10}\,W/cm^{-2}$.

Fig. 4.7 shows absorptive 2D-IR spectra of the aqueous $H_2PO_4^-$ solution with a 1 M concentration for delay times between $T = 0$ fs and $T = 500$ fs. The utilisation of the liquid jet allows for the evaluation of the 2D-IR spectra for $T = 0$ fs and $T = 100$ fs. The chosen spectral region between 1000 cm^{-1} and 1260 cm^{-1} comprises absorption bands of $\nu_S(PO_2^-)$, $\nu_{AS}(PO_2^-)$, and both bending modes δ(P-$(OH)_2$). Bleaching signals due to v=0→ 1 transitions and stimulated emission are illustrated as yellow-red contours, whereas excited state absorptions due to v=1→ 2 transitions are shown as blue contours. All 2D spectra have normalised intensities and adjacent contour lines differ in 10 percentage points.
Strong diagonal peaks of $\nu_S(PO_2^-)$ and $\nu_{AS}(PO_2^-)$ centred around $\nu_3 = \nu_1 = 1075\,cm^{-1}$ and $\nu_3 = \nu_1 = 1150\,cm^{-1}$ are evident in all 2D spectra in Fig. 4.7. Only weak diagonal peaks can be measured for both δ(P-$(OH)_2$) modes around $\nu_3 = \nu_1 = 1200\,cm^{-1}$ because of their shoulder-like linear absorption and, thus, substantially smaller transition dipole moments.
Pronounced off-diagonal cross peaks are observed between $\nu_S(PO_2^-)$ and $\nu_{AS}(PO_2^-)$ around $\nu_3 = 1070\,cm^{-1}$, $\nu_1 = 1150\,cm^{-1}$ and $\nu_3 = 1150\,cm^{-1}$, $\nu_1 = 1070\,cm^{-1}$, which demonstrate a vibrational coupling among the two PO_2^- stretching modes. A further coupling between $\nu_{AS}(PO_2^-)$ and both P-$(OH)_2$ bending modes is obvious as the large yellow contour around $\nu_3 = 1240\,cm^{-1}$, $\nu_1 = 1150\,cm^{-1}$ and the tails around $\nu_3 = 1150\,cm^{-1}$, $\nu_1 = 1240\,cm^{-1}$. Panel (g) shows a weak cross peak between $\nu_S(PO_2^-)$ and both P-$(OH)_2$ bending modes. Complementary (weak) cross peaks can also be found around $\nu_3 = 1070\,cm^{-1}$, $\nu_1 = 1220\,cm^{-1}$ (not shown). Current investigations revealed further cross peaks between the asymmetric stretching mode $\nu_{AS}(P-(OH)_2)$ at 942 cm^{-1} (cf. Figs. 4.2 and 4.6) and the two stretching modes $\nu_S(PO_2^-)$, $\nu_{AS}(PO_2^-)$ [138].
The diagonal and off-diagonal anharmonicities have amplitudes of $\approx 10\,cm^{-1}$ which is small compared to the $\approx 50\,cm^{-1}$ line widths of $\nu_S(PO_2^-)$ and $\nu_{AS}(PO_2^-)$ in the linear absorption spectrum. This leads to a strong overlapping of positive and negative signal contributions within the 2D spectra and, in combination with the distinct cross peaks, to their stripe-like appearance.
The line shapes of the diagonal peaks are essentially round and homogeneous and exhibit only a small tilt along the diagonal. These homogeneous shapes are underlined by the centre lines in panel (a) that are close to a slope of 0. No significant dynamical changes are observed in the line shapes within the measured delay times from $T = 0$ fs to $T = 500$ fs.
An apparent feature is the plateau-like elongation of the excited state absorption of $\nu_S(PO_2^-)$ around $\nu_3 = 1030\,cm^{-1}$, $\nu_1 = 1075\,cm^{-1}$ that can be attributed to a Fermi resonance of the v=1 state of $\nu_S(PO_2^-)$ with the v=2 state of the low-frequency tetrahedron skeleton mode (δ(O=P=O)) [138].
The rising blue contours for longer delay times and especially for $T = 500$ fs around $\nu_3 = 1190\,cm^{-1}$, $\nu_1 = 1150\,cm^{-1}$ can be attributed to a thermal signal contribution due to a blueshift of $\nu_{AS}(PO_2^-)$. Simultaneously, the relative bleaching intensity of $\nu_{AS}(PO_2^-)$ on the diagonal is enhanced. This peculiarity occurs, because the asymmetric PO_2^- stretching vibration $\nu_{AS}(PO_2^-)$ is very sensitive to a temperature change of the surrounding water. In Fig. 4.8, a broadband 2D spectrum is presented for a delay time of $T = 5000$ fs to demonstrate the sensitivity of $\nu_{AS}(PO_2^-)$. At $T = 5000$ fs, all excited phosphate vibrations are completely decayed and the excess energy is transferred into the water environment.

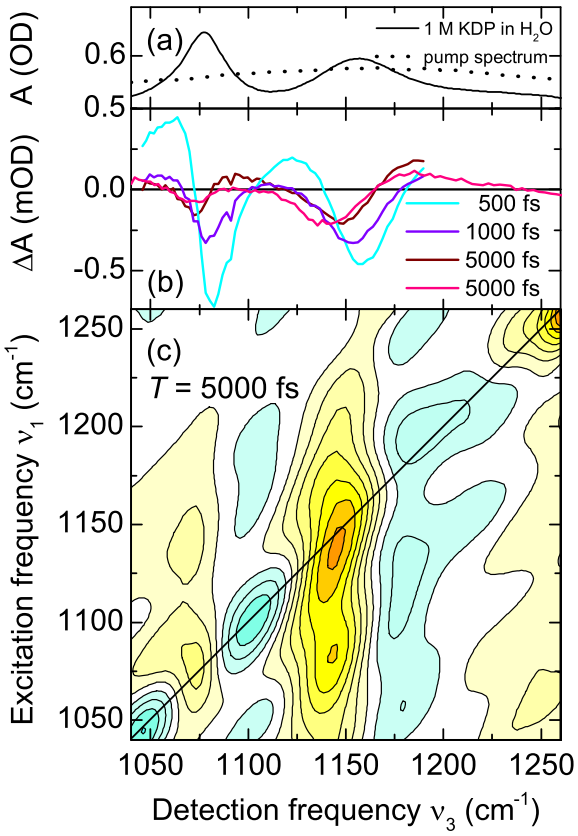

Figure 4.8: Broadband 2D-IR spectrum for phosphate vibrations between 1040 cm^{-1} and 1260 cm^{-1} measured with an aqueous 1 M $H_2PO_4^-$ containing solution in a 10 µm liquid jet. Panel (a) illustrates the linear absorption spectrum of the solution and a partial pump pulse spectrum. (b) Shows transient pump/probe spectra from Fig. 4.6 between 0.5 ps and 5 ps and one broadband pump/probe spectrum (magenta) at 5 ps used to scale and phase the absorptive 2D plot in (c). Adjacent contour lines differ in 10 percentage points. Positive signals are shown as yellow-red contours and negative signals as blue contours. At $T = 5$ ps, all phosphate vibrations are in their ground states such that (c) shows a normalised 2D spectrum with purely thermal signal contributions.

Fig. 4.8 illustrates a hot ground state of the phosphate-water solution around the two PO_2^- stretching vibrations. The pump/probe spectra in panel (b) clearly show a redshift of the non-vanishing bleaching around the fundamental transitions of $\nu_S(PO_2^-)$ and $\nu_{AS}(PO_2^-)$ with a much more pronounced amplitude for $\nu_{AS}(PO_2^-)$. At the same time, enhanced absorption can be observed that is blueshifted to the fundamental transitions. Theses behaviours are in line with a blueshift of $\nu_S(PO_2^-)$ and $\nu_{AS}(PO_2^-)$ caused by the dissipation of excess energy into the water environment of the phosphates and a subsequent heat jump of ≈ 1 K. The heated water leads to a desolvation of $H_2PO_4^-$ and, consequently, to a blueshift of the PO_2^- stretching vibrations, whereby $\nu_{AS}(PO_2^-)$ is much more sensitive to this effect. This also becomes clear in the 2D spectrum in panel (c) where the yellow contours at the diagonal around $\nu_3 = 1140$ cm^{-1}, $\nu_1 = 1140$ cm^{-1} are the most intense features. The general streaky shapes of the peaks in panel (c) that are elongated along ν_1 arise from the pronounced librational manifold of water in this spectral range that couples anharmonically to the PO_2^- stretching vibrations.

4.5.1 Line shape analysis

The upright shape of the diagonal peaks of $\nu_S(PO_2^-)$ and $\nu_{AS}(PO_2^-)$ in Fig. 4.7 with their small tilts along the diagonal suggest a prevalent homogeneous broadening [2]. This visual argument can be hardened with spectral cuts through the 2D spectra along the frequency diagonal $\nu_1 = \nu_3$ (diagonal cuts) and along the ν_3-axis (horizontal cuts). In case the diagonal and horizontal cuts exhibit peaks with similar widths, the peaks are homogeneously broadened. Fig. 4.9 shows the respective cuts for $\nu_S(PO_2^-)$ and $\nu_{AS}(PO_2^-)$ at $T = 0\,\text{fs}$.

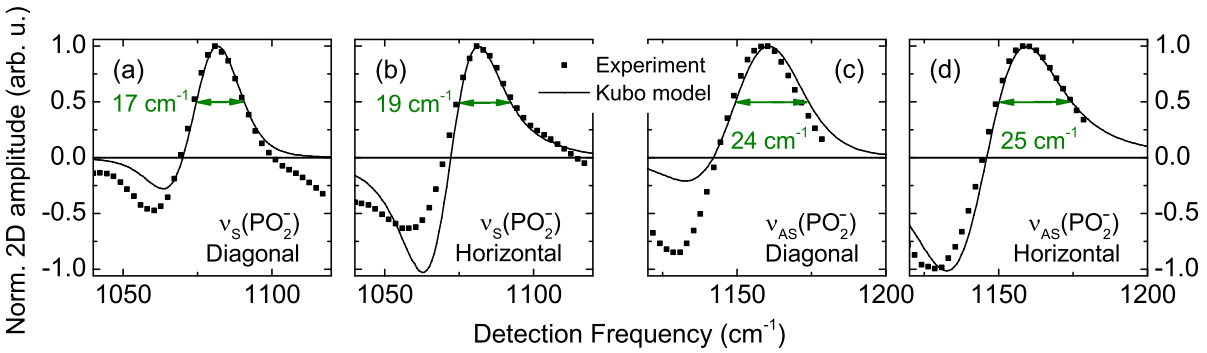

Figure 4.9: Normalised diagonal and horizontal cuts through the 2D spectrum in Fig. 4.7 (a) for $\nu_S(PO_2^-)$ and $\nu_{AS}(PO_2^-)$ (symbols) in combination with calculated cuts (lines) according to Fig. 4.10 and eqn. (4.2). Panel (a) shows cuts for $\nu_S(PO_2^-)$ along $\nu_1 = \nu_3$ (diagonal) and (b) along $\nu_1 = 1075\,\text{cm}^{-1}$ (horizontal). The horizontal cuts cross the maxima of the v=0→ 1 transitions. Panel (c) shows diagonal cuts for $\nu_{AS}(PO_2^-)$ and (d) along $\nu_1 = 1155\,\text{cm}^{-1}$. Olive green arrows and numbers denote the spectral width of the respective cut.

As mentioned before, small diagonal anharmonicities lead to cancellation effects which reduce the spectral peak widths in the cuts through the 2D spectra. In all cases, the peak widths are smaller than the corresponding absorption lines ($\approx 50\,\text{cm}^{-1}$) in the linear absorption spectra (cf. Fig. 4.2). For $\nu_S(PO_2^-)$, the positive peak exhibits a spectral width of $\delta \approx 18\,\text{cm}^{-1}$ for the diagonal and the horizontal cuts, respectively, that convincingly demonstrates the homogeneity of the 2D line shape. A comparable behaviour is measured for $\nu_{AS}(PO_2^-)$. The corresponding positive peaks exhibits a very similar spectral width of $\approx 25\,\text{cm}^{-1}$ and, thus, underline the predominant homogeneous line shape.
A theoretical 2D line shape analysis makes it possible to derive fluctuation amplitudes for $\nu_S(PO_2^-)$ and $\nu_{AS}(PO_2^-)$ and correlation times of the phosphate water interactions. These quantities are components of the time correlation function of frequency fluctuations $C(t)$. With the help of the response functions discussed in Sec. 2.7.2 and Sec. 2.9 and density matrix theory one can generate theoretical 2D spectra and, thus, determine $C(t)$ with the corresponding frequency fluctuations and correlation times [2, 15, 76, 138]. To derive $C(t)$ for $\nu_S(PO_2^-)$ and $\nu_{AS}(PO_2^-)$, Gaussian frequency fluctuations are assumed and a biexponential Kubo approach is chosen. Then, $C(t)$ contains explicit parameters for the fluctuation amplitudes $\delta\nu_1$ and $\delta\nu_2$, as well as for the correlation times τ_{C1} and τ_{C2} and can be written as (cf. eqn. (2.16))

$$C(t) = (\delta\nu_1)^2 e^{-t/\tau_{C1}} + (\delta\nu_2)^2 e^{-t/\tau_{C2}}. \tag{4.1}$$

To properly account for the static, upright shape of the diagonal peaks for $\nu_S(PO_2^-)$ and $\nu_{AS}(PO_2^-)$ in Fig. 4.7, the biexponential Kubo function is supposed to contain an

ultrafast as well as a static term with an infinitely large correlation time τ_{C2}. Then, the Kubo function simplifies to

$$C(t) = (\delta\nu_1)^2 e^{-t/\tau_{C1}} + (\delta\nu_2)^2. \tag{4.2}$$

With the response functions from Sec. 2.7.2 and Sec. 2.9, as well as small anharmonicities for both PO_2^- stretching vibrations of 10 cm^{-1} (Δ in eqn. (2.43)), one can find a parameter set for $\delta\nu_{1,2}$ and $\tau_{C1,C2}$ to reproduce the 2D spectra for $\nu_S(PO_2^-)$ and $\nu_{AS}(PO_2^-)$. A suitable set of parameters is given in Tab. 4.1:

	$\delta\nu_1$ cm^{-1}	τ_{C1} fs	$\delta\nu_2$ cm^{-1}	τ_{C2} fs
$\nu_S(PO_2^-)$	15	50	5	∞
$\nu_{AS}(PO_2^-)$	27	50	7	∞

Table 4.1: Compilation of the fluctuation amplitudes $\delta\nu_1$, $\delta\nu_2$ and the correlation times τ_{C1}, τ_{C2} for $\nu_S(PO_2^-)$ and $\nu_{AS}(PO_2^-)$, respectively, to model the 2D line shapes measured in Fig. 4.7.

With the parameters from Tab. 4.1, a 2D spectrum for the two PO_2^- stretching vibrations can be generated and their line shapes reconstructed, as is shown in Fig. 4.10.

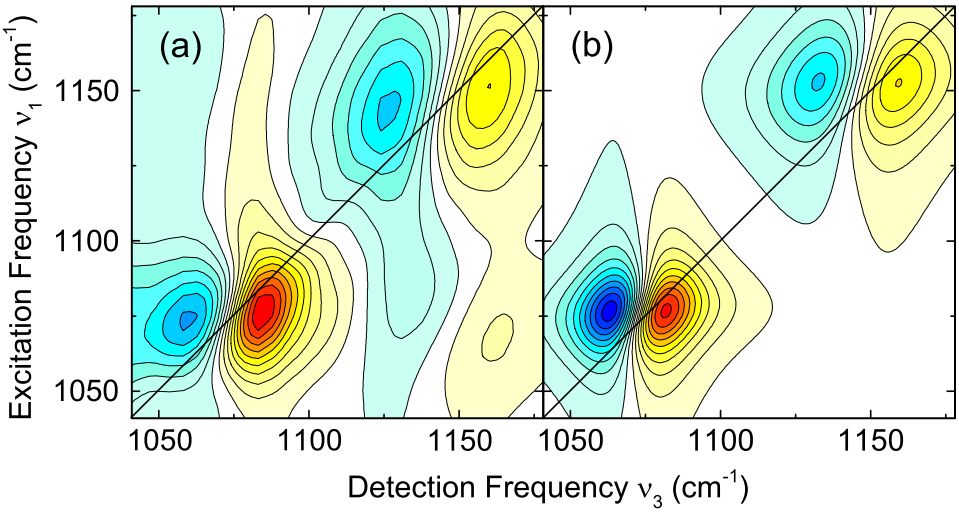

Figure 4.10: Line shape analysis to derive structural fluctuation times and amplitudes for $\nu_S(PO_2^-)$ and $\nu_{AS}(PO_2^-)$. (a) Experimental 2D spectrum at delay time $T = 0$ fs from Fig. 4.7. (b) Theoretical 2D spectrum with the parameters from Tab. 4.1.

Fig. 4.10 illustrates the theoretically derived 2D spectrum for $\nu_S(PO_2^-)$ and $\nu_{AS}(PO_2^-)$ between 1040 cm^{-1} and 1180 cm^{-1} in panel (b) in direct comparison to the experimental one from Fig. 4.7 in panel (a). With the chosen parameters from Tab. 4.1, the line shapes of the diagonal peaks can be reproduced very well. Especially their upright appearance with their small tilt along the diagonal is described convincingly. These results are further underlined in the comparison of the spectral cuts as shown in Fig. 4.9, where both the experimental (symbols) as well as the theoretical cuts (lines) exhibit very similar shapes. Deviations can be found for the negative peaks in Fig. 4.9 panels (b) and (c) that can be attributed to the absence of cross peaks and Fermi resonance couplings in the applied

theoretical approach and to a slight downshift of the v=1→ 2 transition along the excitation frequency axis for $\nu_{AS}(PO_2^-)$.

The first 50 fs correlation time components for $\nu_S(PO_2^-)$ and $\nu_{AS}(PO_2^-)$ depict the dominant ultrafast frequency fluctuations which lead to the upright line shapes and their homogeneously broadened appearance [7]. The second weaker long-lasting components identify a persisting memory of the transition frequencies that continues at least up to 500 fs, a time window in which the major portion of the excited vibrational states have already decayed. Therefore, the second components reflect the inhomogeneous contributions within the measured 2D line shapes of $\nu_S(PO_2^-)$ and $\nu_{AS}(PO_2^-)$, evident as the small tilts along the diagonal.
Even though water does not directly contribute to the nonlinear signals measured around the fingerprint frequencies of $\nu_{AS}(PO_2^-)$ and $\nu_S(PO_2^-)$ (cf. Sec. 4.4), the influence of resonantly excited librational modes on the observed frequency fluctuations should be discussed. Generally, a higher water temperature and/or excited librations lead to stronger structural fluctuations and, therewith, an accelerated loss of structural correlation between individual water molecules [7]. With the experimental conditions used, a spatially randomised portion of $\approx 10^{-3}$ water molecules is excited. Compared to a thermal occupation of water librations that amounts to $e^{-1000\,cm^{-1}/200\,cm^{-1}} \approx 7 \cdot 10^{-3}$, resonantly excited water librations can only play a minor role for the measured frequency fluctuations just as for the pump/probe signals.

4.5.2 Instantaneous frequency fluctuations

For an in-depth analysis of the ultrafast frequency fluctuations of phosphate vibrations in the vicinity of water, ab-initio hybrid quantum-classical calculations were performed [76]. Nuclear configurations of a hydrated $H_2PO_4^-$ ion were calculated by a classical MD trajectory and the relaxed instantaneous normal modes of $\nu_S(PO_2^-)$, $\nu_{AS}(PO_2^-)$ and δ(P-(OH)$_2$) along this MD trajectory were derived. The results of this ab-initio calculation are illustrated in the following Fig. 4.11.

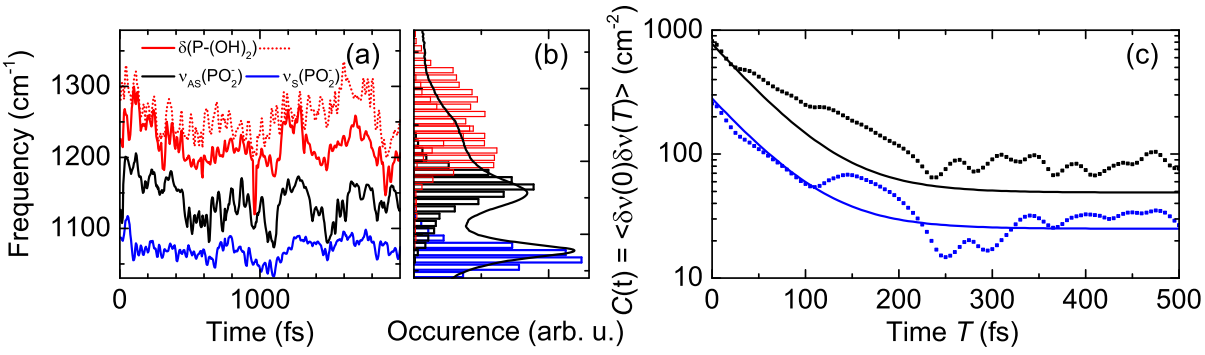

Figure 4.11: Instantaneous frequency fluctuations of $\nu_S(PO_2^-)$, $\nu_{AS}(PO_2^-)$, and δ(P-(OH)$_2$) from time-dependent nuclear configurations in a classical MD trajectory. (a) Instantaneous frequencies over 2 ps from the mixed quantum-classical model (cf. Fig. 2.4). (b) Theoretical frequency distributions in comparison with the linear absorption spectrum of the aqueous $H_2PO_4^-$ solution from Fig. 4.2. (c) Frequency-frequency fluctuation correlation functions ($C(t) = \langle\delta\nu(0)\delta\nu(T)\rangle$, cf. eqn. (2.16)) of $\nu_S(PO_2^-)$ and $\nu_{AS}(PO_2^-)$ derived from the mixed quantum-classical model (squares) and from the biexponential Kubo model (lines) (cf. Fig. 4.1, eqn. (4.2)).

Instantaneous frequency fluctuations are shown in Fig. 4.11 (a) for $\nu_S(PO_2^-)$, $\nu_{AS}(PO_2^-)$,

and both δ(P-$(OH)_2$) modes within a time window of 2 ps. The time evolutions of the frequencies are characterised by ultrafast 50 fs fluctuations as a consequence of modulated spatial configurations of phosphate and water molecules within the HB network. Frequency fluctuations are most pronounced for both δ(P-$(OH)_2$) modes (bandwidths of $\approx 50\,\mathrm{cm}^{-1}$, respectively), somewhat less for $\nu_{\mathrm{AS}}(PO_2^-)$ (bandwidth of $\approx 30\,\mathrm{cm}^{-1}$), and least pronounced for $\nu_{\mathrm{S}}(PO_2^-)$ (bandwidth of $\approx 15\,\mathrm{cm}^{-1}$), indicating that $\nu_{\mathrm{AS}}(PO_2^-)$ is more sensitive to local field fluctuations than $\nu_{\mathrm{S}}(PO_2^-)$. A histogram of normal mode frequencies over 12 ps reveals Gaussian-like fluctuations with bandwidths very close to the experimentally observed ones, as shown in (b).
Panel (c) shows correlation functions for frequency fluctuations derived from the instantaneous frequencies of the MD trajectory (squares) and from 2D line shape simulations (lines) for $\nu_{\mathrm{S}}(PO_2^-)$ and $\nu_{\mathrm{AS}}(PO_2^-)$ (cf. Sec. 4.5.1). Qualitative agreement, especially concerning the fluctuation time scales, is evident between both models. Quick initial decays are observed and after 300 fs, most of the correlations are lost. Quantitative differences occur due to incomplete convergences in the mixed quantum-classical model [97, 139].
The experimentally and theoretically observed 50 fs fluctuation time scale for phosphate vibrations in the vicinity of bulk water and the corresponding quick decay of the correlation functions illustrate that HB breaking and formation events contribute only subsidiary to the derived fluctuation dynamics. Lifetimes of HBs between water molecules and $H_2PO_4^-$ ions exceed 10 ps, derived from MD simulations (cf. Sec. 4.3), and, thus, outlive 50 fs fluctuations. Hence, librations of water molecules within the first solvation shells of $H_2PO_4^-$ are responsible for the measured homogeneous 2D line shapes.

4.5.3 Comparison with phospholipid and DNA model systems

Complementary to isolated $H_2PO_4^-$ ions in bulk water, phosphate vibrations in phospholipid and DNA model systems are sensitive probes for the hydration at biologically relevant interfacial sites (cf. Fig. 4.1). In those systems, 2D line shapes of phosphate vibrations are essentially inhomogeneously broadened and the frequency correlation functions decay significantly slower, which is illustrated in Fig. 4.12 [31, 34, 117, 118].

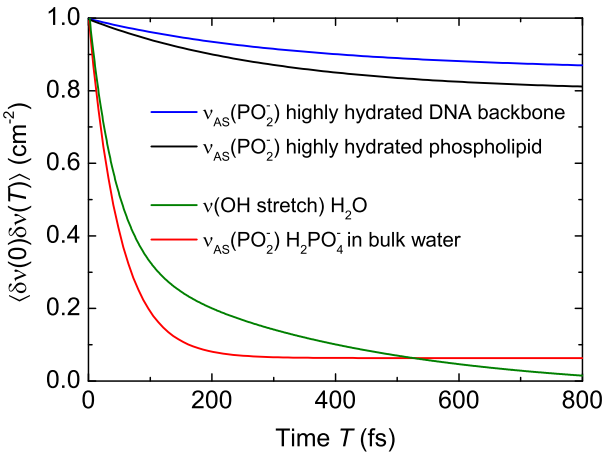

Figure 4.12: Correlation functions of frequency fluctuations $\langle \delta\nu(0)\delta\nu(T)\rangle$ for the stretching vibration of water and the asymmetric stretching vibrations of phosphates embedded in different environments. The highly fluctuating nature of bulk water causes the fast decay of the correlation functions for $\nu_{\mathrm{AS}}(PO_2^-)$ $H_2PO_4^-$ (taken from Fig. 4.11 panel (c)) and ν(OH stretch) H_2O (taken from ref. [140]). For DNA at a hydration level of 92 % and phospholipids arranged as reverse micelles with a hydration level of $w_0 = 16$, the correlation functions for $\nu_{\mathrm{AS}}(PO_2^-)$ decay significantly slower due to decelerated water fluctuations at the corresponding interface (taken from [34, 117, 118].)

Structural characteristics at the interface can have a strong impact on hydration and the dynamics of hydration shells. Water molecules at phospholipid-water interfaces are exposed to a strong Coulomb field caused by the head group dipole moment of typically 20 D (cf. Fig. 4.1) [31, 34, 141]. The particular orientation of the dipole arranges the water molecules around the phosphate head group up to distances of ≈ 6 Å or 3 solvation shells [142]. Consequently, the interfacial water molecules are oriented, immobilised, and intermolecular HB lifetimes extend up to > 10 ps [34,119]. Furthermore, the strong dipole moment of the head group and its spatial arrangement partially shields the bulk water with its full spectrum of fluctuations [34]. These factors lead to a relatively rigid water network around the phosphate groups in phospholipids with significantly inhibited fluctuating molecular motions. Thus, the corresponding correlation function for $\nu_{\mathrm{AS}}(\mathrm{PO}_2^-)$ (black line in Fig. 4.12) decays with an initial 300 fs time constant substantially slower than the correlation function for ν(OH stretch) of bulk water (green line in Fig. 4.12).

Comparable results have been reported for DNA-water interfaces [9, 40, 77, 91, 93, 113, 115, 119, 143]. Within those interfaces, it is the DNA backbone that contains the polar phosphate groups with distinct hydration shells (cf. Fig. 4.1). But not only phosphate groups serve as hydration sites, hydration also involves HBs to particular DNA sites or sugar rings [9, 117–119]. Spatial constraints constituted by the major and minor grooves and the presence of an oriented dipole moment due to counterions decelerate the water dynamics at the DNA-water interface, very similar to the phospholipid-water interface. Consequently, the corresponding correlation function for $\nu_{\mathrm{AS}}(\mathrm{PO}_2^-)$ of a phosphate group at the DNA-water interface (blue line in Fig. 4.12) decays with an initial 300 fs time constant likewise markedly slower than the correlation function for ν(OH stretch) of bulk water.

In strong contrast, the small $\mathrm{H_2PO_4^-}$ ions measured here are local probes for the fluctuation dynamics of bulk water. The dihydrogen phosphate ion is exposed to the unperturbed molecular motions of water and, thus, to the full extend of fluctuating electric fields. More pronounced fluctuation dynamics and larger fluctuation amplitudes compared to the discussed DNA and phospholipid systems are the consequence as is evident in the quick decay of the correlation function for $\nu_{\mathrm{AS}}(\mathrm{PO}_2^-)$, red line in Fig. 4.12 (cf. Figs. 4.11 and 4.1).

4.6 Conclusions and outlook

Phosphate vibrations of the molecule $H_2PO_4^-$ in a 1 M aqueous solution were investigated with femtosecond pump/probe and 2D-IR measurements in a self-designed free-standing liquid jet to evaluate their sensitivity for structural fluctuations of bulk water. Therefore, the symmetric and asymmetric stretching vibrations $\nu_S(PO_2^-)$ and $\nu_{AS}(PO_2^-)$, the symmetric and asymmetric bending vibrations δ_S(P-$(OH)_2$) and δ_{AS}(P-$(OH)_2$), as well as the asymmetric stretching vibration ν_{AS}(P-$(OH)_2$) were studied in a frequency range between 850 cm^{-1} and 1350 cm^{-1}. Due to the utilisation of the 10 µm thin liquid jet and the resulting absence of nonlinear signal contributions caused by a sample holder, the time resolution of the performed experiments could be increased. This allowed for the evaluation of 2D-IR spectra and pump/probe signals of $H_2PO_4^-$ for delay times between 0 fs and 100 fs.

Lifetimes of the excited vibrational states were determined to be 350 fs for $\nu_S(PO_2^-)$, 260 fs for $\nu_{AS}(PO_2^-)$, 290 fs for δ_S(P-$(OH)_2$) and δ_{AS}(P-$(OH)_2$), as well as 390 fs for ν_{AS}(P-$(OH)_2$). After a delay time of $\approx$ 1.5 ps, the pump/probe signals manifested distinct and persisting contributions from a hot ground state. Relaxation of excess energy into the water leads to a $\approx$ 1 K heat jump of the solution and, thus, to a desolvation of $H_2PO_4^-$ with an accompanied blueshift of $\nu_S(PO_2^-)$ and $\nu_{AS}(PO_2^-)$ and a redshift of ν_{AS}(P-$(OH)_2$). Signatures of a hot ground state are also evident in 2D-IR spectra for delay times $\geq$ 300 fs. A 2D-IR spectrum measured at a delay time of 5 ps, for which all excited vibrational states are decayed and a pure hot ground has developed, shows a larger sensitivity of $\nu_{AS}(PO_2^-)$ to changes in the surrounding HB network compared to $\nu_S(PO_2^-)$.
Broadband 2D-IR measurements on $\nu_S(PO_2^-)$ and $\nu_{AS}(PO_2^-)$ revealed predominant homogeneously broadened and static line shapes for both normal modes in a delay time window from 0 fs to 500 fs. Pronounced cross peaks were measured between $\nu_S(PO_2^-)$ and $\nu_{AS}(PO_2^-)$, $\nu_S(PO_2^-)$ and both δ(P-$(OH)_2$) bending modes, as well as between $\nu_{AS}(PO_2^-)$ and both δ(P-$(OH)_2$) bending modes, pointing to anharmonic couplings among the normal modes. Small diagonal anharmonicities for $\nu_S(PO_2^-)$ and $\nu_{AS}(PO_2^-)$ of $\approx$ 10 cm^{-1}, respectively, were observed.
An analysis of frequency fluctuations and correlation times on the basis of a biexponential Kubo function illustrated that frequency fluctuations on a 50 fs timescale determine the upright and, thus, homogeneous 2D line shapes of $\nu_S(PO_2^-)$ and $\nu_{AS}(PO_2^-)$. These 50 fs-fluctuations arise from ultrafast water librations. A small fluctuation component with an infinitely large correlation time represents persisting structural inhomogeneities within the phosphate-water system and, therewith, accounts for small inhomogeneities in the 2D line shapes measured. The fluctuation amplitudes for $\nu_{AS}(PO_2^-)$ are larger compared to those of $\nu_S(PO_2^-)$, which is in line with a higher sensitivity of $\nu_{AS}(PO_2^-)$ on structural modifications within the phosphate solvation shells.
Hybrid quantum-classical model calculations supported the experimental findings and yielded microscopic insights into the phosphate-water interactions. 12 water molecules have been found to form the first hydration shell of $H_2PO_4^-$ that are linked to the phosphate ion via $\approx$ 10 HBs which crucially determine the normal mode frequencies of the phosphate vibrations. These HBs exhibit lifetimes of $\approx$ 10 ps and, thus, outlive ultrafast 50 fs water librations. The water librations cause structural reorientations of water molecules in the first solvation shell and lead to normal mode frequency excursions on an according 50 fs timescale for $\nu_S(PO_2^-)$, $\nu_{AS}(PO_2^-)$ and both δ(P-$(OH)_2$) bending modes.

The investigations on $H_2PO_4^-$ dissolved in water successfully demonstrated that phosphate vibrations are not only sensitive probes for decelerated water fluctuations at interfacial sites but that they are especially suitable to map bulk water fluctuations. Even though $\nu_S(PO_2^-)$ and $\nu_{AS}(PO_2^-)$ exhibit small diagonal anharmonicities in the direct comparison with the OH-stretch vibration of water ($\approx 10\,cm^{-1}$ for $\nu_S(PO_2^-)$ and $\nu_{AS}(PO_2^-)$, $\approx 150\,cm^{-1}$ for OH-stretch H_2O), these phosphate vibrations map structural fluctuations of water on a 50 fs timescale, just as the OH-stretch vibration of water molecules. Thus, $H_2PO_4^-$ with its phosphate vibrations is a new reference system to study structural fluctuations in the vicinity of water. The performed measurements underline the suitability of phosphate vibrations to get a direct experimental access to the intrinsic structural dynamics of water not only at interfacial sites but especially in the bulk. This concept to use ions as local probes could also be applied on other molecular ions, such as e.g. SO_4^{2-} or NO_3^-.

Another system worth studying is ATP. Many aspects, such as its geometrical structure, chemical reactions that involve the phosphate groups, or thermodynamical aspects are well characterised [82, 83, 144–146]. But investigations on ultrafast vibrational energy relaxation or microscopic ATP-water interactions have not been performed so far [147–149]. In ATP, further complexity arises from the modified character of PO-vibrations that are delocalised over more than one phosphate group. Since water plays a crucial role in the dephosphorylation process, insights into the microscopic phosphate-water interactions on an ultrafast timescale might be beneficial for the understanding of metabolism in living cells and to go beyond thermodynamic considerations.

5 Ultrafast vibrational dynamics of BH_4^- ions in liquid and crystalline environments

5.1 $NaBH_4$ as a hydrogen and energy carrier

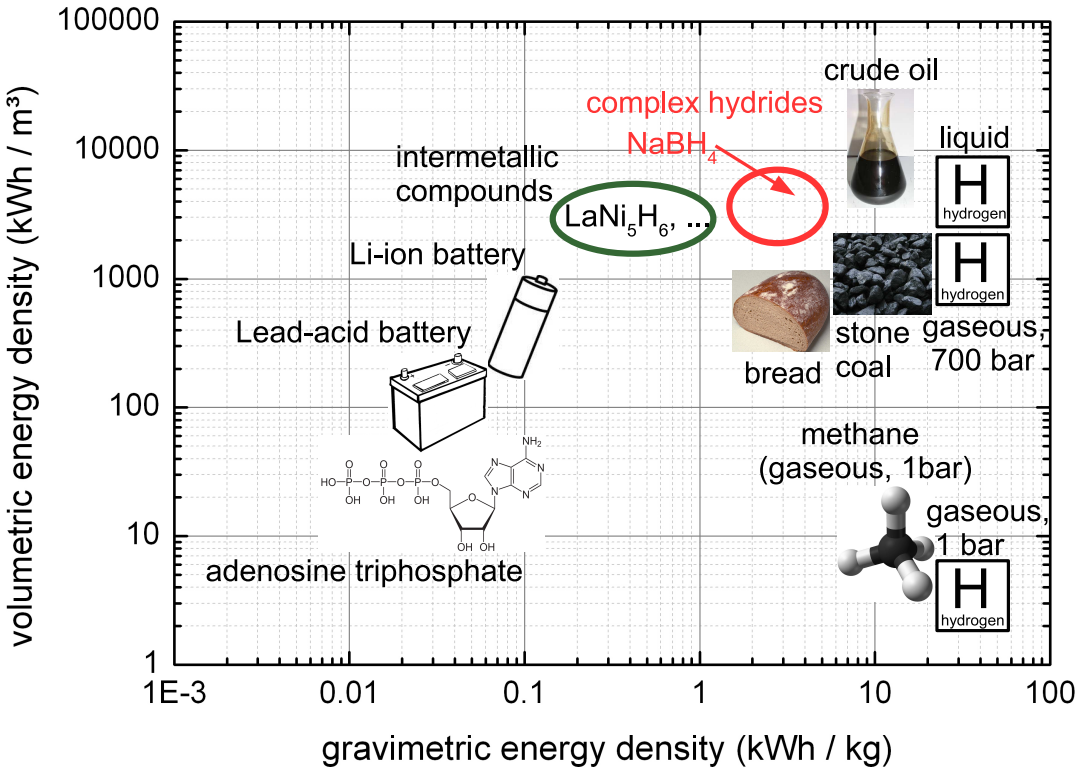

Figure 5.1: Double logarithmic illustration of the gravimetric and volumetric energy densities of several materials and compounds, according to Fig. 7 in [150]. The hydrogen carriers "intermetallic compounds" and "complex hydrides" are highlighted [151, 152]. Their denoted energy densities are based on the particular hydrogen content and the standard enthalpy of reaction during combustion [153].

Energy storage and the usability of energy carriers in mobile applications are two of the most prominent technological challenges of the early 21st century. Even though a plurality of modern and environmentally friendly drive concepts for vehicles are present nowadays, none of these concepts has established to initiate the period beyond petrol and combustion engines. This circumstance is caused by complex reasons, one of which is the operability of petrol. It is liquid at ambient conditions and exhibits a high gravimetric

energy density of 11.5 kWh/kg^{-1} and a high volumetric energy density of 8600 kWh/m^{-3} (cf. Fig. 5.1). These values are much larger than the energy densities of modern batteries, such as the Li-ion battery, or of hydrogen saturated intermetallic compounds, such as $LaNi_5H_6$. However, the direct comparison also reveals hydrogen to be the most suitable energy carrier with a gravimetric energy density of 33 kWh/kg^{-1} and a $CO_{1,2}$-free combustion; two major reasons to study the light-induced hydrogen generation, e.g. out of water [152, 154–161].
Its very low boiling temperature of 21 K necessitates compression to reach volumetric energy densities comparable to petrol at ambient conditions, which requires pressure vessels operating at very high pressures of a couple of hundred bar. Alternatively, liquid hydrogen offers an appropriate volumetric energy density, but presupposes the handling with extremely cold liquids.
An approach to overcome the engineering challenges is to use metal lattices with a high amount of absorbed hydrogen instead, called "intermetallic compounds" or "interstitial hydrides" [152, 162–164]. One of their major drawbacks is the high-mass metallic host lattice that strongly limits their gravimetric energy density. Very recently, a class of materials has come to the fore again, the so-called complex hydrides. These are saline materials in which the hydrogen is covalently bound to (low-mass) central atoms in complex anions, resulting in a much higher gravimetric energy density in comparison with intermetallic compounds as represented in Fig. 5.2 [152, 165]. Due to the covalently bonded hydrogen, the complex hydrides are also termed non-interstitial hydrides.

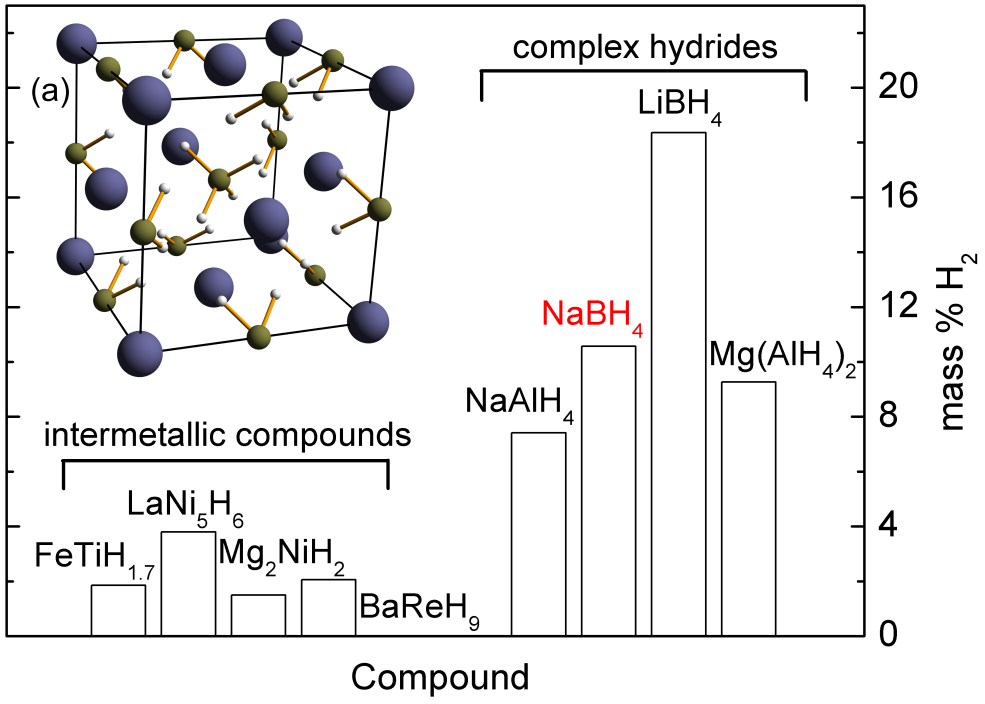

Figure 5.2: Comparative illustration of the hydrogen content of several intermetallic compounds (interstitial hydrides) and complex hydrides (non-interstitial hydrides) [152]. (a) Cubic unit cell of $NaBH_4$ ($Fm\bar{3}m$) with the lattice constant $a = 0.6151$ nm (under ambient conditions), blue: Na, green: B, white: H [166, 167]. Each unit cell contains four BH_4^- units. $NaBH_4$ exhibits a hydrogen mass density of $\rho_m = 113.1\,kg/m^3$ resulting in a relative hydrogen content of 10.57 wt% [165, 168].

Complex hydrides are, therefore, considered candidates for mobile hydrogen and energy carriers. In the 1940s and 1950s they have been investigated thoroughly to determine their phonon spectra and crystal structures. Further work deepened structural knowledge

and addressed the electronic band structure [169]. However, the focus of investigations has shifted significantly, because nowadays the dehydrogenation and hydrogenation are investigated intensively [164, 168]. These processes have limited reaction kinetics, the hydrogenation is very energy consuming and to some extent irreversible [165, 170]. In order to enhance the hydrogen uptake and release, the application of catalysts, such as titanium or zirconium, have been demonstrated to be beneficial [165].
The central unit in understanding hydrogen kinetics and dynamics is the BH_4^- tetrahedron. Its thermal decomposition in the gas phase proceeds in a simplified picture in two stages [164]: i) B-H bonds are elongated and weakened and ii) an energetically favorable intra-H$\cdots$H pairing occurs. While the former stage proceeds along the normal coordinates for B-H stretching, the latter one evolves along the H-B-H bending modes [164]. These stretching and bending modes have typical oscillation periods of 10 fs and decay on a ps-timescale. Thus, it is essential to study these modes on their intrinsic timescale to get an in-depth understanding of hydrogenation and dehydrogenation of complex hydrides.
Investigations of ultrafast dynamics of vibrational excitations in BH_4^- are very rare [44, 171]. However, they are not only relevant for hydrogen dynamics, but in particular also to allow for insights in energy dissipation mechanisms and fundamental couplings between vibrational modes, e.g. stretching and bending vibrations.
Relaxation pathways, 2D line shapes, and lifetimes of the stretching vibration ν_3 in $LiBH_4$, $LiBD_4$, and isotopically diluted derivatives have been studied recently [44]. The excited stretch vibrations exhibited a lifetime of 1.5 ps, independent on the isotopic constitution. Measured 2D line shapes were purely homogeneously broadened due to temperature induced fluctuations of the crystal lattice. Energy dissipation occurred from the stretching vibration over the bending vibration into a heat bath of low-frequency phonons. A 3 ps lifetime for the bending mode ν_4 was estimated without direct experimental evidence, whereas a 100 ps thermalisation time constant was explicitly derived.
Very recently, the vibrational dynamics of BH_4^- ions dissolved in water were addressed [171]. Special focus was put on so-called dihydrogen bonds between hydridic hydrogen of BH_4^- ions and protonic hydrogen of bulk, strongly alkaline water. HOD molecules were used as local probes for B-H–D-O dihydrogen bondings. It was found that the B-H stretching mode shows spectral diffusion kinetics that are identical to those of OD stretch of HOD in bulk water. A vibrational lifetime of 2.9 ps was measured for the BH_4^- stretching oscillator ν_3.
However, two critical aspects have not been analysed so far. These are i) the exact relaxation mechanism within the BH_4^- unit and ii) interactions among different BH_4^- tetrahedrons in the crystalline phase. Their high density in the crystal could cause a pronounced intermolecular coupling among them, that might, e.g. delocalise vibrational energy or cause coherent collective effects. $NaBH_4^-$ is a highly suitable candidate to study these phenomena because of three reasons. It is chemically more stable than, e.g. $NaAlH_4$ or $LiBH_4$, it is soluble in a couple of prevalent solvents, and it features a high density favouring interactions among BH_4^- tetrahedrons.

Within this chapter, an in-depth investigation of the vibrational dynamics in crystalline $NaBH_4$ is presented in combination with benchmark experiments on BH_4^- ions dissolved in a liquid solution. The results are embedded in an analysis of the vibrational structure of BH_4^-, theoretical modelling of the measured nonlinear responses performed by Michael Wörner, and temperature-difference measurements on crystalline $NaBH_4$. Chapter 5 refers to ref. [172], where the major experimental and theoretical results are published.

5.2 Vibrations of $NaBH_4$ and dissolved BH_4^- ions

Hydrogen in BH_4^- is covalently bound to boron in a tetrahedral geometry. In the highly symmetric (cubic) crystal $NaBH_4$ (space group $Fm\bar{3}m$ at T = 300 K), the ideal tetrahedral structure is preserved just as in the liquid phase [166, 167, 173, 174]. In a less symmetric crystal structure, such as $LiBH_4$ (space group $Pnma$ at T = 300 K), the tetrahedrons are distorted with consequences on the vibrational absorption spectrum [175–179]. In the ionic crystal $NaBH_4$, Na^+ cations surround the BH_4^- anions octahedrally. The hydrogen bondings of the BH_4^- tetrahedrons are aligned along the space diagonals of the unit cell, pointing to its corners (cf. Fig. 5.1). This geometry allows for two different BH_4^- orientations, each with 4 hydrogen bondings pointing to 4 different of the 8 corners of the unit cell, respectively [180]. Both orientations are equally occupied and the required energy for a reorientation amounts to 110 meV (925 cm^{-1}), which represents a source of structural fluctuations [181–183].

Vibrational modes in crystalline borohydrides connected to B-H oscillations are named internal phonon modes. These (high-frequency) internal phonon modes occur next to (low-frequency) external phonon modes that accompany relative interionic Na^+-BH_4^- displacements, such as optical and acoustic phonons [181, 184]. The excitation energies of the external phonon modes are in a range of couple of 100 cm^{-1} and were studied with e.g. inelastic neutron scattering, density functional theory, or inelastic scattering of synchroton radiation [169,184,185]. Fig. 5.3 shows the infrared absorption spectra of internal BH_4^- vibrations of BH_4^- embedded in $NaBH_4$ and dissolved in isopropylamine (ISPA).

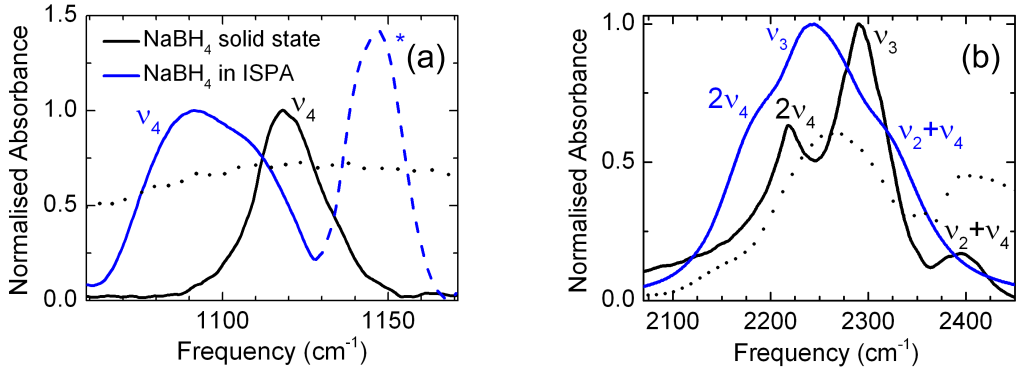

(c)	$\nu_4(BH_4^-)$	$\nu_3(BH_4^-)$	$\nu_2(BH_4^-)+\nu_4(BH_4^-)$
solid state	1120 cm^{-1}	2290 cm^{-1}	2400 cm^{-1}
in solution	1100 cm^{-1}	2245 cm^{-1}	2320 cm^{-1}

Figure 5.3: Normalised vibrational absorption spectra of crystalline $NaBH_4$ (black lines) and of a 0.8 M $NaBH_4$-ISPA solution (blue lines), covering the B-H vibrations. Panel (a) displays the spectral region around the B-H-bending mode ν_4 and (b) the spectral region around the B-H-stretching mode ν_3 with band assignments as reported by [66, 186–191]. The dotted lines are exemplary pump spectra. Solvent absorption is subtracted from the solution spectra (blue lines) whereas a solvent-related absorption band around 1145 cm^{-1} (*) remains. For ν_3 and ν_4, the molar absorption coefficients in ISPA amount to $\epsilon_{\nu 3} \approx 300\,M^{-1}cm^{-1}$ and $\epsilon_{\nu 4} \approx 100\,M^{-1}cm^{-1}$. (c) Graphical charts of the normal modes shown together with the corresponding experimental frequencies, green: boron, white: hydrogen [16].

BH_4^- tetrahedrons are isostructural to methane and exhibit 4 vibrational modes. They are denoted as $\nu_1 - \nu_4$ and are either Raman-active (ν_1, ν_2) or IR-active (ν_3, ν_4) [16]. The Raman-active modes are the symmetric stretching vibration ν_1 at $\approx 2340\,\mathrm{cm}^{-1}$ and the symmetric bending vibration ν_2 at $\approx 1280\,\mathrm{cm}^{-1}$, which is twofold degenerated [189, 190, 192]. Fig. 5.3 shows IR-absorption spectra of $NaBH_4$ (black lines) with its asymmetric BH_4^- stretching vibration ν_3 at $\approx 2290\,\mathrm{cm}^{-1}$ and its asymmetric bending vibration ν_4 at $\approx 1120\,\mathrm{cm}^{-1}$ [66, 186–188, 191, 193–195]. Both modes are threefold degenerated, respectively. A Fermi resonance between the ν_3 stretching vibration and the overtone of the ν_4 bending vibration causes the dipole forbidden $2\nu_4$ overtone, redshifted to ν_3, to be IR-active. A further Fermi resonance between the Raman-active bending vibration ν_2 and the IR-active bending vibration ν_4 enables the dipole forbidden combination mode $\nu_2 + \nu_4$ to be weakly IR-active, resulting in an absorption peak blueshifted to ν_3. This general vibrational structure describes the BH_4^- absorption in the solid state $NaBH_4$ and dissolved in ISPA (blue lines in Fig. 5.3). However, $\approx 2\,\%$ higher frequencies and 50 % smaller peak widths can be observed for the solid state due to the considerably different dielectric properties of the static crystal lattice of $NaBH_4$ compared to the liquid solvent ISPA. Furthermore, the solvent ISPA provides a vibrational manifold that enables coupling between BH_4^- vibrations and solvent modes [196–198].
The measured $NaBH_4$-ISPA solution featured a concentration of 0.8 M and ISPA is 12 molar, giving a ratio of 1/15. This causes $NaBH_4$ to dissolve into spatially separated Na^+ and BH_4^- ions in ISPA, underlined by the polarity of a single ISPA molecule of 1.3 D, and the static dielectric constant of the neat solvent of $\epsilon = 5$ [199, 200]. An infrared absorption spectrum similar to Fig. 5.3 has been found for lower concentrations, which supports the interpretation of a complete dissociation at 0.8 M.
Some ISPA solvent modes are in the range of the bending mode ν_4 that are not shown in Fig. 5.3 because the blue curve in panel (a) illustrates an absorption spectrum with subtracted solvent absorption. However, ISPA exhibits two absorption lines around the ν_4 absorption band, the CH_3 rock in-plane and in-phase vibration at $1133\,\mathrm{cm}^{-1}$, and the CH_3 rock in-plane and out-of-phase vibration at $1171\,\mathrm{cm}^{-1}$ [196, 197]. Both vibrations experience a slight variation in oscillator strength and spectral position due to the presence of Na^+ cations and BH_4^- anions, as well as the residual absorption lines of ISPA (not shown). Furthermore, an additional absorption band of ISPA occurs at $\approx 1145\,\mathrm{cm}^{-1}$ (dashed line) due to the presence of the ions. No solvent-related absorption is existing around the ν_3 mode. The influence of solvent absorption on the time-resolved pump/probe measurements is negligible and discussed separately in Sec. 5.3.1.

5.3 Vibrational lifetimes of BH_4^- vibrations in the solution

5.3.1 Lifetimes of BH_4^- vibrations

The vibrational lifetimes of $\nu_3(BH_4^-)$ and $\nu_4(BH_4^-)$ are investigated in one-colour and two-colour pump/probe experiments using pump pulses with centre frequencies at 2250 cm^{-1} and 1080 cm^{-1}, respectively (pulse spectra in Fig. 5.4 (a,g)). Transmission geometry is used and the thickness of the liquid sample embedded in a Harrick cell between two 1 mm thick BaF_2 windows amounts to either 25 µm (for measurements on ν_3) or 1 µm (for measurements on ν_4). Fig. 5.4 summarises pump/probe spectra and the time evolution at certain probe frequencies.

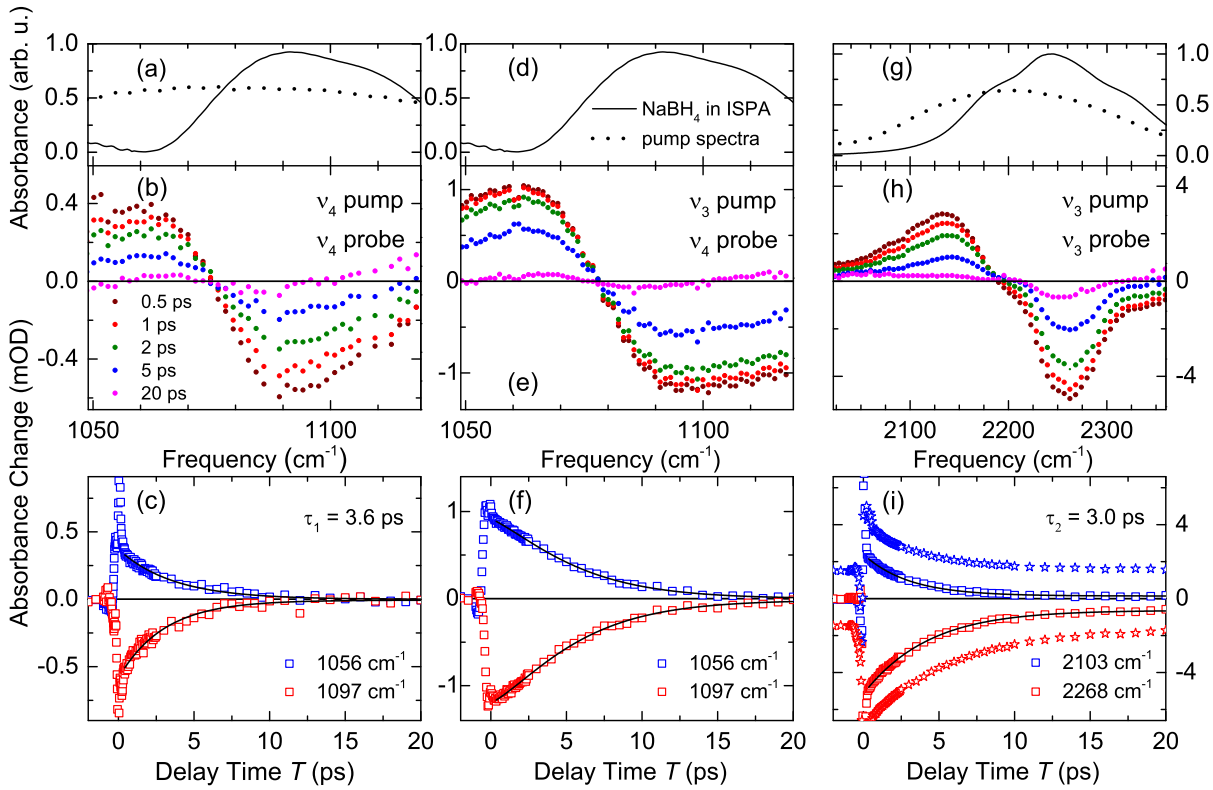

Figure 5.4: Nonlinear spectra and transients of pump/probe measurements on the asymmetric BH_4^- stretching and bending vibrations ν_3 and ν_4 of a 0.8 M $NaBH_4$-ISPA solution; $\Delta A = -\log(I/I_0)$. (a,d,g) Linear absorption and pump spectra. Left column: results for ν_4 pump/ν_4 probe, middle column: ν_3 pump/ν_4 probe, right column: ν_3 pump/ν_3 probe. Time-resolved spectra for delay times between 0.5 ps and 20 ps are shown in (b,e,h). Parallel linear polarisations for the pump and probe pulses are used. Transients at fixed probe frequencies are plotted with respect to the delay time T in (c,f,i). For $T \approx 0$ fs, nonresonant nonlinear effects such as pump/probe coupling overlie the measured responses of BH_4^-. The excited state decays of the BH_4^- vibrations ν_3 and ν_4 in (c) and (i) are numerically fitted to extract the time constants τ_1 (c) and τ_2 (i) (solid lines). Transients for $NaBH_4$ dissolved in DMSO (starlets in (i)) are shifted and rescaled to facilitate a direct comparison. Transients in (f) could be reproduced (solid lines) with eqns. (5.3) and (5.4). Measurements on ν_3 were performed under N_2 atmosphere. Pump pulse energy: $E_{pump} \approx 1.5\,\mu J \mathrel{\widehat{=}} 6 \cdot 10^{10}\,W/cm^{-2}$.

Fig. 5.4 shows nonlinear spectra in panels (b), (e), (h) and transients at fixed probe frequencies of the excited ν_3 and ν_4 oscillators in panels (c), (f), (i) for population times between 0.5 and 20 ps. Decreased absorptions in the range of the fundamental transitions are caused by bleaching of the respective v=0 ground state and stimulated emission result-

ing from the relaxation of excited states into their ground states, v=1→0 (cf. Fig. 2.6). Redshifted enhanced absorptions result from v=1→2 transitions of the excited ν_3 and ν_4 oscillators. Signal contributions around the delay time $T \approx 0\,\mathrm{fs}$ originate from pump probe coupling in the liquid sample, as well as in the utilised window materials, and for $T < 0$ from PFID (cf. Sec. 2.10). All oscillators show an immediate response after resonant excitation that decays within $\approx 20\,\mathrm{ps}$. However, the particular oscillators also exhibit clear differences in their relaxation kinetics.

Pumping and probing the ν_3 oscillator (right column in Fig. 5.4) reveals a strong bleaching signal centred at $2262\,\mathrm{cm}^{-1}$ and some minor bleaching contributions beyond $2325\,\mathrm{cm}^{-1}$, due to the excited Fermi resonance enhanced combination tone $\nu_2 + \nu_4$ (cf. Fig. 5.3). The redshifted excited state absorption peaks around $2130\,\mathrm{cm}^{-1}$ with an underlying anharmonicity of $\approx 20\,\mathrm{cm}^{-1}$ [44]. It decays monoexponentially with a time constant of 3.0 ps, as shown in panel (i). The bleaching at $2268\,\mathrm{cm}^{-1}$ exhibits a 4.5 ps decay which is followed by a significantly slower decay on a $> 100\,\mathrm{ps}$ timescale. The vibrational relaxation leads to dissipation of excess energy into the solvent that is, accordingly, heated by about $1 - 2\,\mathrm{K}$ [198]. An anharmonic coupling of BH_4^- modes to thermally populated modes of the solvents vibrational manifold leads to the residual bleaching signal around the fundamental transition beyond 20 ps. Since all BH_4^- modes are relaxed to their ground states after 20 ps, these persisting absorption changes are attributed to a hot ground state. Reference measurements on $NaBH_4$-ISPA solutions with lower BH_4^- concentrations revealed a reduced or suppressed residual bleaching while the kinetics were unaltered (not shown).

In two-colour pump/probe experiments (ν_3 pump/ν_4 probe), the ν_3 stretching oscillator is excited and the response on the ν_4 bending oscillator is probed. As is evident in the nonlinear signals given in the middle column of Fig. 5.4, an immediate response occurs on the ν_4 oscillator, providing evidence for a coupling between ν_3 and ν_4. The transients measured within the bleaching at $1097\,\mathrm{cm}^{-1}$ and within the excited state absorption at $1056\,\mathrm{cm}^{-1}$ (panel (f)) exhibit complex nonexponential decay kinetics.

The nonlinear response of the ν_4 oscillator in a ν_4 pump/ν_4 probe experiment is given in the left column of Fig. 5.4. Now, the transient measured within the excited state absorption at $1056\,\mathrm{cm}^{-1}$ (c) decays monoexponentially with a time constant of 3.6 ps. The bleaching at $1097\,\mathrm{cm}^{-1}$ decays with a similar time constant. From ν_4, the vibrational excess energy dissipates into the vibrational manifold of the solvent with a hot ground state less pronounced compared to ν_3.

Two further aspects should be commented on here. The significantly higher signal amplitudes on the ν_4 oscillator in (e,f) compared to (b,c) are caused by two factors. One of them is the higher pump pulse energy of 2 µJ at $2250\,\mathrm{cm}^{-1}$ compared to 1 µJ at $1080\,\mathrm{cm}^{-1}$. The other factor is the much higher dipole moment of ν_3 compared to ν_4 (≈ 15 times larger). This also causes the more pronounced hot ground state measured after ν_3 excitation compared to the hot ground state measured after ν_4 excitation. Furthermore, the nonlinear response around $1120\,\mathrm{cm}^{-1}$ contains minor positive signal contributions due to excited state absorption of the excited solvent absorption band at $1145\,\mathrm{cm}^{-1}$, whereas the excited state absorption of ν_4 below $1070\,\mathrm{cm}^{-1}$ is unaffected.

In a set of reference measurements with BH_4^- ions dissolved in dimethyl sulfoxide (DMSO) at a similar concentration of 0.8 M, solvent related effects on the linear absorption and relaxation dynamics are investigated. BH_4^- exhibits a similar absorption structure around the ν_3 transition in DMSO, but the absorption bands are $\approx 30\,\%$ narrower and $\approx 30\,\mathrm{cm}^{-1}$ redshifted compared to ISPA, just as the excited state and bleaching signals in a ν_3 pump/ν_3 probe experiment. Corresponding transients measured in the bleaching region around the fundamental ν_3 transition and in the range of the excited state absorption,

shown in (i) (starlets), reveal a similar time evolution as for BH_4^- in ISPA. The excited state absorption decays with $\tau_{\mathrm{DMSO}} = 3.4\,\mathrm{ps}$ (at $2082\,\mathrm{cm}^{-1}$) and the bleach signal with a time constant of 5.0 ps (at $2223\,\mathrm{cm}^{-1}$). The very similar ESA decays in ISPA of $\tau_{\mathrm{ISPA}} = 3.0\,\mathrm{ps}$ and DMSO of $\tau_{\mathrm{DMSO}} = 3.4\,\mathrm{ps}$, in combination with the decay measured in water of $\tau_{\mathrm{water}} = 2.9\,\mathrm{ps}$ by C. H. Giammanco et al., suggest that the solvent affects the relaxation kinetics of the stretching oscillator only minorly [171]. Another reference measurement with $LiBH_4$ dissolved in DMSO revealed a ν_3 v=1 lifetime of 3.5 ps and a bleaching decay of 5.5 ps, results very similar to those of $NaBH_4$ dissolved in DMSO. Consequently, also the cations in the solution influence the vibrational relaxation behaviour of the BH_4^- anions only minorly.

5.3.2 Relaxation scheme

The measured vibrational lifetimes of ν_3 and ν_4 from the one-colour and two-colour pump/probe experiments can be used to develop a relaxation scheme. This relaxation scheme contains both oscillators that are coupled via a Fermi resonance to enable population transfer. Coupling between BH_4^- ions is not considered, which can be justified by the following estimate. Resonant energy transfer among vibrationally excited and unexcited BH_4^- ions can be described by the non-radiative Förster transfer [201]. It is based on dipole-dipole coupling and is very sensitive to the separation distances of the involved excited molecules (donors) and the involved unexcited molecules (acceptors), between which energy transfer takes place. At a certain distance, the so-called Förster radius $r_{\mathrm{Förster}}$, the rate of resonant energy transfer is equal to the rate of fluorescence [202]. The Förster radius is correlated with a transfer time $t_{\mathrm{Förster}}$ for the resonant energy transfer. It scales with $t_{\mathrm{Förster}} \propto r_{\mathrm{Förster}}^6$, underlining the strong dependence on the separation distance between donor and acceptor. Following the definitions by [116, 202], the Förster radius for BH_4^- ions in ISPA amounts to 3.7 Å. Under consideration of the mean separation distance between two BH_4^- ions in the solution of 14 Å (at a concentration of 0.8 M), the energy transfer time accounts for about 15 ns. This long timescale implies that the process of Förster resonant energy transfer and, thus, coupling between BH_4^- molecules in the solution can be excluded as a process during the vibrational energy relaxation.

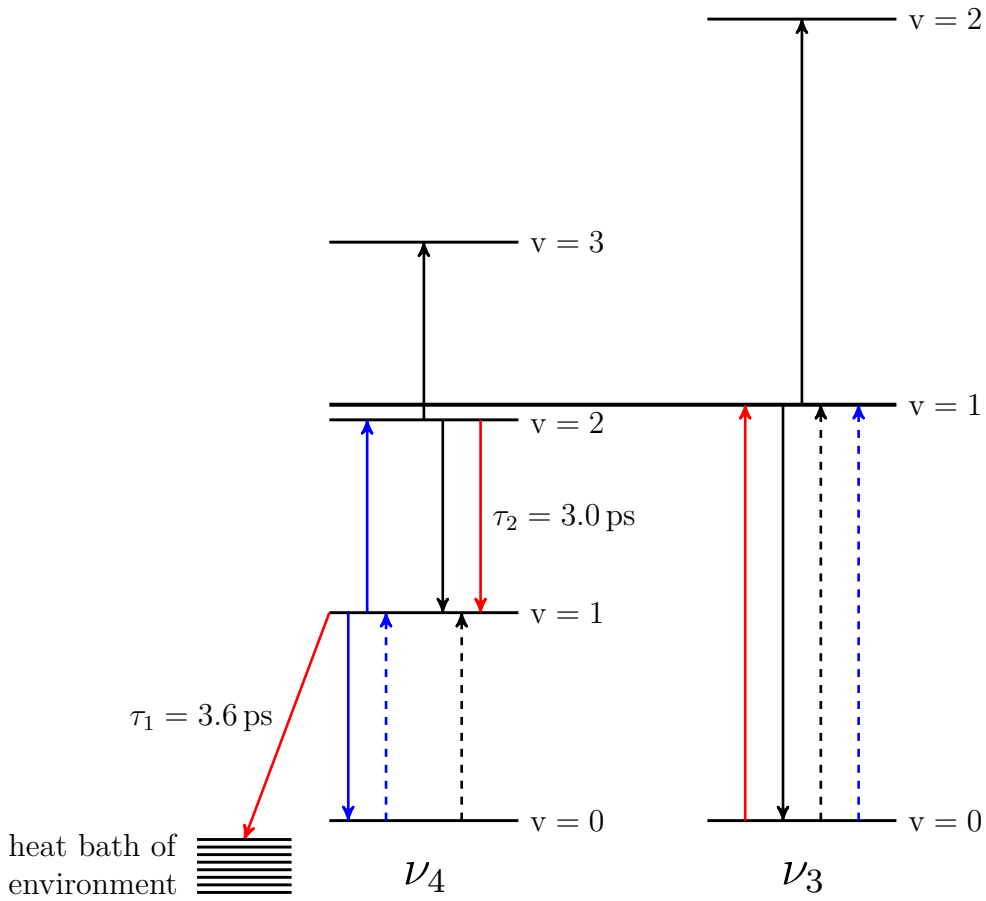

Figure 5.5: Energy level diagram and relaxation scheme for internal BH_4^- modes of $NaBH_4$ dissolved in ISPA. Excitation of ν_3(v = 1) leads to a population of ν_4(v = 2) due to the Fermi resonance coupling (upward red arrow). Vibrational energy relaxation evolves from ν_4(v = 2) via ν_4(v = 1) into the vibrational manifold of the liquid solvent with time constants of 3.0 ps and 3.6 ps, respectively (downward red arrows). The upward black arrows show excited state absorption from ν_3(v = 1 → 2) and ν_4(v = 2 → 3). Bleaching of the ground states ν_4(v = 0) and ν_3(v = 0) is given by the upward black dashed arrows. The upward blue dashed arrows show bleaching of the ground states ν_4(v = 0) and ν_3(v = 0) after population of ν_4(v = 1). Excited state absorption from ν_4(v = 1 → 2) is illustrated with an upward blue arrow. The downward blue arrow shows stimulated emission on ν_4(v = 1 → 0) after population of ν_4(v = 1). Finally, stimulated emission on ν_3(v = 1 → 0) and ν_4(v = 2 → 1) is represented by the downward black arrows.

The relaxation scheme in Fig. 5.5 involves the states v=0,1,2 of ν_3 and v=0,1,2,3 of ν_4. The Fermi resonance occurs between ν_3(v=1) and ν_4(v=2), illustrated as the thick black line. An energy relaxation pathway from the high frequency stretching oscillator via the low frequency bending oscillator into the heat bath of the environment (that corresponds to the vibrational manifold of ISPA) is depicted with red arrows. Pumping ν_3 leads to a population of its v=1 state and, due to the Fermi resonance coupling, to a population of ν_4 in its v=2 state. The dynamics of this population transfer are considered to evolve instantaneously here, a detailed discussion is given in Sec. 5.5.1 (Fig. 5.9). Once the coupled state is excited, it decays with the time constant $\tau_2 = 3.0\,\mathrm{ps}$ into the v=1 state of ν_4 that is, accordingly, populated. Final energy dissipation into the heat bath occurs with a time constant of $\tau_1 = 3.6\,\mathrm{ps}$. Here, the v=1 state of ν_4 is depopulated and the ground state v=0 of populated (cf. left column Fig. 5.4).
Population of excited states and relaxation are connected with several signal contributions that lead to the nonlinear responses illustrated in Fig. 5.4. The main contributions are shown as arrows in the relaxation scheme of Fig. 5.5. Upright black and blue arrows show

contributions due to excited state absorption, e.g. $\nu_3(\mathrm{v} = 1 \rightarrow 2)$. Downward black and blue arrows stand for stimulated emission, e.g. $\nu_4(\mathrm{v} = 1 \rightarrow 0)$. Dashed upright arrows in black or blue depict bleaching contributions, e.g. $\nu_3(\mathrm{v} = 0 \rightarrow 1)$. The colour of the arrows indicate the kind of excitation, black corresponds to an excitation of ν_3 and blue to an excitation of ν_4. In this manner, the relaxation scheme clearly shows that an excitation of ν_3 induces a response on ν_4 and vice versa. A mathematical description for the time dependent populations of the involved states needs to include all discussed transitions and is given in the following. Special emphasis is put on the v=1 state of ν_4, that can be populated from v=2 and relaxes into v=0, which can lead to the complex nonexponential behaviour measured in Fig. 5.4 (f).
The redshifted enhanced absorption $\Delta\mathrm{A}^{\nu4}_{\mathrm{enh}}(t)$ and the reduced absorption $\Delta\mathrm{A}^{\nu4}_{\mathrm{red}}(t)$ on the fundamental transition of ν_4 are composed of the following contributions [172]:

$$\Delta\mathrm{A}^{\nu4}_{\mathrm{enh}}(t) = + \sigma^{\nu4}_{23} n^{\nu4}_{\mathrm{v}=2}(t) + \sigma^{\nu4}_{12} n^{\nu4}_{\mathrm{v}=1}(t) \tag{5.1}$$

$$\Delta\mathrm{A}^{\nu4}_{\mathrm{red}}(t) = - \sigma^{\nu4}_{12} n^{\nu4}_{\mathrm{v}=2}(t) - \sigma^{\nu4}_{01} n^{\nu4}_{\mathrm{v}=1}(t) - \sigma^{\nu4}_{01} \left(n^{\nu4}_{\mathrm{v}=1}(t) + n^{\nu4}_{\mathrm{v}=2}(t) \right). \tag{5.2}$$

This elementary description contains the populations $n^{\nu4}_{\mathrm{v}=0,1,2}$ of the individual states with $n^{\nu4}_{\mathrm{v}=0} + n^{\nu4}_{\mathrm{v}=1} + n^{\nu4}_{\mathrm{v}=2} = 1$ and the cross sections $\sigma^{\nu4}_{ij}$ for the transitions from state i to j. The enhanced absorption consists of two components, a positive component on the v=2→3 transition, as long as v=2 is populated, and a further positive component on the v=1→ 2 transition, as long as v=1 is populated. While the time dependence of $n^{\nu4}_{\mathrm{v}=2}(t)$ is characterised by the lifetime of the coupled state between ν_3 and ν_4 ($\tau_2 = 3.0\,\mathrm{ps}$), $n^{\nu4}_{\mathrm{v}=1}(t)$ depends on both, τ_1 and τ_2. Once the excited states are populated, stimulated emission on the v=2→ 1 and v=1→ 0 transitions leads to a reduced absorption, described by the two left terms in eqn. (5.2). Further contributions are caused by a bleaching on the v=0→ 1 transition as long as excited states are populated. All components of $\Delta\mathrm{A}^{\nu4}_{\mathrm{red}}(t)$ have a negative sign.
The expressions (5.1) and (5.2) can be simplified with the help of harmonically approximated absorption cross sections $\sigma_{01} = \sigma_{12}/2 = \sigma_{23}/3$. Inserting those, eqns. (5.1), (5.2) simplify to

$$\Delta\mathrm{A}^{\nu4}_{\mathrm{enh}}(t) = +3\sigma^{\nu4}_{01} \cdot (n^{\nu4}_{\mathrm{v}=2}(t) + 2/3 \cdot n^{\nu4}_{\mathrm{v}=1}(t)) \tag{5.3}$$

$$\Delta\mathrm{A}^{\nu4}_{\mathrm{red}}(t) = -3\sigma^{\nu4}_{01} \cdot (n^{\nu4}_{\mathrm{v}=2}(t) + 2/3 \cdot n^{\nu4}_{\mathrm{v}=1}(t)). \tag{5.4}$$

Considering these relative amplitudes of the different contributions, the population dynamics of the excited states can be formulated. It is particularly simple for $n^{\nu4}_{\mathrm{v}=2}(t)$, since this state decays monoexponentially with $\tau_2 = 3.0\,\mathrm{ps}$, as demonstrated in the experiments on ν_3 (cf. Fig. 5.4 right column). $n^{\nu4}_{\mathrm{v}=1}(t)$ decays with $\tau_1 = 3.6\,\mathrm{ps}$, but can be repopulated from $n^{\nu4}_{\mathrm{v}=2}(t)$. So the differential equations for $n^{\nu4}_{\mathrm{v}=1}(t)$ and $n^{\nu4}_{\mathrm{v}=2}(t)$ can be formulated in a rate-equation system with the two experimentally gained time constants τ_1 and τ_2

$$\dot{n}^{\nu4}_{\mathrm{v}=2}(t) = -n^{\nu4}_{\mathrm{v}=2}(t)/\tau_2 \tag{5.5}$$

$$\dot{n}^{\nu4}_{\mathrm{v}=1}(t) = +n^{\nu4}_{\mathrm{v}=2}(t)/\tau_2 - n^{\nu4}_{\mathrm{v}=1}(t)/\tau_1. \tag{5.6}$$

While the population of $\nu_4(\mathrm{v}=2)$ can only be reduced, $\nu_4(\mathrm{v}=1)$ can be populated and depopulated, indicated by the different signs in eqn. (5.6). With the initial conditions of $n^{\nu 4}_{\mathrm{v}=2}(0) = n$ and $n^{\nu 4}_{\mathrm{v}=1}(0) = 0$, the eqns. (5.5), (5.6) can be formulated as

$$n^{\nu 4}_{\mathrm{v}=2}(t) = n e^{-t/\tau_2} \tag{5.7}$$

$$n^{\nu 4}_{\mathrm{v}=1}(t) = n \frac{\tau_1}{\tau_2 - \tau_1} \left(e^{-t/\tau_2} - e^{-t/\tau_1} \right). \tag{5.8}$$

Now, eqns. (5.7) and (5.8) can be inserted into eqns. (5.3) and (5.4) to simulate the dynamics of the excited state and reduced absorption of ν_4 measured in the experiments. As is evident by the numerical fits in Fig. 5.4 (f), the measured population dynamics of ν_4 after excitation of ν_3 are reproduced very well in this model. A simple monoexponential decay is sufficient to describe the time dependence of the enhanced absorption and bleaching of ν_4 after excitation into its first excitation state v=1, illustrated with the numerical fits in (c). While the excited state absorption of ν_3 also follows a monoexponential decay after excitation in its v=1 state, the reduced absorption exhibits contributions of persisting bleaching signals due to a population transfer from $\nu_3(\mathrm{v}=1)$ to $\nu_4(\mathrm{v}=1)$, extending the decay to a time constant of 5 ps (i). Eqns. (5.9) and (5.10) describe this process

$$\Delta \mathrm{A}^{\nu 3}_{\mathrm{enh}}(t) = + \sigma^{\nu 3}_{12} n^{\nu 3}_{\mathrm{v}=1}(t) \tag{5.9}$$

$$\Delta \mathrm{A}^{\nu 3}_{\mathrm{red}}(t) = - \sigma^{\nu 3}_{01} n^{\nu 3}_{\mathrm{v}=1}(t) - \sigma^{\nu 3}_{01} \left(n^{\nu 3}_{\mathrm{v}=1}(t) + n^{\nu 4}_{\mathrm{v}=1}(t) \right). \tag{5.10}$$

So a stepwise relaxation model describes the internal redistribution of vibrational excess energy within the BH_4^- ion from high-frequency to low-frequency modes, supported by a Fermi resonance. A very similar behaviour is documented for vibrational energy relaxation in e.g. H_2O and $H_2PO_4^-$ [121, 127, 138].

An aspect not considered so far are reorientational dynamics. Rotational motions of vibrationally excited molecules can cause modified relaxation dynamics in pump/probe experiments [31]. For a molecule such as BH_4^-, symmetry causes the influence of reorientational dynamics on the measured relaxation dynamics to be negligible. The symmetry of the BH_4^- molecule is represented in the point group T_d [185]. Correspondingly, T_2 is an irreducible representation for the triply degenerated infrared active stretching vibrations along the coordination axis x, y, z and T_1 an irreducible representation for the triply degenerated infrared active bending vibrations [16]. Consequently, a stochastic distribution of transition dipole orientations is excited by a linearly polarised pump pulse. The subsequently interacting probe pulse also experiences stochastically distributed orientations of transition dipoles and, thus, is only sensitive on pure relaxation dynamics. However, C. H. Giammanco et al. measured a small anisotropy decay for BH_4^- ions in water mediated by dihydrogen bonds with a time constant of 200 fs [171]. They argue that ultrafast structural fluctuations of the surrounding water slightly reorient the transition dipoles, which contributes to an anisotropy decay. Structural fluctuations of DMSO compared to water are much less pronounced and occur on slower timescales so that this mechanism cannot be applied for BH_4^- dissolved in DMSO and the oriented transition dipoles remain stochastically distributed [203].

5.4 Vibrational dynamics of $NaBH_4$ in the crystalline phase

5.4.1 IR-induced vibrational dynamics

So far, the experiments on the solutions revealed the vibrational relaxation dynamics of "isolated" or uncoupled BH_4^- molecules. This situation changes drastically in the $NaBH_4$ crystal that exhibits a densely packed arrangement of BH_4^- ions. One BH_4^- ion has 12 oriented nearest neighbours at a distance of 4.35 Å in the crystal lattice which, according to Sec. 5.3.2 and [116,202], in principle allows for a resonant Förster energy transfer within a transfer time of picoseconds, in strong contrast to a ≈ 15 ns transfer time in the solution caused by the large mean separation distance of ≈ 14 Å. The following section presents detailed results on the vibrational dynamics of BH_4^- ions in the densely packed crystalline phase and clarifies couplings among them. As for BH_4^- ions in the liquid solution, one- and two-colour pump/probe experiments are performed on the ν_3 oscillator, as well as one-colour experiments on the ν_4 oscillator.

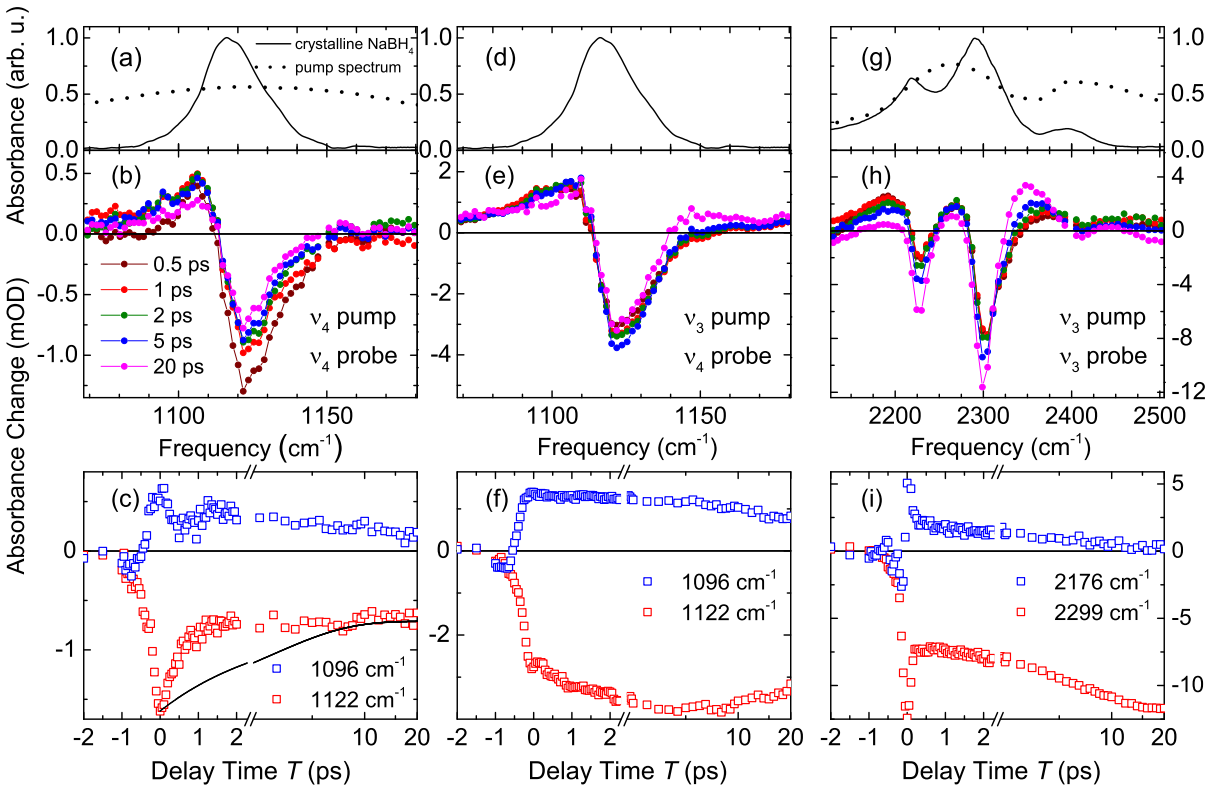

Figure 5.6: Nonlinear spectra and transients of pump/probe measurements on the asymmetric BH_4^- stretching and bending vibrations ν_3 and ν_4 of crystalline $NaBH_4$; $\Delta A = -\log(I/I_0)$. (a,d,g) Linear absorption and partial pump spectra. Left column: results for ν_4 pump/ν_4 probe, middle column: ν_3 pump/ν_4 probe, right column: ν_3 pump/ν_3 probe. Time-resolved spectra between 0.5 ps and 20 ps are given in (b,e,h). Parallel linear polarisations for the pump and probe pulses are used. Transients at fixed probe frequencies are plotted with respect to the delay time T in (c,f,i). For $T \approx 0$ fs, nonresonant nonlinear effects such as pump/probe coupling overlie the measured responses of $NaBH_4^-$ and contributions from collective radiative damping are evident. Solid line in (c): normalised transient taken from Fig. 5.4 panel (c) for a direct comparison of the initial decay. Pump pulse energy: $E_{pump} \approx 1.5\,\mu J \mathrel{\widehat{=}} 6 \cdot 10^{10}\,W/cm^{-2}$.

Fig. 5.6 shows nonlinear spectra in panels (b), (e), (h) and transients at fixed probe frequencies of the excited ν_3 and ν_4 oscillators in panels (c), (f), (i) for delay times between 0.5 and 20 ps. Their respective linear absorption spectra are given in panels (a), (d), (g)

in combination with the spectra of pump pulses centred around 2280 cm^{-1} and 1120 cm^{-1}. The pump/probe spectra of crystalline $NaBH_4$ exhibit similarities and strong differences to the results on BH_4^- in the liquid phase (cf. Fig. 5.4). Similarities can be found in the general shape of the nonlinear spectra for small delay times < 2 ps. Bleaching signals at the fundamental transitions (at 2300 cm^{-1} and 1122 cm^{-1}) and the $2\nu_4$, $\nu_2 + \nu_4$ bands (at 2225 cm^{-1} and 2400 cm^{-1}) are present as well as redshifted enhanced absorption bands. All nonlinear spectra in panels (b), (e), (h) exhibit pronounced persisting signals up to 20 ps, in strong contrast to the liquid phase. Due to the higher density of BH_4^- ions, the signal amplitudes are larger in the $NaBH_4$ crystal. Around the transition frequencies of ν_3 and $2\nu_4$, bleaching signals are measured with $\approx$ 10 mOD and $\approx$ 6 mOD amplitude, respectively, whereas the bleaching around the transition frequency of the $\nu_2 + \nu_4$ Fermi resonance is least pronounced with an amplitude of $<$ 1 mOD. The nonlinear spectra around the ν_4 oscillator exhibit bleaching signals at the fundamental transition frequency and redshifted enhanced absorption, both contributions are with amplitudes of $\approx$ 4 mOD and $\approx$ 2 mOD, respectively, 4 times larger in the ν_3 pump/ν_4 probe experiment, compared to the one-colour experiment on ν_4.

The corresponding transients show complex nonexponential behaviours. A resonant excitation of the ν_3 oscillator (right column Fig. 5.6) leads to a growing bleaching signal at 2299 cm^{-1}, whereas the excited state absorption decays monotonously. An immediate response occurs on the ν_4 oscillator after excitation of ν_3, just as in the liquid phase (middle column). After a quick initial increase, an almost constant signal amplitude of the bleaching and the excited state absorption describes the evolution of the transients within 20 ps, shown in (f).

Transients measured on the ν_4 oscillator show significantly different characteristics after its resonant excitation (left column). A quick partial decay with a time constant of $\approx$ 500 fs characterises the evolution within the first 2 ps of the transients in (c) after an initial rise, followed by a constant bleaching at 1122 cm^{-1} and a slightly decreasing amplitude at 1096 cm^{-1}. The quick partial decay is a feature not present in the liquid phase, as demonstrated by the black curve in (c), and is a fingerprint to a coupling, namely radiative coupling and damping, among the BH_4^- ions (cf. Sec. 2.2.2).

Collective radiative coupling and damping can occur in the dense $NaBH_4$ crystal, because i) the vibrational absorption coefficients are with values of $\alpha_{\nu 3} \approx 18\,000\ cm^{-1}$ and $\alpha_{\nu 4} \approx 7000\ cm^{-1}$ much higher than in the solution and, ii) the sample thickness L is with $L \approx 1$ µm small compared to the excitation wavelengths of 4.5 µm for ν_3 and 9 µm for ν_4. Thus, $L \ll \lambda$ is fulfilled as well as $\alpha L \geq 1$ which represent the conditions for radiative coupling and damping to occur. A superradiant damping time of $\approx$ 500 fs is expected for ν_4 under utilisation of the Friedberg-Hartmann relation (cf. eqn. (2.10), Sec. 2.2.2) which agrees very well with the measured 500 fs partial decay. This timescale is in the same range of the pure dephasing time of ν_4 of about 400 fs, given by its spectral width of 25 cm^{-1}. Performing the same estimation for the stretching oscillator ν_3, one expects a superradiant damping time on a sub-100 fs timescale; a value that is beyond the time resolution of the experiments.

The strong signals at delay times beyond 20 ps point to a redistribution of excess energy and heating of the crystal and, thus, to the formation of a hot ground state. Due to the high density of BH_4^- tetrahedrons in crystalline $NaBH_4$, the absorbed energy per unit volume is much higher than in the solution. According to the parameters of the IR-pump/IR-probe experiments, around 30 $pJ/µm^3$ are absorbed in the $NaBH_4$ crystal, in contrast to $\approx 1\ pJ/µm^3$ in the solution which corresponds to an amount of $\approx 60 \cdot 10^7/µm^3$, and $\approx 2 \cdot 10^7/µm^3$ vibrationally excited BH_4^- oscillators, respectively.

In principle, the vibrational relaxation pathway for BH_4^- discussed for the liquid phase is also appropriate within the crystalline environment. But the high packing density and a coupling between internal BH_4^- modes and strongly anharmonic external phonon modes enable the formation of a pronounced hot ground state that leads to spectral shifts and reshapings of the internal modes ν_3 and ν_4 in their v=0 states [44, 169, 175, 204]. Thus, the measured hot ground state is much more distinct in the $NaBH_4$ crystal. In contrast, the vibrational modes of BH_4^- dissolved in ISPA couple anharmonically to the vibrational manifold of the heated solvent to form a significantly weaker hot ground state.
Consequently, vibrational energy relaxation in combination with interactions among BH_4^- ions and the formation of a hot ground state within the crystal cause the dynamical kinetic differences measured in the crystalline compared to the liquid phase.
To get more insights into the vibrational behaviour of the BH_4^- ions in the crystalline phase, a couple of subsequent measurements have been performed, including UV-pump/IR-probe experiments and temperature difference measurements that are discussed in the following. In Sec. 6.5.1, theoretical model calculations are performed to get in-depth insights into collective radiative coupling and damping, as well as energy relaxation and dissipation.

5.4.2 UV-induced vibrational dynamics

The nonlinear response of the normal modes ν_4 and ν_3 and their Fermi resonances $2\nu_4$ and $\nu_2 + \nu_4$ are measured under UV irradiation in a setup comparable to the one introduced in Fig. 3.4. So far, only theoretical calculations exist that describe the bandstructure of $NaBH_4$. G. Lee et al. reported a bandgap of 6 eV for $NaBH_4$ which is in the same range as the results calculated for e.g. NaH or $NaAlH_4$ [169, 205–208]. Correspondingly, the excitation wavelength has been chosen to be 266 nm (4.66 eV), so that $NaBH_4$ can be excited above its bandgap in a two-photon absorption process. To reduce signal contributions from the sample holder windows, 100 µm thin LiF windows were used. The results of the UV-pump/IR-probe experiments on the BH_4^- stretching and bending vibrations are summarised in Fig. 5.7.

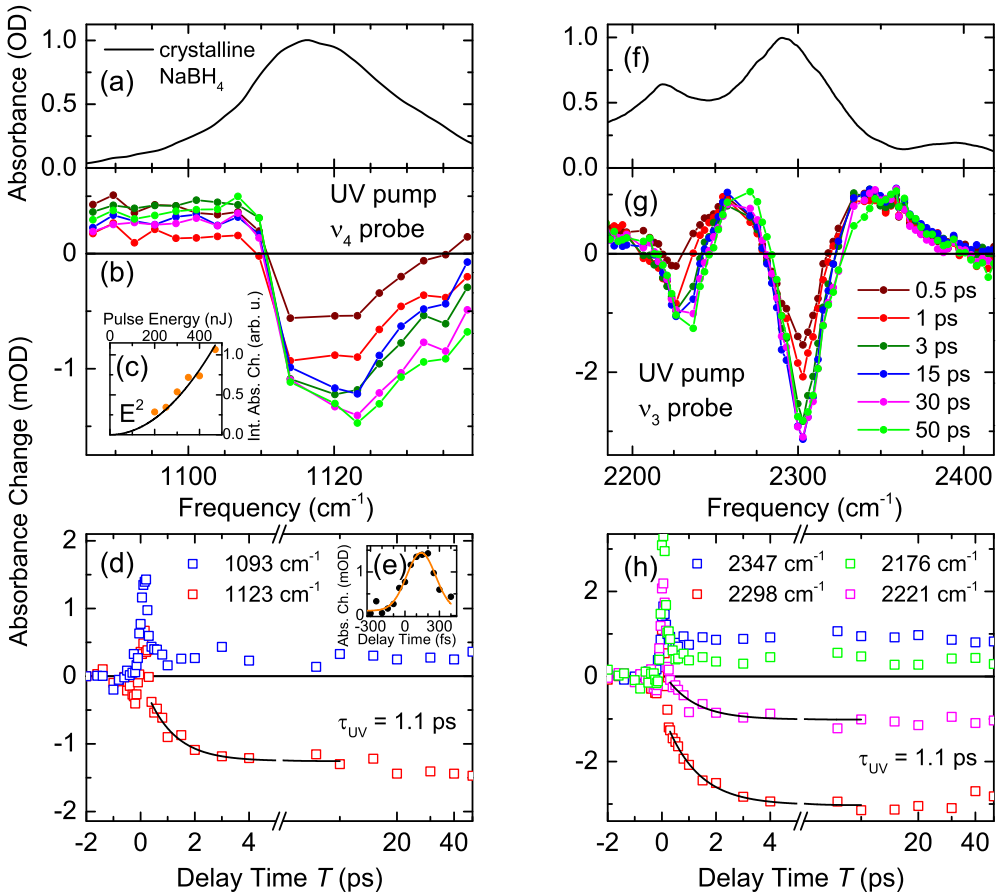

Figure 5.7: Nonlinear spectra and transients of pump/probe measurements on the asymmetric BH_4^- stretching and bending vibrations ν_3 and ν_4 of crystalline $NaBH_4$ with UV excitation (266 nm); $\Delta A = -\log(I/I_0)$. (a,f) Linear absorption spectra. Time-resolved spectra for delay times between 0.5 ps and 50 ps are shown in (b,g). Parallel linear polarisations for the pump and probe pulses were used. Transients at fixed probe frequencies are plotted with respect to the delay time T in (d,h). Panel (c) shows the integrated bleach signal of ν_4 at 40 ps as a function of the UV pump pulse energy, suggesting a quadratic dependence (black curve). Transients from the bleaching regions of ν_4, $2\nu_4$, and ν_3 are uniformly fitted with a monoexponential function and a time constant of $\tau_{UV} = 1.1$ ps (black lines in (d,h)). The delay time axis is logarithmic after the axis break. For $T \approx 0$ fs, signal contributions from cross correlations between UV pump pulses and IR probe-pulses in the LiF windows with a width of 300 fs at 1100 cm^{-1} (panel (e)) and 210 fs at 2300 cm^{-1} (not shown) occur. Pump pulse energy: $E_{pump} \approx 0.5\,\mu J \mathrel{\widehat{=}} 3 \cdot 10^{10}\,W/cm^{-2}$.

Fig. 5.7 shows nonlinear spectra of ν_3 and ν_4 after UV excitation in panels (b) and (g), transients at fixed probe frequencies in panels (d) and (h), as well as linear absorption spectra in panels (a) and (f). Excitation density dependent absorption changes at a delay

time of 40 ps on the ν_4 oscillator have been integrated to evaluate the excitation characteristics, illustrated in (c). For the applied peak intensities of up to $\approx 1 \cdot 10^{10}\,\mathrm{W/cm^{-2}}$ (at $\approx 500\,\mathrm{nJ}$ pulse energy), the integrated nonlinear signal correlates quadratically with the incoming intensity. Comparable ionic crystals, such as NaBr or NaCl, exhibit two-photon absorption at slightly lower intensities of $\approx 2 \cdot 10^{9}\,\mathrm{W/cm^{-2}}$ with a two-photon absorption coefficient of e.g. $\beta = 3.6\,\mathrm{cm/10^9 W}$ at 266 nm for NaCl [209, 210]. For comparison, KDP exhibits a coefficient of $\beta = 2.7\,\mathrm{cm/10^{10} W}$, roughly ten times smaller than for NaCl [209, 211–213]. These similar order of magnitudes strongly suggest a two-photon absorption process in $NaBH_4$ under the chosen excitation conditions and, thus, an electronic excitation.

This electronic excitation of $NaBH_4$ leads to immediate responses on the ν_4 and ν_3 oscillators and on the Fermi resonances $2\nu_4$ and $\nu_2 + \nu_4$. While strong bleaching signals are present in the nonlinear spectra in (b) and (f) within the range of the fundamental v=0 $\rightarrow$ 1 transitions of the ν_3 and ν_4 modes, smaller bleaching signals are observed for $2\nu_4$ and $\nu_2 + \nu_4$. Redshifted enhanced absorption bands occur, together with a shoulder emerging around $2340\,\mathrm{cm^{-1}}$. The described spectral shapes are very similar to the results from the IR-pump/IR-probe experiments from Sec. 5.4, whereas the temporal evolution of the nonlinear signals are strikingly different. After a cross-correlation between the UV and IR pulses during their temporal overlaps in the used LiF windows (peaks at $T \approx 0$), the enhanced absorption shows an immediate and persisting response with basically no further dynamics between 0.5 ps and 50 ps, illustrated in Fig. 5.7 (d), (h). In contrast, all bleaching signals increase after the excitation with a uniform time constant of $\tau_{\mathrm{UV}} = 1.1\,\mathrm{ps}$. The corresponding maxima are reached after $\approx 4\,\mathrm{ps}$, while no significant changes are present up to 50 ps. Long-term measurements up to 500 ps (not shown) have revealed a slight further increase of bleaching and enhanced absorption contributions, as well as a moderate blueshift of the nonlinear spectra. Small fingerprints of this behaviour are evident in the nonlinear spectra for a delay time of 50 ps.

Comparing the results from resonantly excited ν_3 and ν_4 modes of $NaBH_4$ in an IR-pump/IR-probe experiment with the results from an electronically excited $NaBH_4$ crystal manifests two major differences and one distinct similarity. While resonantly excited ν_3 and ν_4 modes clearly relax in a downhill process with a respective time evolution of the nonlinear response, all modes exhibit exactly the same time evolution under UV excitation of the $NaBH_4$ crystal. Secondly, explicit contributions of excited state absorption are measurable for the resonant IR-excitation which is in contrast to a fairly flat redshifted enhanced absorption under UV excitation. A very striking similarity is the general congruence of the nonlinear spectra after UV and IR excitation at late delay times ($T > 20\,\mathrm{ps}$) that can be attributed to the signature of a heated crystal or hot ground state, discussed in detail in the next section 5.4.3.

The nonlinear spectra, transients, and the comparison to the IR-pump/IR-probe measurements lead to the following interpretation. No significant populations of the excited v=1 states of ν_3 and ν_4 are created. Instead, an anharmonical coupling to low-frequency phonon modes, such as external modes, can cause the identical temporal behaviours of all bleaching signals while excited state contributions are essentially absent. This is supported by the ionic crystal lattice of $NaBH_4$ that features a manifold of (low-frequency) polar phonons, to which e.g. excited electrons, polarons, or excitons can couple [169, 185, 214–217]. Excitonic lifetimes on a sup-picosecond to 10 ps timescale are not unusual, hence, it is conceivable that excitons are created under two-photon absorption that decay with a $\tau_{\mathrm{UV}} = 1.1\,\mathrm{ps}$ lifetime and release their excess energy into the phonon manifold and, thus, heat up the crystal [218–220]. A second conceivable sce-

nario is an ultrafast partial relaxation of "hot" excitons in which the energy difference of $E_{\mathrm{exc}}(2 \cdot 4.55\,\mathrm{eV}) - E_{\mathrm{gap}}(6\,\mathrm{eV})$ is released and redistributed on a 1.1 ps timescale, including longer lifetimes of the partially relaxed excitons beyond 50 ps. However, further investigations are required to thoroughly evaluate the electronic processes after UV excitation of $NaBH_4$.

5.4.3 Temperature difference spectra

The resonant IR excitation leads to a population of the internal BH_4^- modes and a subsequent decay and randomisation of the excess energy into the phonon bath of external phonon modes. As opposed to this, the resonant UV excitation leads to a more direct randomisation of the excess energy. In both cases, the excitations result in a temperature jump ΔT of the $NaBH_4$ crystal caused by population of low-lying external phonon modes, the population of a hot ground state.
To verify this heat jump assumption, temperature difference spectra were generated with linear absorption spectra measured at two different temperatures in order to compare them with nonlinear spectra from the pump/probe experiments. Fig. 5.8 contains the direct comparison.

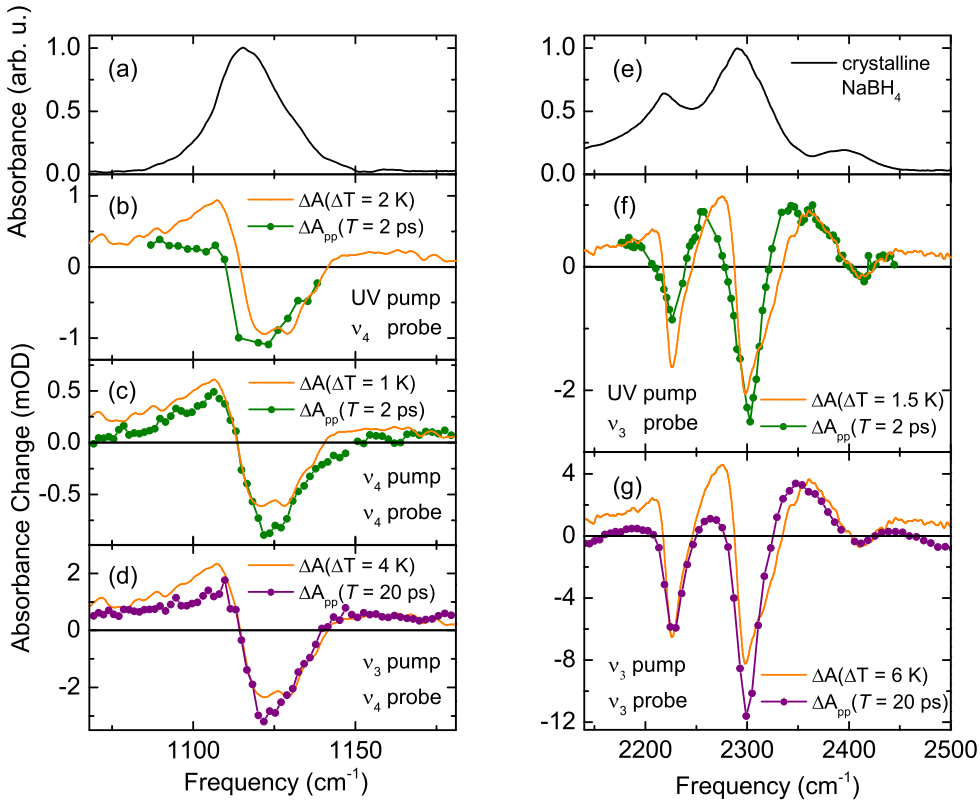

Figure 5.8: Comparison of temperature difference spectra with transient spectra taken from Figs. 5.6 and 5.7. Panels (a,e) show the linear absorption of crystalline $NaBH_4$. Nonlinear spectra from the UV pump/ν_3,ν_4 probe experiments at a delay time of $T = 2\,\mathrm{ps}$ correlate well with a heat jump of $\approx 2\,\mathrm{K}$ (b,f). The nonlinear spectrum from the ν_4 pump/ν_4 probe experiment at a delay time of $T = 2\,\mathrm{ps}$ shows well accordance with a heat jump of $1\,\mathrm{K}$ (c). ν_3 pump/ν_3,ν_4 probe results in a higher heat jump of $\approx 5\,\mathrm{K}$, proven with transient spectra at a delay time of $T = 20\,\mathrm{ps}$ in (d,g).

Fig. 5.8 represents scaled temperature difference spectra $\Delta A(\Delta T)$ together with selected pump/probe spectra of crystalline $NaBH_4$ after IR-excitation (cf. Fig. 5.6) and after UV-excitation (cf. Fig. 5.7). Two linear IR absorption spectra measured at temperatures of $T = 310\,\mathrm{K}$ and $T = 295\,\mathrm{K}$ are used to evaluate the induced heat jumps via the equation $\Delta A(\Delta T) = (A(310\,\mathrm{K}) - A(295\,\mathrm{K})) \cdot \Delta T/15\,\mathrm{K}$. The general accordance between the spectra from the pump/probe experiments and the temperature difference spectra with respect to the spectral shapes and relative peak amplitudes underlines the formation of a hot ground state and a temperature jump in the crystalline phase after all investigated excitations. Different excitation conditions lead to bigger or smaller temperature jumps in the $NaBH_4$ sample, e.g. UV pump: $\approx 2\,\mathrm{K}$ (b), (f); ν_4 pump: $\approx 1\,\mathrm{K}$ (c); and ν_3 pump:

$\approx 5\,\mathrm{K}$ (d), (g).
The comparison in Fig. 5.8 also illustrates the different durations of excess energy redistribution within the $NaBH_4$ crystal. While a convincing congruence is present between the transient spectra after UV- and ν_4-excitation at a delay time of 2 ps, transient spectra for later delay times of 20 ps reproduce the temperature difference spectra better after ν_3-excitation. This behaviour is caused by the cascaded excess energy relaxation after ν_3-excitation in contrast to the more direct coupling to the low-frequency phonon modes after UV- and ν_4-excitation. A comparison of timescales reveals that the 3.6 ps lifetime of $\nu_4(\mathrm{v} = 1)$ in the liquid solution is somewhat longer than the 2 ps required to create a hot ground state in the crystalline phase. The strong coupling of the internal phonon modes to the external phonon modes in $NaBH_4$ can cause this behaviour. A comparable strong signature in temperature-dependent IR- and Raman spectra was also reported for $LiBH_4$ and attributed to a strong anharmonic coupling between vibrational modes, potentially via rotational degrees of freedom [44, 175].
The decay of the hot ground state is expected to occur on a 100 ps timescale [44]. Hence, in the pump/probe measurements, final heat transfer to the surrounding atmosphere and the substrate window occurs within two subsequently interacting pump pulses, so that a completely relaxed sample is present before each pump-induced heat jump.
$NaBH_4$ is reported to exhibit a heat capacity at $\mathrm{T} = 300\,\mathrm{K}$ of $\mathrm{C}_{\mathrm{NaBH_4}} = 2280\,\mathrm{Jkg^{-1}K^{-1}}$ [221]. For an absorbed pump pulse energy of $\approx 0.5\,\mu\mathrm{J}$ and an irradiated volume of $\approx (125\,\mu\mathrm{m})^2 \times 1\,\mu\mathrm{m}$, the mentioned heat capacity leads to an IR pump pulse induced heat jump of $\approx 15\,\mathrm{K}$, higher than the estimations based on the temperature difference spectra. An explanation for this difference is collective coupling and damping that leads to an immediate re-emission of pump pulse energy and, thus, to a less amount of deposited energy and heat.
To account for the measured results on crystalline $NaBH_4$ with its peculiarities in the temporal evolution and similarities to temperature difference spectra, model calculations are performed that are discussed in the following section 5.5.1.

5.5 Model calculations

5.5.1 Population dynamics and radiative coupling and damping

In the model calculations performed, all significant aspects measured in the linear and nonlinear experiments such as the Fermi resonance between ν_3 and ν_4, the cascaded energy relaxation from ν_3 to ν_4, radiative coupling and damping, as well as a hot ground state are comprised to develop an extensive picture of the nonlinear response of $NaBH_4$ after resonant IR-excitation [172].
The prepared and measured thin film of $NaBH_4$ is a polycrystalline layer consisting of an ensemble of randomly oriented crystallites (cf. Sec. 3.8), just as it is the case for randomly oriented BH_4^- molecules in the solution discussed in Sec. 5.3.2. As for the solution, the symmetry properties of BH_4^- ions in the crystalline $NaBH_4$ at ambient conditions are described in the point group T_d, a direct consequence of the cubic space group of $NaBH_4$. Both, the random orientations and the tetrahedral symmetry of BH_4^- ions in the crystalline phase cause the polarisations of the interacting light pulses to be insignificant. Consequently, all model calculations were performed with fixed linear polarisations of the interacting light fields.
The following calculations contain two steps. In the first step, a Hamiltonian for the BH_4^- ion is formulated that includes the stretching vibration ν_3, the bending vibration ν_4, the Fermi resonance enhanced overtone $2\nu_4$, and a term for the light matter interaction that explicitly includes radiative coupling and damping. In the second step, the Maxwell-Liouville equation is solved for the system described by a density matrix ρ to properly account for the coherent radiative coupling, an effect not included in the RWA and slowly varying amplitude approximations. The chosen approach contains phase relaxation for ν_3 and phase as well as energy relaxation for ν_4, in order to evaluate the transient behaviour of both vibrational modes. Transition frequencies, dipole moments, and anharmonicities were verified with the linear absorption spectrum of $NaBH_4$.

The Hamiltonian relies on the creation (a_3^+, a_4^+) and destruction (a_3, a_4) operators to model the excitations of the two vibrational normal modes ν_3 and ν_4. The used ladder operators fulfill the commutation relations of harmonic oscillators, i.e., $[a_i^+, a_j] = \delta_{i,j}$, $[a_i^+, a_j^+] = 0$, and $[a_i, a_j] = 0$. Individual anharmonicities of the excited states of ν_3 and ν_4 are included with the parameters η_3 and η_4. Then, allowing for a coupling among ν_3 and ν_4 via a Fermi resonance and a coupling to the light field results in the following Hamiltonian [172]:

$$
\begin{aligned}
H &= \hbar\omega_3\, a_3^+ a_3 + \frac{\eta_3}{2}\left(a_3^+ a_3 a_3^+ a_3 - a_3^+ a_3\right) && (5.11)\\
&\quad + \hbar\omega_4\, a_4^+ a_4 + \frac{\eta_4}{2}\left(a_4^+ a_4 a_4^+ a_4 - a_4^+ a_4\right) && (5.12)\\
&\quad + \frac{\eta_{34}}{2}\left[\left(a_4^+\right)^2 a_3 + a_3^+ \left(a_4\right)^2\right] && (5.13)\\
&\quad + \left[E_{\mathrm{in}}(t) + E_{\mathrm{em}}(t)\right]\left(d_3\,\frac{a_3^+ + a_3}{\sqrt{2}} + d_4\,\frac{a_4^+ + a_4}{\sqrt{2}}\right). && (5.14)
\end{aligned}
$$

The first two terms (5.11) and (5.12) give rise to the vibrational modes ν_3 and ν_4 with their respective anharmonicities and transition frequencies ω_3 and ω_4. The third term (5.13) creates a Fermi resonance between v=1 of ν_3 and v=2 of ν_4, due to a third order anharmonic coupling with the coupling strength η_{34}. A second Fermi resonance between ν_2 and ν_4 is present in the linear absorption spectrum of crystalline $NaBH_4$ (cf. Fig. 5.3) that is not considered here due to its small oscillator strength. The fourth term (5.14) describes the interaction of ν_3 and ν_4 with the light fields $E_{\mathrm{in}}(t)$ and $E_{\mathrm{em}}(t)$. $E_{\mathrm{in}}(t)$ is the incident light field defined by the experimental pump pulse parameters and $E_{\mathrm{em}}(t)$ is the emitted light field caused by all vibrational oscillators. The parameters d_3 and d_4 are the transition dipole moments and define the strength of the interaction between the light fields and the oscillators. The thin film geometry of the measured sample ($L << \lambda$) allows for an addition of $E_{\mathrm{em}}(t)$ to $E_{\mathrm{in}}(t)$, whereas the emitted light field $E_{\mathrm{em}}(t)$ is given by [19–21, 23, 222] :

$$
\begin{aligned}
E_{\mathrm{em}}(t) &= -\frac{N_{BH_4^-}\, L\, Z_0}{1 + n_{\mathrm{sub}}}\, j(t) && (5.15)\\
j(t) &= \omega_3\, d_3\, \mathrm{Tr}\left(\frac{i a_3^+ - i a_3}{\sqrt{2}}\,\rho\right) && (5.16)\\
&\quad + \omega_4\, d_4\, \mathrm{Tr}\left(\frac{i a_4^+ - i a_4}{\sqrt{2}}\,\rho\right). && (5.17)
\end{aligned}
$$

It is decisively described by the current contribution $j(t)$ of single ν_3 and ν_4 oscillators, given in eqn. (5.16) and eqn. (5.17). Furthermore, the density of oscillators $N_{BH_4^-}$ is essential, the thickness $L = 1\,\mu\mathrm{m}$ of the sample, the vacuum impedance $Z_0 = 377\,\Omega$, and the refractive index of the sample holder window ($n_{\mathrm{sub}} = n_{MgF_2} \approx 1.3$) [23]. Each unit cell of $NaBH_4$ contains four BH_4^- units so that $N_{BH_4^-} = 4/(232.5\,\text{Å}^3)$, which corresponds to a density of $1.72 \cdot 10^{22}\,\mathrm{cm}^{-3}$ (cf. Sec. 5.2). ρ denotes the density matrix of the statistical ensemble of ν_3 and ν_4 oscillators. Hence, geometric aspects define the emitted light field E_{em} caused by radiative coupling and damping, as well as the transition frequencies of the involved oscillators with their respective transition dipole moments. The additive implementation of E_{em} and, thus, of radiative coupling and damping in eqn. (5.14), makes

it possible to simulate its influence on the dynamics of ν_3 and ν_4 via setting it to either "0" or "E_{em}".
Formulating the equations (5.11)-(5.17) and, hence, the Hamiltonian for the system of BH_4^- oscillators with included radiative coupling and damping, completes the first step of the model calculations. In the second step, the Liouville equation is solved.

The Liouville equation describes the propagation of the density matrix ρ. Here, phenomenological energy and phase relaxation for both oscillators ν_3 and ν_4, respectively, are included according to the concept of Walls and Milburn, who formulated a theory for dissipation in a macroscopic superposition of quantum states [223].

$$\frac{d\rho}{dt} = \frac{1}{i\,\hbar}\,[H,\rho] \tag{5.18}$$

$$+ \frac{\Gamma_3}{2}\left(2a_3\rho a_3^+ - a_3^+ a_3\rho - \rho a_3^+ a_3\right) \tag{5.19}$$

$$+ \frac{\Gamma_4}{2}\left(2a_4\rho a_4^+ - a_4^+ a_4\rho - \rho a_4^+ a_4\right) \tag{5.20}$$

$$+ \frac{\gamma_3}{2}\left(2a_3^+ a_3\rho a_3^+ a_3 - a_3^+ a_3 a_3^+ a_3\rho - \rho a_3^+ a_3 a_3^+ a_3\right) \tag{5.21}$$

$$+ \frac{\gamma_4}{2}\left(2a_4^+ a_4\rho a_4^+ a_4 - a_4^+ a_4 a_4^+ a_4\rho - \rho a_4^+ a_4 a_4^+ a_4\right) \tag{5.22}$$

Here, dissipation is defined by the terms (5.19)-(5.22). While (5.19) and (5.20) characterise energy relaxation of ν_3 and ν_4 with the damping constants Γ_3 and Γ_4, phase relaxation is governed by (5.21) and (5.22) with the damping constants γ_3 and γ_4. The experimental finding (cf. Fig. 5.5) that ν_3 relaxes via ν_4, supported by a Fermi resonance, is embedded here by setting $\Gamma_3 = 0$. Furthermore, the hot ground state can be simulated with the trace of summand (5.20) and using the Hamiltonian without light-matter interaction, thereby describing a heat reservoir for excess energy.
In order to formulate the dynamics of ν_3 and ν_4 with the introduced model, all of the parameters used in (5.11)-(5.22) need to be determined. The basis to find suitable parameters are the linear and nonlinear absorption spectra of the measured thin film of crystalline $NaBH_4$ (cf. Figs. 5.6 and 5.3). A phenomenological adjustment of the parameters yields $\hbar\omega_3 = 2277\,\mathrm{cm}^{-1}$, $\hbar\omega_4 = 1119\,\mathrm{cm}^{-1}$, $\eta_{34} = 330\,\mathrm{cm}^{-1}$, $\gamma_3 = (400\,\mathrm{fs})^{-1}$, $\gamma_4 = (400\,\mathrm{fs})^{-1}$, $\eta_3 = 0$, and $\eta_4 = 0$. The Fermi resonance with its large coupling parameter $\eta_{34} = 330\,\mathrm{cm}^{-1}$ transfers oscillator strength from ν_3 to $2\nu_4$. The individual anharmonicities η_3 and η_4 are neglected, an approximation validated by the small anharmonicites measured in the nonlinear spectra (cf. Fig. 5.6) and by further theoretical investigations [44]. Keeping $\Gamma_3 = 0$ and setting $\Gamma_4 = (1.5\,\mathrm{ps})^{-1}$ allows for an appropriate description of the time-dependent nonlinear spectra.
A direct comparison of the so achieved theoretical and experimental vibrational dynamics of ν_3 and ν_4 within the BH_4^- oscillator in the crystalline phase is given in Fig. 5.9.

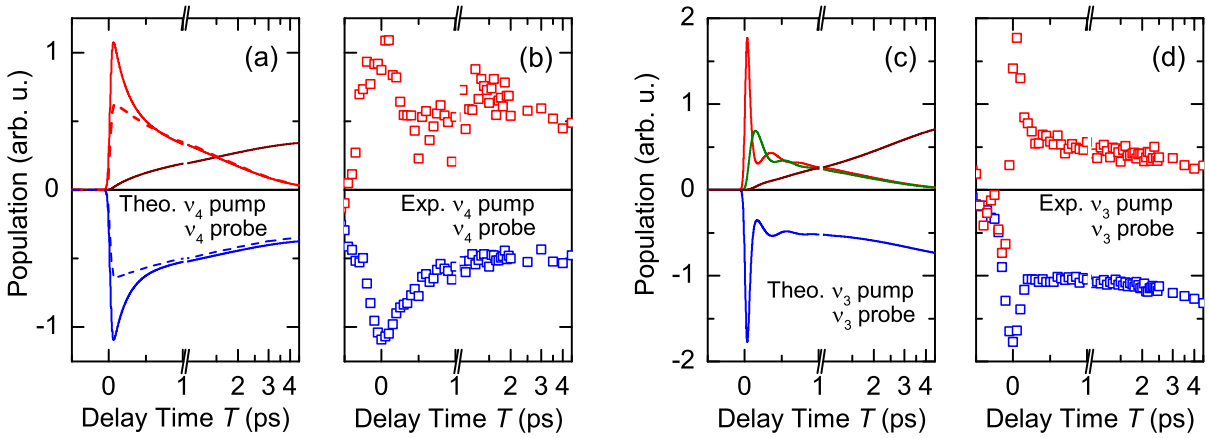

Figure 5.9: Comparison of calculated (a,c) and measured (b,d) population dynamics on ν_4 and ν_3 from BH_4^- in crystalline $NaBH_4$. Measured transients were taken from Fig. 5.6. Left: ν_4 pump/ν_4 probe and right: ν_3 pump/ν_3 probe. (a) Dynamics of the ν_4(v = 1) state (red) and bleaching of the ground state (blue) calculated with (solid lines) and without (dashed lines) radiative coupling and damping. An increasing population of the hot ground state (brown) is caused by the gradual deposition of excess energy. (c) Dynamics of the ν_3(v = 1) state (red) and bleaching of the ground state (blue) calculated with (solid lines) and without (dashed lines) radiative coupling and damping. The population of ν_4(v = 2) is shown in green. The Fermi resonance between ν_3 and $2\nu_4$ causes the illustrated (oscillating) population exchange. The corresponding population of the hot ground state is given in brown. The calculated population dynamics including radiative coupling and damping agree very well with the experimentally measured population dynamics.

The left-hand side of Fig. 5.9 shows the responses on the ν_4 oscillator after its resonant excitation. The different population kinetics represented as dashed and solid lines in (a) clearly illustrate the influence of radiative coupling and damping. While a strong initial decay within the first 500 fs is evident for implemented radiative coupling and damping in eqn. (5.14), it is absent for "$E_{\mathrm{em}} = 0$". In both cases, the transients exhibit identical decay kinetics beyond 500 fs that are mainly characterised by the damping rate Γ_4. The comparison with the experimental data in (b) demonstrates that radiative coupling and damping dominates the initial decay of resonantly excited ν_4 oscillators in the pump/probe experiment on crystalline $NaBH_4$. Due to the higher frequency of ν_3 and its higher transition dipole moment compared to ν_4, the theoretically expected initial decay obeys a sub-100 fs timescale, illustrated in (c). This quick response cannot be clearly resolved in the performed experiments. However, the transients shown in (d) adumbrate radiative coupling and damping even though further coherent contributions, such as pump/probe coupling, need to be considered in the range of delay times around $T = 0$ fs. Furthermore, a sub-ps population exchange between v=1 of ν_3 (red line) and v=2 of ν_4 (green line) occurs due to the strong Fermi resonance coupling with an identical population on both states after 1 ps. The population oscillation is strongly damped due to phase relaxation determined by the large damping constants $\gamma_3 = \gamma_4 = (400\,\mathrm{fs})^{-1}$ (cf. terms (5.21) and (5.22)). In the simpler model discussed for BH_4^- in ISPA (cf. Sec. 5.3.2), both states were assumed to have identical populations during the complete relaxation.
The brown curves in Fig. 5.9 (a) and (c) illustrate the increasing population of the hot ground state in which the vibrational excess energy is released. It increases monotonically after excitation of ν_3 and ν_4 with slightly different slopes at delay times < 1 ps and for delay times > 2 ps. The energy damping constants $\Gamma_3 = 0$ and $\Gamma_4 = (1.5\,\mathrm{ps})^{-1}$ allow for a quick initial population of the hot ground state after resonant excitation of ν_4, and only a somewhat slowed down population of the hot ground state after excitation of ν_3, due to its suppressed energy damping and anharmonic coupling to ν_4.

Finally, the transients in (b) and (d) as well as the residual transients from Fig. 5.6 can be described as spectrally dependent superpositions of the curves in (a) and (c). These curves explicitly include radiative coupling and damping, the formation of a hot ground state, and vibrational energy relaxation that are all necessary to account for the complex nonexponential decay kinetics measured in the pump/probe experiments on BH_4^- in the crystalline phase.

5.6 Conclusions and outlook

Ultrafast hydrogen dynamics of the potential hydrogen and energy carrier for mobile applications $NaBH_4$ were investigated in a comparative study. In one-colour and two-colour pump/probe experiments, the asymmetric BH_4^- stretching vibration ν_3 and the asymmetric BH_4^- bending vibration ν_4 revealed significantly different dynamics in crystalline $NaBH_4$ compared to BH_4^- ions dissolved in isopropylamine.
For BH_4^- ions in the liquid solution, vibrational v=1 lifetimes of 3.0 ps were measured for ν_3 and v=1 lifetimes of 3.6 ps for ν_4. A strong Fermi resonance between ν_3 and ν_4 supported a cascaded vibrational energy relaxation from the ν_3(v=1) state over the $\nu_4(v = 2)$ state into $\nu_4(v = 1)$ and, finally, into the vibrational manifold of the solvent. The vibrational modes of the thereby heated solvent coupled anharmonically to ν_3 and ν_4 that lead to the formation of a hot ground state with slightly redshifted fundamental transitions.
In contrast, a strong hot ground state could be measured for BH_4^- tetrahedrons embedded in crystalline $NaBH_4$ after the cascaded energy relaxation and population of external phonon modes. Thermal difference spectra revealed pump pulse induced heat jumps between 1 K and 6 K, dependent on the excitation conditions. Furthermore, the densely packed BH_4^- ions in $NaBH_4$ showed a coherently driven radiative coupling and damping at delay times below $\approx$ 500 fs, which lead to a partial initial depopulation of excited ν_3 and ν_4 states. Model calculations including the Fermi resonance between ν_3 and $2\nu_4$, the hot ground state, as well as radiative coupling and damping could account for the complex relaxation behaviour of ν_3 and ν_4 in the crystalline phase.
Two-photon absorption of $NaBH_4$ in the UV resulted in an immediate response on the ν_4 and ν_3 oscillators, which exhibited bleaching signals at the fundamental transitions that increased with a time constant of 1.1 ps, and enhanced absorption redshifted to the fundamental transitions with no further temporal dynamics within 50 ps. A comparison of transient spectra 2 ps after UV excitation revealed strong similarities with temperature difference spectra and transient spectra after IR excitation, underlining a quick population of external phonon modes.
An interesting aspect to study might be the influence of oscillator distances on the radiative damping. $NaBH_4$, KBH_4, $RbBH_4$, as well as $CsBH_4$ crystallise in the same cubic space group ($Fm\bar{3}m$) at ambient conditions, respectively, but exhibit different lattice constants and, hence, different separation distances between single BH_4^- oscillators ($a_{NaBH_4} = 6.151$ Å, $a_{CsBH_4} = 7.406$ Å). A reduced optical density is the consequence and the supperradiant lifetime should be extended.
Even though the secession of hydrogen in the gas phase occurs in an idealised picture via B-H stretching and bending vibrations, no measurable decomposition of $NaBH_4$ was recognised during the performed measurements [164]. The reason for this are thermodynamic barriers that emerge in the solid state $NaBH_4$. Decomposition temperatures of $\approx$ 800 K are reported for $NaBH_4$ that are clearly beyond the pump-induced temperature jumps of about 5 K measured here, so that light-induced decomposition via hydrogen release can be excluded [170, 224].

However, it could be very instructive to study vibrational dynamics of other complex hydrides such as alanates (e.g. $KAlH_4$) or chemical hydrides such as ammonia borane (NH_3BH_3) with significantly different hydration structures on the way to understand better the different processes during hydrogenation and dehydrogenation of complex hydrides.

6 Ultrafast nonlinear response of a bulk plasmon in a highly Ga-doped ZnO layer

Plasmons constitute the centre of investigations in the very wide and popular field of "plasmonics" [225–227]. They are either related with "surface plasmon polaritons" (SPP's) that represent collective electronic excitations confined to surfaces or with "bulk plasmons" that are spatially expanded collective electronic excitations [228, 229]. While SPP's occur at metal-air interfaces or semiconductor-air interfaces, bulk plasmons cannot only be excited in metals or semiconductors, but also in free electron (or ion) plasmas as e.g. in the sun [227,229,230]. In both cases, the collective electronic excitation is a plasma oscillation with a characteristic plasma frequency $\omega_\mathrm{p} = \sqrt{\frac{N_\mathrm{e} e^2}{m_\mathrm{eff}} \epsilon_0}$, dependent on the electron density N_e, the effective electron mass m_eff, and the electron charge e as well as the dielectric constant ϵ_0 [37, 62].

SPP's are considered to exhibit a "hybrid nature" due to their combined properties of light waves and charge oscillations [229]. This circumstance in combination with highly sophisticated methods to modify and structure surfaces and interfaces has, on the one hand, lead to fundamental physical insights and, on the other hand, to a wide range of applications [227, 231–234]. For example, plasmonic enhanced light absorption in photovoltaic absorber materials and cells is reported [226, 235–239]. Furthermore, selectively designed microstructures make it possible to enter the subwavelength regime, i.e., to guide light through interfaces way smaller than its wavelength and to enter the "beyond diffraction limit" [229, 240–242]. In all cases, momentum conservation at the interface requires the light to have an appropriate in-plane wave vector, realised e.g. in the Kretschmann and Otto configurations or by grating structures at the interface [62, 243–245].

Time-resolved interactions of SPP's with light pulses on an ultrafast timescale have been demonstrated in a manifold of experiments, e.g. by revealing ultrafast optical modulations of SPP's in waveguides or the coherent response of nanoantennas [18, 246, 247]. Furthermore, plasmonic nonlinearities in tailored structures can be used to drive e.g. second harmonic or third harmonic generation with the help of local field enhancements [248]. From the late 1990's until today the nonlinear optical responses of plasmon resonances in metallic nanoparticles have been investigated intensively. Topics, such as optically induced damping of surface plasmon resonances in gold colloids, coherent acoustic mode oscillation in silver nanoparticles, or the ultrafast response of the nonlinear refractive index of silver nanocrystals embedded in glass, were addressed [249–255].

In strong contrast, optical experiments on bulk plasmons are very rare. They have mainly been investigated in metallic films using methods, such as XPS (X-ray Photoelectron Spectroscopy), AES (Auger Electron Spectroscopy), or EELS (Electron Energy Loss Spectroscopy) [228, 256–259]. The reason behind this is the longitudinal and spatially extended character of bulk plasmons, easier excitable by momentum transfer via particle impact [227]. Their dispersion relations were investigated with EELS, X-ray scattering and theoretical methods beyond the random phase approximation (RPA) [260–262].

However, the investigation of bulk plasmons with light is greatly beneficial, since it allows for a direct access to quantities like the plasma frequency (and, thus to the electron density and the effective electron mass), the dispersion relation via varying the interaction geometry, or the momentum relaxation rate that determines the width of the plasma resonance [37, 62]. But especially, the investigation with light allows for the study of bulk plasmon dynamics on an ultrafast femtosecond timescale. Furthermore, the application of intense ultrashort light pulses enables the access in the nonlinear regime, two aspects that have not been reported to date. They are of particular relevance since they constitute fundamental insights into the nature of bulk plasmons and the basis to study couplings between e.g. bulk plasma oscillations and vibrational excitations of molecules on their intrinsic timescale.

In this chapter, the linear and nonlinear optical properties and responses of a specifically designed bulk plasmon are investigated. The system under study is a structure consisting of highly n-doped ZnO layers, recently introduced by S. Kalusniak et al., that makes it possible to address a bulk plasmon with optical methods [62]. Geometrical aspects are discussed that need to be fulfilled in order to effectuate a pronounced coupling between an inherently transversal light wave and the longitudinal excitation "bulk plasmon". Intense femtosecond pump pulses were applied to get access into the nonlinear regime of the bulk plasmon response and to resolve it on an ultrafast timescale. The experimental findings are supported by model calculations performed by Michael Wörner. Chapter 6 refers to ref. [37] where major experimental and theoretical results are published.

6.1 Basic aspects of plasmons

The upcoming sections 6.1-6.3 summarise the fundamental experimental and theoretical tools to describe plasmons and their interactions with light fields in metals. Bulk plasmons as well as SPP's are discussed and how they are correlated to the dielectric properties of a metal. Furthermore, the investigated ZnO:Ga sample is introduced in detail. Subsequently, the time-resolved nonlinear response of the ZnO:Ga sample is presented and extensively discussed.

6.1.1 Longitudinal solution of the wave equation

Plasmons are collective, longitudinal oscillations of an electron plasma relative to an ionic or polar crystal lattice [37, 228, 263]. They are a solution of the wave equation and correspond to the root of the dielectric function describing the medium the wave is propagating in, which is briefly discussed now [228].
The wave equation for electromagnetic waves in the absence of external charge and current densities can be deduced from the Maxwell equations for a conductive medium [17, 227, 264]. Assuming an electromagnetic field of the form $\mathbf{E}(\mathbf{r},t) = E \cdot \mathrm{e}^{i(\mathbf{kr}-\omega t)}$ yields the wave equation

$$\nabla \times \nabla \times \mathbf{E}(\mathbf{r},t) = \mathbf{k}(\mathbf{k} \cdot \mathbf{E}(\mathbf{r},t)) - k^2\mathbf{E}(\mathbf{r},t) = \epsilon(\mathbf{k},\omega)\frac{\omega^2}{c^2}\mathbf{E}(\mathbf{r},t). \tag{6.1}$$

This equation contains the wave vector $\mathbf{k}$ of $\mathbf{E}(\mathbf{r},t)$, its absolute value k, the angular frequency ω, and the velocity of light c. Optical properties of the medium the wave is propagating in are covered by the medium specific dielectric function $\epsilon(\mathbf{k},\omega)$. The dielectric function exhibits a real and an imaginary part and can be written as $\epsilon = \epsilon_1 + i\epsilon_2$, where ϵ_1 denotes the real and ϵ_2 the imaginary part, respectively [265, 266]. The wave equation has two different solutions, one of which for transversal waves and one for longitudinal waves. Transversal waves fulfill the condition $\mathbf{k} \cdot \mathbf{E} = 0$ which gives the generic dispersion relation

$$k^2 = \epsilon(\mathbf{k},\omega)\frac{\omega^2}{c^2}. \tag{6.2}$$

Longitudinal waves fulfill the condition $\mathbf{k} \cdot \mathbf{E} = kE$ which implies the dielectric function to vanish (cf. eqn. (6.1)), resulting in

$$\epsilon(\mathbf{k},\omega) = 0. \tag{6.3}$$

Hence, longitudinal oscillations can exclusively occur at frequencies corresponding to zeros of $\epsilon(\mathbf{k},\omega)$ [227]. Only p-polarised light (or TM polarisation) allows for the excitation of these longitudinal oscillations [37, 62, 227, 228, 267]. $\mathrm{E_x}$, $\mathrm{E_z}$, and $\mathrm{H_y}$ are the only non-vanishing field components for p-polarised light, where x, y, and z denote Cartesian coordinates and $\mathbf{H}$ the magnetic field. Longitudinal charge density oscillations are a form of elementary excitations and are called plasmons. They correspond to a periodically displaced electron gas in e.g. a thin metallic film. Bulk plasmons and SPP's are distinguished which are illustrated in Fig. 6.1 and Fig. 6.2.

6.1.2 Bulk plasmons

Bulk plasmons are longitudinal electron density oscillations with a spatially expanded character typically occurring in thin metallic films [227, 228]. The oscillation of electron density is parallel to the surface normal of the thin film and comprises its complete thickness. A graphical illustration of a bulk plasmon is given in the following Fig. 6.1.

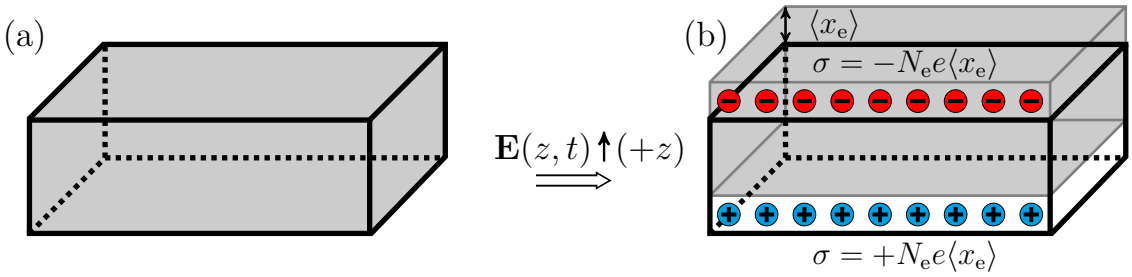

Figure 6.1: (a) Cross section of a thin metal film, (b) cross section of a thin metal film under the presence of the external electric field $\mathbf{E}(z,t)$ that excites a plasma oscillation, according to Fig. 14.5 in [228], [227]. The collective shift of the electron plasma is parallel to the electric field, illustrating its longitudinal character. The positively charged static ions of the crystal lattice are illustrated in blue, whereas effectively shifted electrons are illustrated in red. The thin metal film is electrically neutral.

In Fig. 6.1, the conduction band electrons are treated as a homogeneous and dense electron plasma and are illustrated in the form of a gray box [228]. This box is shifted relative to the static crystal lattice as a result of a driving external electric field $\mathbf{E}(z,t)$, e.g. given by a p-polarised light pulse. The collective shift leads to a positive surface charge density $\sigma = +N_\mathrm{e} e \langle x_\mathrm{e}\rangle$ at the bottom and to a negative surface charge density $\sigma = -N_\mathrm{e} e \langle x_\mathrm{e}\rangle$ at the top of the gray box. The region in the middle is electrically neutral. N_e denotes the electron density, e the charge of one electron and $\langle x_\mathrm{e}\rangle$ the collective, ensemble-averaged spatial displacement of the electron plasma. This displacement is time-dependent with alternating directions towards $+z$ and $-z$. A depolarisation field $E = \frac{N_\mathrm{e} e \langle x_\mathrm{e}\rangle}{\epsilon_0}$ is the consequence of the collective charge displacement, which limits the amplitude of $\langle x_\mathrm{e}\rangle$. The corresponding, damping free, equation of motion for a unit volume of the electron plasma with the ensemble averaged electron mass m_eff is given by

$$\frac{\mathrm{d}^2\langle x_\mathrm{e}\rangle}{\mathrm{d}t^2} + \frac{N_\mathrm{e} e^2 \langle x_\mathrm{e}\rangle}{\epsilon_0 m_\mathrm{eff}} = \frac{\mathrm{d}^2\langle x_\mathrm{e}\rangle}{\mathrm{d}t^2} + \omega_\mathrm{p}^2 \langle x_\mathrm{e}\rangle = 0, \tag{6.4}$$

which is identical to the equation of motion of an harmonic oscillator. Substituting

$$\omega_\mathrm{p}^2 = \frac{N_\mathrm{e} e^2}{\epsilon_0 m_\mathrm{eff}} \tag{6.5}$$

reveals the plasma frequency ω_p, the electron plasma is oscillating with. Damping of the bulk plasmon due to losses in the dielectric medium is governed by the damping constant γ_m. Correspondingly, the equation of motion for a damped bulk plasmon is given by

$$\frac{\mathrm{d}^2\langle x_\mathrm{e}\rangle}{\mathrm{d}t^2} + \omega_\mathrm{p}^2 \langle x_\mathrm{e}\rangle + \gamma_\mathrm{m} \langle x_\mathrm{e}\rangle = 0. \tag{6.6}$$

6.1.3 Surface plasmon polaritons (SPP's)

SPP's are longitudinal surface waves or electron density oscillations confined to an interface [60, 62, 227, 229]. This interface typically consists of a metal or semiconductor with the dielectric function ϵ_M and a non-conductive dielectric, such as air with a dielectric function ϵ_A (cf. Fig. 6.2). Furthermore, an interface consisting of two different metals is possible [60]. The skin depths in both media of the interface determine the confinement, whereas the surface wave essentially propagates along the interface [227, 229, 244]. The main characteristics of such a SPP at a single metal-air interface are illustrated in the following Fig. 6.2.

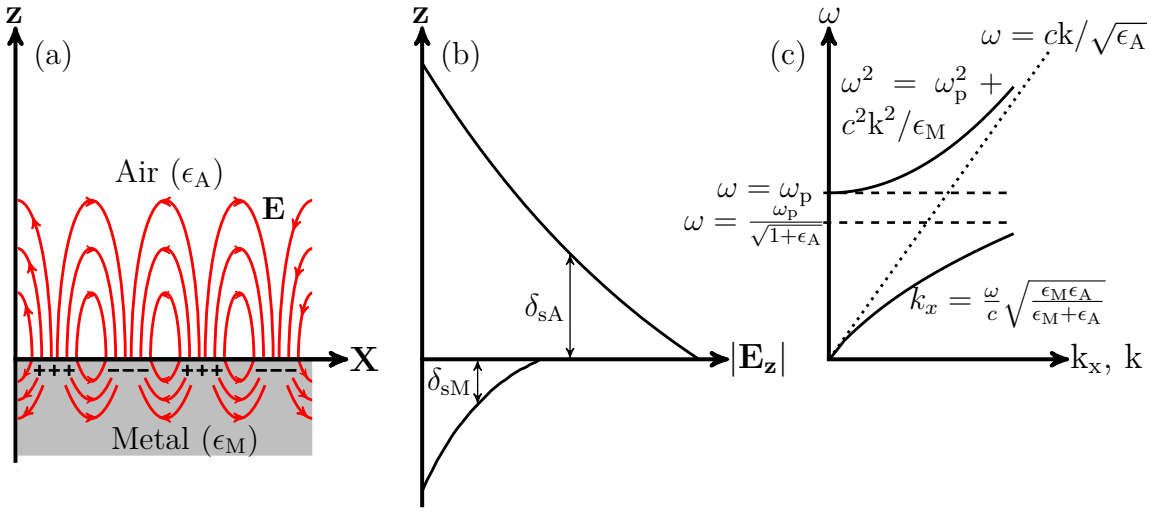

Figure 6.2: A SPP at the metal-air interface, according to Box 1 in [229], [62, 227, 268]. (a) Shows the hybrid nature of the electromagnetic wave and the oscillating surface charge with **E** pointing in z- and x-direction (red field lines) and **H** pointing in y-direction (not shown). The z-component of **E** leads to a surface charge in the metal with an exponentially decreasing character into ϵ_M and ϵ_A, underlining the confined character with propagation tolerance parallel to the surface (x-direction). The evanescent behaviour of E_z within the metal (ϵ_M) is schematically illustrated in (b). The penetration depth of E_z in the metal is the skin depth δ_{sM}, whereas the decay length in air δ_{sA} is roughly half the wavelength of the light involved [229]. The dispersion relations of a bulk plasmon (upper solid line) and a surface plasmon (lower solid line) are represented in (c), together with the dispersion of a free space photon (dotted line). The surface plasmon behaves photon-like for small momenta k_x and exhibits an increasing momentum mismatch to the free space photon for big momenta with the asymptotic limit $\omega = \omega_p/\sqrt{1+\epsilon_A}$. The bulk plasmon shows a big momentum mismatch to the free space photon for small momenta k and behaves photon-like for big momenta. Its minimal frequency is $\omega = \omega_p$. The forbidden frequency range between $\omega_p/\sqrt{1+\epsilon_A}$ and ω_p arises from total reflection at the metal-dielectric interface for $\omega < \omega_p$ in the transversal case and the strongly increasing momentum mismatch in the longitudinal case.

Once a sufficient in-plane light field component is given (e.g. by grating structures on the surface [229,244]), momentum conservation in ϵ_M and ϵ_A for the field components parallel to the surface normal and parallel to the interface (in-plane) is required. This necessitates the interaction with p-polarised light, as well as with dielectric media possessing a positive and a negative dielectric constant, respectively, conditions typically fulfilled for metal-insulator interfaces [227, 265]. In metal-metal interfaces, two different plasma frequencies are required to allow for the formation of SPP's [60]. Then, the **E** field components parallel to the surface normal (z-direction) fulfill the continuity relation [268]

$$\frac{k_{zA}}{\epsilon_A} + \frac{k_{zM}}{\epsilon_M} = 0 \tag{6.7}$$

where k_{zi} ($i = A, M$) are the appropriate complex wave vector components into ϵ_A and ϵ_M. These field components decay corresponding to $e^{-|k_z||z|}$ with the wave vector components [227, 268]

$$k_{zi} = \frac{\omega}{c}\sqrt{\frac{\epsilon_i^2}{\epsilon_A + \epsilon_M}}, \tag{6.8}$$

underlining the confined character. k_{zi} is an important quantity since it makes it possible to deduce the penetration depths δ_{si} of the interacting light field into ϵ_A and ϵ_M. The penetration depths are defined by the reciprocal real part of k_{zi} [227, 268],

$$\delta_{si} = \frac{1}{\mathrm{Re}(k_{zi})}. \tag{6.9}$$

6.2 ZnO:Ga sample geometry

6.2.1 Optical coupling between bulk plasmons and light

In order to investigate a bulk plasmon with optical methods, three experimental conditions need to be fulfilled [267]. Firstly, the longitudinal character of the bulk plasmon necessitates the metallic sample to be a thin film, if possible on top of a highly reflecting metallic layer. Secondly, the interacting light has to be p-polarised. And thirdly, the angle of incidence has to deviate from 0°. The last two conditions ensure a vectorial projection of the polarised electric field of the light wave to be parallel to the plasma oscillation. The first condition is valid for a film thickness that is smaller than the wavelength of the interacting light field and guarantees a non-propagating wave in the medium with a small amount of attenuation due to absorption of the longitudinal resonance. A highly reflecting metallic layer underneath the thin film causes a vanishing contribution of absorption due to transversal resonances in a reflection geometry [267]. An experimental setup that fulfills the enumerated conditions and, thus, is suitable to couple light to longitudinal resonances is given in Figs. 3.7 and 6.3.
These conditions were formulated and experimentally as well as theoretically validated in 1963 by D. W. Berreman to measure the absorption of longitudinal optical phonons in LiF [267]. They are of great importance, since they constitute the principles to couple transversal light waves to any longitudinal excitations in solids.

6.2.2 Linear absorption of the ZnO:Ga sample

The investigated ZnO:Ga sample fulfills the geometrical conditions from section 6.2.1 to allow for a direct coupling between light and a bulk plasmon. Its specific structure and linear absorption in reflection geometry is illustrated in Fig. 6.3 (cf. Fig. 3.7).

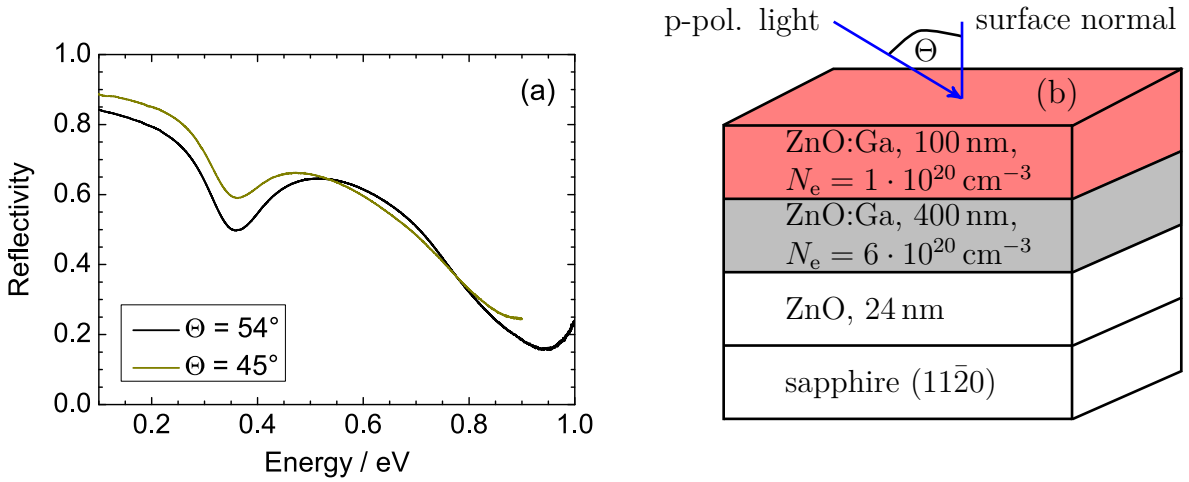

Figure 6.3: (a) Linear reflectivity spectra of the investigated ZnO:Ga sample for two different angles of incident with p-polarisation. The linear reflectivity spectra exhibit two characteristic absorption maxima at 360 meV, representing the bulk plasmon resonance in the upper layer under further investigation, and at 950 meV, which originates from the plasma resonance of the highly Ga-doped bottom layer (gray in (b)). Panel (b) shows the not to scale cross section of the ZnO:Ga sample with its four layers. Only the first two layers (red and gray) of the sandwich structure interact with light in the discussed linear and nonlinear experiments. The thin 24 nm ZnO layer stabilises the upper layers on the sapphire substrate [59].

The absorption resonance at 360 meV in Fig. 6.3 constitutes the bulk plasmon in the top layer ($N_e = 1 \cdot 10^{20}\,\mathrm{cm}^{-3}$) of the sandwich structure, whereas the absorption resonance around 950 meV originates from the plasma resonance of the highly doped bottom layer ($N_e = 6 \cdot 10^{20}\,\mathrm{cm}^{-3}$). Decreasing the angle of incidence leads to a higher overall reflectivity of the sample, especially at the plasma frequency in the top layer. This is due to a reduced vectorial ratio of the electric field of the incoming beam parallel to the plasma oscillation. A spectral shift of the plasma frequency with respect to the angle of incidence is not observed. The spectral width of the plasmon resonance is determined by the momentum relaxation rate $\gamma_m(\mathbf{k})$ (cf. eqns. (6.12) and (6.14)). It amounts to 106 meV in the investigated sample.
In the performed pump/probe experiments, the ZnO:Ga sample is excited at the plasmonic resonance of the upper layer with light pulses centred at 360 meV or 3.4 µm (cf. Fig. 6.5). Calculating the penetration depth of the incoming light pulse into the upper layer for an isolated, semi-infinite metal-air interface, one receives a value of $\delta_{sMA} \approx 1$ µm (cf. eqn. (6.9)), much larger than the layer thickness of 100 nm. This is important, since these numbers, in combination with the wavelength of the exciting light pulse, underline the thin film limit, a condition to couple to the bulk plasmon in the upper layer (cf. Sec. 6.2.1). Furthermore, it guarantees a completely excited layer and a homogeneous field strength along the z-direction.
Due to the large penetration depth, an interaction with the second metal-metal interface occurs. The second layer exhibits a much higher doping concentration of $N_e = 6 \cdot 10^{20}\,\mathrm{cm}^{-1}$ and, thus, its plasma resonance is not excited and the penetration depth into the second layer is much smaller. Assuming a semi-infinite metal-metal interface, one receives a value of $\delta_{sMM} \approx 400$ nm. Consequently, the second highly doped layer essentially acts as a metallic mirror at which the incoming light as reflected.

6.2.3 Polariton dispersion of the ZnO:Ga sample

In principle, the metal-air and the metal-metal interface of the ZnO:Ga sample could be regarded as a system of two coupled SPP's. A common approach to calculate the polariton dispersion for such a coupled system is presented now. Details for the calculation of the polariton dispersion of a thin layer with thickness d and permittivity ϵ_2 embedded between two semi-infinite media possessing the permittivities ϵ_1 (top) and ϵ_3 (bottom), respectively, are given in [61, 62, 227]. In short, the polariton dispersion of such a system of coupled SPP's can be expressed by pairs of (k_{zj}, ω) $(j = 1, 2, 3)$ with the z-components of the complex wave vectors in the regions 1,2, and 3, respectively. Each pair satisfies the equation

$$1 + \frac{\epsilon_1 k_{z3}}{\epsilon_3 k_{z1}} = i \tan(k_{z2} d) \left(\frac{\epsilon_2 k_{z3}}{\epsilon_3 k_{z2}} + \frac{\epsilon_1 k_{z2}}{\epsilon_2 k_{z1}} \right), \tag{6.10}$$

whereas all (k_{zj}, ω) correspond to a zero crossing in the complex wavevector k-plane and a mode (or branch) of the described sandwich structure [61, 62]. The thickness d, or the spatial separation distance between ϵ_1 and ϵ_3, strongly influences the coupling of the SPP's from the singular interfaces and the resulting polariton dispersion. Eqn. (6.10) can be deduced under utilisation of the transfer matrix method or Fresnel reflection coefficients [61, 62].
The dispersion relations for the investigated ZnO:Ga sandwich structure are presented in Fig. 6.4. They are solutions of eqn. (6.10) and plotted together with polariton dispersions of singular interfaces (cf. Fig. 6.1).

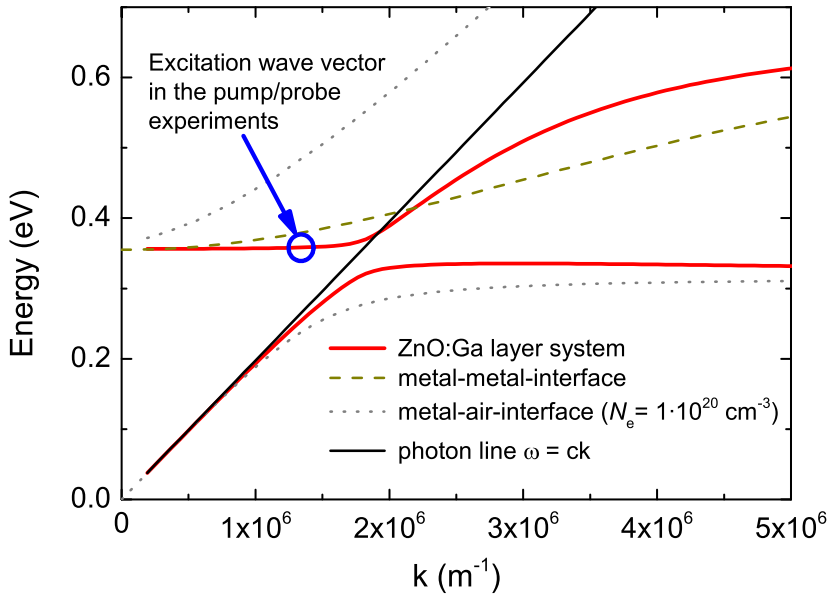

Figure 6.4: Dispersion relations for the coupled SPP's of the multilayer ZnO:Ga system (cf. Fig. 6.3) and for isolated single interfaces. The dispersion of the coupled SPP's is represented in red. Further dispersions are from the metal ($N_e = 1 \cdot 10^{20}\,cm^{-3}$) - metal ($N_e = 6 \cdot 10^{20}\,cm^{-3}$) interface (yellow dashed) and from the metal ($N_e = 1 \cdot 10^{20}\,cm^{-3}$) - air interface (gray dotted). The photon line is shown in black. The excitation conditions used in the pump/probe experiments are highlighted in blue.

The coupled SPP dispersion of the sample exhibits an extremely flat characteristic for wave vectors $k < 1.6 \cdot 10^6\,m^{-1}$. This behaviour is contrasted by the dispersions of the isolated metal-metal interface and especially by the isolated metal-air interface for $N_e = 1 \cdot 10^{20}\,cm^{-3}$ that are only flat for $k = 0$ or $k \to \infty$ and show a strong wave vector

dependence.
The flat curve progression of the (red) left branch for wave vectors $k < 1.6 \cdot 10^6\,m^{-1}$ is very typical for bulk plasmons whose frequency is not dependent on k (cf. eqn. (6.5)). So even in a polariton picture of coupled SPP's, the investigated absorption resonance of the ZnO:Ga sample is best described as an excitation of a bulk plasmon within the upper layer of a sandwich structure, exhibiting a thickness of 100 nm and a doping concentration of $N_e = 1 \cdot 10^{20}\,cm^{-3}$.
The chosen excitation conditions in the pump/probe experiments are highlighted in form of a blue circle, determining the exciting wave vector $k = \omega/c\sqrt{\epsilon_{air}}\sin\Theta = 1.3 \cdot 10^6\,m^{-1}$ for $\Theta = 45°$ (cf. Fig. 3.7) at an excitation energy of 360 meV. It is clearly located on the left of the photon line $\omega = ck$ together with one branch of the red dispersion curve of the ZnO:Ga sample, underlining the radiative character of the investigated mode and the possibility to excite it from free space [61].

6.3 Bulk plasmon in ZnO:Ga

6.3.1 The dielectric function of the electron plasma

Since the bulk plasmon is connected to the root of the dielectric function as shown in eqn. (6.3), it is crucial to find a suitable description for it in order to understand the linear and nonlinear properties of the bulk plasmon. The dielectric function $\epsilon(\mathbf{k}, \omega)$ of a medium describes its interaction with a light field and contains its electrical as well as optical properties. In the long-wavelength limit ($k \to 0$) $\epsilon(0, \omega)$, collective excitations, such as surface or bulk plasmons, are covered, whereas in the low-frequency limit ($\omega \to 0$) $\epsilon(\mathbf{k}, 0)$ screening of electron-electron or electron-lattice interactions are comprised [228].
The long-wavelength limit is valid as long as the wavelength of the interacting light field is much longer than the characteristic dimensions in the medium, such as the mean free path of the electrons or its spatial dimensions [227]. This limit is, therefore, considered to describe the "spatially local" dielectric function. Paul Drude has introduced a microscopic theory to describe the polarisation $\mathbf{P}(\omega)$ of a free electron plasma in this limit. In this theory, the interaction of the electron plasma with an external light field $\mathbf{E}(\omega)$ is considered as an harmonic displacement of charge density, fulfilling the equation [17, 228]

$$\mathbf{D}(\omega) = \epsilon_0\mathbf{E}(\omega) + \mathbf{P}(\omega) = \left(1 + \chi^{(1)}\right)\epsilon_0\mathbf{E} = \epsilon_0\epsilon(\omega)\mathbf{E}(\omega) \tag{6.11}$$

with the displacement field $\mathbf{D}(\omega)$, the permittivity of the free space ϵ_0, and the linear susceptibility $\chi^{(1)}$. The frequency dependent longitudinal dielectric function $\epsilon(0, \omega) = \epsilon(\omega)$ is a complex function of the form

$$\epsilon(\omega) = 1 - \frac{\omega_p^2}{\omega^2 + i\gamma\omega} \tag{6.12}$$

with a momentum relaxation rate γ that is inversely proportional to the mean collision time τ ($\gamma = 1/\tau$) of the electrons. Here, one finds a direct correlation between the longitudinal oscillation of the electron plasma with the plasma frequency ω_p and the dielelectric function. Its imaginary component describes losses within the medium such as absorption. An approximated absorption spectrum of the bulk plasmon can be calculated by $\mathrm{Im}\,(1/\epsilon(\omega))$ [37]. High angular frequencies ($\omega\tau \gg 1$) lead to a simplified $\epsilon(\omega)$, defined as [5]

$$\epsilon(\omega) = 1 - \frac{\omega_p^2}{\omega^2} \qquad (\text{for } \omega\tau \gg 1). \tag{6.13}$$

Eqn. (6.12) slightly modifies for an electron plasma embedded in the conduction band of a semiconductor such as ZnO. Ga-doping up to $N_\mathrm{e} = 1 \cdot 10^{20}\,\mathrm{cm}^{-3}$ leaves the ZnO structure essentially unaltered so that parameters of pure ZnO can be used to describe an electron plasma in the conduction band of the ZnO:Ga sample [59]. In the expression

$$\epsilon_c(\omega) = \epsilon_\infty^c - \frac{2e_0^2}{V} \sum_{\vec{k}} \frac{f(\mathbf{k})}{m_\mathrm{eff}^c(\mathbf{k})\,[\omega^2 + i\omega\ \gamma_\mathrm{m}(\mathbf{k})]}, \tag{6.14}$$

ZnO specific quantities such as the dielectric constant ϵ_∞^c caused by interband transitions, the wave vector dependent effective electron mass $m_\mathrm{eff}^c(\mathbf{k})$, the cycle-averaged non-equilibrium free electron distribution $f(\mathbf{k})$, and the momentum relaxation rate $\gamma_\mathrm{m}(\mathbf{k})$, are considered [37]. The volume of the crystal is given by V, the different spin states of the electrons are described by the factor 2, and e_0 is the elementary charge. Summation over $\mathbf{k}$ includes all electrons of the plasma. Eqn. (6.14) results from the Boltzmann transport equation for intraband transitions [37]. Since the optical absorption of the plasmon is inherently linked to the dielectric function via $\mathrm{Im}\,(1/\epsilon_c(\omega))$, all parameters represented in eqn. (6.14) contribute to the plasmonic absorption resonance of the ZnO:Ga sample. The parameters ϵ_∞^c, V, $f(\mathbf{k})$, and $m_\mathrm{eff}^c(\mathbf{k})$ determine the spectral position of the plasmonic resonance. The momentum relaxation rate $\gamma_\mathrm{m}(\mathrm{k})$ specifies its spectral width. Thus, an absorption resonance as shown in Fig. 6.3 (a) can be described by eqn. (6.14).

6.3.2 Thomas-Fermi screening length

One common approximation to describe the low-frequency limit of the dielectric function is given by the so called Thomas-Fermi method. It treats the electron-electron interaction in the semiclassical limit of the Lindhard theory for slowly varying external potentials [5]. The deduced dielectric function of the electron plasma in the limit $\epsilon(\mathbf{k}, 0) = \epsilon(\mathbf{k})$ is given by the expression

$$\epsilon(\mathrm{k}) = 1 + \frac{\mathrm{q}_\mathrm{TF}^2}{\mathrm{k}^2}. \tag{6.15}$$

This equation contains the Thomas-Fermi wave vector q_TF which, for electron temperatures below the Fermi temperature ($\mathrm{T} \ll \mathrm{T_F}$), is defined as [5, 269]

$$\mathrm{q}_\mathrm{TF} = 2N_\mathrm{e}^{1/6}(3/\pi)^{1/6}a_0^{-1/2}. \tag{6.16}$$

The definition of the Thomas-Fermi wave vector comprises the effective Bohr radius $a_0 = \frac{4\pi\epsilon_\infty^c\epsilon_0\hbar^2}{m_\mathrm{eff}\cdot e^2}$ and the density of the electron plasma N_e. q_TF is a reciprocal distance beyond which the disturbance of an external charge is effectively screened by the electron plasma [5]. The effective Bohr radius for ZnO is $\approx 7 \cdot 10^{-10}\,\mathrm{m}$, so that $\mathrm{q}_\mathrm{TF}(\mathrm{ZnO{:}Ga}) \approx 1.6 \cdot 10^9\,\mathrm{m}^{-1}$ and $\lambda_\mathrm{TF} = 1/\mathrm{q}_\mathrm{TF} \approx 6 \cdot 10^{-10}\,\mathrm{m}$. This value is much smaller than the layer thickness of 100 nm. Thus, screening is very efficient in the dense electron plasma of the Ga-doped ZnO layer so that the electron plasma can be described by a spatially local dielectric function.

In conclusion, the sections 6.1-6.3 introduce SPP's and bulk plasmons and present a new layered sample system consisting of thin, differently Ga-doped ZnO layers to facilitate the excitation of a longitudinal bulk plasmon with optical methods. This statement is based on the conditions formulated by Berreman to couple light on longitudinal excitations in solids [267]. The first layer of the ZnO:Ga sample fulfills the required thin film limit. Its thickness of 100 nm is much smaller than the 3.4 µm wavelength of the pump (and probe) pulses and, at the same time, it is much smaller than the 1 µm penetration depth of the light. Furthermore, the thin film is located on top of a highly reflecting metallic mirror allowing for optical experiments in reflection geometry. The applied reflection geometry provides an angle of incidence of 45° so that p-polarised light can effectively couple to the bulk plasmon in the upper layer. The derived polariton dispersion for the ZnO:Ga sample clearly underlines the dominating bulk character of the investigated plasmon due to the absence of a k-dependence of the plasma frequency.
In addition, the Thomas-Fermi screening length in the upper layer is with $\lambda_{\mathrm{TF}} \approx 6 \cdot 10^{-10}\,\mathrm{m}$ much shorter than its thickness, allowing, on the one hand, for sharp interfaces to the air and to the highly doped bottom layer and, on the other hand, for a spatially local description of the dielectric properties. In particular, this makes it possible to describe the optical properties of the bulk plasmon in ZnO:Ga with eqn. (6.14).

Consequently, optical pump/probe methods in combination with the tailored sample design and the utilised reflection measurement geometry permit the direct investigation of the time-resolved nonlinearities of a bulk plasmon, discussed in detail in the following.

6.4 Ultrafast nonlinear response of a bulk plasmon in ZnO:Ga

Spectrally resolved pump/probe spectra for different probe frequencies and delay times were measured and merged together as broadband contour plots in Fig. 6.5 according to eqn. (2.45). The pronounced spectral width of the plasmonic absorption and the limited spectral width of the probe pulses of ≈ 35 meV necessitated probe pulses with 16 different centre frequencies and, thus, spectral windows, to cover the required spectral range. All pump and probe pulses were p-polarised. The pump frequency was kept constant and centred at 360 meV for different pulse energies. The excitation frequency is well below the optical bandgap of ZnO that amounts up to 3.3 eV [270, 271].

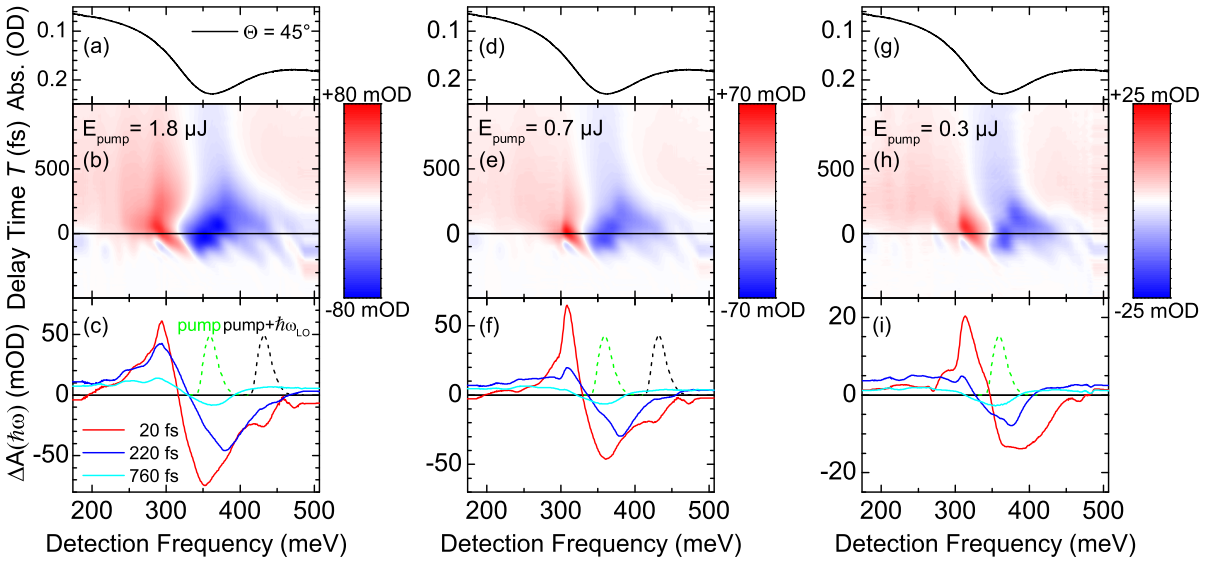

Figure 6.5: Nonlinear contour plots and spectra of pump/probe measurements on the ZnO:Ga sample. Panels (a,d,g) show the linear absorbance according to Fig. 6.3 and (b,e,h) contour plots of the merged femtosecond pump/probe spectra for different pump pulse energies. The absorbance change $\Delta A = -\log(R/R_0)$ is plotted as a function of the probe frequency (energy) and the delay time T. Cuts through the contour plots at fixed different delay times are given in (c,f,i). The dispersive shapes of the spectra show a transient redshift of the plasmon resonance for all pump pulse energies. Higher excitation densities lead to a stronger redshift, as well as to higher signal amplitudes. A LO phonon sideband is observed ≈ 70 meV blueshifted to the centre frequency of the pump pulse for pump pulse energies ≥ 0.7 µJ [272]. The measured (broadband) spectral width covers more than 300 meV from 174 meV (1400 cm^{-1}) to 507 meV (4100 cm^{-1}). All spectra shown here are measured with p/p polarisations. Pump pulse energy: ≤ E_{pump} = 1.8 µJ ≙ $7 \cdot 10^{10}$ W/cm^{-2}.

The resonantly excited bulk plasmon in the top layer of the ZnO:Ga sample exhibits a strong nonlinear response. At early delay times around $T = 20$ fs, broad bleaching signals are observed with a minimum around 350 meV for a pump energy of E_{pump} = 1.8 µJ. This minimum is blueshifted for smaller pump energies by about ≈ 25 meV. In contrast, a redshifted enhanced absorption is measured with a maximum at 295 meV for E_{pump} = 1.8 µJ that is also blueshifted by about 20 meV for smaller pump energies. The signal amplitudes reach absolute values of 75 mOD for the bleaching and 60 mOD for the enhanced absorption, which are both major portions of the overall plasmon absorption of ≈ 110 mOD (panel (a)), underlining the strong nonlinear response of the bulk plasmon. The described nonlinear behaviour is in line with a transiently redshifted plasma frequency of the excited bulk plasmon.

The integrated bleaching signals are larger than the integrated enhanced absorption signals ($I_{\text{int. bleach}}(T = 20\,\text{fs}, 1.8\,\mu\text{J})/I_{\text{int. enh. abs.}}(T = 20\,\text{fs}, 1.8\,\mu\text{J}) \approx 2.1$). This points to a reduced, frequency-dependent oscillator strength.
At later delay times ($\approx 200\,\text{fs}$), the redshift is still measurable with reduced signal amplitudes and slightly altered peak positions for all excitation densities. Beyond $\approx 200\,\text{fs}$, a spectrally flat contribution with a positive sign over all frequencies apart from the centre frequency of the plasma resonance is observable, pointing to a spectrally broadened bulk plasmon resonance.
A phonon sideband is apparent as an additional dip at 435 meV for delay times around $T = 20\,\text{fs}$ and pump pulse energies $\geq 0.7\,\mu\text{J}$. Its spectral position of $435\,\text{meV} = 365\,\text{meV}(\hbar\omega_{\text{pump}}) + 70\,\text{meV}(\hbar\omega_{\text{LO}})$ and its pump pulse energy dependence strongly indicate a distinct interaction of the bulk plasmon with LO phonons within the ZnO layer [273–275]. The spectral difference agrees very well with the excitation energies of LO phonons in ZnO that exhibit 72 meV [272].
Fig. 6.6 contains time-resolved transients of the discussed absorption changes at fixed probe frequencies.

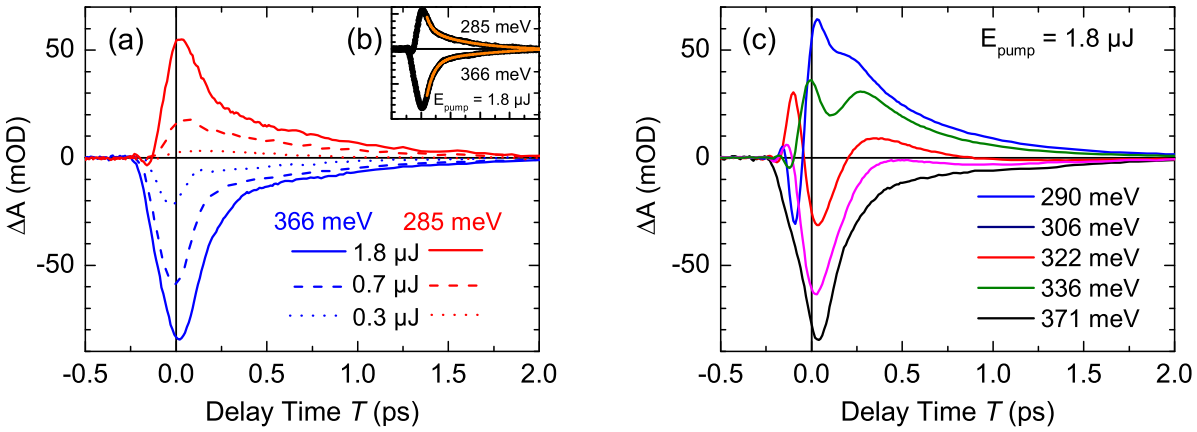

Figure 6.6: Transients of pump/probe measurements on the ZnO:Ga sample at different fixed spectral positions and for different excitation densities. Panel (a) shows transients taken from the regions of enhanced absorption and bleaching. Inset (b) illustrates biexponential fits for the transients. Panel (c) shows transients for a fixed excitation density and different spectral positions along the probe energy axis. The measurement data shown here are raw data in contrast to Fig. 6.5, which illustrates merged measurement data, i.e., weighted by the particular probe-pulse spectra.

The transients shown in Fig. 6.6 (a) illustrate the time evolution in the spectral regions of maximal signal amplitudes. They exhibit a quick signal increase before delay time 0 fs that is characterised by the time resolution of the experiment. The absence of perturbed free induction decay points to a very short transverse relaxation time T_2. After the initial increase, a quick decay is followed by a somewhat slower signal decrease until 2 ps, after which no residual signal is measurable anymore. Both, the bleaching as well as the enhanced absorption signal contributions exhibit similar decay kinetics. A biexponential description of the measured dynamics is plotted in the inset of panel (a) with time constants of $\tau_1(366\,\text{meV}, 285\,\text{meV}) = 100\,\text{fs}$ and $\tau_2(366\,\text{meV}) = 1500\,\text{fs}$, $\tau_2(285\,\text{meV}) = 800\,\text{fs}$ with different amplitudes, respectively, that underline the ultrafast relaxation of the signals. Different excitation densities lead to very similar decay kinetics, whereas the relative signal amplitudes point to a saturation with increasing pump fluence.
Panel (b) shows different transients for probe energies along the probe energy axis. Strong deviations from the behaviour shown in (a) are observable, especially for probe energies

around 320 meV, where the transients follow a kind of oscillatory evolution. The reasons behind this are three simultaneously occurring, correlated effects. There is i) a general transient signal decay for $T \geq 20$ fs, ii) a transient spectral shift of the plasma frequency, and iii) a spectral broadening of the plasma resonance. A combination of these three effects cause the strong probe energy dependent behaviour of the transients measured at fixed probe energies.
The pump fluence dependence and the temporal evolution of the transient zero crossings are illustrated in the following Fig. 6.7.

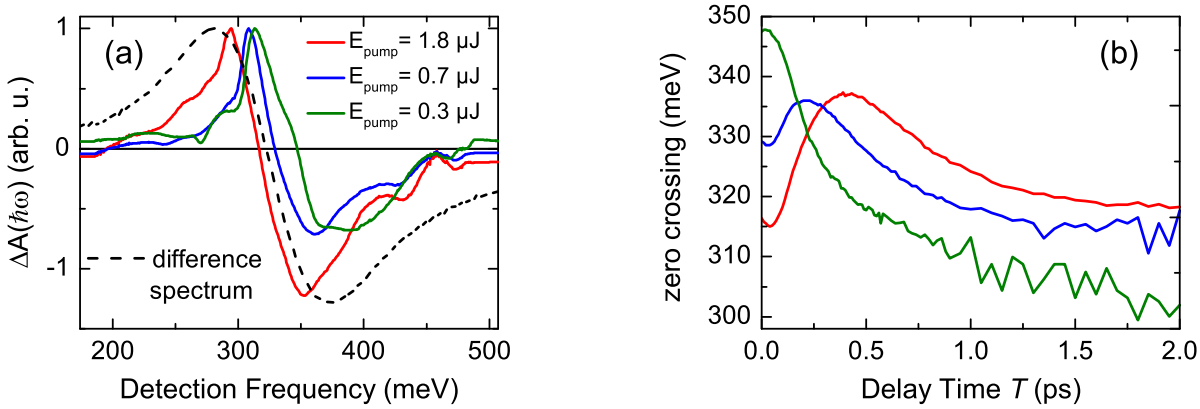

Figure 6.7: Panel (a) shows normalised cross sections through the contour plots from Fig. 6.5 at $T = 20$ fs for different pump energies (coloured solid lines), respectively. The dashed line illustrates a normalised difference spectrum between the linear reflectivity of the bulk plasmon (cf. Fig. 6.3) and a 50 meV redshifted reflectivity with 20 % reduced amplitude. As shown in Fig. 6.5, higher pump energies lead to a stronger redshift of the nonlinear signal and the LO-phonon sideband is only observable for pump energies ≥ 0.7 µJ. (b) Time-dependent zero crossings around 330 meV of the contour plots from Fig. 6.5 panels (b,e,h) for delay times between 0 and 2 ps.

A comparison of normalised transient spectra for different pump fluences at $T = 20$ fs is shown in Fig. 6.7 panel (a). Regarding the spectral positions of maximal signal amplitude and the zero crossings, one observes a clearly stronger redshift for higher pump fluences. In addition, a more pronounced bleaching contribution is evident. The cross section for $E_{pump} = 1.8$ µJ shows comparable characteristics as the dashed difference spectrum pointing to a plasma frequency shift of ≈ 50 meV.
The temporal evolution of the zero crossings for different pump fluences is shown in panel (b). At time delay 0 fs, the largest shift of the zero crossing is given for $E_{pump} = 1.8$ µJ that can be found at 315 meV, roughly 50 meV away from the equilibrium plasma frequency of 360 meV. The subsequent evolution of the zero crossings exhibit a strong pump fluence dependence. While the zero crossing monotonously shifts towards lower energies for $E_{pump} = 0.3$ µJ, a more complex behaviour is found for $E_{pump} \geq 0.7$ µJ. This behaviour involves an initial zero crossing energy increase with a maximum some 100 fs after $T = 0$ fs and a subsequent decrease with slower kinetics.
These discrepancies point to varied dominating effects during the relaxation after excitation with different pump fluences. For $E_{pump} = 0.3$ µJ, the dispersive shape of the nonlinear spectra around $T = 0$ fs changes within 150 fs into nonlinear spectra characteristic for a broadened plasmon resonance (cf. Fig. 6.5) that results in the monotonous shift of the corresponding zero crossing energy. In contrast, the dispersive shape of the nonlinear spectra typical for a redshift of the plasma frequency characterises the nonlinear spectra for $E_{pump} = 0.7$ µJ until 250 fs (peak, blue line in (b)) and for $E_{pump} = 1.8$ µJ until 450 fs (peak, red line in (b))) (cf. Fig. 6.5), after which the fingerprint of a spectrally broadened plasma resonance becomes evident, respectively.

In a series of measurements with rotated polarisations of the pump and probe pulses the bulk plasmon character of the investigated ZnO:Ga response is confirmed.

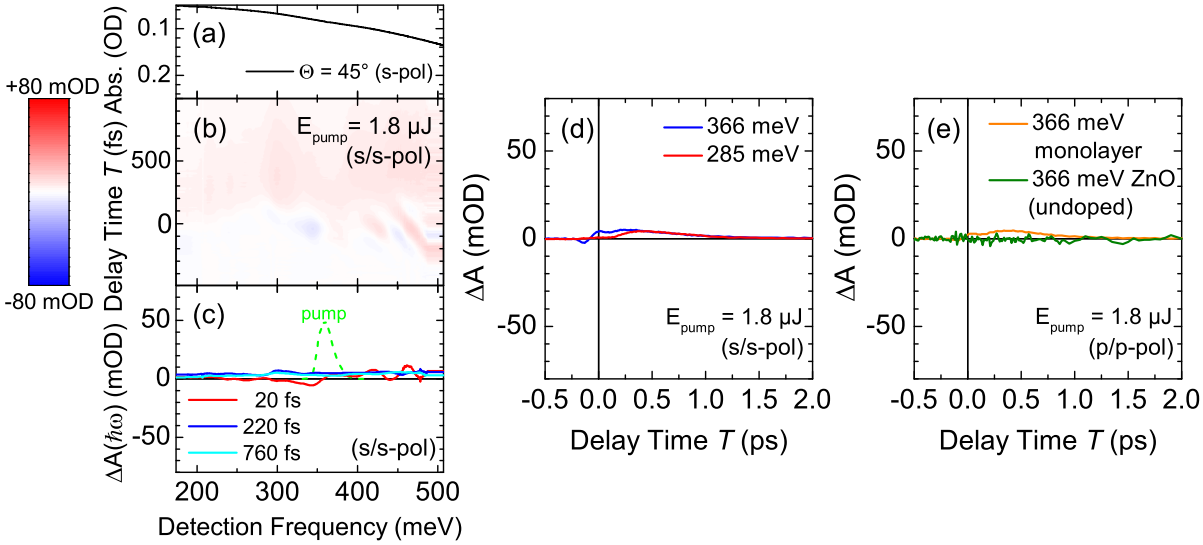

Figure 6.8: Reference measurements to confirm the optical excitation of the bulk plasmon and, thus, the investigation of its nonlinearities. (a) Absorbance $\Delta A = -\log R/R_0$ of the ZnO:Ga sample with s-polarisation. (b) Contour plot of the merged femtosecond pump/probe spectra with s/s-polarisation. (c) Cuts through the contour plot at fixed delay times and (d) time-resolved absorption changes at fixed spectral positions with s/s-polarisation, respectively. (e) Time-resolved absorption changes for a highly doped ZnO:Ga monolayer ($N_e = 6 \cdot 10^{20}\,\mathrm{cm}^{-3}$, 400 nm thick) and for an undoped ZnO substrate with p/p-polarisation. The scaling of the plots is the same as in Fig. 6.5 to simplify a direct comparison and to underline the more than one order of magnitude reduced signal intensity with positive signal contributions only with s/s-polarisation and for samples without the necessary sandwich structure.

Under utilisation of s-polarised (TE polarised) pump and probe pulses with no longitudinal electric field component, the nonlinear response of the ZnO:Ga sample is strongly different. No bleaching signals are observed after $T = 20\,\mathrm{fs}$. Instead, spectrally flat positive signal contributions over the entire spectral range are evident with a ≈ 15 times reduced intensity, as shown in (b) and (c). The transients in (d) exhibit maximal signal amplitudes of $\approx 5\,\mathrm{mOD}$ at delay times somewhat after $T = 0\,\mathrm{fs}$ with a subsequent exponential decay. For $T \leq 20\,\mathrm{fs}$, perturbed free induction decay influences the nonlinear response.
In a further set of measurements, a ZnO:Ga monolayer and an undoped ZnO substrate were measured under the same experimental conditions as the bulk plasmon in the ZnO:Ga sandwich structure, i. e., with p/p-polarisation. The ZnO:Ga monolayer exhibited no transient bleaching around the plasmonic absorption, but positive signals only with an amplitude and temporal evolution comparable to the results on the ZnO:Ga sandwich structure with s/s-polarisation, as shown in (e). The undoped ZnO substrate featured a much smaller reflectivity and no pump-induced absorption changes could be measured.

In principle, more effects than the redshift of the plasma frequency and a broadening of the absorption resonance could contribute to the strong nonlinear response of the ZnO:Ga sample. For instance, in metallic nanoparticles and thin films, acoustic phonon oscillations, an ultrafast response of the nonlinear refractive index, and a modification of the momentum relaxation rate γ were measured [249–255, 276–279]. In ZnO, the sound velocity along the c-axis adds up to $v_s = 6100\,\mathrm{ms}^{-1}$, which corresponds to a back and forth propagation time of 33 ps in the measured 100 nm thin layer, well above the dynamics

illustrated in Figs. 6.5 and 6.6 [280]. Furthermore, the nonlinear refractive index of ZnO is $n_2 = 23 \cdot 10^{-13}\,\mathrm{esu} \approx 5 \cdot 10^{-15}\,\mathrm{cm}^{-2}/\mathrm{W}$, which results under the used experimental conditions in a Kerr-induced change of $\Delta n \approx 10^{-4}$ [281]. Via $n = \sqrt{\epsilon}$, this alters the dielectric function of the thin ZnO:Ga layer on the order of $\Delta\epsilon \approx 10^{-8}$ and, thus, negligibly. Changes of γ lead to spectral broadening of the plasma resonance, so that none of the listed effects can account for the measured response of the ZnO:Ga sample with its particular amplitude as well as temporal and spectral properties.

The presented measurements, reference measurements and estimations lead to the conclusion that it is the bulk plasmon that causes the strong nonlinear response in the ZnO:Ga sandwich structure with p/p-polarisation, while further contributions can only be marginal. In the following section 6.5, model calculations are introduced that describe the strong measured nonlinear response with a bulk plasmon exhibiting a plasma temperature dependent effective electron mass to account for the transient redshift of the plasma resonance.

6.5 Model calculations

6.5.1 Stationary response of bulk plasmons

Model calculations were performed to theoretically account for the nonlinear response of the bulk plasmon [37]. These are based on three major steps. In a first step, the frequency dependent longitudinal dielectric function eqn. (6.14), whose inverse imaginary part $\mathrm{Im}(1/\epsilon_c(\omega))$ reproduces an absorption spectrum, is used to describe linear optical properties of the bulk plasmon in the ZnO:Ga multilayer system. It is given by

$$\epsilon_c(\omega) = \epsilon_\infty^c - \frac{2e_0^2}{V}\sum_{\mathbf{k}} \frac{f(\mathbf{k})}{m_{\mathrm{eff}}^c(\mathbf{k})\left[\omega^2 + i\omega\ \gamma_{\mathrm{m}}(\mathbf{k})\right]}. \tag{6.17}$$

In ZnO, the high-frequency dielectric constant amounts to $\epsilon_\infty^c = 3.7$. V denotes the volume of the ZnO crystal. The interaction of a strong pump pulse with the bulk plasmon leads to a deposition of $\approx 0.5\,\mu\mathrm{J}$ (30 % of the pump pulse energy) into the 100 nm thin ZnO:Ga layer. Accordingly, the electron gas in the conduction band of ZnO:Ga is heated up to several thousand Kelvin. The large momentum relaxation rate $\gamma_{\mathrm{m}}(\mathbf{k}) = 106\,\mathrm{meV}$ (cf. Fig. 6.3) corresponds to a mean collision time among damped electrons of $\tau = 1/\gamma_{\mathrm{m}}(\mathbf{k}) \approx 10\,\mathrm{fs}$, in agreement with the dephasing time T_2. This leads to a very efficient redistribution of the excess energy within the electron gas on a 10 fs-timescale, well below the time resolution of the performed experiments, so that $f(\mathbf{k})$ can be approximated as a thermalised (hot) Fermi distribution at any time. A reference for this assumption is offered by time-resolved experiments on photoexcited electrons and holes in GaAs [282,283]. Even though the plasma densities were 3 orders of magnitude smaller than for the ZnO:Ga sample in those experiments, an initial thermalisation within 100 fs occurred.
A hot Fermi distribution involves a slightly modified $\gamma_{\mathrm{m}}(\mathbf{k})$. Since Kerr-nonlinearities (cf. Sec. 6.4) do not play a role and the volume as well as the electron density in ZnO:Ga stay unaltered during the excitation and relaxation, it is exclusively the effective electron mass $m_{\mathrm{eff}}^c(\mathbf{k})$ that can account for the redshift measured in the experiments.
So, in a second step, the temperature-dependent effective electron mass in ZnO is modeled around the conduction band minimum with the help of a hyperbolic dispersion that significantly deviates from parabolic bands. The hyperbolic model of Kane, given by

$$E(\mathbf{k}) = \frac{1}{2}\sqrt{E_{\mathrm{gap}}^2 + \frac{2E_{\mathrm{gap}}\hbar^2k^2}{m_{\mathrm{eff}}^c(0)}} - \frac{E_{\mathrm{gap}}}{2} \tag{6.18}$$

was used to approximate the band structure. It includes the direct bandgap E_{gap} of ZnO ($E_{\mathrm{gap}}(\mathrm{ZnO}) = 3.45\,\mathrm{eV}$ at 300 K) and the effective electron mass of an electron at the conduction band minimum $m_{\mathrm{eff}}^c(k=0) = 0.275\,m_{\mathrm{e}}$ (m_{e}: free electron mass) [59, 271, 284–287]. In-depth band structures of ZnO can be found in ref. [271] but are unnecessary here due to the limitation of small $\mathbf{k}$-vectors around the conduction band minimum. Using the hyperbolic model of Kane, the $\mathbf{k}$-dependent effective electron mass tensor can be approximated. Under consideration of the pump-induced longitudinal elongation of the electrons along the z-axis of ZnO in the ZnO:Ga sample, the corresponding zz-component is given by

$$\left(\frac{1}{m_{\mathrm{eff}}^c(\mathbf{k})}\right)_{zz} = \frac{1}{\hbar^2}\frac{\partial^2 E(\mathbf{k})}{\partial k_z^2}. \tag{6.19}$$

Therefore, the pump pulse creates a hot Fermi distribution of conduction band electrons in ZnO:Ga that are elongated along the non-parabolic **k**-space, which leads to a modification of the cycle-averaged effective electron mass and, consequently, to a redshift of the bulk plasmon frequency defined by $\omega_\mathrm{p} = \sqrt{\frac{N_\mathrm{e} e^2}{m^c_\mathrm{eff} \epsilon_0}}$. No interband excitations occur, instead pure intraband excitations account for the measured processes [271].

In Fig. 6.9, the first two steps of the model calculations are discussed including the optical absorption properties of the bulk plasmon in ZnO:Ga at two different electron temperatures. Eqn. (6.18) was used to model the different electron temperatures and eqn. (6.17) to derive the absorption properties.

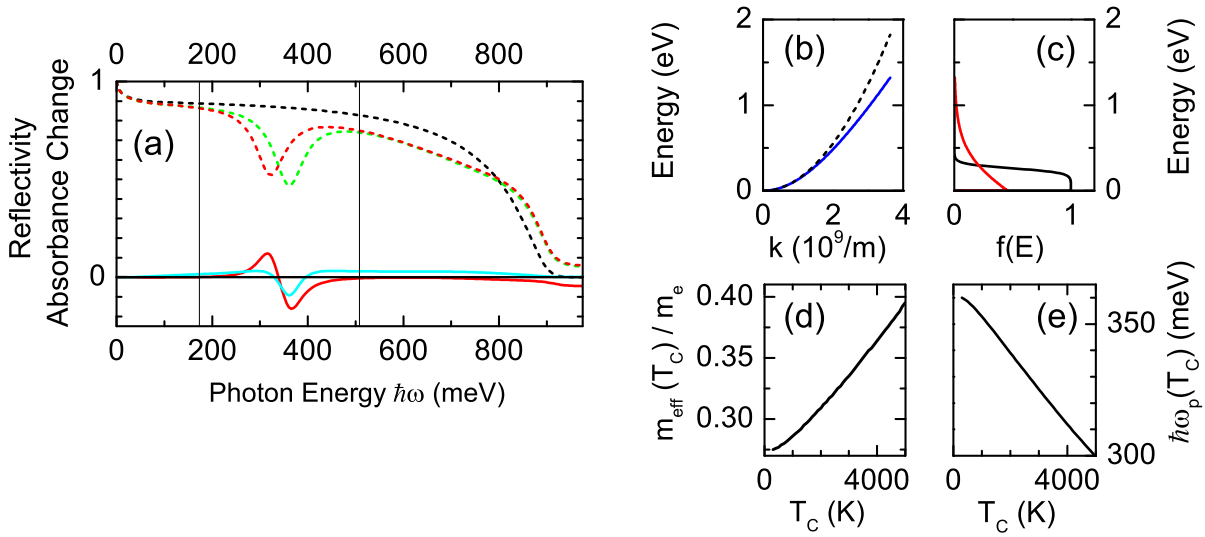

Figure 6.9: Model calculations for the nonlinear response of the bulk plasmon in the ZnO:Ga sample. (a) Shows the calculated reflectivities of a ZnO:Ga monolayer exhibiting an electron concentration of $N_e = 6 \cdot 10^{20}\,\mathrm{cm}^{-3}$ with a plasma frequency of 950 meV (black dashed line) and of a ZnO:Ga sandwich structure with a 100 nm thick layer on top, exhibiting an electron concentration of $N_e = 1 \cdot 10^{20}\,\mathrm{cm}^{-3}$ with a plasma frequency of $\hbar\omega_\mathrm{p}(300\,\mathrm{K}) = 360\,\mathrm{meV}$ (green dashed line), in agreement with the measured sample (cf. Fig. 6.3). The red dashed line shows the reflectivity of the sandwich structure with a heated electron gas in the upper layer ($\mathrm{T_C} = 3500\,\mathrm{K}$) and a correspondingly shifted plasma frequency of $\hbar\omega_\mathrm{p}(3500\,\mathrm{K}) = 320\,\mathrm{meV}$. The solid lines represent absorbance changes $\Delta\mathrm{A} = -\log(R/R_0)$. The red solid line shows a redshift of the plasma frequency, whereas the blue solid line shows a broadening of the plasma resonance. The thin vertical lines illustrate the spectral window measured in the pump/probe experiments. (b) Hyperbolic (blue line) vs. parabolic (dashed black line) band structure of ZnO around the conduction band minimum [271]. (c) Fermi distributions for a cold ($\mathrm{T_C} = 300\,\mathrm{K}$) (black line) and a hot ($\mathrm{T_C} = 3500\,\mathrm{K}$) (red line) electron plasma at a concentration of $N_e = 1 \cdot 10^{20}\,\mathrm{cm}^{-3}$ (upper layer of the sample). (d) Calculated zz-component of the effective electron mass for conduction band electrons in ZnO at different carrier temperatures. (e) Calculated energy of the plasma resonance $\hbar\omega_\mathrm{p}(\mathrm{T_C})$ for different carrier temperatures.

In Fig. 6.9 panel (b) there are two curves describing both, the hyperbolic band structure of ZnO with the model of Kane (blue) and, as a reference, the parabolic dispersion (black dashed). For small wave vectors $k < 1 \cdot 10^9\,\mathrm{m}^{-1}$, both models yield similar results, whereas increasing discrepancies become evident beyond $k = 1 \cdot 10^9\,\mathrm{m}^{-1}$, where the curve of the hyperbolic model exhibits a significantly smaller slope. A thermalised Fermi distribution of an electron plasma with a constant electron density of $N_\mathrm{e} = 1 \cdot 10^{20}\,\mathrm{cm}^{-3}$ at 300 K is shown as a black line in (c), together with a Fermi distribution of the same electron plasma at 3500 K (red line). These two temperatures describe the electron plasma during and directly after the excitation and after the full relaxation. Different electron

temperatures lead to different Fermi distributions and, thus, to different elongations in the hyperbolic band structure. The corresponding temperature dependent zz-component of the effective electron mass is given in (d) that undergoes an increase of about 50 % from 0.275 m_e to roughly 0.40 m_e between 300 K and 5000 K. Accordingly, the electron temperature dependent plasma frequency $\hbar\omega_p(T_c)$ decreases for higher temperatures from 360 meV at 300 K to about 300 meV at 5000 K.
Under utilisation of $A \propto \mathrm{Im}(1/\epsilon_c(\omega))$, the dielectric function $\epsilon_c(\omega)$ (eqn. (6.17)) is used in combination with the Fresnel equations to deduce reflectivity spectra for the experimentally measured multilayer ZnO:Ga structure (cf. Fig. 6.9 (a)). $A \propto \mathrm{Im}(1/\epsilon_c(\omega))$ is a good approximation as long as i) $d \ll \lambda$ is valid for the thickness of the top layer, and ii) the metallic bottom layer behaves like an ideal mirror, both is given by the measured sample and the experimental conditions. In the case of a non-ideal mirror and a larger layer thickness, the dispersive real part $\mathrm{Re}(1/\epsilon_c(\omega))$ contributes to the line shape of the bulk plasmon absorption resonance. In (a), the black dashed line shows the linear reflectivity spectrum of a bulk ZnO:Ga monolayer exhibiting an electron concentration of $N_e = 6 \cdot 10^{20}\,\mathrm{cm}^{-3}$ and an according plasma resonance at 950 meV. Once an additional 100 nm thick layer is located on top with $N_e = 1 \cdot 10^{20}\,\mathrm{cm}^{-3}$, a further plasma resonance occurs at $\hbar\omega_p = 360$ meV for an electron temperature of 300 K, due to absorption in this top layer (green dashed line). An increase of the electron temperature to 3500 K leads to a redshift of the plasma resonance in combination with a reduced oscillator strength (red dashed line). A numerical value of $\hbar\omega_p(3500\,\mathrm{K}) = 320$ meV and a ≈ 20 % reduced oscillator strength can be deduced.
The accompanied absorption change for electron temperatures of $T_C = 300$ K and $T_C = 3500$ K is illustrated as the red solid line in (a). It exhibits the characteristic bleaching around 360 meV and a redshifted enhanced absorption. Furthermore, the solid blue line illustrates the absorbance change for an increased momentum relaxation rate $\gamma_m(\mathbf{k})$ at a constant T_C that results in a spectral broadening with a bleaching around 360 meV and combined blue- and redshifted enhanced absorption.
So far, the model calculations have the increase of the ensemble-averaged effective electron mass and the resulting redshift of the plasma frequency identified to be the physical mechanism determining the nonlinear response of the bulk plasmon in ZnO:Ga. To account for the measured ultrafast relaxation timescale and to derive $\omega_p = \omega_p(T)$, the third step includes dynamical model calculations.

6.5.2 Carrier dynamics

Relaxation of the hot electrons and, thus, the time-dependent plasma frequency $\omega_p(T)$, is covered in the third step of the model calculations. Due to the pronounced polarity of the ionic crystal ZnO, a strong coupling among electrons and the lattice occurs. Hot electrons dissipate their excess energy via the emission of longitudinal optical (LO) phonons on a sub-ps to ps timescale, which changes over to the emission of acoustic phonons on a significantly slower timescale [288–290]. Hence, the dynamical model calculations need to comprise hot carrier relaxation in an electron-phonon plasma to reproduce the time-resolved pump/probe signals illustrated in Fig. 6.5. The model calculations discussed here rely on established theoretical methods that are described in detail in refs. [282, 291–296]. Quasielastic electron-electron and inelastic electron-LO phonon scattering are described using the loss-function concept that includes full dynamical screening in the plasma of coupled electrons and LO-phonons. Initially, scattering rates are derived on the basis of a general q- and ω-dependent dielectric function to deduce the energy loss of the hot

electrons and the time-dependent plasma temperature T_C. Then, the equation of motion for an anharmonic damped oscillator, which describes the dynamical behaviour of the bulk plasmon in the ZnO:Ga sample, is solved (cf. eqn. (6.6)).

I. Dielectric function and scattering rates

To account for the electron-phonon interaction, the more general ω- and q-dependent longitudinal dielectric function needs to be applied for the conduction band electrons in the ZnO:Ga sample that is given by [37, 293]

$$\epsilon(q,\omega,T_C) = \epsilon_\infty^c - \epsilon_\infty^c \frac{\omega_{TO}^2 - \omega_{LO}^2}{\omega_{TO}^2 - \omega^2} - \chi_{plasma}(q,\omega,T_C). \tag{6.20}$$

It is based on the random phase approximation (RPA) and exhibits three terms that contain the angular frequencies of transversal (ω_{TO} with $\hbar\omega_{TO} = 47\,\text{meV}$) as well as longitudinal optical (ω_{LO} with $\hbar\omega_{LO} = 72\,\text{meV}$) phonons and the plasma susceptibility χ_{plasma} [272, 293]. The first term ϵ_∞^c is a constant and describes the high-frequency limit. The second term is the frequency-dependent lattice susceptibility and contributes to the dielectric function via the polar TO- and LO-phonons. The last term covers the electron plasma and, next to ω, explicitly depends on the q-vector and the plasma temperature T_C. Thus, the approach includes coupling between the electron plasma and the optical phonons, so that effects, such as full dynamical screening, that are important for high plasma temperatures on the order of a couple of thousand Kelvin, are covered.
Due to the high doping concentration of the ZnO:Ga sample, electron-electron and electron-LO phonon scattering are the dominating scattering mechanisms, since they combine high scattering rates on the one hand and a large energy transfer per scattering event on the other hand [293]. Momentum and energy relaxation of the electron plasma can only occur due to inelastic electron-phonon scattering, because quasielastic electron-electron scattering preserves the total momentum of the electron plasma [297]. Considering the dielectric function eqn. (6.20), an electron at the wave vector $\mathbf{k}$ exhibits the scattering rate [293]

$$\begin{aligned} W(\mathbf{k}) &= \frac{2\pi}{\hbar}\int \frac{d^3\mathbf{q}}{(2\pi)^3}\frac{e^2}{\epsilon_0 q^2}\int_{-\infty}^{\infty}\frac{d\hbar\omega}{\pi}\left[n(\omega)+1\right]G(\mathbf{k},\mathbf{k}+\mathbf{q})\left[1-f(\mathbf{k}+\mathbf{q})\right] \\ &\quad\times\text{Im}\left[-\frac{1}{\epsilon(q,\omega,T_C)}\right]\delta\left[E(\mathbf{k}+\mathbf{q})-E(\mathbf{k})+\hbar\omega\right]. \end{aligned} \tag{6.21}$$

Next to the dielectric function $\epsilon(q,\omega,T_C)$, the scattering rate also depends on the G-factor $G(\mathbf{k},\mathbf{k}+\mathbf{q})$ that is the overlap of two electron wave functions with momentum $\mathbf{k}$ in the initial state and momentum $\mathbf{k}+\mathbf{q}$ in the final state, respectively, with peak value 1. Furthermore, $n(\omega)$ describes the Bose-Einstein factor and $f(\mathbf{k}+\mathbf{q})$ the distribution function in the final state. $E(\mathbf{k})$ and $E(\mathbf{k}+\mathbf{q})$ are given by the hyperbolic band structure eqn. (6.18). An integration over ω and $\mathbf{q}$ is necessary to include all possible frequencies and wave vectors of the coupled system of electrons and optical phonons.

II. Energy relaxation

According to the equation (6.21) for $W(\mathbf{k})$, the ensemble averaged energy loss rate per electron $\left\langle \frac{dE}{dt}(\mathrm{T_C}) \right\rangle_{\mathrm{loss}}$ can be deduced via multiplying the integrand of eqn. (6.21) with $\hbar\omega$ and subsequent integration over $\mathbf{k}$ and normalisation [293]

$$\left\langle \frac{dE}{dt}(\mathrm{T_C}) \right\rangle_{\mathrm{loss}} = \int d^3\mathbf{k} f(\mathbf{k}) R(\mathbf{k}) \Big/ \int d^3\mathbf{k} f(\mathbf{k}) \tag{6.22}$$

$$\begin{aligned} R(\mathbf{k}) = {} & \frac{2\pi}{\hbar} \int \frac{d^3\mathbf{q}}{(2\pi)^3} \frac{e^2}{\epsilon_0 q^2} \int_{-\infty}^{\infty} \hbar\omega \frac{d\hbar\omega}{\pi} \left[n(\omega)+1\right] G(\mathbf{k}, \mathbf{k}+\mathbf{q}) \left[1 - f(\mathbf{k}+\mathbf{q})\right] \\ & \times \mathrm{Im}\left[-\frac{1}{\epsilon(q,\omega,\mathrm{T_C})}\right] \delta\left[E(\mathbf{k}+\mathbf{q}) - E(\mathbf{k}) + \hbar\omega\right]. \end{aligned} \tag{6.23}$$

The distribution function of the electrons $f(\mathbf{k}) = f\left(\mathbf{k}, \mathrm{T_C}, \mu(\mathrm{T_C})\right)$ is assumed to be thermalised at any time, which is supported by the large momentum relaxation rate of $\gamma_{\mathrm{m}} < 10\,\mathrm{fs}^{-1}$ of the ZnO:Ga sample (cf. Fig. 6.3) and the 100 fs time resolution of the experiment. The amount of electrons in the plasma and the plasma density stays unaltered during the excitation and relaxation process. Thus, the electron distribution is determined by the plasma temperature $\mathrm{T_C}$ and the quasi Fermi level $\mu(\mathrm{T_C})$.
The calculated energy loss per electron of the excited electron plasma in the ZnO:Ga sample according to eqn. (6.22) is shown in Fig. 6.10 (a) and the cooling rate according to eqn. (9) in ref. [291] in (b). Both situations are discussed, energy loss and cooling rates with full dynamical screening and without screening. Heating is simulated corresponding to the experimental pump pulse parameters (cf. Figs. 6.4 and 6.5), whereas the multilayer system is described by Fresnel equations [37, 291].

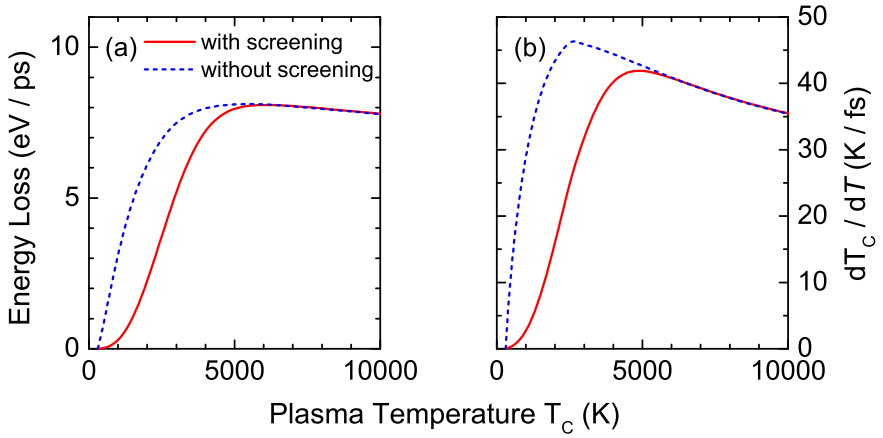

Figure 6.10: Dynamical model calculations for the energy loss (a) and the carrier cooling rate (b) per electron of the excited electron plasma in ZnO:Ga for plasma temperature $\mathrm{T_C}$ between 0 K and 10 000 K. The red solid lines illustrate the behaviour with full dynamical screening according to eqn. (6.20) and the blue dashed lines without screening, i.e., under neglect of χ_{plasma} in eqn. (6.20).

The energy loss as well as the cooling rate $\mathrm{dT_C}/\mathrm{d}T$ exhibit a strong plasma temperature dependence for considered and not considered screening. Both rise strongly up to $\approx$ 4000 K and slightly decrease for higher plasma temperatures. Very high energy loss rates of up to 8 eV/s around $\mathrm{T_C} = 4000$ K can be found as well as very high cooling rates of more than 40 K/fs for plasma temperatures around 3500 K. Screening plays a major role in the

relaxation process for plasma temperatures smaller than 5000 K. In this temperature range and especially below 1000 K, the plasma screens the interaction between electrons and LO phonons and leads to a reduced amount of emitted LO phonons and, thus, to smaller energy loss and cooling rates. While the plasma is very dense below 5000 K, it is diluted along the **k**-space for higher plasma temperatures, which consequently reduces the impact of screening and leads to the identical characteristics of the blue and red curves in Fig. 6.10 above 5000 K. Due to the applied hyperbolic band structure, the heat capacity of the electron plasma increases for high plasma temperatures, which results in the slight decrease of the energy loss and cooling rates above 5000 K.
From the cooling rate $\mathrm{d}T_\mathrm{C}/\mathrm{d}T$, one can deduce the temporal evolution of the plasma temperature $T_\mathrm{C}(T)$ via an integration over the delay time T. The resulting curve for $T_\mathrm{C}(T)$ is given in Fig. 6.11 (f).

III. Temporally and spectrally resolved response of the bulk plasmon

So far, the static and dynamical model calculations have shown how an excited (hot) electron plasma in the hyperbolic conduction band structure of ZnO around the conduction band minimum (Γ-point) modifies the optical properties of the bulk plasmon and how the electron plasma dissipates its absorbed excess energy. Strong pump pulses lead to an increased ($\approx 50\,\%$) and time-dependent effective electron mass $m_\mathrm{eff}(t)$ that causes the large spectral shift (≈ 50 meV) of the bulk plasmon frequency $\omega_\mathrm{p}(t)$ in Fig. 6.5. A pronounced coupling of the electron plasma to optical phonons in ZnO allows for a quick transfer of excess energy into the lattice on a ps-timescale which explains the vanishing measurement signals in the experiments after 2 ps. Thus, the equation of motion for a damped harmonic oscillator (cf. Sec. 6.1.2) with a time-dependent effective electron mass and a time-dependent coupling to the pump and probe light fields as well as to the emitted light field should model the measured dynamics of the bulk plasmon in ZnO:Ga. This approach is formulated with the following equations (6.24)-(6.28) [37].

$$\frac{\mathrm{d}\langle x_\mathrm{e}\rangle}{\mathrm{d}t} = \langle v_\mathrm{e}\rangle = \frac{\langle p_\mathrm{e}\rangle}{m_\mathrm{eff}(t)} \tag{6.24}$$

$$\frac{\mathrm{d}\langle p_\mathrm{e}\rangle}{\mathrm{d}t} = -\gamma_m\langle p_\mathrm{e}\rangle + eE_\mathrm{tot}(t) \tag{6.25}$$

$$= \overbrace{-\gamma_m\langle p_\mathrm{e}\rangle - \frac{N_\mathrm{e}e^2\langle x_e\rangle}{\epsilon_0\epsilon_\infty^c}}^{\text{damped bulk plasmon, cf. eqn. (6.6)}} + eE_\mathrm{loc}(t) \tag{6.26}$$

$$E_\mathrm{loc}(t) = (1+r_\mathrm{p})\sin(\Theta)\left[E_\mathrm{in}(t) + E_\mathrm{em}(t)\right] \tag{6.27}$$

$$E_\mathrm{em}(t) = -\frac{Z_0 d}{2}\tan(\Theta)N_\mathrm{e}e\langle v_\mathrm{e}(t)\rangle \tag{6.28}$$

As in Sec. 6.1.2, $\langle x_e\rangle$ and $\langle p_e\rangle$ denote the ensemble-averaged displacement of an electron in the plasma and its momentum, $\frac{N_\mathrm{e}e\langle x_e\rangle}{\epsilon_0\epsilon_\infty}$ describes the depolarisation field due to the displacement. The depolarisation field is a part of the total electric field $E_\mathrm{tot}(t)$ the electron plasma is interacting with. It further consists of the local optical field $E_\mathrm{loc}(t)$ to which the incident light field E_in contributes, as well as the re-emitted light field E_em originating from the induced plasma current. Because of the applied reflection geometry and the multilayer structure of the sample with the $d = 100$ nm thick layer on top of a highly reflecting bottom layer (cf. Figs. 6.3 and 3.7), E_em and E_in are reflected at the bottom layer. The corresponding reflection coefficient for p-polarised light fields and an angle

of incidence Θ ($\Theta = 45°$) is given by r_p. $Z_0 = 377\,\Omega$ denotes the vacuum impedance. An ultrashort pump pulse and ultrashort probe pulses (of 100 fs duration, respectively) at different delay times T were then applied to compute $E_{loc}(t,T)$ as a function of the real time t and the delay time T between pump and probe pulses and $E_{em}(t,T)$ that is generated by the plasma current in the 100 nm thick top layer. The small thickness d of the top layer fulfills the conditions for radiative coupling and damping to occur (just as in eqn. (5.15), Sec. 6.5.1), an effect covered by the chosen approach to solve the differential equation (6.25) and to calculate $E_{em}(t,T)$, which is based on a non-local Green's-function formalism [37, 298]. Eqn. (6.25) explicitly includes the time-dependent effective electron mass $m_{eff}(t)$ and, thus, the time-dependent plasma-frequency $\omega_p(t)$, so that a Fourier transformation of $E_{em}(t,T)$ along t should reproduce the spectrally resolved nonlinear dynamics of the bulk plasmon measured in Fig. 6.5 which is represented in the following Fig. 6.11.

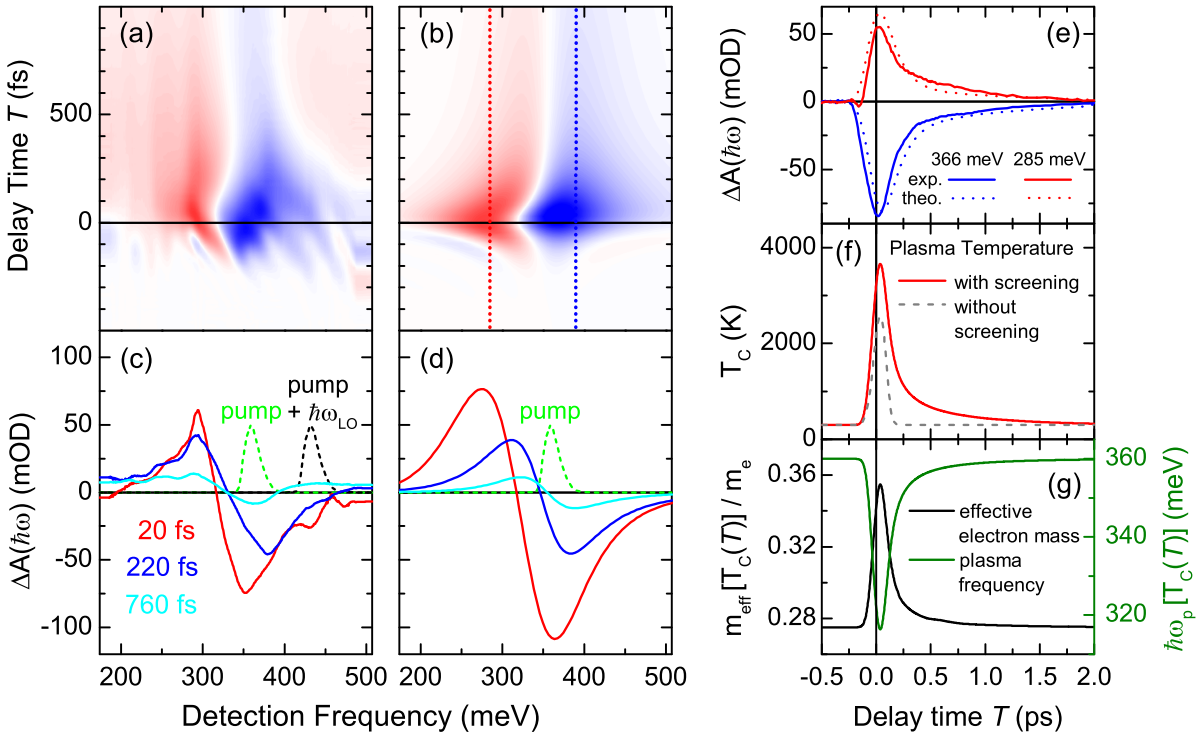

Figure 6.11: Panels (a,c) show an experimental contour plot and spectral cuts from Fig. 6.5. Panels (b,d) illustrate a theoretical contour plot and spectral cuts according to the model calculations, scale from −110 mOD to +110 mOD [37]. (e) Comparative plot between experimental transients (solid lines) and calculated transients (dotted lines) at fixed probe frequencies. The experimental curves are taken from Fig. 6.6 and the theoretical curves are from the labeled frequencies in (b). Panel (f) shows the time dependence of the calculated plasma temperature with and without screening. Panel (g) shows the calculated effective electron mass m_{eff} and the plasma frequency $\hbar\omega_p$ with respect to the delay time T.

Even though the model calculations do not contain any fit parameters, but only experimental parameters and ZnO-specific constants, such as the bandgap E_{gap}, the effective electron mass at the conduction band minimum $m^c_{eff}(0)$, the high frequency dielectric constant ϵ^c_∞, and the LO-, TO-phonon frequencies (ω_{LO}, ω_{TO}), the agreement between the measurement and the model calculations in (a) and (b) is convincing. Especially the dispersive shapes of the transient spectra and the temporal evolution of the plasma temperature agree very well with the measured transient spectra and transients. The plasma temperature is the driving magnitude in the investigated redshift of the plasmon

resonance. Its dynamics determine the temporal evolution of the effective electron mass and, thereby, the dynamics of the plasma frequency, as shown in (f) and (g). Heating of the plasma to 3500 K occurs on a 100 fs-timescale, according to the time resolution of the experiment that is implemented in the model calculations. The maximum of the plasma temperature is obtained briefly after $T = 0$ fs, due to the temporal extent of the pump pulse. Because of the strong coupling of the hot electron plasma to the optical phonons, a significant amount of absorbed pump pulse energy is dissipated into the ZnO lattice already during the heating process.
A free electron gas exhibits a heat capacity of $C_{\mathrm{el}} = \frac{\pi^2 N K_{\mathrm{B}} \mathrm{T}}{\mathrm{T_F}}$, with the amount of electrons N, the Boltzmann constant k_{B}, and the Fermi temperature $\mathrm{T_F}$ [228]. Regarding the absorption of 0.5 µJ pump pulse energy ($\approx$ 30 % of 1.8 µJ), an excited volume of 100 nm $\times$ $\pi \cdot (75\,\mu\mathrm{m})^2$, and the electron density of $N_e = 1 \cdot 10^{20}\,\mathrm{cm}^{-3}$, an electron temperature of several ten thousands Kelvin is expected, a value higher than the 3500 K discussed in Fig. 6.9 (f), underlining the immediate energy dissipation into the lattice. Electron temperature dependent loss rates of ≈ 50 K/fs are found and discussed in detail in Fig. 6.10.
Next to the immediate energy dissipation, a modified heat capacity of the electron gas in the doped ZnO determined by the hyperbolic band structure causes the large difference in the maximal plasma temperatures to a free electron gas.
The plasma temperature decreases from 3500 K to 1000 K within 300 fs. Below 1000 K, a strong screening of the interaction among electrons and phonons causes a substantially reduced cooling rate, induced by the plasma susceptibility $\chi_{\mathrm{plasma}}(q, \omega, \mathrm{T_C})$ with its $\mathrm{T_C}$-dependence (cf. eqn. (6.20)). The equilibrium temperature of 300 K is reached after 2 ps. Similar characteristics can be found for the transients in (e).
A significantly different temporal behaviour of the plasma temperature is obtained for deactivated screening, i.e., $\chi_{\mathrm{plasma}}(q, \omega, \mathrm{T_C}) = 0$ (dashed gray curve in (f)). There, the full electron-phonon interaction occurs over all temperatures and especially below 1000 K, such that an extremely efficient dissipation of excess energy into the ZnO lattice takes place on a sub-100 fs timescale. Consequently, the maximum plasma temperature does not reach 3500 K, but only 2600 K, and the equilibrium temperature is measured already after 250 fs. These characteristics are in strong contrast to the dynamics obtained in the experiments. Thus, screening within the electron-phonon-plasma plays a major role in the electron-phonon interaction and is essential to describe and understand the nonlinear response of the bulk plasmon in ZnO:Ga.
A difference between the model calculations and the measured nonlinear response is given by the approximately 40 % larger signal amplitude for the model calculations. An "ideal" metallic mirror underneath the 100 nm thick top layer in the model calculations in contrast to a "non-ideal" metallic mirror in the ZnO:Ga sample can cause such a difference. Furthermore, the model calculations do not include a broadening of the plasma absorption that occurs for $T > 500$ fs, due to a slight modification of γ_{m} in the experiments. Fingerprints of PFID are apparent for $T < 0$ fs in both cases, but are of different shape, respectively. The reason behind this is the dependence of the PFID on the probe pulse spectrum with its bandwidth and its central frequency [49]. In the experiment, probe pulses with 16 different centre frequencies were applied with spectral bandwidths of ≈ 35 meV, whereas in the calculations only one broad probe pulse with a bandwidth > 350 meV and a centre frequency of 360 meV was used.

6.6 Conclusions and outlook

A bulk plasmon in a tailored system of highly Ga-doped ZnO layers was studied with pump/probe methods in the IR spectral range. The special design of the investigated sample in combination with a reflection geometry enabled the direct measurement of the optical response of a longitudinal bulk plasmon.
Absorption of intense femtosecond pump pulses resonant to the bulk plasmon frequency lead to an interband excitation and, consequently, heating of conduction band electrons in ZnO while any intraband transitions were absent. Due to hyperbolic non-parabolicities in the conduction band of ZnO, the ensemble-averaged effective electron mass became dependent on the plasma temperature of the conduction band electrons. Maximal plasma temperatures of $\approx 3500\,\mathrm{K}$ were reached that resulted in a $\approx 50\,\mathrm{meV}$ redshited plasma frequency, in excellent agreement with performed model calculations. Due to large electron-electron scattering rates, thermalised Fermi distributions were measured at any time during the experiments. In contrast, a pronounced inelastic electron-phonon scattering facilitated momentum- and energy relaxation into the phonon bath of ZnO on a 300 fs-timescale, accompanied by a regression of the redshift and a persisting broadening of the plasma resonance. No nonlinear signals were measurable beyond a delay time of 2 ps. Furthermore, a coherently excited longitudinal optical phonon side band was measured within the plasmon absorption.
Reference measurements on doped and undoped ZnO monolayers featured more than one order of magnitude smaller responses with qualitatively different spectral shapes. Investigations on the ZnO sandwich structure with s/s-polarisation revealed likewise much smaller nonlinear responses so that the performed reference measurements can experimentally underline the direct addressing of the longitudinal bulk plasmon in the main experiments.

The strong nonlinear response of the layered Ga-doped ZnO system offers the possibility for a manifold of applications. The tunable intrinsic bulk plasmon frequency (by changing the doping concentrations), in combination with the controllable transient shift of the plasma frequency, could be used to tailor a switchable coupling between bulk plasmons and molecular excitations. Molecules on top of the ZnO:Ga sample with preferentially polar vibrations (such as e.g. phosphate or carbonyl vibrations) could be resonantly excited by a transient shift of the bulk plasmon frequency. A bulk plasmon pump/molecular vibration probe experiment could reveal the transient existence of such a "hybrid particle" consisting of a collective electron oscillation, a light field, and a molecular vibration.
A further application is an ultrafast polarisation switch. The p-polarisation sensitive plasmon absorption could be used to control the polarisation of a non-polarised cw light beam. For an unexcited bulk plasmon, the cw light beam would exhibit an s-polarisation after a resonant interaction with the bulk plasmon, due to absorption of the p-components. Once the plasma frequency is shifted by a strong optical excitation, no absorption and, hence, no polarisation of the cw light beam would occur. As shown by the $\approx 300\,\mathrm{fs}$ timescale in the experiments, a clearly sub-ps polarisation switch is possible in this way.
As documented with these two examples, a lot of continuative investigations are thinkable that do not only cover the field of "plasmonics", but can also enter neighboring disciplines, such as ultrafast vibrational spectroscopy.

7 Summary

In this work, the vibrational dynamics of dissolved $H_2PO_4^-$ and BH_4^- ions and of BH_4^- ions in a crystalline environment were studied with methods of linear infrared and nonlinear infrared spectroscopy in the femtosecond range. Furthermore, the nonequilibrium dynamics of a bulk plasmon in an n-doped ZnO layer system were investigated.

Phosphates are important building blocks of biomolecules, such as DNA or phospholipids, and constitute their major hydration sites. Hence, a strong interaction occurs among phosphates and their surrounding water shells, allowing for a mapping of hydrogen bond dynamics and structural fluctuations within the network of water molecules. Here, phosphate vibrations of the ion $H_2PO_4^-$ in an aqueous solution are introduced as local probes for the full spectrum of bulk water fluctuations, in contrast to phosphate vibrations at interfacial sites that are local probes for decelerated water dynamics. In 2D-IR experiments on a 1 M KDP solution in a free standing liquid jet, homogeneously broadened line shapes are observed for the asymmetric and symmetric phosphate vibrations $\nu_{\mathrm{AS}}(PO_2^-)$ and $\nu_{\mathrm{S}}(PO_2^-)$ with an underlying correlation time of 50 fs determined by ultrafast librational water dynamics. A second infinitely large correlation time is measured, which describes a weak inhomogeneous contribution resulting from quasi-static spatial configurations of the phosphate-water system. Vibrational lifetimes of ≈ 300 fs are measured for the first excited states of $\nu_{\mathrm{AS}}(PO_2^-)$, $\nu_{\mathrm{S}}(PO_2^-)$, the asymmetric and symmetric P-$(OH)_2$ bending vibrations, and 400 fs for the first excited state of the asymmetric P-$(OH)_2$ stretching vibration. Cluster calculations reveal hydrogen bonds between phosphate and water molecules to be stronger than between water molecules, manifested e.g. by enhanced hydrogen bond lifetimes of ≈ 10 ps. The PO_2^- coordination site forms on average 6.5 hydrogen bonds and, thereby, more than the P-$(OH)_2$ coordination site with 1.9 hydrogen bonds. Furthermore, the asymmetric phosphate vibration $\nu_{\mathrm{AS}}(PO_2^-)$ has been identified to be very sensitive on structural fluctuations and heat jumps of the surrounding water. Consequently, even though phosphate vibrations of $H_2PO_4^-$ have a small diagonal anharmonicity of $\approx 10\,\mathrm{cm}^{-1}$, they are suitable local probes for bulk water fluctuations.

$NaBH_4$ as a complex hydride is a potential hydrogen and, thus, energy carrier for mobile applications. It combines two crucial properties: i) a large volumetric hydrogen content as well as ii) a low overall mass, especially in comparison to intermetallic compounds containing absorbed hydrogen. To get a detailed microscopic understanding of B-H vibrations and, therewith, of hydrogen dynamics, BH_4^- ions dissolved in a liquid solution and embedded in the crystalline environment $NaBH_4$ were investigated. A strong Fermi resonance coupling of the asymmetric BH_4^- stretching vibration ν_3 with the first overtone of the asymmetric BH_4^- bending vibration ν_4 allows for the dissipation of vibrational excess energy from ν_3 over ν_4 into either the vibrational manifold of the solvent or the low-frequency phonon modes of $NaBH_4$, revealed by two-colour pump/probe measure-

ments. In one-colour pump/probe measurements, a 3.0 ps lifetime of $\nu_3(v = 1)$ and a 3.6 ps lifetime of $\nu_4(v = 1)$ are observed. Due to the high packing density of BH_4^- tetrahedrons in the $NaBH_4$ crystal and the thin film geometry of the measured sample, a radiative coupling occurs among them, which leads to a quick reemission of absorbed excess energy on a sub-500 fs timescale. Furthermore, a strong anharmonic coupling of excited low-frequency modes in $NaBH_4$ to ν_3 and ν_4 leads to much more intense thermal pump/probe signatures in the $NaBH_4$ crystal compared to the liquid solution.

Bulk plasmons represent collective longitudinal excitations of free electron gases in ionic or polar crystal lattices. In contrast to widely explored surface plasmon polaritons, the nonlinear response of bulk plasmons with optical methods and a femtosecond time resolution has not been investigated so far, but is very meaningful for ultrafast applications. A bulk plasmon resonance of a highly Ga-doped ZnO layer in a particularly designed layer system was investigated in reflection geometry. Intraband excitation of conduction band electrons in ZnO leads to a heating of the electron gas. Due to hyperbolic non-parabolicities in the conduction band structure of ZnO, the heating results in an increase of the ensemble averaged electron mass and, thus, to a reduction (or redshift) of the bulk plasmon frequency. Momentum redistribution in the heated electron gas occurs within $\approx$ 10 fs caused by the large density ($1 \cdot 10^{20}\,cm^{-3}$) of the electron gas, so that only thermalised Fermi-distributions were measured. A strong polar-optical coupling of the electron gas with longitudinal optical phonons in ZnO allowed for the relaxation of excess energy via the emission of longitudinal optical phonons on a 300 fs timescale. The time-dependent redshift is accompanied by a broadening of the plasma resonance. All nonlinear signals decayed completely within 2 ps.

These studies underline the multifacetedness of IR spectroscopy to gain e.g. detailed microscopic insights into the ultrafast structural fluctuation dynamics of $H_2PO_4^-$ ions in liquid water, into B-H dynamics in complex metal hydrides, and into the dynamics of collective longitudinal charge oscillations in Ga-doped ZnO layers.

Zusammenfasung

In dieser Arbeit wurden mit Methoden der linearen Infrarotspektroskopie und nichtlinearen Infrarotspektroskopie im Femtosekundenbereich die Schwingungsdynamiken von $H_2PO_4^-$- und BH_4^- Ionen in flüssiger und, für BH_4^-, in kristalliner Umgebung untersucht. Ein weiteres Thema war die Nichtgleichgewichtsdynamik des Volumenplasmons in einem n-dotierten ZnO-Schichtsystem. In den Experimenten wurden Anrege/Abfrage-Techniken und Methoden der zweidimensionalen Spektroskopie eingesetzt.

Phosphate sind wesentliche, strukturgebende Einheiten von Biomolekülen wie DNS oder Phospholipiden und bilden deren vorrangige Hydratisierungsstellen. Daher wechselwirken sie intensiv mit den wässrigen Solvatationsschalen und erlauben somit die Abbildung von Wasserstoffbrückenbindungsdynamiken und strukturellen Fluktuationen im Wassernetzwerk. In dieser Arbeit wurden die Phosphatschwingungen des Ions $H_2PO_4^-$ in wässriger Lösung als lokale Sonden für das volle Spektrum von Volumenfluktuationen des Wassers eingeführt, die eine Referenz bilden zu Phosphatschwingungen an Grenzflächen, an denen Wasser eine verlangsamte Fluktuationsdynamik aufweist. Mit Hilfe von 2D-IR Experimenten, in denen eine 1 M KDP Lösung in einem freistehenden Flüssigkeitsfilm gemessen wurde, konnten homogen verbreiterte Linienformen für die asymmetrischen und symmetrischen Phosphatschwingungen $\nu_{AS}(PO_2^-)$ und $\nu_S(PO_2^-)$ gemessen werden,

denen eine 50 fs Korrelationszeit zu Grunde liegt. Eine weitere, unendlich große Korrelationszeit beschreibt eine schwache, quasistatische räumliche Anordnung des Phosphat-Wasser-Systems. Schwingungslebensdauern von ≈ 300 fs wurden für die ersten angeregten Zustände der asymmetrischen Phosphatschwingung $\nu_{\mathrm{AS}}(\mathrm{PO_2^-})$ und der symmetrischen Phosphatschwingung $\nu_{\mathrm{S}}(\mathrm{PO_2^-})$ sowie der asymmetrischen und symmetrischen P-$(\mathrm{OH})_2$ Biegemode gemessen. Eine 400 fs Schwingungslebensdauer konnte für den ersten angeregten Zustand der asymmetrischen P-$(\mathrm{OH})_2$ Streckschwingung ermittelt werden. Cluster-Rechnungen haben ergeben, dass die Wasserstoffbrückenbindungen zwischen Phosphat- und Wassermolekülen stärker ausgeprägt sind als zwischen Wassermolekülen, was u. a. durch eine erhöhte Bindungslebensdauer von ≈ 10 ps belegt werden konnte. Im Mittel werden 6.5 Wasserstoffbrückenbindungen an der $\mathrm{PO_2^-}$ Koordinationsseite gebildet und damit mehr als an der P-$(\mathrm{OH})_2$ Koordinationsseite, die 1.9 Wasserstoffbrückenbindungen aufweist. Darüber hinaus konnte gezeigt werden, dass die asymmetrische Phosphatschwingung $\nu_{\mathrm{AS}}(\mathrm{PO_2^-})$ sehr empfindlich auf strukturelle Veränderungen und Temperaturschwankungen in der Solvatationshülle reagiert. Damit sind Phosphatschwingungen trotz ihrer geringen diagonalen Anharmonizitäten von etwa $10\,\mathrm{cm^{-1}}$ geeignete Sonden, um die volle Fluktuationsdynamik von Volumenwasser zu erfassen.

$\mathrm{NaBH_4}$ gehört zur Stoffklasse der komplexen Hydride und ist ein potenzieller Wasserstoff- und damit Energieträger für Anwendungen, die eine große Mobilität benötigen. Es kombiniert zwei wesentliche Eigenschaften: i) einen großen volumetrischen Wasserstoffanteil sowie ii) eine niedrige Masse, insbesonders im direkten Vergleich mit intermetallischen Verbindungen, in denen Wasserstoff absorbiert wurde. Um ein detailliertes Verständnis von B-H Schwingungen und damit Wasserstoffdynamiken zu erzielen, wurden $\mathrm{BH_4^-}$ Ionen in flüssiger Lösung und in kristalliner Umgebung, eingebettet in $\mathrm{NaBH_4}$, untersucht. Eine starke Fermi-Resonanz Kopplung zwischen der asymmetrischen $\mathrm{BH_4^-}$ Streckschwingung ν_3 und dem ersten Überton der asymmetrischen Biegeschwingung ν_4 erlaubt eine Umverteilung von Schwingungsenergie von ν_3 nach ν_4 mit anschließender Dissipation in die Badmoden des Lösungsmittels oder niederfrequente Phononenmoden des $\mathrm{NaBH_4}$ Kristalls, was durch Zwei-Farben Anrege/Abfrage Messungen direkt belegt werden konnte. Mit Hilfe von Ein-Farben Anrege/Abfrage Experimenten konnten Schwingungslebensdauern von 3.0 ps für $\nu_3(\mathrm{v}=1)$ und 3.6 ps für $\nu_4(\mathrm{v}=1)$ gefunden werden. Aufgrund der hohen Packungsdichte von $\mathrm{BH_4^-}$ Tetraedern im $\mathrm{NaBH_4}$ Kristall und der Dünnschichtgeometrie der untersuchten Probe kam es zu einer radiativen Kopplung zwischen den Tetraedern, die zu einer schnellen Reemission von absorbierter Schwingungsenergie auf einer sub-500 fs Zeitskala führte. Darüber hinaus wurden deutlich ausgeprägtere thermische Anrege/Abfrage Signaturen im $\mathrm{NaBH_4}$ Kristall gemessen als in der Lösung, die auf eine starke anharmonische Kopplung von ν_3 und ν_4 mit angeregten niederfrequenten Phononenmoden zurückgeführt werden konnten.

Volumenplasmonen repräsentieren kollektive, longitudinale Anregungen eines freien Elektronengases in ionischen oder polaren Kristallstrukturen. Im Gegensatz zu intensiv studierten Oberflächen-Plasmon-Polaritonen ist die nichtlineare Antwort eines Volumenplasmons mit optischen Methoden und einer Femtosekunden-Zeitauflösung noch nicht untersucht worden, obwohl sie Potenzial für eine Vielzahl von Anwendungen bietet. In einer hoch Ga-dotierten ZnO-Schicht eines speziell entworfenen Schichtsystems konnte ein Volumenplasmon in Reflektionsgeometrie optisch angeregt werden. Dabei führte die Intrabandanregung von Leitungsbandelektronen zur Erhitzung des Elektronengases. Hyperbolische Nichtparabolizitäten in der Leitungsbandstruktur von ZnO resultierten in

einer Erhöhung des Kollektivmittelwerts der Masse der erhitzten Leitungsbandelektronen, welche eine Reduzierung bzw. Rotverschiebung der Plasmafrequenz des Volumenplasmons bewirkten. Impulsumverteilung innerhalb des aufgeheizten Elektronengases erfolgte auf einer 10 fs Zeitskala, so dass zu jedem Zeitpunkt thermalisierte Fermiverteilungen gemessen wurden. Aufgrund von starker polar-optischer Kopplung des Elektronengases mit longitudinal optischen Phononen im ZnO kam es zu einer Energierelaxation auf einer 300 fs Zeitskala. Eine Verbreiterung der Plasmaresonanz wurde neben der Rotverschiebung festgestellt. Nach einer Wartezeit von 2 ps waren alle nichtlinearen Messsignale zerfallen.

Mit diesen Untersuchungen konnte u. a. das Facettenreichtum von IR-Spektroskopie demonstriert werden, mit der es möglich war, detaillierte Einsichten in die ultraschnelle Fluktuationsdynamik von $H_2PO_4^-$ Ionen in wässriger Lösung zu erlangen, in B-H Dynamiken von komplexen Metallhydriden und in die Dynamiken von kollektiven longitudinalen Ladungsdichteschwankungen in einem stark Ga-dotierten ZnO-Schichtsystem.

Bibliography

[1] J. M. Chalmers and P. R. Griffiths, *Handbook of Vibrational Spectroscopy*, vol. 1. Chichester, UK: Wiley, 2002.

[2] P. Hamm and M. Zanni, *Concepts and Methods of 2D Infrared Spectroscopy*, vol. 1. USA, New York: Cambridge University Press, 2011.

[3] R. A. Kaindl, *Ultrafast mid-infrared studies of low-energy excitations in solids*. PhD thesis, Humboldt-Universität zu Berlin, 2000.

[4] R. A. Kaindl, M. Woerner, T. Elsaesser, D. C. Smith, J. F. Ryan, G. A. Farnan, M. P. McCurry, and D. G. Walmsley, "Ultrafast mid-infrared response of $YBa_2Cu_3O_{7-\delta}$," *Science*, vol. 287, no. 5452, pp. 470–473, 2000.

[5] N. W. Ashcroft and N. D. Mermin, *Solid State Physics*. Cornell University: Harcourt College Publishers, 1976.

[6] T. Elsaesser and W. Kaiser, "Visible and infrared spectroscopy of intramolecular proton transfer using picosecond laser pulses," *Chem. Phys. Lett.*, vol. 128, no. 3, pp. 231–237, 1986.

[7] D. Kraemer, M. L. Cowan, A. Paarmann, N. Huse, E. T. J. Nibbering, T. Elsaesser, and R. J. D. Miller, "Temperature dependence of the two-dimensional infrared spectrum of liquid H_2O," *Proc. Natl. Acad. Sci. USA*, vol. 105, no. 2, pp. 437–442, 2008.

[8] M. L. Cowan, B. D. Bruner, N. Huse, J. R. Dwyer, B. Chugh, E. T. J. Nibbering, T. Elsaesser, and R. J. D. Miller, "Ultrafast memory loss and energy redistribution in the hydrogen bond network of liquid H_2O," *Nature*, vol. 434, no. 7030, pp. 199–202, 2005.

[9] Ł. Szyc, M. Yang, E. T. J. Nibbering, and T. Elsaesser, "Ultrafast vibrational dynamics and local interactions of hydrated DNA," *Angew. Chem. Int. Ed.*, vol. 49, no. 21, pp. 3598–3610, 2010.

[10] N. Del Fatti, C. Voisin, M. Achermann, S. Tzortzakis, D. Christofilos, and F. Vallée, "Nonequilibrium electron dynamics in noble metals," *Phys. Rev. B*, vol. 61, no. 24, pp. 16956–16966, 2000.

[11] A. Furube, L. Du, K. Hara, R. Katoh, and M. Tachiya, "Ultrafast plasmon-induced electron transfer from gold nanodots into TiO_2 nanoparticles," *J. Am. Chem. Soc.*, vol. 129, no. 48, pp. 14852–14853, 2007.

[12] V. I. Klimov, C. J. Schwarz, D. W. McBranch, C. A. Leatherdale, and M. G. Bawendi, "Ultrafast dynamics of inter- and intraband transitions in semiconductor nanocrystals: Implications for quantum-dot lasers," *Phys. Rev. B*, vol. 60, no. 4, pp. R2177–R2180, 1999.

[13] J. Wang, M. W. Graham, Y. Ma, G. R. Fleming, and R. A. Kaindl, "Ultrafast spectroscopy of midinfrared internal exciton transitions in separated single-walled carbon nanotubes," *Phys. Rev. Lett.*, vol. 104, no. 17, p. 177401, 2010.

[14] B. L. Wehrenberg, C. Wang, and P. Guyot-Sionnest, "Interband and intraband optical studies of PbSe colloidal quantum dots," *J. Phys. Chem. B*, vol. 106, no. 41, pp. 10634–10640, 2002.

[15] S. Mukamel, *Principles of Nonlinear Optical Spectroscopy*. United States of America, New York: Oxford University Press, 1995.

[16] G. Herzberg, *Molecular Spectra and Molecular Structure II. Infrared and Raman Spectra of Polyatomic Molecules*. Princeton, New York, Toronto, London: D. Van Nostrand Company, Inc., 1945.

[17] R. W. Boyd, *Nonlinear Optics*. United States of America, New York: Academic Press, Elsevier, 2008.

[18] C. Ropers, D. J. Park, G. Stibenz, G. Steinmeyer, J. Kim, D. S. Kim, and C. Lienau, "Femtosecond light transmission and subradiant damping in plasmonic crystals," *Phys. Rev. Lett.*, vol. 94, no. 11, p. 113901, 2005.

[19] T. Stroucken, A. Knorr, P. Thomas, and S. W. Koch, "Coherent dynamics of radiatively coupled quantum-well excitons," *Phys. Rev. B*, vol. 53, no. 4, pp. 2026–2033, 1996.

[20] T. Shih, K. Reimann, M. Woerner, T. Elsaesser, I. Waldmüller, A. Knorr, R. Hey, and K. H. Ploog, "Nonlinear response of radiatively coupled intersubband transitions of quasi-two-dimensional electrons," *Phys. Rev. B*, vol. 72, no. 19, p. 195338, 2005.

[21] W. Kuehn, P. Gaal, K. Reimann, M. Woerner, T. Elsaesser, and R. Hey, "Coherent ballistic motion of electrons in a periodic potential," *Phys. Rev. Lett.*, vol. 104, no. 14, p. 146602, 2010.

[22] L. Allen and J. H. Eberly, *Optical Resonance and Two-Level Atoms*. New York: Dover Publications, Inc., 1987.

[23] P. Bowlan, E. Martinez-Moreno, K. Reimann, M. Woerner, and T. Elsaesser, "Terahertz radiative coupling and damping in multilayer graphene," *New J. Phys.*, vol. 16, no. 1, p. 013027, 2014.

[24] R. Friedberg and S. R. Hartmann, "Superradiant damping and absorption," *Phys. Lett. A*, vol. 37, no. 4, pp. 285–286, 1971.

[25] R. Friedberg and S. R. Hartmann, "Superradiant lifetime: Its definitions and relation to absorption length," *Phys. Rev. A*, vol. 13, no. 1, pp. 495–496, 1976.

[26] J. A. White, E. Schwegler, G. Galli, and F. Gygi, "The solvation of Na^+ in water: First-principles simulations," *J. Chem. Phys.*, vol. 113, no. 11, p. 4668, 2000.

[27] M. F. Kropman and H. J. Bakker, "Dynamics of water molecules in aqueous solvation shells," *Science*, vol. 291, no. 5511, pp. 2118–2120, 2001.

[28] E. T. J. Nibbering and T. Elsaesser, "Ultrafast vibrational dynamics of hydrogen bonds in the condensed phase," *Chem. Rev.*, vol. 104, no. 4, pp. 1887–1914, 2004.

[29] R. Kubo, "A stochastic theory of line shape," *Adv. Chem. Phys.*, vol. 15, pp. 101–127, 1969.

[30] A. J. Lock, *Ultrafast vibrational dynamics of water*. PhD thesis, University of Amsterdam, 2004.

[31] R. Costard, *Ultrafast Dynamics of Phospholipid-Water Interfaces Studied by Nonlinear Time-Resolved Vibrational Spectroscopy*. PhD thesis, Humboldt-Universität zu Berlin, 2014.

[32] M. D. Fayer, "Dynamics of molecules in condensed phases: Picosecond holographic grating experiments," *Ann. Rev. Phys. Chem.*, vol. 33, pp. 63–87, 1982.

[33] K. Duppen and D. A. Wiersma, "Picosecond multiple-pulse experiments involving spatial and frequency gratings: a unifying nonperturbational approach," *J. Opt. Soc. Am. B*, vol. 3, no. 4, pp. 614–621, 1986.

[34] R. Costard, I. A. Heisler, and T. Elsaesser, "Structural dynamics of hydrated phospholipid surfaces probed by ultrafast 2D spectroscopy of phosphate vibrations," *J. Phys. Chem. Lett.*, vol. 5, no. 3, pp. 506–511, 2014.

[35] N. A. Kurnit, I. D. Abella, and S. R. Hartmann, "Observation of a photon echo," *Phys. Rev. Lett.*, vol. 13, no. 19, pp. 567–568, 1964.

[36] N. Huse, *Multidimensional Vibrational Spectroscopy of Hydrogen-Bonded Systems in the Liquid Phase: Coupling Mechanisms and Structural Dynamics*. PhD thesis, Humboldt-Universität zu Berlin, 2006.

[37] T. Tyborski, S. Kalusniak, S. Sadofev, F. Henneberger, M. Woerner, and T. Elsaesser, "Ultrafast nonlinear response of bulk plasmons in highly doped ZnO layers," *Phys. Rev. Lett.*, vol. 115, no. 14, p. 147401, 2015.

[38] W. T. Pollard, S. L. Dexheimer, Q. Wang, L. A. Peteanu, C. V. Shank, and R. A. Mathies, "Theory of dynamic absorption spectroscopy of nonstationary states. 4. application to 12-fs resonant impulsive Raman spectroscopy of bacteriorhodopsin," *J. Phys. Chem.*, vol. 96, no. 15, pp. 6147–6158, 1992.

[39] M. Khalil, N. Demirüven, and A. Tokmakoff, "Obtaining absorptive line shapes in two-dimensional infrared vibrational correlation spectra," *Phys. Rev. Lett.*, vol. 90, no. 4, p. 047401, 2003.

[40] M. Yang, *Ultrafast two-dimensional infrared spectroscopy of hydrogen-bonded systems in the liquid phase: Coupling mechanisms and structural dynamics*. PhD thesis, Humboldt-Universität zu Berlin, 2012.

[41] C. Greve, *Ultrafast vibrational dynamics of nucleobases and base pairs in solution and DNA oligomers*. PhD thesis, Humboldt-Universität zu Berlin, 2014.

[42] L. Lepetit, G. Chériaux, and M. Joffre, "Linear techniques of phase measurement by femtosecond spectral interferometry for applications in spectroscopy," *J. Opt. Soc. Am. B*, vol. 12, no. 12, pp. 2467–2474, 1995.

[43] A. Tokmakoff, "Two-dimensional line shapes derived from coherent third-order nonlinear spectroscopy," *J. Phys. Chem. A*, vol. 104, no. 18, pp. 4247–4255, 2000.

[44] E. R. Andresen, R. Gremaud, A. Borgschulte, A. J. Ramirez-Cuesta, A. Züttel, and P. Hamm, "Vibrational dynamics of $LiBH_4$ by infrared pump-probe and 2-D spectroscopy," *J. Phys. Chem. A*, vol. 113, no. 46, pp. 12838–12846, 2009.

[45] R. Costard, C. Greve, I. A. Heisler, and T. Elsaesser, "Ultrafast energy redistribution in local hydration shells of phospholipids: A two-dimensional infrared study," *J. Phys. Chem. Lett.*, vol. 3, no. 23, pp. 3646–3651, 2012.

[46] W. Kaiser, *Ultrashort Laser Pulses and Applications*, vol. 60. Springer-Verlag Berlin Heidelberg, 1988.

[47] M. Rini, *Femtosecond Mid-Infrared Spectroscopy of Elementary Photoinduced Reactions*. PhD thesis, Humboldt-Universität zu Berlin, 2003.

[48] M. Chachisvilis, H. Fidder, and V. Sundström, "Electronic coherence in pseudo two-colour pump-probe spectroscopy," *Chem. Phys. Lett.*, vol. 234, no. 1-3, pp. 141–150, 1995.

[49] P. Hamm, "Coherent effects in femtosecond infrared spectroscopy," *Chem. Phys.*, vol. 200, pp. 415–429, 1995.

[50] P. F. Moulton, "Spectroscopic and laser characteristics of Ti:Al_2O_3," *J. Opt. Soc. Am. B*, vol. 3, no. 1, pp. 125–133, 1986.

[51] D. E. Spence, P. N. Kean, and W. Sibbett, "60-fsec pulse generation from a self-mode-locked Ti:sapphire laser," *Opt. Lett.*, vol. 16, no. 1, pp. 42–44, 1991.

[52] R. A. Kaindl, D. C. Smith, M. Joschko, M. P. Hasselbeck, M. Woerner, and T. Elsaesser, "Femtosecond infrared pulses tunable from 9 to 18 μm at an 88-MHz repetition rate," *Opt. Lett.*, vol. 23, no. 11, pp. 861–863, 1998.

[53] R. A. Kaindl, F. Eickemeyer, M. Woerner, and T. Elsaesser, "Broadband phase-matched difference frequency mixing of femtosecond pulses in GaSe: Experiment and theory," *Appl. Phys. Lett.*, vol. 75, no. 8, pp. 1060–1062, 1999.

[54] R. A. Kaindl, M. Wurm, K. Reimann, P. Hamm, A. M. Weiner, and M. Woerner, "Generation, shaping, and characterization of intense femtosecond pulses tunable from 3 to 20 μm," *J. Opt. Soc. Am. B*, vol. 17, no. 12, pp. 2086–2094, 2000.

[55] K. W. DeLong, R. Trebino, and D. J. Kane, "Comparison of ultrashort-pulse frequency-resolved-optical-gating traces for three common beam geometries," *J. Opt. Soc. Am. B*, vol. 11, no. 9, pp. 1595–1608, 1994.

[56] J. Ratner, G. Steinmeyer, T. C. Wong, R. Bartels, and R. Trebino, "Coherent artifact in modern pulse measurements," *Opt. Lett.*, vol. 37, no. 14, pp. 2874–2876, 2012.

[57] M. L. Cowan, J. P. Ogilvie, and R. J. D. Miller, "Two-dimensional spectroscopy using diffractive optics based phased-locked photon echoes," *Chem. Phys. Lett.*, vol. 386, no. 1-3, pp. 184–189, 2004.

[58] M. J. Tauber, R. A. Mathies, X. Chen, and S. E. Bradforth, "Flowing liquid sample jet for resonance Raman and ultrafast optical spectroscopy," *Rev. Sci. Instrum.*, vol. 74, no. 11, p. 4958, 2003.

[59] S. Sadofev, S. Kalusniak, P. Schäfer, and F. Henneberger, "Molecular beam epitaxy of n-Zn(Mg)O as a low-damping plasmonic material at telecommunication wavelengths," *Appl. Phys. Lett.*, vol. 102, no. 18, p. 181905, 2013.

[60] P. Halevi, "Electromagnetic wave propagation at the interface between two conductors," *Phys. Rev. B*, vol. 12, no. 10, pp. 4032–4035, 1975.

[61] S. Campione, I. Brener, and F. Marquier, "Theory of epsilon-near-zero modes in ultrathin films," *Phys. Rev. B*, vol. 91, no. 12, p. 121408(R), 2015.

[62] S. Kalusniak, S. Sadofev, and F. Henneberger, "ZnO as a tunable metal: New types of surface plasmon polaritons," *Phys. Rev. Lett.*, vol. 112, no. 13, p. 137401, 2014.

[63] S. Kalusniak, S. Sadofev, and F. Henneberger, "Resonant interaction of molecular vibrations and surface plasmon polaritons: The weak coupling regime," *Phys. Rev. B*, vol. 90, no. 12, p. 125423, 2014.

[64] D. Thomas, "Infrared absorption in zinc oxide crystals," *J. Phys. Chem. Solids*, vol. 10, no. 1, pp. 47–51, 1959.

[65] J. Mao, Z. Guo, I. P. Nevirkovets, H. K. Liu, and S. X. Dou, "Hydrogen de-/absorption improvement of $NaBH_4$ catalyzed by titanium-based additives," *J. Phys. Chem. C*, vol. 116, no. 1, pp. 1596–1604, 2012.

[66] C. J. H. Schutte, "The infra-red spectrum of thin films of sodium borohydride," *Spectrochim. Acta*, vol. 16, pp. 1054–1059, 1960.

[67] R. Cooke and I. D. Kuntz, "The properties of water in biological systems," *Annu. Rev. Biophys. Bioeng.*, vol. 3, pp. 95–126, 1974.

[68] G. Ling, "What determines the normal water content of a living cell?," *Physiol. Chem. Phys. & Med. NMR*, vol. 36, pp. 1–19, 2004.

[69] E. Gouaux and R. MacKinnon, "Principles of selective ion transport in channels and pumps," *Science*, vol. 310, no. 5753, pp. 1461–1465, 2005.

[70] W. Tezara, V. J. Mitchell, S. D. Driscoll, and D. W. Lawlor, "Water stress inhibits plant photosynthesis by decreasing coupling factor and ATP," *Nature*, vol. 401, no. 6756, pp. 914–917, 1999.

[71] S. K. Pal and A. H. Zewail, "Dynamics of water in biological recognition," *Chem. Rev.*, vol. 104, no. 4, pp. 2099–2123, 2004.

[72] P. Ball, "Water as an active constituent in cell biology," *Chem. Rev.*, vol. 108, no. 1, pp. 74–108, 2008.

[73] I. Dalle-Donne, R. Rossi, D. Giustarini, A. Milzani, and R. Colombo, "Protein carbonyl groups as biomarkers of oxidative stress," *Clin. Chim. Acta*, vol. 329, no. 1-2, pp. 23–38, 2003.

[74] C. D. Frisbie, L. F. Rozsnyai, A. Noy, M. S. Wrighton, and C. M. Lieber, "Functional group imaging by chemical force microscopy," *Science*, vol. 265, no. 5181, pp. 2071–2074, 1994.

[75] F. H. Westheimer, "Why nature chose phosphates," *Science*, vol. 235, no. 4793, pp. 1173–1178, 1987.

[76] R. Costard, T. Tyborski, B. P. Fingerhut, and T. Elsaesser, "Ultrafast phosphate hydration dynamics in bulk H_2O," *J. Chem. Phys.*, vol. 142, no. 21, p. 212406, 2015.

[77] D. J. Floisand and S. A. Corcelli, "Computational study of phosphate vibrations as reporters of DNA hydration," *J. Phys. Chem. Lett.*, vol. 6, no. 20, pp. 4012–4017, 2015.

[78] N. M. Levinson, E. E. Bolte, C. S. Miller, S. A. Corcelli, and S. G. Boxer, "Phosphate vibrations probe local electric fields and hydration in biomolecules," *J. Am. Chem. Soc.*, vol. 133, no. 34, pp. 13236–13239, 2011.

[79] M. H. F. Wilkins, A. E. Blaurock, and D. M. Engelman, "Bilayer structure in membranes," *Nat. New Biol.*, vol. 230, no. 11, pp. 72–76, 1971.

[80] M. S. Bretscher, "Asymmetrical lipid bilayer structure for biological membranes," *Nat. New Biol.*, vol. 236, no. 53, pp. 11–12, 1972.

[81] M. R. Villarreal, "https://commons.wikimedia.org/wiki/file:phospholipids_aqueous_solution_structures.svg," Aug 2015.

[82] M. Klingenberg, "The ADP-ATP translocation in mitochondria, a membrane potential controlled transport," *J. Membrane Biol.*, vol. 56, no. 2, pp. 97–105, 1980.

[83] G. M. Cooper, *The Cell: A Molecular Approach*. Sunderland (MA): Sinauer Associates, Inc., 2000.

[84] W. Saenger, W. N. Hunter, and O. Kennard, "DNA coformation is determined by economics in the hydration of phosphate groups," *Nature*, vol. 324, no. 27, pp. 385–388, 1986.

[85] M. Ströck, "https://de.wikipedia.org/wiki/desoxyribonukleinsäure#/media/file:dna_overview.png," Aug 2015.

[86] J. D. Watson and F. H. Crick, "Molecular structure of nucleic acids," *Nature*, vol. 171, no. 4356, pp. 737–738, 1953.

[87] T. Umehara, S. Kuwabara, S. Mashimo, and S. Yagihara, "Dielectric study on hydration of B-, A-, and Z-DNA," *Biopolymers*, vol. 30, no. 7-8, pp. 649–656, 1990.

[88] B. Schneider, K. Patel, and H. M. Berman, "Hydration of the phosphate group in double-helical DNA," *Biophys. J.*, vol. 75, no. 5, pp. 2422–2434, 1998.

[89] A. C. Fogarty, E. Duboue-Dijon, F. Sterpone, J. T. Hynes, and D. Laage, "Biomolecular hydration dynamics: a jump model perspective," *Chem. Soc. Rev.*, vol. 42, no. 13, pp. 5672–5683, 2013.

[90] S. J. Marrink and A. E. Mark, "Molecular dynamics simulation of the formation, structure, and dynamics of small phospholipid vesicles," *J. Am. Chem. Soc.*, vol. 125, no. 49, pp. 15233–15242, 2003.

[91] M. Yang, Ł. Szyc, and T. Elsaesser, "Vibrational dynamics of the water shell of DNA studied by femtosecond two-dimensional infrared spectroscopy," *J. Photochem. Photobiol. A: Chem.*, vol. 234, pp. 49–56, 2012.

[92] M. Yang, Ł. Szyc, and T. Elsaesser, "Femtosecond two-dimensional infrared spectroscopy of adenine-thymine base pairs in DNA oligomers," *J. Phys. Chem. B*, vol. 115, no. 5, pp. 1262–1267, 2011.

[93] S. K. Pal, L. Zhao, and A. H. Zewail, "Water at DNA surfaces: ultrafast dynamics in minor groove recognition," *Proc. Natl. Acad. Sci. USA*, vol. 100, no. 14, pp. 8113–8118, 2003.

[94] P. Auffinger and E. Westhoff, "Water and ion binding around RNA and DNA (C,G) oligomers," *J. Mol. Biol.*, vol. 300, no. 5, pp. 1113–1131, 2000.

[95] L. Yang and B. M. Pettitt, "B to A transition of DNA on the nanosecond time scale," *J. Phys. Chem.*, vol. 100, no. 7, pp. 2564–2566, 1996.

[96] J. Bredenbeck, A. Ghosh, H. K. Nienhuys, and M. Bonn, "Interface-specific ultrafast two-dimensional vibrational spectroscopy," *Acc. Chem. Res.*, vol. 42, no. 9, pp. 1332–1342, 2009.

[97] J. J. Loparo, S. T. Roberts, and A. Tokmakoff, "Multidimensional infrared spectroscopy of water. I. Vibrational dynamics in two-dimensional IR line shapes," *J. Chem. Phys.*, vol. 125, no. 19, p. 194521, 2006.

[98] J. B. Asbury, T. Steinel, K. Kwak, S. A. Corcelli, C. P. Lawrence, J. L. Skinner, and M. D. Fayer, "Dynamics of water probed with vibrational echo correlation spectroscopy," *J. Chem. Phys.*, vol. 121, no. 24, pp. 12431–12446, 2004.

[99] C. P. Lawrence and J. L. Skinner, "Vibrational spectroscopy of HOD in liquid D_2O. III. Spectral diffusion, and hydrogen-bonding and rotational dynamics," *J. Chem. Phys.*, vol. 118, no. 1, pp. 264–272, 2003.

[100] D. Laage and J. T. Hynes, "Do more strongly hydrogen-bonded water molecules reorient more slowly?," *Chem. Phys. Lett.*, vol. 433, no. 1-3, pp. 80–85, 2006.

[101] R. Rey, F. Ingrosso, T. Elsaesser, and J. T. Hynes, "Pathways for H_2O bend vibrational relaxation in liquid water," *J. Phys. Chem. A*, vol. 113, no. 31, pp. 8949–8962, 2009.

[102] G. M. Gale, G. Gallot, F. Hache, and N. Lascoux, "Femtosecond dynamics of hydrogen bonds in liquid water: A real time study," *Phys. Rev. Lett.*, vol. 82, no. 5, pp. 1068–1071, 1999.

[103] D. Laage and J. T. Hynes, "A molecular jump mechanism of water reorientation," *Science*, vol. 311, no. 5762, pp. 832–835, 2006.

[104] C. J. Fecko, J. D. Eaves, J. J. Loparo, A. Tokmakoff, and P. L. Geissler, "Ultrafast hydrogen-bond dynamics in the infrared spectroscopy of water," *Science*, vol. 301, no. 5640, pp. 1698–1702, 2003.

[105] S. Woutersen and H. J. Bakker, "Resonant intermolecular transfer of vibrational energy in liquid water," *Nature*, vol. 402, no. 6752, pp. 507–509, 1999.

[106] P. Hamm and J. Savolainen, "Two-dimensional-Raman-terahertz spectroscopy of water: Theory," *J. Chem. Phys.*, vol. 136, no. 9, p. 094516, 2012.

[107] P. Hamm, "2D-Raman-THz spectroscopy: a sensitive test of polarizable water models," *J. Chem. Phys.*, vol. 141, no. 18, p. 184201, 2014.

[108] J. Savolainen, S. Ahmed, and P. Hamm, "Two-dimensional Raman-terahertz spectroscopy of water," *Proc. Natl. Acad. Sci. USA*, vol. 110, no. 51, pp. 20402–20407, 2013.

[109] G. R. Low and H. G. Kjaergaard, "Calculation of OH-stretching band intensities of the water dimer and trimer," *J. Chem. Phys.*, vol. 110, no. 18, pp. 9104–9115, 1999.

[110] P. C. Singh, S. Nihonyanagi, S. Yamaguchi, and T. Tahara, "Ultrafast vibrational dynamics of water at a charged interface revealed by two-dimensional heterodyne-detected vibrational sum frequency generation," *J. Chem. Phys.*, vol. 137, no. 9, p. 094706, 2012.

[111] S. Pal, P. K. Maiti, B. Bagchi, and J. T. Hynes, "Multiple time scales in solvation dynamics of DNA in aqueous solution: The role of water, counterions, and cross-correlations," *J. Phys. Chem. B*, vol. 110, no. 51, pp. 26396–26402, 2006.

[112] S. Pal, P. K. Maiti, and B. Bagchi, "Exploring DNA groove water dynamics through hydrogen bond lifetime and orientational relaxation," *J. Chem. Phys.*, vol. 125, no. 23, p. 234903, 2006.

[113] K. E. Furse and S. A. Corcelli, "The dynamics of water at DNA interfaces: Computational studies of Hoechst 33258 bound to DNA," *J. Am. Chem. Soc.*, vol. 130, no. 39, pp. 13103–13109, 2008.

[114] W. Zhao, D. E. Moilanen, E. E. Fenn, and M. D. Fayer, "Water at the surfaces of aligned phospholipid multibilayer model membranes probed with ultrafast vibrational spectroscopy," *J. Am. Chem. Soc.*, vol. 130, no. 42, pp. 13927–13937, 2008.

[115] Ł. Szyc, M. Yang, and T. Elsaesser, "Ultrafast energy exchange via water-phosphate interactions in hydrated DNA," *J. Phys. Chem. B*, vol. 114, no. 23, pp. 7951–7957, 2010.

[116] N. E. Levinger, R. Costard, E. T. J. Nibbering, and T. Elsaesser, "Ultrafast energy migration pathways in self-assembled phospholipids interacting with confined water," *J. Phys. Chem. A*, vol. 115, no. 43, pp. 11952–11959, 2011.

[117] T. Siebert, B. Guchhait, Y. Liu, R. Costard, and T. Elsaesser, "Anharmonic backbone vibrations in ultrafast processes at the DNA-water interface," *J. Phys. Chem. B*, vol. 119, no. 30, pp. 9670–9677, 2015.

[118] B. Guchhait, Y. Liu, T. Siebert, and T. Elsaesser, "Ultrafast vibrational dynamics of the DNA backbone at different hydration levels mapped by two-dimensional infrared spectroscopy," *Struct. Dyn.*, vol. 3, no. 4, p. 043202, 2016.

[119] M. Yang, Ł. Szyc, and T. Elsaesser, "Decelerated water dynamics and vibrational couplings of hydrated DNA mapped by two-dimensional infrared spectroscopy," *J. Phys. Chem. B*, vol. 115, no. 44, pp. 13093–13100, 2011.

[120] R. Costard and T. Elsaesser, "Femtosecond OH bending dynamics of water nanopools confined in reverse micelles," *J. Phys. Chem. B*, vol. 117, no. 49, pp. 15338–15345, 2013.

[121] R. Costard, N. E. Levinger, E. T. J. Nibbering, and T. Elsaesser, "Ultrafast vibrational dynamics of water confined in phospholipid reverse micelles," *J. Phys. Chem. B*, vol. 116, no. 19, pp. 5752–5759, 2012.

[122] E. Steger and K. Herzog, "Infrarot- und Raman-spektren von Phosphatlösungen," *Z. anorg. allg. Chemie*, vol. 331, no. 3-4, pp. 169–182, 1964.

[123] S. A. Brándan, S. B. Díaz, R. C. Picot, E. A. Disalvo, and A. B. Altabef, "Hydration of inorganic phosphates in crystal lattices and in aqueous solution. An experimental and theoretical study," *Spectrochim. Acta Mol. Biomol. Spectrosc.*, vol. 66, no. 4-5, pp. 1152–1164, 2007.

[124] M. Klähn, G. Mathias, C. Kötting, M. Nonella, J. Schlitter, K. Gerwert, and P. Tavan, "IR spectra of phosphate ions in aqueous solution: Predictions of a DFT/MM approach compared with observations," *J. Phys. Chem. A*, vol. 108, no. 29, pp. 6186–6194, 2004.

[125] J. VandeVondele, P. Tröster, P. Tavan, and G. Mathias, "Vibrational spectra of phosphate ions in aqueous solution probed by first-principles molecular dynamics," *J. Phys. Chem. A*, vol. 116, no. 10, pp. 2466–2474, 2012.

[126] H. R. Zelsmann, "Temperature dependence of the optical constants for liquid H_2O and D_2O in the far IR region," *J. Mol. Struct.*, vol. 350, no. 2, pp. 95–114, 1995.

[127] S. Ashihara, N. Huse, A. Espagne, E. T. J. Nibbering, and T. Elsaesser, "Ultrafast structural dynamics of water induced by dissipation of vibrational energy," *J. Phys. Chem. A*, vol. 111, no. 5, pp. 743–746, 2007.

[128] R. Kumar, J. R. Schmidt, and J. L. Skinner, "Hydrogen bonding definitions and dynamics in liquid water," *J. Chem. Phys.*, vol. 126, no. 20, p. 204107, 2007.

[129] O. Markovitch and N. Agmon, "Reversible geminate recombination of hydrogen-bonded water molecule pair," *J. Chem. Phys.*, vol. 129, no. 8, p. 084505, 2008.

[130] E. Tang, D. Di Tommaso, and N. H. de Leeuw, "Hydrogen transfer and hydration properties of $H_nPO_4^{3-n}$ ($n = 0 - 3$) in water studied by first principles molecular dynamics simulations," *J. Chem. Phys.*, vol. 130, no. 23, p. 234502, 2009.

[131] H. S. Lee and M. E. Tuckerman, "Dynamical properties of liquid water from *ab initio* molecular dynamics performed in the complete basis set limit," *J. Chem. Phys.*, vol. 126, no. 16, p. 164501, 2007.

[132] A. Bankura, V. Carnevale, and M. L. Klein, "Hydration structure of salt solutions from *ab initio* molecular dynamics," *J. Chem. Phys.*, vol. 138, no. 1, p. 014501, 2013.

[133] A. B. Pribil, T. S. Hofer, B. R. Randolf, and B. M. Rode, "Structure and dynamics of phosphate ion in aqueous solution: An *ab initio* QMCF MD study," *J. Comput. Chem.*, vol. 29, no. 14, pp. 2330–2334, 2008.

[134] A. Luzar and D. Chandler, "Hydrogen-bond kinetics in liquid water," *Nature*, vol. 379, no. 6560, pp. 55–57, 1996.

[135] N. Huse, S. Ashihara, E. T. J. Nibbering, and T. Elsaesser, "Ultrafast vibrational relaxation of O-H bending and librational excitations in liquid H_2O," *Chem. Phys. Lett.*, vol. 404, no. 4-6, pp. 389–393, 2005.

[136] S. Ashihara, N. Huse, A. Espagne, E. T. J. Nibbering, and T. Elsaesser, "Vibrational couplings and ultrafast relaxation of the O-H bending mode in liquid H_2O," *Chem. Phys. Lett.*, vol. 424, no. 1-3, pp. 66–70, 2006.

[137] S. Ashihara, S. Fujioka, and K. Shibuya, "Temperature dependence of vibrational relaxation of the OH bending excitation in liquid H_2O," *Chem. Phys. Lett.*, vol. 502, no. 1-3, pp. 57–62, 2011.

[138] R. Costard, T. Tyborski, and B. P. Fingerhut, "Anharmonicities and coherent vibrational dynamics of phosphate ions in bulk H_2O," *Phys. Chem. Chem. Phys.*, vol. 17, no. 44, pp. 29906–29917, 2015.

[139] J. D. Eaves, J. J. Loparo, C. J. Fecko, S. T. Roberts, A. Tokmakoff, and P. L. Geissler, "Hydrogen bonds in liquid water are broken only fleetingly," *Proc. Natl. Acad. Sci. USA*, vol. 102, no. 37, pp. 13019–13022, 2005.

[140] T. L. Jansen, B. M. Auer, M. Yang, and J. L. Skinner, "Two-dimensional infrared spectroscopy and ultrafast anisotropy decay of water," *J. Chem. Phys.*, vol. 132, no. 22, p. 224503, 2010.

[141] K. Gawrisch, D. Ruston, J. Zimmerberg, V. A. Parsegian, R. P. Rand, and N. Fuller, "Membrane dipole potentials, hydration forces, and the ordering of water at membrane surfaces," *Biophys. J.*, vol. 61, no. 5, pp. 1213–1223, 1992.

[142] M. Pasenkiewicz-Gierula, Y. Takaoka, H. Miyagawa, K. Kitamura, and A. Kusumi, "Hydrogen bonding of water to phosphatidylcholine in the membrane as studied by a molecular dynamics simulation: Location, geometry, and lipid-lipid bridging via hydrogen-bonded water," *J. Phys. Chem. A*, vol. 101, no. 20, pp. 3677–3691, 1997.

[143] Ł. Szyc, *Ultrafast Vibrational Dynamics of Hydrogen-Bonded Base Pairs and Hydrated DNA*. PhD thesis, Humboldt-Universität zu Berlin, Berlin, 2011.

[144] P. Hansia, N. Guruprasad, and S. Vishveshwara, "Ab initio studies on the tri- and diphosphate fragments of adenosine triphosphate," *Biophys. Chem.*, vol. 119, no. 2, pp. 127–136, 2006.

[145] F. Xia, T. Rudack, Q. Cui, C. Kotting, and K. Gerwert, "Detailed structure of the $H_2PO_4^-$-guanosine diphosphate intermediate in Ras-GAP decoded from FTIR experiments by biomolecular simulations," *J. Am. Chem. Soc.*, vol. 134, no. 49, pp. 20041–20044, 2012.

[146] J. Akola and R. O. Jones, "ATP hydrolysis in water - a density functional study," *J. Phys. Chem. B*, vol. 107, no. 42, pp. 11774–11783, 2003.

[147] V. Cepus, A. J. Scheidig, R. S. Goody, and K. Gerwert, "Time-resolved FTIR studies of the GTPase reaction of H-*Ras* P21 reveal a key role for the beta-phosphate," *Biochemistry*, vol. 37, no. 28, pp. 10263–10271, 1998.

[148] A. Barth, K. Hauser, W. Maentele, J. E. T. Corrie, and D. R. Trentham, "Photochemical release of ATP from "Caged ATP" studied by time-resolved infrared spectroscopy," *J. Am. Chem. Soc.*, vol. 117, no. 41, pp. 10311–10316, 1995.

[149] J. Chen and B. Kohler, "Base stacking in adenosine dimers revealed by femtosecond transient absorption spectroscopy," *J. Am. Chem. Soc.*, vol. 136, no. 17, pp. 6362–6372, 2014.

[150] A. Züttel, A. Remhof, A. Borgschulte, and O. Friedrichs, "Hydrogen: the future energy carrier," *Philos. Trans. R. Soc.*, vol. 368, no. 1923, pp. 3329–3342, 2010.

[151] A. Züttel, A. Borgschulte, and L. Schlapbach, *Hydrogen as a Future Energy Carrier*. Weinheim: WILEY-VCH Verlag GmbH & Co. KGaA, 2008.

[152] L. Schlapbach and A. Züttel, "Hydrogen-storage materials for mobile applications," *Nature*, vol. 414, no. 6861, pp. 353–357, 2001.

[153] J. Graetz, "New approaches to hydrogen storage," *Chem. Soc. Rev.*, vol. 38, no. 1, pp. 73–82, 2009.

[154] K. Maeda, T. Takata, M. Hara, N. Saito, Y. Inoue, H. Kobayashi, and K. Domen, "GaN:ZnO solid solution as a photocatalyst for visible-light-driven overall water splitting," *J. Am. Chem. Soc.*, vol. 127, no. 23, pp. 8286–8287, 2005.

[155] X. Wang, K. Maeda, A. Thomas, K. Takanabe, G. Xin, J. M. Carlsson, K. Domen, and M. Antonietti, "A metal-free polymeric photocatalyst for hydrogen production from water under visible light," *Nat. Mater.*, vol. 8, no. 1, pp. 76–80, 2009.

[156] A. Fujishima and K. Honda, "Electrochemical photolysis of water at a semiconductor electrode," *Nature*, vol. 238, no. 5358, pp. 37–38, 1972.

[157] T. Tyborski, C. Merschjann, S. Orthmann, F. Yang, M. C. Lux-Steiner, and T. Schedel-Niedrig, "Crystal structure of polymeric carbon nitride and the determination of its process-temperature-induced modifications," *J. Phys.: Condens. Matter.*, vol. 25, no. 39, p. 395402, 2013.

[158] T. Tyborski, C. Merschjann, S. Orthmann, F. Yang, M. C. Lux-Steiner, and T. Schedel-Niedrig, "Tunable optical transition in polymeric carbon nitrides synthesized via bulk thermal condensation," *J. Phys.: Condens. Matter.*, vol. 24, no. 16, p. 162201, 2012.

[159] C. Merschjann, T. Tyborski, S. Orthmann, F. Yang, K. Schwarzburg, M. Lublow, M. C. Lux-Steiner, and T. Schedel-Niedrig, "Photophysics of polymeric carbon nitride: An optical quasimonomer," *Phys. Rev. B*, vol. 87, no. 20, p. 205204, 2013.

[160] F. Yang, M. Lublow, S. Orthmann, C. Merschjann, T. Tyborski, M. Rusu, S. Kubala, A. Thomas, R. Arrigo, M. Havecker, and T. Schedel-Niedrig, "Metal-free photocatalytic graphitic carbon nitride on p-type chalcopyrite as a composite photocathode for light-induced hydrogen evolution," *ChemSusChem*, vol. 5, no. 7, pp. 1227–1232, 2012.

[161] C. Merschjann, S. Tschierlei, T. Tyborski, K. Kailasam, S. Orthmann, D. Hollmann, T. Schedel-Niedrig, A. Thomas, and S. Lochbrunner, "Complementing graphenes: 1D interplanar charge transport in polymeric graphitic carbon nitrides," *Adv. Mater.*, vol. 27, no. 48, pp. 7993–7999, 2015.

[162] P. Dantzer, "Properties of intermetallic compounds suitable for hydrogen storage applications," *Mater. Sci. Eng.*, vol. A329-331, pp. 313–320, 2002.

[163] M. Gupta, "Electronic structure and stability of hydrides of intermetallic compounds," *J. Alloy. Compd.*, vol. 293-295, pp. 190–201, 1999.

[164] W. Grochala and P. P. Edwards, "Thermal decomposition of the non-interstitial hydrides for the storage and production of hydrogen," *Chem. Rev.*, vol. 104, no. 3, pp. 1283–1315, 2004.

[165] S.-i. Orimo, Y. Nekamori, J. R. Eliseo, A. Züttel, and C. M. Jensen, "Complex hydrides for hydrogen storage," *Chem. Rev.*, vol. 107, no. 10, pp. 4111–4132, 2007.

[166] A. M. Soldate, "Crystal structure of sodium borohydride," *J. Am. Chem. Soc.*, vol. 69, no. 5, pp. 987–988, 1947.

[167] R. S. Kumar and A. L. Cornelius, "Structural transitions in $NaBH_4$ under pressure," *Appl. Phys. Lett.*, vol. 87, no. 26, p. 261916, 2005.

[168] Y. Song, "New perspectives on potential hydrogen storage materials using high pressure," *Phys. Chem. Chem. Phys.*, vol. 15, no. 35, pp. 14524–14547, 2013.

[169] G. Lee, J.-Y. Lee, and J. S. Kim, "Ab initio P-T phase diagram of $NaBH_4$," *Solid State Commun.*, vol. 139, no. 10, pp. 516–521, 2006.

[170] J. Urgnani, F. Torres, M. Palumbo, and M. Baricco, "Hydrogen release from solid state $NaBH_4$," *Int. J. Hydrogen Energy*, vol. 33, no. 12, pp. 3111–3115, 2008.

[171] C. H. Giammanco, P. L. Kramer, and M. D. Fayer, "Dynamics of dihydrogen bonding in aqueous solutions of sodium borohydride," *J. Phys. Chem. B*, vol. 119, no. 8, pp. 3546–3559, 2015.

[172] T. Tyborski, R. Costard, M. Woerner, and T. Elsaesser, "Ultrafast vibrational dynamics of BH_4^- ions in liquid and crystalline environments," *J. Chem. Phys.*, vol. 141, no. 3, p. 034506, 2014.

[173] P. Fischer and A. Züttel, "Order-disorder phase transition in $NaBD_4$," *Mater. Sci. Forum*, vol. 443-444, pp. 287–290, 2004.

[174] V. Juvé, M. Holtz, F. Zamponi, M. Woerner, T. Elsaesser, and A. Borgschulte, "Field-driven dynamics of correlated electrons in LiH and $NaBH_4$ revealed by femtosecond X-Ray diffraction," *Phys. Rev. Lett.*, vol. 111, no. 21, p. 217401, 2013.

[175] A.-M. Racu, J. Schoenes, Z. Łodziana, A. Borgschulte, and A. Züttel, "High-resolution Raman spectroscopy study of phonon modes in $LiBH_4$ and $LiBD_4$," *J. Phys. Chem. A*, vol. 112, no. 40, pp. 9716–9722, 2008.

[176] V. D'Anna, L. M. Lawson Daku, and H. Hagemann, "Vibrational spectra and structure of borohydrides," *J. Alloy. Compd.*, vol. 580, pp. S122–S124, 2013.

[177] R. Gremaud, A. Züttel, A. Borgschulte, A. J. Ramirez-Cuesta, K. Refson, and D. Colognesi, "Origin of the large anharmonicity in the phonon modes of $LiBH_4$," *Chem. Phys.*, vol. 427, pp. 22–29, 2013.

[178] J. Stingl, F. Zamponi, B. Freyer, M. Woerner, T. Elsaesser, and A. Borgschulte, "Electron transfer in a virtual quantum state of $LiBH_4$ induced by strong optical fields and mapped by femtosecond X-Ray diffraction," *Phys. Rev. Lett.*, vol. 109, no. 14, p. 147402, 2012.

[179] J.-P. Soulié, G. Renaudin, R. Černý, and K. Yvon, "Lithium boro-hydride $LiBH_4$ I. Crystal structure," *J. Alloy. Compd.*, vol. 346, no. 1-2, pp. 200–205, 2002.

[180] R. L. Davis, "Structure of sodium tetradeuteroborate, $NaBD_4$," *J. Solid State Chem.*, vol. 59, no. 3, pp. 393–396, 1985.

[181] A. Remhof, Z. Łodziana, F. Buchter, P. Martelli, F. Pendolino, O. Friedrichs, A. Züttel, and J. P. Embs, "Rotational diffusion in $NaBH_4$," *J. Phys. Chem. C*, vol. 113, no. 38, pp. 16834–16837, 2009.

[182] N. Verdal, M. R. Hartman, T. Jenkins, D. J. DeVries, J. J. Rush, and T. J. Udovic, "Reorientational dynamics of $NaBH_4$ and KBH_4," *J. Phys. Chem. C*, vol. 114, no. 21, pp. 10027–10033, 2010.

[183] A. Remhof, Z. Łodziana, P. Martelli, O. Friedrichs, A. Züttel, A. V. Skripov, J. P. Embs, and T. Strässle, "Rotational motion of BH_4 units in $M BH_4$ (M=Li,Na,K) from quasielastic neutron scattering and density functional calculations," *Phys. Rev. B*, vol. 81, no. 21, p. 214304, 2010.

[184] D. Chernyshov, A. Bosak, V. Dmitriev, Y. Filinchuk, and H. Hagemann, "Low-lying phonons in $NaBH_4$ studied by inelastic scattering of synchrotron radiation," *Phys. Rev. B*, vol. 78, no. 17, p. 172104, 2008.

[185] D. G. Allis and B. S. Hudson, "Inelastic neutron scattering spectra of $NaBH_4$ and KBH_4: reproduction of anion mode shifts via periodic DFT," *Chem. Phys. Lett.*, vol. 385, no. 3-4, pp. 166–172, 2004.

[186] J. A. A. Ketelaar and C. J. H. Schutte, "The borohydride ion (BH_4^-) in a face-centred cubic alkali-halide lattice," *Spectrochim. Acta*, vol. 17, no. 12, pp. 1240–1243, 1961.

[187] W. C. Price, W. F. Sherman, and G. R. Wilkinson, "Infra-red studies on polyatomic ions isolated in alkali-halide lattices," *Spectrochim. Acta*, vol. 16, no. 6, pp. 663–676, 1960.

[188] M. T. Memon, G. R. Wilkinson, and W. F. Sherman, "Vibrational studies of BH_4^- and BD_4^- isolated in alkali halides," *J. Mol. Struct.*, vol. 80, pp. 113–116, 1982.

[189] M. I. Memon, W. F. Sherman, and G. R. Wilkinson, "BH_4^-, isolated in RbI internal and external modes of vibration as function of temperature and pressure as studied by Raman and i.r. spectroscopy," *Spectrochim. Acta*, vol. 37A, no. 7, pp. 461–472, 1981.

[190] G. Renaudin, S. Gomes, H. Hagemann, L. Keller, and K. Yvon, "Structural and spectroscopic studies on the alkali borohydrides MBH_4 (M = Na, K, Rb, Cs)," *J. Alloy. Compd.*, vol. 375, no. 1-2, pp. 98–106, 2004.

[191] O. Zavorotynska, M. Corno, A. Damin, G. Spoto, P. Ugliengo, and M. Baricco, "Vibrational properties of MBH_4 and MBF_4 crystals (M = Li, Na, K): A combined DFT, infrared, and Raman study," *J. Phys. Chem. C*, vol. 115, no. 38, pp. 18890–18900, 2011.

[192] K. B. Harvey and N. R. McQuaker, "Infrared and Raman spectra of potassium and sodium borohydride," *Can. J. Chem.*, vol. 49, no. 20, pp. 3272–3281, 1971.

[193] M. I. Memon, W. F. Sherman, and G. R. Wilkinson, "The Raman spectra of BH_4^- and BD_4^- isolated in alkali halides at 80 K," *J. Raman Spectrosc.*, vol. 13, no. 1, pp. 96–99, 1982.

[194] T. J. Tague and L. Andrews, "Reactions of pulsed-laser evaporated boron atoms with hydrogen. Infrared spectra of boron hydride intermediate species in solid argon," *J. Am. Chem. Soc.*, vol. 116, no. 11, pp. 4970–4976, 1994.

[195] P. Carbonnière and H. Hagemann, "Fermi resonances of borohydrides in a crystalline environment of alkali metals," *J. Phys. Chem. A*, vol. 110, no. 32, pp. 9927–9933, 2006.

[196] J. R. Durig, G. A. Guirgis, and D. A. C. Compton, "Analysis of torsional spectra of molecules with two internal C_{3v} rotors. 13.† vibrational assignments, torsional potential functions, and gas phase thermodynamic functions of isopropylamine$-d_0$ and $-d_2$," *J. Phys. Chem*, vol. 83, no. 10, pp. 1313–1323, 1979.

[197] J. R. Durig, J. J. Klaassen, I. D. Darkhalil, W. A. Herrebout, J. J. J. Dom, and B. J. van der Veken, "Conformational and structural studies of isopropylamine from temperature dependent Raman spectra of xenon solutions and ab initio calculations," *J. Mol. Struct.*, vol. 1009, pp. 30–41, 2012.

[198] T. Elsaesser and W. Kaiser, "Vibrational and vibronic relaxation of large polyatomic molecules in liquids," *Annu. Rev. Phys. Chem.*, vol. 42, pp. 83–107, 1991.

[199] W. T. Cronenwett and L. W. Hoogendoorn, "Low-frequency dielectric constant of methylamine, *n*-propylamine, and isopropylamine," *J. Chem. Eng. Data*, vol. 17, no. 3, pp. 298–300, 1972.

[200] R. J. Ouellette and J. D. Rawn, *Organic Chemistry: Structure, Mechanism, and Synthesis*. USA: Elsevier, 2014.

[201] T. Förster, "Zwischenmolekulare Energiewanderung und Fluoreszenz," *Ann. Phys.*, vol. 437, no. 1-2, pp. 55–75, 1948.

[202] A. Tokmakoff, "Lecture notes on Förster resonance energy transfer." MIT Departement of Chemistry, 3/25/08, 2008.

[203] D. B. Wong, K. P. Sokolowsky, M. I. El-Barghouthi, E. E. Fenn, C. H. Giammanco, A. L. Sturlaugson, and M. D. Fayer, "Water dynamics in water/DMSO binary mixtures," *J. Phys. Chem. B*, vol. 116, no. 18, pp. 5479–5490, 2012.

[204] H. Hagemann, Y. Filinchuk, D. Chernyshov, and W. Van Beek, "Lattice anharmonicity and structural evolution of $LiBH_4$: an insight from Raman and X-ray diffraction experiments," *Phase Transitions*, vol. 82, no. 4, pp. 344–355, 2009.

[205] M. J. van Setten, V. A. Popa, G. A. de Wijs, and G. Brocks, "Electronic structure and optical properties of lightweight metal hydrides," *Phys. Rev. B*, vol. 75, no. 3, p. 035204, 2007.

[206] P. Vajeeston, P. Ravindran, A. Kjekshus, and H. Fjellvåg, "Structural stability and electronic structure for Li_3AlH_6," *Phys. Rev. B*, vol. 69, no. 2, p. 020104(R), 2004.

[207] A. Aguayo and D. J. Singh, "Electronic structure of the complex hydride $NaAlH_4$," *Phys. Rev. B*, vol. 69, no. 15, p. 155103, 2004.

[208] Z. F. Hou, "First-principles investigation of $Mg(AlH_4)_2$ complex hydride," *J. Power Sources*, vol. 159, no. 1, pp. 111–115, 2006.

[209] P. Liu, W. L. Smith, H. Lotem, J. H. Bechtel, N. Bloembergen, and R. S. Adhav, "Absolute two-photon absorption coefficients at 355 and 266 nm," *Phys. Rev. B*, vol. 17, no. 12-15, pp. 4620–4632, 1978.

[210] M. Rumi and J. W. Perry, "Two-photon absorption: an overview of measurements and principles," *Adv. Opt. Photonics*, vol. 2, no. 4, pp. 451–518, 2010.

[211] A. Dragomir, J. G. McInerney, D. N. Nikogosyan, and P. G. Kazansky, "Two-photon absorption properties of commercial fused silica and germanosilicate glass at 264 nm," *Appl. Phys. Lett.*, vol. 80, no. 7, pp. 1114–1116, 2002.

[212] G. G. Gurzadyan and R. K. Ispiryan, "Two-photon absorption peculiarities of potassium dihydrogen phosphate crystal at 216 nm," *Appl. Phys. Lett.*, vol. 59, no. 6, pp. 630–631, 1991.

[213] S. A. Slattery and D. N. Nikogosyan, "Two-photon absorption at 210 nm in fused silica, crystalline quartz and some alkali halides," *Opt. Commun.*, vol. 228, no. 1-3, pp. 127–131, 2003.

[214] J. Tomkinson and T. C. Waddington, "Inelastic neutron scattering from the alkali metal borohydrides and calcium borohydride," *J. Chem. Soc., Faraday Trans. 2*, vol. 72, no. 0, pp. 528–538, 1976.

[215] P. Gaal, W. Kuehn, K. Reimann, M. Woerner, T. Elsaesser, and R. Hey, "Internal motions of a quasiparticle governing its ultrafast nonlinear response," *Nature*, vol. 450, no. 7173, pp. 1210–1213, 2007.

[216] C. Merschjann, D. Berben, M. Imlau, and M. Wöhlecke, "Evidence for two-path recombination of photoinduced small polarons in reduced $LiNbO_3$," *Phys. Rev. Lett.*, vol. 96, no. 18, p. 186404, 2006.

[217] O. F. Schirmer, M. Imlau, C. Merschjann, and B. Schoke, "Electron small polarons and bipolarons in $LiNbO_3$," *J. Phys.: Condens. Matter*, vol. 21, no. 12, p. 123201, 2009.

[218] W. H. Knox, R. L. Fork, M. C. Downer, D. A. B. Miller, D. S. Chemla, C. V. Shank, A. C. Gossard, and W. Wiegmann, "Femtosecond dynamics of resonantly excited excitons in room-temperature GaAs quantum wells," *Phys. Rev. Lett.*, vol. 54, no. 12, pp. 1306–1309, 1985.

[219] B. Deveaud, F. Clérot, N. Roy, K. Satzke, B. Sermage, and D. Katzer, "Enhanced radiative recombination of free excitons in GaAs quantum wells," *Phys. Rev. Lett.*, vol. 67, no. 17, pp. 2355–2358, 1991.

[220] E. Varene, L. Bogner, C. Bronner, and P. Tegeder, "Ultrafast exciton population, relaxation, and decay dynamics in thin oligothiophene films," *Phys. Rev. Lett.*, vol. 109, no. 20, p. 207601, 2012.

[221] T. B. Douglas and A. W. Harman, "Heat content of sodium borohydride and of potassium borohydride from 0 ° to 400 °C," *J. Res. Natl. Bur. Stand.*, vol. 60, no. 2, pp. 117–124, 1958.

[222] K. Reimann, "Table-top sources of ultrashort THz pulses," *Rep. Prog. Phys.*, vol. 70, no. 10, pp. 1597–1632, 2007.

[223] D. F. Walls and G. J. Milburn, "Effect of dissipation on quantum coherence," *Phys. Rev. A*, vol. 31, no. 4, pp. 2403–2408, 1985.

[224] P. Martelli, R. Caputo, A. Remhof, P. Mauron, A. Borgschulte, and A. Züttel, "Stability and decomposition of $NaBH_4$," *J. Phys. Chem. C*, vol. 114, no. 15, pp. 7173–7177, 2010.

[225] E. Ozbay, "Plasmonics: Merging photonics and electronics at nanoscale dimensions," *Science*, vol. 311, no. 189, pp. 189–193, 2006.

[226] H. A. Atwater and A. Polman, "Plasmonics for improved photovoltaic devices," *Nat. Mater.*, vol. 9, no. 3, pp. 205–213, 2010.

[227] S. A. Maier, *Plasmonics: Fundamentals and Applications*. Bath, UK: Springer Science+Business Meia LLC, 2007.

[228] C. Kittel, *Einführung in die Festkörperphysik*, vol. 14. München: Oldenbourg Wissenschaftsverlag GmbH, 2006.

[229] W. L. Barnes, A. Dereux, and T. W. Ebbesen, "Surface plasmon subwavelength optics," *Nature*, vol. 424, no. 6950, pp. 824–830, 2003.

[230] B. D. Fried and R. W. Gould, "Longitudinal ion oscillations in a hot plasma," *Phys. Fluids*, vol. 4, no. 1, pp. 139–147, 1961.

[231] J. B. Pendry, L. Martin-Moreno, and F. J. Garcia-Vidal, "Mimicking surface plasmons with structured surfaces," *Science*, vol. 305, no. 847, pp. 847–848, 2004.

[232] S. Chakraborty, O. P. Marshall, T. G. Folland, Y.-J. Kim, A. N. Grigorenko, and K. S. Novoselov, "Gain modulation by graphene plasmons in aperiodic lattice lasers," *Science*, vol. 351, no. 6270, pp. 246–248, 2016.

[233] S. Schietinger, M. Barth, T. Aichele, and O. Benson, "Plasmon-enhanced single photon emission from a nanoassembled metal-diamond hybrid structure at room temperature," *Nano Lett.*, vol. 9, no. 4, pp. 1694–1698, 2009.

[234] S. Schietinger, T. Aichele, H.-Q. Wang, T. Nann, and O. Benson, "Plasmon-enhanced upconversion in single $NaYF_4$:Yb^{3+}/Er^{3+} codoped nanocrystals," *Nano Lett.*, vol. 10, no. 1, pp. 134–138, 2010.

[235] A. P. Kulkarni, K. M. Noone, K. Munechika, S. R. Guyer, and D. S. Ginger, "Plasmon-enhanced charge carrier generation in organic photovoltaic films using silver nanoprisms," *Nano Lett.*, vol. 10, no. 4, pp. 1501–1505, 2010.

[236] K. R. Catchpole and A. Polman, "Plasmonic solar cells," *Opt. Express*, vol. 16, no. 26, pp. 21793–21800, 2008.

[237] K. Nakayama, K. Tanabe, and H. A. Atwater, "Plasmonic nanoparticle enhanced light absorption in GaAs solar cells," *Appl. Phys. Lett.*, vol. 93, no. 12, p. 121904, 2008.

[238] M. Schmid, R. Klenk, M. C. Lux-Steiner, M. Topič, and J. Krč, "Modeling plasmonic scattering combined with thin-film optics," *Nanotechnology*, vol. 22, no. 2, p. 025204, 2011.

[239] M. Schmid, J. Klaer, R. Klenk, M. Topič, and J. Krč, "Stability of plasmonic metal nanoparticles integrated in the back contact of ultra-thin Cu(In,Ga)S_2 solar cells," *Thin Solid Films*, vol. 527, pp. 308–313, 2013.

[240] D. K. Gramotnev and S. I. Bozhevolnyi, "Plasmonics beyond the diffraction limit," *Nature Photon.*, vol. 4, no. 2, pp. 83–91, 2010.

[241] T. W. Ebbesen, H. J. Lezec, H. F. Ghaemi, T. Thio, and P. A. Wolff, "Extraordinary optical transmission through sub-wavelength hole arrays," *Nature*, vol. 391, no. 6668, pp. 667–669, 1998.

[242] B. Lee, I.-M. Lee, S. Kim, D.-H. Oh, and L. Hesselink, "Review on subwavelength confinement of light with plasmonics," *J. Mod. Opt.*, vol. 57, no. 16, pp. 1479–1497, 2010.

[243] E. Kretschmann, "Die Bestimmung optischer Konstanten von Metallen durch Anregung von Oberflächenplasmaschwingungen," *Z. Phys.*, vol. 241, no. 4, pp. 313–324, 1971.

[244] C. Ropers, C. C. Neacsu, T. Elsaesser, M. Albrecht, M. B. Raschke, and C. Lienau, "Grating-coupling of surface plasmons onto metallic tips: A nanoconfined light source," *Nano Lett.*, vol. 7, no. 9, pp. 2784–2788, 2007.

[245] A. K. Sharma, R. Jha, and B. D. Gupta, "Fiber-optic sensors based on surface plasmon resonance: A comprehensive review," *IEEE Sensors J.*, vol. 7, no. 8, pp. 1118–1129, 2007.

[246] K. F. MacDonald, Z. L. Sámson, M. I. Stockman, and N. I. Zheludev, "Ultrafast active plasmonics," *Nature Photon.*, vol. 3, no. 1, pp. 55–58, 2008.

[247] D. Brinks, M. Castro-Lopez, R. Hildner, and N. F. van Hulst, "Plasmonic antennas as design elements for coherent ultrafast nanophotonics," *Proc. Natl. Acad. Sci. USA*, vol. 110, no. 46, pp. 18386–18390, 2013.

[248] M. Kauranen and A. V. Zayats, "Nonlinear plasmonics," *Nature Photon.*, vol. 6, no. 11, pp. 737–748, 2012.

[249] Y. Hamanaka, A. Nakamura, S. Omi, N. Del Fatti, F. Vallée, and C. Flytzanis, "Ultrafast response of nonlinear refractive index of silver nanocrystals embedded in glass," *Appl. Phys. Lett.*, vol. 75, no. 12, p. 1712, 1999.

[250] N. Del Fatti, C. Voisin, F. Chevy, F. Valleé, and C. Flytzanis, "Coherent acoustic mode oscillation and damping in silver nanoparticles," *J. Chem. Phys.*, vol. 110, no. 23, p. 11484, 1999.

[251] M. Perner, P. Bost, U. Lemmer, G. von Plessen, J. Feldmann, U. Becker, M. Mennig, M. Schmitt, and H. Schmidt, "Optically induced damping of the surface plasmon resonance in gold colloids," *Phys. Rev. Lett.*, vol. 78, no. 11, pp. 2192–2195, 1997.

[252] H. Inouye, K. Tanaka, I. Tanahashi, and K. Hirao, "Ultrafast dynamics of nonequilibrium electrons in a gold nanoparticle system," *Phys. Rev. B*, vol. 57, no. 18, pp. 11334–11340, 1998.

[253] S. Link and M. A. El-Sayed, "Spectral properties and relaxation dynamics of surface plasmon electronic oscillations in gold and silver nanodots and nanorods," *J. Phys. Chem. B*, vol. 103, no. 40, pp. 8410–8426, 1999.

[254] C. Voisin, N. Del Fatti, D. Christofilos, and F. Vallée, "Ultrafast electron dynamics and optical nonlinearities in metal nanoparticles," *J. Phys. Chem. B*, vol. 105, no. 12, pp. 2264–2280, 2001.

[255] G. V. Hartland, "Optical studies of dynamics in noble metal nanostructures," *Chem. Rev.*, vol. 111, no. 6, pp. 3858–3887, 2011.

[256] W. S. M. Werner, A. Ruocco, F. Offi, S. Iacobucci, W. Smekal, H. Winter, and G. Stefani, "Role of surface and bulk plasmon decay in secondary electron emission," *Phys. Rev. B*, vol. 78, no. 23, p. 233403, 2008.

[257] W. J. Pardee, G. D. Mahan, D. E. Eastman, R. A. Pollak, L. Ley, F. R. McFeely, S. P. Kowalczyk, and D. A. Shirley, "Analysis of surface- and bulk-plasmon contributions to X-Ray photoemission spectra," *Phys. Rev. B*, vol. 11, no. 10, pp. 3614–3616, 1975.

[258] P. M. T. M. van Attekum and J. M. Trooster, "Bulk- and surface-plasmon-loss intensities in photoelectron, Auger, and electron-energy-loss spectra of Mg metal," *Phys. Rev. B*, vol. 20, no. 6, pp. 2335–2340, 1979.

[259] L. Marton, J. A. Simpson, H. A. Fowler, and N. Swanson, "Plural scattering of 20-kev electrons in aluminum," *Phys. Rev.*, vol. 126, no. 1, pp. 182–192, 1962.

[260] L. Serra, F. Garcias, M. Barranco, N. Barberán, and J. Navarro, "Bulk-plasmon dispersion relations in metals," *Phys. Rev. B*, vol. 44, no. 4, pp. 1492–1498, 1991.

[261] J. Sprösser-Prou, A. vom Felde, and J. Fink, "Aluminum bulk-plasmon dispersion and its anisotropy," *Phys. Rev. B*, vol. 40, no. 8, pp. 5799–5801, 1989.

[262] D. M. Miliotis, "Bulk-plasmon dispersion spectrum of Be using an X-Ray scattering technique," *Phys. Rev. B*, vol. 3, no. 3, pp. 701–705, 1971.

[263] D. Pines and D. Bohm, "A collective description of electron interactions: II. Collective vs individual particle aspects of the interactions," *Phys. Rev.*, vol. 85, no. 2, pp. 338–353, 1952.

[264] W. Nolting, *Grundkurs Theoretische Physik 3 Elektrodynamik*, vol. 8. Berlin: Springer, 2007.

[265] M. A. Ordal, L. L. Long, R. J. Bell, S. E. Bell, R. R. Bell, R. W. Alexander, and C. A. Ward, "Optical properties of the metals Al, Co, Cu, Au, Fe, Pb, Ni, Pd, Pt, Ag, Ti, and W in the infrared and far infrared," *Appl. Opt.*, vol. 22, no. 7, pp. 1099–1119, 1983.

[266] H. U. Yang, J. D'Archangel, M. L. Sundheimer, E. Tucker, G. D. Boreman, and M. B. Raschke, "Optical dielectric function of silver," *Phys. Rev. B*, vol. 91, no. 23, p. 235137, 2015.

[267] D. W. Berreman, "Infrared absorption at longitudinal optic frequency in cubic crystal films," *Phys. Rev.*, vol. 130, no. 6, pp. 2193–2198, 1963.

[268] J. M. Pitarke, V. M. Silkin, E. V. Chulkov, and P. M. Echenique, "Theory of surface plasmons and surface-plasmon polaritons," *Rep. Prog. Phys.*, vol. 70, no. 1, pp. 1–87, 2007.

[269] E. O. Kane, "Thomas-Fermi approach to impure semiconductor band structure," *Phys. Rev.*, vol. 131, no. 1, pp. 79–88, 1963.

[270] B. Ullrich, A. K. Singh, M. Bhowmick, P. Barik, D. Ariza-Flores, H. Xi, and J. W. Tomm, "Photoluminescence lineshape of ZnO," *AIP Adv.*, vol. 4, no. 12, p. 123001, 2014.

[271] B.-C. Shih, Y. Xue, P. Zhang, M. L. Cohen, and S. G. Louie, "Quasiparticle band gap of ZnO: High accuracy from the conventional G^0W^0 approach," *Phys. Rev. Lett.*, vol. 105, no. 14, p. 146401, 2010.

[272] B. H. Bairamov, A. Heinrich, G. Irmer, V. V. Toporov, and E. Ziegler, "Raman study of the phonon halfwidths and the phonon-plasmon coupling in ZnO," *Phys. Status Solidi B*, vol. 119, no. 1, pp. 227–234, 1983.

[273] A. Mooradian and G. B. Wright, "Observation of the interaction of plasmons with longitudinal optical phonons in GaAs," *Phys. Rev. Lett.*, vol. 16, no. 22, pp. 999–1001, 1966.

[274] B. B. Varga, "Coupling of plasmons to polar phonons in degenerate semiconductors," *Phys. Rev.*, vol. 137, no. 6A, pp. A1896–A1902, 1965.

[275] Z. Wang, K. Reimann, M. Woerner, T. Elsaesser, D. Hofstetter, J. Hwang, W. J. Schaff, and L. F. Eastman, "Optical phonon sidebands of electronic intersubband absorption in strongly polar semiconductor heterostructures," *Phys. Rev. Lett.*, vol. 94, no. 3, p. 037403, 2005.

[276] G. L. Eesley, "Observation of nonequilibrium electron heating in copper," *Phys. Rev. Lett.*, vol. 51, no. 23, pp. 2140–2143, 1983.

[277] C. Thomsen, J. Strait, Z. Vardeny, H. J. Maris, J. Tauc, and J. J. Hauser, "Coherent phonon generation and detection by picosecond light pulses," *Phys. Rev. Lett.*, vol. 53, no. 10, pp. 989–992, 1984.

[278] C. Thomsen, H. T. Grahn, H. J. Maris, and J. Tauc, "Surface generation and detection of phonons by picosecond light pulses," *Phys. Rev. B*, vol. 34, no. 6, pp. 4129–4138, 1986.

[279] M. van Exter and A. Lagendijk, "Ultrashort surface-plasmon and phonon dynamics," *Phys. Rev. Lett.*, vol. 60, no. 1, pp. 49–52, 1988.

[280] S. Adachi, *Handbook on Physical Properties of Semiconductors*, vol. 3 II-VI Compound Semiconductors. USA: Kluwer Academic Publishers, 2004.

[281] R. Adair, L. L. Chase, and S. A. Payne, "Nonlinear refractive index of optical crystals," *Phys. Rev. B*, vol. 39, no. 5, pp. 3337–3350, 1989.

[282] T. Elsaesser, J. Shah, L. Rota, and P. Lugli, "Initial thermalization of photoexcited carriers in GaAs studied by femtosecond luminescence spectroscopy," *Phys. Rev. Lett.*, vol. 66, no. 13, pp. 1757–1760, 1991.

[283] R. A. Kaindl, K. Reimann, M. Woerner, T. Elsaesser, R. Hey, and K. H. Ploog, "Homogeneous broadening and excitation-induced dephasing of intersubband transitions in a quasi-two-dimensional electron gas," *Phys. Rev. B*, vol. 63, no. 16, p. 161308(R), 2001.

[284] E. O. Kane, "Zener tunneling in semiconductors," *J. Phys. Chem. Solids*, vol. 12, no. 2, pp. 181–188, 1959.

[285] W. S. Baer, "Faraday rotation in ZnO: Determination of the electron effective mass," *Phys. Rev.*, vol. 154, no. 3, pp. 785–789, 1967.

[286] A. R. Hutson, "Piezoelectric scattering and phonon drag in ZnO and CdS," *J. Appl. Phys.*, vol. 32, no. 10, pp. 2287–2292, 1961.

[287] K. Hümmer, "Interband magnetoreflection of ZnO," *Phys. Status Solidi B*, vol. 56, no. 1, pp. 249–260, 1973.

[288] E. Šermukšnis, J. Liberis, M. Ramonas, A. Matulionis, M. Toporkov, H. Y. Liu, V. Avrutin, U. Özgür, and H. Morkoç, "Hot-electron energy relaxation time in Ga-doped ZnO films," *J. Appl. Phys.*, vol. 117, no. 6, p. 065704, 2015.

[289] A. Yamamoto, T. Kido, T. Goto, Y. Chen, T. Yao, and A. Kasuya, "Dynamics of photoexcited carriers in ZnO epitaxial thin films," *Appl. Phys. Lett.*, vol. 75, no. 4, pp. 469–471, 1999.

[290] M. Guk, C. Merschjann, I. Bodnar, T. Tyborski, T. Schedel-Niedrig, M. Lux-Steiner, and E. Arushanov, "Photoluminescence spectra of $MnIn_2S_4$," *Opt. Mater.*, vol. 34, no. 5, pp. 915–919, 2012.

[291] M. Woerner, T. Elsaesser, and W. Kaiser, "Relaxation processes of hot holes in p-type germanium studied by picosecond infrared spectroscopy," *Phys. Rev. B*, vol. 45, no. 15, pp. 8378–8387, 1992.

[292] M. Woerner, W. Frey, M. T. Portella, C. Ludwig, T. Elsaesser, and W. Kaiser, "Ultrafast thermalization of nonequilibrium holes in p-type germanium studied by femtosecond infrared spectroscopy," *Phys. Rev. B*, vol. 49, no. 24, pp. 17007–17010, 1994.

[293] M. Woerner and T. Elsaesser, "Ultrafast thermalization of nonequilibrium holes in p-type tetrahedral semiconductors," *Phys. Rev. B*, vol. 51, no. 24, pp. 17490–17498, 1995.

[294] J. F. Young and P. J. Kelly, "Many-body treatment of hot-electron scattering from quasiequilibrium electron-hole plasmas and coupled plasmon - longitudinal-optic-phonon modes in GaAs," *Phys. Rev. B*, vol. 47, no. 11, pp. 6316–6329, 1993.

[295] A. F. J. Levi and Y. Yafet, "Nonequilibrium electron transport in bipolar devices," *Appl. Phys. Lett.*, vol. 51, no. 1, pp. 42–44, 1987.

[296] P. Sippel, W. Albrecht, J. C. van der Bok, R. J. A. Van Dijk-Moes, T. Hannappel, R. Eichberger, and D. Vanmaekelbergh, "Femtosecond cooling of hot electrons in CdSe quantum-well platelets," *Nano Lett.*, vol. 15, no. 4, pp. 2409–2416, 2015.

[297] P. Bowlan, W. Kuehn, K. Reimann, M. Woerner, T. Elsaesser, R. Hey, and C. Flytzanis, "Nonlinear electron transport in an electron-hole plasma," *Phys. Rev. B*, vol. 85, no. 16, p. 165206, 2012.

[298] I. Waldmüller, J. Förstner, S.-C. Lee, A. Knorr, M. Woerner, K. Reimann, R. A. Kaindl, T. Elsaesser, R. Hey, and K. H. Ploog, "Optical dephasing of coherent intersubband transitions in a quasi-two-dimensional electron gas," *Phys. Rev. B*, vol. 69, no. 20, p. 205307, 2004.

Danksagung

Die Forschungsarbeit, die dieser Dissertation zu Grunde liegt, hat durch viele beteiligte Personen maßgebliche Unterstützung erhalten. Diesen Personen möchte ich an dieser Stelle ausdrücklich meinen Dank aussprechen.
Bei meiner Kristina möchte ich mich für das stets warme Umfeld bedanken und die viele Rücksicht, die ich für das Gelingen dieser Arbeit genossen habe.
Meinen Eltern danke ich für die stetige und vorbehaltlose Unterstützung, die ich seit jeher von ihnen erfahren habe.
Bei meinem Bruder Christoph möchte ich mich für einen intrinsischen Konkurrenzdruck bedanken, den das Zwillingsdasein ja doch irgendwie bereithält. Meiner Schwester Bettina und ihrer Familie danke ich für schöne Stunden abseits des Doktorandenlebens.
Herrn Thomas Elsässer danke ich für die erhaltene Möglichkeit am Max-Born-Institut mit dessen außergewöhnlich guter experimenteller Ausstattung als Doktorand zu arbeiten und zu promovieren. Darüber hinaus möchte ich mich bei ihm für die Betreuung und den Einsatz beim Bewältigen der Forschungsprojekte bedanken, die durch seine zahlreichen Beiträge, Ideen und Hinweise substanziell vorangetrieben wurden.
Den Verantwortlichen der Graduate-School "DinL - Dynamics in new Light" Martin Weinelt und Marc Vrakking sowie Andreas Knorr bin ich für deren Administration und Betreuung zu Dank verpflichtet.
Bei den zwei weiteren Gutachtern meiner schriftlichen Arbeit Herr Peter Hamm und Herr Oliver Benson sowie bei den weiteren Kommissionsmitgliedern Herr Jürgen P. Rabe und Herr Achim Peters möchte ich mich für die eingebrachte Zeit und Mühe bedanken.
Günter Steinmeyer danke ich für das mir entgegengebrachte Vertrauen während des Bewerbungsprozesses und zahlreiche fachbezogene Diskussionen.
Michael Wörner hat durch stetige fachliche Unterstützung entscheidend zum Gelingen dieser Arbeit beigetragen. Für die vielen beantworteten Fragen, Modellrechnungen und den Einsatz im Labor möchte ich ihm herzlich danken.
Erik Nibbering konnte ich jederzeit mit Fragen zur Chemie und Schwingungsspektroskopie ansprechen um sachdienliche Tipps und Hinweise zu erhalten.
Bei Klaus Reimann bin ich stets auf ein offenes Ohr gestoßen, um physikalische Sachverhalte zu klären, die von theoretischer Natur sein konnten oder eine experimentelle Umsetzung im Labor beinhalteten.
In Zusammenarbeit mit René Costard habe ich die IR-Labore und insbesondere 2D-IR-Spektroskopie kennengelernt. Für die Geduld und die Betreuung beim Aneignen der nötigen Kenntnisse zum selbständigen Arbeiten und darüber hinaus möchte ich mich bei ihm bedanken.
Bei Benjamin P. Fingerhut möchte ich mich für die Aufnahme in sein sehr ruhiges und damit angenehmes Büro bedanken und die vielen beanworteten Fragen im Bereich der molekularen Schwingungsdynamik.
Meinen ehemaligen Kollegen Thomas Schedel-Niedrig und Christoph Merschjann danke ich herzlich für die anhaltende und konstruktive Zusammenarbeit.
Einer Vielzahl weiterer Personen bin ich zu Dank verpflichtet. Der verstorbene Fritz Henneberger hat durch sein Engagement und die zur Verfügung gestellten ZnO:Ga-Proben die Grundlage für das Projekt zur Bestimmung der nichtlinearen Antwort eines Volumenplasmons gelegt. Christos Flytzanis und Jens W. Tomm haben mir allerlei Denkanstöße zu Plasmonen und auch zu Themen darüber hinaus gegeben. Der Glasbläsermeister Horst Müller aus Adlershof hat durch äußerst kurzfristige und unentgeltliche Hilfe bei der Herstellung und Modifikation der Glaskomponenten des liquid jets zu dessen schneller

Realisierung beigetragen. Regina Lendt, Peter Scholze und Monika Tischer haben durch ausgeklügelte Beiträge im Chemielabor und bei der technischen Umsetzung von Versuchsaufbauten gewichtig zum Gelingen der experimentellen Projekte beigetragen. Meinen aktuellen und ehemaligen Doktorandenkollegen/innen Sebastian Friede, Bastian Borchers, Simon Birkholz, Martin Hempel, Christian Greve, Benjamin Freyer, Johannes Stingl, Marcel Holtz, Jannick Weißhaupt, Carmine Somma, Giulia Folpini, Antonio Hernandez Salvador, Mirabelle Prémont-Schwarz, Yingliang Liu, Peter Trabs, Janne Hyyti und Mara Oßwald danke ich für ein lockeres, kommunikatives und hilfsbereites Umfeld.
Den Wissenschaftlern und Post-Doktoranden Flavio Zamponi, Torsten Siebert, Vincent Juvé, Sascha Kalusniak, Martin Richter, Sergey Sadofev, Maria Ekimova, Sergei Kühn und Biswajit Guchhait danke ich ebenfalls für einen hilfsbereiten Umgang und häufiger zweckdienlicher Unterstützung.
Claudia Brigel, Alexandra Wettstein, Margret Lehmann und Gabriele Kordaß danke ich für Hilfe bei verwaltungstechnischen Vorgängen.

Selbständigkeitserklärung

Hiermit erkläre ich, dass die vorliegende Dissertation selbständig von mir und nur unter Verwendung der angegebenen Literatur und Hilfsmittel verfasst wurde.

Ich habe mich nicht anderwärts um einen Doktorgrad im Promotionsfach Physik beworben und besitze auch keinen entsprechenden Doktorgrad.

Darüber hinaus habe ich die Promotionsordnung aus dem Jahr 2009, die dem laufenden Promotionsverfahren zu Grunde liegt, zu Kenntnis genommen.